



université de bretagne
occidentale



THÈSE DE DOCTORAT
UNIVERSITÉ DE BRETAGNE OCCIDENTALE
sous le sceau de l'Université européenne de Bretagne
pour obtenir le titre de
DOCTEUR DE L'UNIVERSITÉ DE BRETAGNE OCCIDENTALE
Mention : océanographie physique

présentée par

Fabien Leckler

Préparée à l'IFREMER

Observation et modélisation du déferlement des vagues

Thèse soutenue le 18 Décembre 2013

devant le jury composé de :

Xavier CARTON

Professeur, Université de Bretagne Occidentale
Président de jury

Philippe FORGET

Directeur de recherche, Université du Toulon
Rapporteur

Alain WEILL

Directeur de recherche, Université Pierre et Marie Curie
Rapporteur

Danièle HAUSER

Directrice de recherche, Université Pierre et Marie Curie
Examinatrice

Alvise BENETAZZO

Chercheur, CNR-ISMAR, Venezia, Italia
Examineur

Fabrice ARDHUIN

Chercheur, IFREMER
Directeur de thèse

Résumé

Les récentes paramétrisations utilisées dans les modèles spectraux de vagues offrent des résultats intéressants en termes de prévision et rejeux des états de mer. Cependant, de nombreux phénomènes physiques présents dans ces modèles sont encore mal compris et donc mal modélisés, notamment le terme de dissipation lié au déferlement des vagues. Le travail présenté dans cette thèse vise dans un premier temps à analyser et critiquer les paramétrisations existantes de la dissipation, au travers de la modélisation explicite des propriétés du déferlement sous-jacentes. Du constat de l'échec de ces paramétrisations à reproduire les observations *in situ* et satellite du déferlement, une nouvelle méthode d'observation et d'analyse des déferlements est proposée à l'aide de systèmes de stéréovidéo. Cette méthode permet l'observation des déferlements sur des surfaces de mer reconstruites à haute résolution par stéréotriangulation. Ainsi, une méthode complète de reconstruction des surfaces de mer en présence de vagues déferlantes est proposée et validée. La détection des vagues déferlantes sur les images et leur reprojection sur les surfaces reconstruites est également discutée. Bien que peu d'acquisitions soient disponibles, les différents paramètres observables grâce à l'utilisation de la stéréovidéo sont mis en avant. Ce travail montre l'intérêt des systèmes vidéo stéréo pour une meilleure observation et compréhension du déferlement des vagues, pour le développement des paramétrisations de la dissipation dans les modèles spectraux de vague.

Abstract

The recent parameterizations used in spectral wave models provide today interesting results in terms of forecast and hindcast of the sea states. Nevertheless, many physical phenomena present in these models are still poorly understood and therefore poorly modeled, in particular the dissipation source term due to breaking. First, the work presented in this thesis is aimed at analyzing and criticizing the existing parameterizations of the dissipation through the explicit modeling of the underlying properties of breaking. The finding of the failure of these parameterizations to reproduce the *in situ* and satellite observations, a new method for the observation and the analysis of breaking is proposed using stereo video systems . This method allows the observation of breaking waves on the high-resolution stereo-reconstructed sea surfaces. Therefore, a complete method for reconstruction of the sea surfaces in the presence of breaking waves is proposed and validated. The detection of breaking waves on the images and their reprojection on reconstructed surface is also discussed. Although too few acquisitions are available to draw firm results, an overview of the various observable parameters through the use of stereo video is given. This work shows the importance of stereo video systems to a better observation and understanding of the breaking waves, required in order to improve dissipation source term in spectral wave models.

Acknowledgments

Je souhaite, avant de vous présenter mes travaux de thèse, présenter mes remerciements à bon nombre de personnes dont l'aide et le soutien, tant professionnel que personnel, ont fait de mes trois ans de doctorat une expérience de travail, de rencontres et de vie que je n'oublierai jamais. Ceux qui sont passés par là le savent, la thèse est un moment difficile, qui demande beaucoup d'investissement et de travail de l'étudiant, mais dont le succès ne peut être attribué uniquement à celui-ci. En effet, ce succès dépend également pour beaucoup d'un grand nombre personnes, qui parfois sans le savoir, jouent un rôle essentiel. Ces quelques lignes leur sont dédiées.

Tout d'abord, je souhaiterais remercier mon directeur de recherche, Fabrice Ardhuin, non pas car il en est de coutume, mais car il a été le pilier essentiel, non seulement de mes travaux, mais aussi de mon moral et de ma motivation. Plus qu'un chercheur brillant, Fabrice a fait preuve d'une grande patience et d'un soutien sans faille dans les moments difficiles. Sa motivation, sa persévérance et sa détermination ont été pour moi une source d'inspiration constante. Toutes ses qualités, tant scientifiques qu'humaines, ont fait de ces trois années de travail intense à ses côtés, une expérience très agréable.

Je présente également mes chaleureux remerciements à l'ensemble de mes collègues du Laboratoire d'Océanographie Spatiale, tout particulièrement Bertrand Chapron, directeur du laboratoire, pour son encadrement et ses remarques et conseils avisés. Mickael, plus que d'avoir m'assurer un soutien informatique indispensable, nos pauses café et nos "expérimentations *in situ*" au Minou, Dalbos et Déolen ont été de très bons moments. Je remercie également Alexei pour ces remarques toujours sincères et justes. Séverine, merci pour les nombreuses relectures d'anglais, nos discussions et notre amitié (sans oublier les macarons au pot de ma soutenance). Ma gratitude se tourne aussi vers tous ceux que je n'ai pas cité, mais qui se reconnaîtront, pour avoir été des collègues attentionnés, voire pour nombres d'entre eux d'être devenus de bons amis.

J'adresse aussi mes remerciements aux personnels de l'école doctorale, tout particulièrement Elisabeth Bondu, pour sa tolérance lorsque les deadlines venaient à être allègrement dépassées, mais aussi et surtout pour son soutien technique pour les tâches administratives et la préparation de ma soutenance.

Je sais gré à mes rapporteurs, Alain Weill et Philippe Forget, ainsi qu'aux membres du jury, Xavier Carton, Danièle Hauser et Alvis Benetazzo pour la lecture consciencieuse et

attentionnée de mon manuscrit et leurs remarques pertinentes et constructives sur mon travail. Merci à eux également de s'être déplacés peu avant Noël pour ma soutenance et ainsi de m'avoir permis de passer des fêtes de fins d'années plus sereinement.

Хочу выразить благодарность команде Морского Гидрофизического Института В.В. Малиновскому, В.А. Дулову, В.Е. Смолу, А.С. Миронову, М.В. Юровской, Ю.Ю. Юровскому и А.Е. Кориненко за научно-техническую поддержку во время проведения экспериментов на платформе. Спасибо за помощь в организации быта и питания, включая суп из свежельвленной рыбы в сопровождении местных напитков. Этот незабываемый опыт останется со мной навсегда.

Vorrei ringraziare i team italiani di ISMAR/CNR e di PROTECNO per il loro supporto tecnico, per l'installazione di WASS e per l'elaborazione dei dati stereo. Un ringraziamento particolare va ad Alvis Benetazzo e a sua moglie, per il contributo significativo nello sviluppare gli algoritmi di elaborazione dei dati stereo e per l'accoglienza che ho ricevuto a Venezia: una splendida visita della città ed un risotto squisito!

I warmly thank Johannes Gemmrich, Mickael Banner and Russel Morison for providing breaking wave and wave spectra data from the FAIRS experiment.

I also thank Magdalena Anguelova and Ferris Webster for sharing their global whitecap database.

Merci aussi à tous mes amis, de Brest, des Landes et d'ailleurs, pour leur soutien, pour les soirées musique (ou autres), pour les vacances passées avec eux, ..., pour tous ces moments qui m'ont permis de décompresser, d'oublier mes erreurs de compilation, mes problèmes de *deadline* souvent bien trop courtes, ou encore, pour votre présence à ma soutenance.

Enfin, je remercie beaucoup ma compagne, Carine, pour son soutien quotidien indéfectible et son optimisme contagieux vis à vis de mon travail. Sa patience sans faille et son écoute attentive ont été les garants de mon moral dans les moments de doutes. Je souligne également son indulgence et sa bienveillance envers moi surtout durant les derniers mois lorsque le manque de sommeil a sévèrement érodé ma délicatesse et ma gentillesse : il devrait exister un diplôme pour les compagnes de doctorant ! A défaut, je lui dédicace ce manuscrit.

Ces remerciements ne peuvent bien évidemment pas s'achever sans une douce pensée pour mes parents et ma sœur. Malgré l'éloignement géographique, votre amour et vos encouragements m'ont accompagné tout au long de ma vie, pour faire de moi la personne que je suis aujourd'hui, et ont joué un rôle significatif dans la réussite de ce projet.

This work was supported by a FP7-ERC young investigator grant number 240009 for the IOWAGA project, the U.S. National Ocean Partnership Program, under grant U.S. Office of Naval Research grant N00014-10-1-0383. Additional support from ESA and

CNES for the Globwave project is gratefully acknowledged.

Contents

Résumé	1
Abstract	3
Acknowledgments	5
Table of content	9
List of figures	11
1 Introduction	19
2 Wave breaking modeling	33
2.1 Introduction	33
2.2 Investigated dissipation parameterizations	36
2.2.1 Description of the parameterizations	37
2.2.2 Correction of swell dissipation	41
2.2.3 Adaptation of TEST500 into TEST570	41
2.2.4 Model settings for the different parameterizations	50
2.3 Dissipation source terms and breaking crest length densities	50
2.3.1 Academic case: Uniform infinite deep ocean	50
2.3.2 Wave-breaking experiment: FAIRS hindcast	55
2.4 Whitecap coverage and mean foam thickness at the global scale	57
2.5 Conclusion and Perspectives	63
3 Sea surface reconstruction	65
3.1 Introduction	65
3.2 Experiment description	66
3.3 Theoretical background	68
3.3.1 Pinhole camera model	68
3.3.2 From 3D coordinates to 2D pixel coordinates	72
3.3.3 Epipolar geometry and stereo triangulation	77
3.4 Camera calibration and image rectification	78
3.4.1 Short historical of camera calibrations	78
3.4.2 Camera intrinsic calibration	80
3.4.3 Camera extrinsic calibration	92

3.4.4	Image rectification	94
3.5	Sea surface reconstruction	95
3.5.1	Point matching processing	96
3.5.2	Triangulation processing	103
3.5.3	Mean surface plane definition	107
3.5.4	Surfaces in world reference system	108
3.5.5	Correction for the asymmetric projection	108
3.5.6	Griding and smoothing of the surfaces	110
3.6	Analyses of sea surface reconstructions	110
3.6.1	Probability density function of the elevation	110
3.6.2	Non directional frequency spectra	111
3.6.3	Frequency-wavenumber directional spectra	111
3.6.4	Wavenumber spectra	111
3.6.5	Mean Square Slopes of elevation maps	123
3.7	Conclusion	123
4	Breaking Observation	127
4.1	Introduction	127
4.2	Automatic detection of breaking events	130
4.2.1	Image binarization	131
4.2.2	Event filtering method	135
4.3	Crest length density	141
4.4	Breaking probabilities	143
4.5	Wave scale analysis	147
4.6	Saturation spectrum	148
4.7	Conclusion	150
5	Conclusion	153
	Bibliography	157

List of Figures

1.1	<p>Illustration of wave-by-wave analysis for a sea surface elevation time series obtained from capacitance wave gauge in the Black Sea on 1/10/2013. The wave field is composed only by a developing wind sea. Top panel: Measured sea surface elevation (blue line) and decomposition into individual waves using zero down-crossing method (red circle). H_i and T_i respectively represent the wave height and the wave period of the individual wave i. Lower panels : Probability Density Function of wave height H (left) and wave period T (right). Red dashed line represent the Rayleigh distribution that describes the statistical distribution of the individual wave heights for linear gaussian waves and stationary sea state. The average of the one-third of highest individual waves is $H_{1/3} = 0.24 m$.</p>	27
1.2	<p>Frequency analysis of a sea surface elevation time series obtained from capacitance wave gauge in the Black Sea on 3/10/2013. The wave field is composed by both variance from the developing wind sea (right part of the spectrum) and from swell wave (left part of the spectrum). The global significant wave height is: $H_{\text{sig}} = 4\sqrt{\int_0^\infty E(f)df} = 0.35\text{m.}$ The significant wave height of swell waves is: $H_{\text{sig,swell}} = 4\sqrt{\int_0^{0.23} E(f)df} = 0.12\text{m.}$ The significant wave height of wind sea waves is: $H_{\text{sig,wind sea}} = 4\sqrt{\int_{0.23}^\infty E(f)df} = 0.33\text{m.}$</p>	28
1.3	<p>Typical example of directional frequency wave spectrum in the tropical zone, measured with buoy 51001, 350km north-west of Kauai island, on January, 11th 2007.</p>	29
1.4	<p>Sketch showing the features of a spilling breaker. The waves is moving from left to right and has a whitecap on its forward face. The figure is extracted from Reul and Chapron (2003), the notation are modified to agree the present thesis.</p>	29
1.5	<p>Typical example of depth-induced wave breaking occurring on sandy beach of the Atlantic French coast (La Piste, Capbreton).</p>	30
1.6	<p>Picture of deep-water wave breaking taken by the author from a boat off the north coast of Bretagne.</p>	30
1.7	<p>Various published wind-driven whitecap coverage formula. Figure extracted from Anguelova and Webster (2006).</p>	31

2.1	Picture of deep-water wave breaking taken by the author from a boat off the north coast of Bretagne. Before the passage of the breaking front, sea surface is covered by ripples waves whereas, in the breaking front wake, sea surface is smoothed. Same process is observed for all wave scales.	38
2.2	Top: Global NRMS Error for parameterizations TEST441b (left) and TEST451 (right). Middle: Comparison of PDF of wave heights (left) and Normalized bias vs wave height (right). Bottom: Comparison of Normalized RMS Error (left) and Scatter Index vs wave height (right).	42
2.3	Top: Rectangular filtering windows W_{f_i} (colors) over integrated spectrum (black line). Bottom: Breaking probabilities P_{b,f_i} obtained for each wave scale f_i (colors) and breaking probability $P_b(k)$ obtained with averaging (Black line).	43
2.4	Normalized RMS Error for new parameterization TEST570 compared to TEST451 (Ardhuin et al., 2010) and BJA (Bidlot et al., 2005) parameterizations for whole 2006 year. In all three cases the model is driven by ECMWF operational wind analyses.	45
2.5	Normalized Bias, RMS Error and Scatter Index on H_s for new parameterization TEST570 compared to TEST451 and BJA parameterizations. . . .	46
2.6	Mean values of mss_{ku} binned as a function of H_s (x-axis) and U_{10} (y-axis) for TEST570 and TEST451 parameterizations and satellite observations. . .	47
2.7	Wave spectra (top panels), mean direction (middle panels) and directional spread (bottom panels) on 3 November 1999 at buoy X2 and X4, averaged over the time window 12:00-17:00 EST, from observations and model runs with T451, TEST510 and T570 parameterizations. The swell is excluded due to the frequency range used in the figure.	49
2.8	Breaking probabilities and associated dissipations obtained for a fully developed sea state (3 days of simulation) for TEST570 (left) and TEST451 (right).	51
2.9	Source terms for TEST570, TEST451 and BJA parameterizations using DIA for non-linear interactions after 8 hours of run. The considered model is a uniform infinite deep ocean with a uniform 10 ms^{-1} wind, starting from rest.	53
2.10	Source terms after 8 hours of run for TEST570X, TEST451X and BJAX parameterizations using XNL for non-linear interactions. The considered model is a uniform infinite deep ocean with a uniform 10 ms^{-1} wind, starting from rest.	54
2.11	Spectra (left) and direction-integrated breaking crest length distribution (right) obtained with TEST570 and TEST451 parameterizations for a uniform infinite deep ocean after 3 days of run, when $C_p/U_{10} > 1.2$, with $U_{10} = 5, 10, \text{ and } 15 \text{ m s}^{-1}$. Energy peaks are marked by circles.	55
2.12	Top: Evolution of spectra (left) and direction-integrated breaking crest length distribution (right) for TEST570 (XNL) with increasing wave age (colors), for $U_{10} = 12 \text{ m s}^{-1}$. Bottom: Evolution of $\Lambda(C_p)$ as function of C_p/U_{10} , with TEST570 and TEST451 parameterizations	56

2.13 Direction-integrated Breaking Crest Length Distribution $\Lambda(C)$ from BWHD integration (TEST570,red) and from directional saturation spectrum (TEST451, blue) extracted from hindcast of FAIRS experiment. Squares are observed $\Lambda(C)$ by Gemmrich et al. (2008). 58

2.14 Mean values of W binned under the WindSat track as a function of U_{10} for new parameterization (TEST570) and modified Ardhuin et al. (2010)'s parameterization (TEST451) compared to March 2006 satellite observations by Anguelova et al. (2009). Wind used for binning is the collocated CFSR data, which is independent of the WindSat data until September 2008. Red bars represent minimum and maximum values, black bars are the standard deviations and the blue line represents the empirical fit by Monahan and Woolf (1989). 60

2.15 Q-Q plot of WCC given by TEST570 and TEST451 and satellite observations (Anguelova et al., 2009) on March 2006. Compared values are collocated under WindSat swath. Colors give the values of $\log(N_{\text{val}})$ 61

2.16 Mean values of mean foam thickness ($\bar{\Delta}$) binned as a function of U_{10} for new parameterization (TEST570) and modified Ardhuin et al. (2010)'s parameterization (TEST451). Wind used for binning is the collocated CFSR data, which is independent of the WindSat data until September 2008. Red bars represent minimum and maximum values, black bars are the standard deviations. 62

3.1 Platform of Katsiveli, Crimea, Ukraine. Location of anemometer, wave gauge array and Wave Acquisition Stereo System (WASS). 67

3.2 Top: Waterproof camera case. Bottom, left: 5-mm focal length low distortion lens. Bottom, right: 5 Megapixel BM-500GE JAI cameras. 69

3.3 Evolution of wind and wave conditions during the experiment. Acquisitions were done for wind direction established to West-South-West, with speed up to 10m/s. 70

3.4 Schema of the pinhole camera model. 73

3.5 Schema of the links between 3D points of the scene and their projection on undistorted bit-mapped image. 74

3.6 Illustration of epipolar geometry for a pair of cameras. The points C_1 and C_2 are the center of projection. The image points e_1 and e_2 are epipolar points. The epipolar plane corresponding to scene point P is represented in yellow. The intersection between the epipolar plane and the image planes defined the epipolar line. 79

3.7 Example of images using for left intrinsic camera calibration. Green crosses represent corner detected on the images whereas blue circle are reprojections of 3D points using with calibrated intrinsic and extrinsic parameters. On upper-left panel, red lines represent definition of the world coordinate system. Chessboard square size is 30mm on the four upper images, and 80mm on the two lower ones. 81

3.8 Chessboard and image planes seen as projective planes, so linked by a homography matrix H 85

3.9	Deviation of pixels from rectilinear projection due to distortion for right camera.	89
3.10	Error of reprojection (residual after optimization) for the right camera : $r_u = u - u_p$ and $r_v = v - v_p$. Upper-left panel shows that some reprojections are far from observed corner, nevertheless, these points have small influence on global calibration results, given large number of calibration points. Upper-right panel shows disparity in reprojection errors in both u and v pixel axis. Lower panel gives disparity in reprojection errors for each axis. We note that assumption of error assimilated to a white Gaussian noise looks fine. Directional RMS errors of reprojection are (0.28, 0.20) for left camera and (0.26, 0.18) for right one.	90
3.11	Distribution of intrinsic calibration chessboards in camera reference system for right camera.	91
3.12	Main steps of stereo reconstruction processing: Top panels show set of corresponding points returned by matching point processing. Bottom left panel corresponds to the stereo-triangulation processing. Finally, bottom-right panel represents the sea surface obtained in world coordinate system. Figure presented here shows results obtained for first image pair of the 4 th acquisition.	97
3.13	Example of bad point matching due to foam patch. Size of correlation templates is purposefully increased to 121×61 pixels to exaggerate this phenomenon. Left panels: Matching points obtained between left (top) and right (bottom) images. Color of points are correlation coefficient of matching (top) and standard deviation of pixel values in right correlation window. Green point matching is not disturbed by foam patch whereas red point matching is fully driven by small part of foam patch in correlation window. Top-right: resulting surface after stereo triangulation (§3.5.2) and rotation to world coordinates (§3.5.4). Green point falls on reconstruction in back of wave crest whereas images show that it is in front of the crest. Bad matching leads to unrealistic step around foam patch. Bottom-right: histogram of pixel vertical coordinates disparity between left and right images, with abnormal peak observed around pixel value 101 due to bad matching.	99
3.14	Same figure as 3.13, but matched points are now obtained with decreasing correlation template size, pixel histogram equalization, and left image rectification. Sizes of correlation templates are 121×61 pixels, 41×41 pixels, and 21×21 pixels in subsequent searching steps. Left panels: Matching points obtained between left (top) and right (bottom) images. The point colors represent correlation coefficient of matching (top) and standard deviation of pixel values in right correlation window. Top-right: resulting surface after stereo triangulation (§3.5.2) and rotation to world coordinates (§3.5.4). Bottom-right: histogram of pixel vertical coordinates disparity between left and right images. The abnormal peak observed around pixel value 79 in figure 3.13 is not present here.	101

3.15 Same figure as 3.15, after the smoothing of the disparity map with a 10×10 point (i.e. 20×20 pixel) median filter. Top-right: resulting surface after stereo triangulation (§3.5.2) and rotation to world coordinates (§3.5.4). Bottom-right: histogram of pixel vertical coordinates disparity between left and right images. 102

3.16 Reconstruction zone in which matching processing is done. Results are approximatively rectangular reconstructed sea surface. 104

3.17 Mean vertical (left) and horizontal (right) disparity maps obtained from the average of the 21576 disparity maps of the 4th acquisition. 105

3.18 Triangulated point deviation due to correction for asymmetric projection, applied on the mean disparity map of acquisition 4 (Fig. 3.17) 109

3.19 Probability Density Function (PDF) of the surface elevation. Black lines correspond to the PDF obtained with wave gauges time series. The blue lines correspond to the PDF of the reconstructions obtained with the new processing, including both equalization of pixel intensity histogram and decreasing correlation template size in the matching point processing, and the correction for asymmetric projection. 112

3.20 Frequency Spectra (FS) of the surface elevation. Black lines correspond to the PDF obtained with wave gauges time series. The blue lines correspond to the FS of the reconstructions obtained with the new processing, including both equalization of pixel intensity histogram and decreasing correlation template size in the matching point processing, and the correction for asymmetric projection. 113

3.21 Wave spectrum over wavenumbers and frequencies (i.e. 3D spectrum integrated over directions) on the left panel and cross-sections in the 3D frequency-wavenumber-direction spectrum at fixed frequencies on right panels, for acquisition 1 ($U_{23} = 11.5$ m/s, $H_s = 0.30$ m, $f_p = 0.33$ Hz). The white arrow indicates the wind direction. 114

3.22 Same figure as Fig. 3.21 for acquisition 2 ($U_{23} = 10.9$ m/s, $H_s = 0.36$ m, $f_p = 0.38$ Hz). 115

3.23 Same figure as Fig. 3.21 for acquisition 3 ($U_{23} = 13.2$ m/s, $H_s = 0.45$ m, $f_p = 0.33$ Hz). 116

3.24 Same figure as Fig. 3.21 for acquisition 4 ($U_{23} = 13.9$ m/s, $H_s = 0.55$ m, $f_p = 0.27$ Hz). 117

3.25 Non directional wavenumber spectra $E(k)$ for the 4 acquisition. The black dashed line is the k^{-3} asymptote. 119

3.26 Saturated directional wavenumber spectra $S(k) = E(k)k^3$ for the 4 acquisition. 120

3.27 Wavenumber spectra obtained with the integration over positive frequencies of the 3D spectra presented on the figures 3.21-3.24. The obtained wavenumber spectrum $E(k, \theta)$ is so unambiguous in direction. 121

3.28 Directional spreading (Eq. 3.6.4) computed from the spectra presented in figure 3.27. 122

3.29 Spreading integral (Eq. 3.85) computed from the directional spreading presented in figure 3.28. 125

3.30	Mean Square Slope given by waves longer than 1m computed over the whole set of images for the 4 acquisitions. $mss_{>1m}$ is the global slope variance (left panels), $mss_{>1m}$ is the slope variance along x -axis (center panels) and $mss_{>1m}$ is the slope variance along y -axis (right panels).	126
4.1	A) Image 001028 of acquisition 4 (I). B) Long-lasting brightness component (I_{avg}) resulting from background conditions. C) Instant brightness ($I_g = I - I_{\text{avg}}$) due to surface slope. D) Binarized Images ($I_g > T$).	134
4.2	Brightness variance distribution and probability function obtained for the 4 acquisitions. The blue solid thin line corresponds to the observed $p(I)$ function. The green solid thick line is its corresponding $F(I)$ function. The red dashed line corresponds to $F_0(I)$. The computed threshold value I_T is marked with a blue cross.	134
4.3	Example 1: 1 st detected active breaking event on acquisition 1. The blue contours are white patches detected by threshold method. The red contour is the filtered active breaking.	137
4.4	Example 1: 1 st detected active breaking event on acquisition 1. The black points correspond to the projection of the active foam points (red contour of the figure 4.3) on 3D surfaces. Black contours are the footprint of the images shown on figure 4.3.	138
4.5	Example 2: 54 th detected active breaking event on acquisition 4. The blue contours are white patches detected by threshold method. The red contour is the filtered active breaking.	139
4.6	Example 2: 54 th detected active breaking event on acquisition 4. The black points correspond to the projection of the active foam points (red contour of the figure 4.5) on 3D surfaces. Black contours are the footprint of the images shown on figure 4.5.	140
4.7	Probability density function of breaking to breaking speeds for the 4 acquisitions.	142
4.8	Probability density function of breaking direction relative to the wind direction for the 4 acquisitions.	143
4.9	Probability density function of breaking to breaking speeds and directions for the 4 acquisitions. The black arrows give the wing direction.	144
4.10	Frequency-filtered surfaces (left panels) and the wavenumber-frequency-filtered surfaces (right panels) for $\lambda_c = 1\text{m}$ (top), 3m (middle) and 5m (bottom). The black points are detected to be wave crest points.	145
4.11	Crest length densities for the four acquisitions. Black line represents the crest length densities for monochromatic unidirectional waves.	146
4.12	Breaking probabilities as ratio of breaking crest length to total crest length, breaking or not (triangles, dashed-line) and as ratio of number of breaking waves to total number of waves, breaking or not (square, full line). Number of waves is defined using a wave-by-wave analysis applied on the time series get from each point of the surface.	147
4.13	Directional distribution of the breaking probabilities in each wave scale for the four acquisitions.	148

4.14 Left panel: frequency spectra obtained from wave gauges. Right panel : comparison of the observed unidirectional breaking probabilities with the modeled probabilities of Filipot et al. (2010) computed using the wave gauge frequency spectra. 149

4.15 Saturation spectra (left axis, full lines) and corresponding breaking PDF (right axis, dashed lines) as function of wavenumbers (left panel) and frequencies (right panel). 149

4.16 Comparison of the direction-wavenumber PDF of the detected breaking (left panels) compared to the wavenumber saturation spectra $B(k, \theta)$ (middle panels) and partially integrated wavenumber saturation spectra $B'(k, \theta)$ as defined by equation 2.11 for each acquisition. 151

Chapter 1

Introduction

The breaking of surface gravity waves is an obvious phenomenon at the air-sea interface. The main part of the energy transferred from the wind to surface waves is then dissipated by wave breaking. Wave breaking therefore plays a major role in the limitation of the wave height. The present thesis envisages breaking waves in the context of wave dissipation, particularly with the objective to improve the accuracy of spectral wave models used today for marine meteorology and other geophysical applications. After analyzing the actual parameterizations of breaking-induced dissipation, the work presented here aims to propose a comprehensive method for the observation of the breaking wave with stereo-video systems, as well as highlight its potential contribution to future improvements, calibrations, and validations of the breaking parameterizations. We note that wave breaking also draws attention from scientists as it has profound impacts on other marine and meteorological applications. It mixes the water surface layer by the induced near-surface turbulence (Agrawal et al., 1992; Craig and Banner, 1994; Gemmrich and Farmer, 2004), generates marine aerosols (Smith et al., 1993), enhances gases and heat transfers (Chanson and Cummings, 1992; Melville, 1994), increases the drag of the wind (Banner and Melville, 1976; Kudryavtsev and Makin, 2001) and strongly affects the remote sensing of ocean properties (Reul and Chapron, 2003).

Two approaches can then be used to analyze the evolution of the random waves. The simplest approach is the wave-by-wave analysis, generally applied on sea surface elevation time series on which individual waves are defined by two consecutive zero up-crossings or down-crossings. Then, the height, H , and the period, T (or the wavelength, λ) can be extracted for each individual wave (see Fig. 1.1). The individual wave steepness is then defined with $H\lambda$. This method is very largely used and numerous statistics can be found in the literature. It takes note in particular that wave height distribution follows a well-know Rayleigh distribution. Using wave-by-wave analysis, the global wave height, $H_{1/3}$, is usually defined as the average of the one-third of the highest individual waves. The evolution of $H_{1/3}$ depends on both the 10m-height wind speed, U_{10} , (or wind stress, u^* , which is the shear stress exerted by the wind on the surface) and the wind fetch, D , which is the distance, in the wind direction, that indicates how far the wind affects the sea surface (i.e. the wind fetch is the distance over which waves are still growing under wind action). We nevertheless note that, by construction, this method is not adapted to the study of smaller waves riding over bigger ones, and should be restricted to the study

of the dominant waves.

We note here that the Airy wave theory, usually referred to as the linear wave theory, links the pulsation $\omega = 2\pi/T = 2\pi f$ to the wavenumber $k = 2\pi/\lambda$ with the dispersion relation

$$\omega^2 = gk \tanh(kD), \quad (1.1)$$

where g is the gravity and D is the water. Then, the phase speed is given with

$$C = \frac{\omega}{k}, \quad (1.2)$$

and the group speed, which describes the energy propagation in space, is given by

$$C = \frac{d\omega}{dk}. \quad (1.3)$$

A second analysis method considers the wave field in the Fourier space. The wave field is therefore seen as the quantity of energy linked to the elevation variance distributed over frequencies (or wavenumbers) and directions. Therefore, real waves are a superposition of sinusoidal waves, with different frequencies (or wavenumbers), amplitudes and phases. The shape of the energy wave spectrum gives large amounts of information over the statistical parameters of the wave field. It is in particular possible to distinguish the local wind sea generated by local wind from possible swell(s) corresponding to regular longer period waves that were generated by winds of distant weather systems. Typically, spectral analysis is advised to study real wave fields, which are generally a combination of several wave systems. Figure 1.2 shows the decomposition of the sea surface variance E over frequencies f . The shape of the spectrum clearly expose the presence of swell, with a peak frequency at $f = 0.15\text{Hz}$ and a developing wind sea with a peak frequency at $f = 0.38\text{Hz}$. The significant wave height is here defined with

$$H_{\text{sig}} = 4\sqrt{E} \text{ with } E = \int_0^\infty E(f)df. \quad (1.4)$$

Note that here E is the variance of the surface elevation, and the factor 4 was defined such that H_{sig} is in line with $H_{1/3}$. Using the spectral analysis, we can also define a significant wave height for each wave system (see Fig. 1.2). Analysis of the wave field can also be done in the directional Fourier space. Variance is thus distributed over both frequencies and direction. Figure 1.3 shows the representation of a wave field in the directional Fourier space.

Introducing spectral wave models, Gelci et al. (1957) greatly improved the wave forecasting. Spectral wave models, including the model WAVEWATCH III[®] used in this work, compute the evolution of the energy wave spectrum over frequencies (or wavenumbers) and directions. Note that the phase of the waves is not resolved in these models, so-called phase-averaged models. Waves from each spectral component are supposed to evolve freely, following the Airy wave theory. The evolution of the wave energy spectrum along time and space is mainly driven in spectral models by the spatial energy propagation, the input from the wind, the non-linear wave-wave interaction which causes transfers among spectral components and the dissipation due to wave breaking. Numerous other phenomena can also be added to wave models, such as the dissipation due to bottom friction

or refraction due to the coast. Some of these additional phenomena are discussed in the chapter 2.

Considering free wave evolving, spectral wave models are well suited to represent the wave energy propagation, which well follows the Airy wave theory. Nevertheless, we note that real waves are not linear, and wave field evolution is largely driven by non-linear phenomena. Wave-wave interactions are weakly non-linear phenomena and can be resolved in spectral wave models. Nevertheless, the phase-averaged models are not well adapted to resolve highly non-linear phenomena such as wave growing and wave breaking. These essential terms must therefore be statistically parametrized.

When wind blows over a flat water surface, friction at the air-water interface exerts forces on the surface, resulting in its deformation. Thus, the excess of free surface tension caused by the sea surface deformation compensates the wind induced forces. Wind being strongly turbulent, the pressure field (i.e. the force field) is not uniform over the flat sea surface and random capillarity waves, also called ripples, appears on the sea surface. With wavelengths of few millimeters, these ripples are fully driven by the effects of the surface tension. If the wind stops, they quickly die, their energy being absorbed by viscous dissipation. On the contrary, if the wind is still blowing, a resonant interaction between waves and ripples develops, resulting in the growth of ripples. The mechanism of wave growing is still misunderstood, particularly at small scale. It is evident that in the air-sea boundary layer, air flow and sea surface influence each other permanently, resulting in a strongly non-linear system. Many theories were however proposed to explain the wave generation by the wind (Jeffreys, 1925; Belcher and Hunt, 1993; Miles, 1957, 1962; Phillips, 1957), but no details are given in this work.

Then non-linear phenomena occur. The first phenomenon explains the displacement of the spectral energy to the highest frequency such that wind can create waves with phase speed C_p , higher than its own speed. In simple words, two wave trains can interact and create a third one. This phenomenon was confirmed by experimental results and two main theories were proposed by Hasselmann (1960, 1962) and Zakharov (1968), but not yet fully validated. Details are not given in this work, but we note, however, that these nonlinear effects imply perpetual energy transfers between spectral components. No details will be given in this work.

The present thesis focuses on wave breaking, which represent the main wave energy dissipation. Figure 1.4 gives the geometry of a breaking wave, with the notations used in the thesis. \vec{C}_{crest} is the speed of water particles at the crest. λ is the wavelength of the breaker. Λ_b is the length of breaking front, L_A is the average length of front side of the wave covered by the active breaking¹ and $\bar{\delta}$ is the average thickness of the foam. We obtain the individual whitecap coverage W_b such that

$$W_b = \Lambda_b L_A, \quad (1.5)$$

and mean foam thickness of an individual breaking wave, $\bar{\Delta}_b$, is

$$\bar{\Delta}_b = \Lambda_b L_A \bar{\delta}. \quad (1.6)$$

¹Due to the lifetime of the creates bubbles, foam can remain at the surface behind the breaking crest. Such a residual foam is usually referred to passive foam, in contrast to active foam due to active breaking.

Subsequently, we will use the density Λ (breaking crest length density), W (whitecap coverage), $\bar{\Delta}$ (mean foam thickness), which represents the total quantities (sum over all waves) per unit area such that

$$\Lambda = \frac{1}{S} \sum_1^{N_b} \Lambda_b \quad (1.7)$$

$$W = \frac{1}{S} \sum_1^{N_b} W_b \quad (1.8)$$

$$\bar{\Delta} = \frac{1}{S} \sum_1^{N_b} \bar{\Delta}_b \quad (1.9)$$

where N_b are the number of breaking waves in the surface S .

Generally, in people's minds, wave breaking is associated with the depth-induced breaking occurring at the coastline (Fig. 1.5). Depth-induced breaking is not the main topic of this work but is now succinctly described. Reaching the shoreline, water depth decreases and waves feel the bottom. While water depth is not critical, bottom friction dissipates wave energy and the wave height decreases. Entering shallower water (typically when the water depth becomes less than about half the wavelength), the wavelength is reduced while the frequency remains constant, and the group speed slows down. As the energy flux must remain constant, the group speed decrease is compensated by an increase in the wave height (and thus an increase in the wave energy density). Both the reduction of the wavelength and the increase of the wave height give waves more and more steepness. Non-linear harmonics also develop and make wave crests even more steep. Then, waves become unstable and break. The most famous criterion for depth-induced breaking is the Miche criterion which determines the onset breaking when the wave height is equal to 88% of the water depth. Numerous studies focus on the depth-induced breaking and showed that such a simple criterion is not sufficient (Raubenheimer et al., 1996; Ruessink et al., 2003; Battjes, 1974a,b; Sénéchal et al., 2001). Nevertheless, we note that Miche-like criterion is still widely used for the parameterization of depth-induced wave breaking in numerical models. If depth-induced breaking is an important phenomenon for swell waves, the major dissipation due to wave breaking occurs in deep water. Indeed, a large part of the wave energy coming from wind is quickly dissipated by deep-water breaking.

Deep-water breaking is usually called whitecapping due to the white foam patches created by breaking waves (Fig. 1.6). Wave breaking results from an instability which develops from the wave crest. First efforts were done to relate the breaking criterion to a steepness threshold of the breaking wave, as defined by the wave-by-wave analysis. However, from their observations, Holthuijsen and Herbers (1986) showed that such a criterion cannot be used because of the large overlap observed between breaking and non-breaking wave steepnesses. Actually, the local steepness at the crest is a criterion for breaking, but it generally cannot be obtained from wave-by-wave analysis, which does not take into account the smaller waves riding at the crest of the bigger ones. Indeed, the local steepness at the wave crest of breaking is strongly influenced by the smaller riding waves. Further efforts were focused on the relationship between breaking statistics and the wind forcing. It was however shown that breaking statistics depend on the sea state development (i.e. on the wave age). In particular, Gemmrich et al. (2008) observed that

breaking concerns a large range of phase speed, from dominant waves to smaller wave scale in young wind sea whereas it concerns only waves with phase speed less than half of the phase speed of dominant waves for well developed wind sea. Moreover, Banner et al. (2000) showed that wind effects can become secondary for dominant waves in developed wave fields. Further, the kinematic criterion was also investigated to explain wave breaking. Wave breaking occurs when water particle velocity at the wave crest u_{crest} becomes higher than the wave phase speed C . Furthermore, Stansell and MacFarlane (2002) showed that waves become unstable and inevitably evolve towards breaking for crest particle speed u_{crest} below C . Therefore, wave stability criterion is exceeded before irreversible breaking process yet starts (Babanin et al., 2007). The major advantage of a kinematic criterion is the consideration of the growing non-linearities which cause the wave instability (Tanaka, 1983). Numerous authors have also displayed interest in the the non-linear effects of the long waves on the breaking of the shorter ones. Indeed, the passage of long wave under the smaller ones induces hydrodynamical modulations, resulting in the acceleration of smaller riding waves which may evolve to breaking (Unna, 1947; Stewart, 1960; Longuet-Higgins, 1978; Dulov et al., 2002, among others). The role of non-linear features, resulting typically in wave asymmetry and wave skewness, in the emergence of crest instability was also highlighted by Caulliez (2002).

From an energetic point of view, sea surface assimilates wind energy increasing its surfaces (i.e. generating waves) until the exceeding energy is released by breaking waves (Newell and Zakharov, 1992). We note that breaking waves are local phenomena and can so be related to local energy exceedings. This effect is particularly highlighted by the correlation observed between wave groupiness and wave breaking (Donelan et al., 1972; Holthuijsen and Herbers, 1986). Breaking is observed at the crest of the highest waves of the group, where the energies from the different spectral components converge. This energy convergence was further inquired as the main predictor of breaking (Banner and Tian, 1998; Tulin and Waseda, 1999; Song and Banner, 2002; Banner and Song, 2002). We note that, in laboratories, investigators can create waves that converge and break in a predicted location.

The thesis opens with the chapter 2 dedicated to a discussion and the adjustment of the parameterizations for the spectral evolution associated with wave breaking. We highlight that breaking waves are highly non-linear phenomena where phase relations between spectral components play a major role. This is difficult to reconcile with phase-average wave models, and observations of individual breaking are difficult to link to the spectral dissipation due to wave breaking needed in spectral wave models. Hence, early concepts, such as proposed by Hasselmann (1974), have little relation with measurable quantities. Nevertheless, despite the fact that breaking waves are small local phenomena, a-priori non predictive, their statistics averaged over time and space should be related to wave spectrum. This link between spectra and time-averaged observable properties of breaking waves followed the analysis of Phillips (1984). He proposed the idea of a linearized dissipation rate, and gave a theoretical framework built around a measurable quantity: the length of breaking wave fronts and their distributions across displacement velocities. Then, Melville and Matusov (2002) proposed wave breaking measurements using aerial imaging, and provided a statistical description of related sea-surface processes. They found that the distribution of the breaking front lengths per unit area on the sea

surface is proportional to the cube of the wind speed. They also showed that the fraction of the ocean surface mixed by breaking waves is dominated by wave breaking at low velocities and short wavelengths, consistently with the Phillips (1984)'s theory. Furthermore, the video observations of Gemmrich et al. (2008) showed that the distribution of breaking crest length density peaks at intermediate wave scales and drops off sharply at larger and smaller scales. Similar distribution were found in other observations (Gemmrich and Farmer, 2004; Mironov and Dulov, 2008; Thomson and Jessup, 2008). This drop off at small scale is not explained by the Phillips (1984)'s theory which proposes an increasing dissipation at smaller scale.

Simultaneously, the breaking-induced dissipation of wave energy was studied with a numerical approach in spectral wave models (Alves et al., 2003; van der Westhuysen et al., 2005; Ardhuin et al., 2009; Banner and Morison, 2010; Rogers et al., 2012). These model developments, discussed in the introduction of the chapter 2, showed the increasing need of dissipation with smaller wave scales. Supported by the observations of Banner et al. (1989), these developments lead to the idea that the dissipation of wave energy at a given scale was not only related to the breaking of these same waves, but also to the breaking of waves at larger scales. This so-called "cumulative effect" is necessary to reproduce the observed shapes of spectra (Banner and Morison, 2010).

My work takes up the work developed by Filipot and Ardhuin (2012) who initiated a seamless treatment of wave breaking from deep to shallow water. In particular, I have investigated the modification of their parameterization to make the breaking probabilities used for the dissipation term linked to the breakers themselves consistent with the associated cumulative term. The parameterization of Filipot and Ardhuin (2012), used operationally at NOAA/NCEP for the Great Lakes since 2013 because of its better performance at short fetches is analyzed and compared to the parameterization of Ardhuin et al. (2010), used for operational ocean wave forecasting at NOAA/NCEP since May 2012 for the global ocean. In these recent parameterizations, whitecap occurrence has been related to the steepness of the waves, respectively through the unidirectional wave scale analysis of Filipot et al. (2010) and the observations on saturation spectra of Banner et al. (2000) and Banner et al. (2002). Banner and Morison (2010) showed that an explicit modeling of whitecap properties provides a new constraint on the model dissipation source terms. Nevertheless, there parameterizations have seldom been verified in terms of whitecap properties. In this work, an explicit modeling of the breaking wave front length distribution over phase speed is proposed and compared to the *in situ* observations of Gemmrich and Farmer (2004).

Because of its strong influence on electromagnetic measurements and air-sea gas exchanges, the whitecap coverage was also investigated in many studies (Monahan and Woolf, 1989; Hanson and Phillips, 1999; Reul and Chapron, 2003, among others). Many investigations have resulted in relationships between the whitecap coverage and the wind speed at 10m above the sea surface. This relationship was used more than one century before with the famous Beaufort scale which evaluates the wind speed from whitecap coverage for higher degrees. We note that most of the whitecap coverage used for the correction of the satellite measurements are still today only estimated from the wind speed despite of the large disparity between the published empirical relationships fitted on different observations (see Fig. 1.7, extracted from Angelova and Webster (2006)).

This large variability have been related to environmental and meteorological factors such as air-sea temperature difference, water salinity, or even biological water content, which directly influence surface tension, and to sea state (Monahan and Muirheart, 1981; Banner et al., 2000; Gemmrich et al., 2008). Anguelova and Webster (2006) highlighted the necessity to build an extensive database of whitecap coverage at large scale to investigate the large variability of the observations and proposed to retrieve whitecap coverage at large scale from the satellite-measured brightness temperature. Using the model of foam persistence of Reul and Chapron (2003), a modeling of the whitecap coverage and the mean foam thickness related to the dissipation term are also investigated and compared to the satellite observation database of Anguelova et al. (2009).

This effort on the numerical modeling capabilities highlighted the need of an observation processing able of analyzing the breaking at the scale of the single breaking waves. It also emphasizes the necessity of global-scale validation using well suited proxies for wave breaking parameters derived from remote sensing as proposed by Anguelova and Webster (2006) and the recent work of Reul et al. (2006). This remote sensing aspect is briefly investigated in chapter 2, but will require further work. The detailed measurements of turbulent dissipation rates below breaking waves have been studied elsewhere (Terray et al., 1996; Gemmrich et al., 2008; Thomson et al., 2009, among others). Here we focus on the shape of breaking waves and the relation of breaking events to the evolving shape of waves, based on stereo-video imagery.

The modern quantitative investigation of ocean waves started with stereo-photographic measurements, such as performed during the Meteor expedition in the 1930s (Dankert et al., 1939). The shift to a spectral method for the analysis of ocean waves also started with stereo measurements done during the Stereo Wave Observation Project (Chase et al., 1957; Cote et al., 1960). Later, Banner et al. (1989) also used the stereo-photography for the measurement of the spectrum directionality. Recently, with the development of the numerical photography and video, some investigators involved themselves in wave measurements from stereo observations (Kosnik and Dulov, 2011) or stereo-video (Benetazzo, 2006; Gallego et al., 2008). Nevertheless, the stereo video observation was never used to observe and quantify the breaking. Therefore, chapter 3 proposes a method to reconstruct the sea surface in presence of breaking waves, with enough accuracy for the further study of the breaking.

Wave breaking is a complex non-linear process including various intensive physical phenomena. The wave breaking event is usually split into two parts. The first one is the active breaking. It results from an instability which develops from the wave crest, when water particle velocities exceed wave phase speed (i.e. when the wave crest goes faster than the wave itself). The wave crest thus collapses on the front size of the wave, resulting in wave energy dissipation. Then, due to the lifetime of the bubble, the foam can remain on the sea surface a long time after the active breaking ends. This passive foam, in contrast with active foam produced by active crest breaking, does not imply wave dissipation, and the foam persistence is not investigated in this work.

The breaking phenomenon occurs at all wave scales once they are energetic enough. At microwave scale, breaking occurs without air entrainment. Nevertheless, the laboratory measurements of Jessup et al. (1997) show that micro-scale wave breaking associated with evolving wind waves disturbs the thermal boundary layer at the air-water interface,

producing signatures that can be detected with infrared imagery. Their laboratory observations, under the moderate wind speed conditions, showed a substantial frequency of occurrence and an important areal coverage of the phenomenon. Therefore, micro-scale breaking is undoubtedly widespread over the oceans and may prove to be a significant mechanism for enhancing the transfer of heat and gas across the air-sea interface. These microwave scales are not resolved in the global ocean spectral wave model, and microwave breaking is not studied in this work.

We here focus on longer breaking waves as modeled in spectral wave model. These waves, more energetic, are attended with air entrainment and bubble formation. The formation of foam needs a large quantity of energy, corresponding to the surface tension multiplied by surface excess. Thus, when breaking waves are energetic enough, they generate white bubble clouds which contrast with the darker sea surface, and are so called whitecaps. This signature in the visible frequency spectrum makes the phenomenon easily observable. The chapter 4 proposed a method to detect and discriminate active and passive foam on the images taken by the stereo video system inspired by the work of Mironov and Dulov (2008). By re-projecting the detected events on the reconstructed surfaces, this allows to analyze the breaking at the scale of the single breaking waves. A first analysis of the observations is provided.

The present thesis aims to improve on the wave spectral models, in particular with the development of dissipation parameterizations that better link to the wave breaking. Thus, my work in the next chapter provides a comprehensive analysis of the existing dissipation parameterizations through their implicit breaking properties. Despite the fact that these recent parameterizations are built on wave breaking observations, this chapter points out the failures of these parameterizations to produce model results, in terms of breaking properties, in line the observations. These current parameterizations make numerous uncertain assumptions due to the lack of accurate observations able to investigate them. The following chapters thus propose a first step for the future improvement of dissipation parameterizations. The recent wave studies have shown the potential of the stereo-video systems for sea-wave statistical investigations. Chapter 3 is dedicated to the improvement of the stereo-video analysis for the observation of individual waves. Validated using a large range of sea-wave parameters, the developed method, shows the potential of the stereo video observations for investigations at the scale of single waves. My work finally focuses with chapter 4 on the application of stereo-video observation to breaking analysis. Providing the full accurate 4D time-space evolution of the individual breaking waves, the stereo video observations open to a new world of information. Although the present work does not yet provide an improvement of the dissipation parameterization, it demonstrates the potential of these observations for the future improvements, calibrations, and validations of the breaking parameterizations in spectral models, as well as for a better understanding of the breaking phenomenon itself.

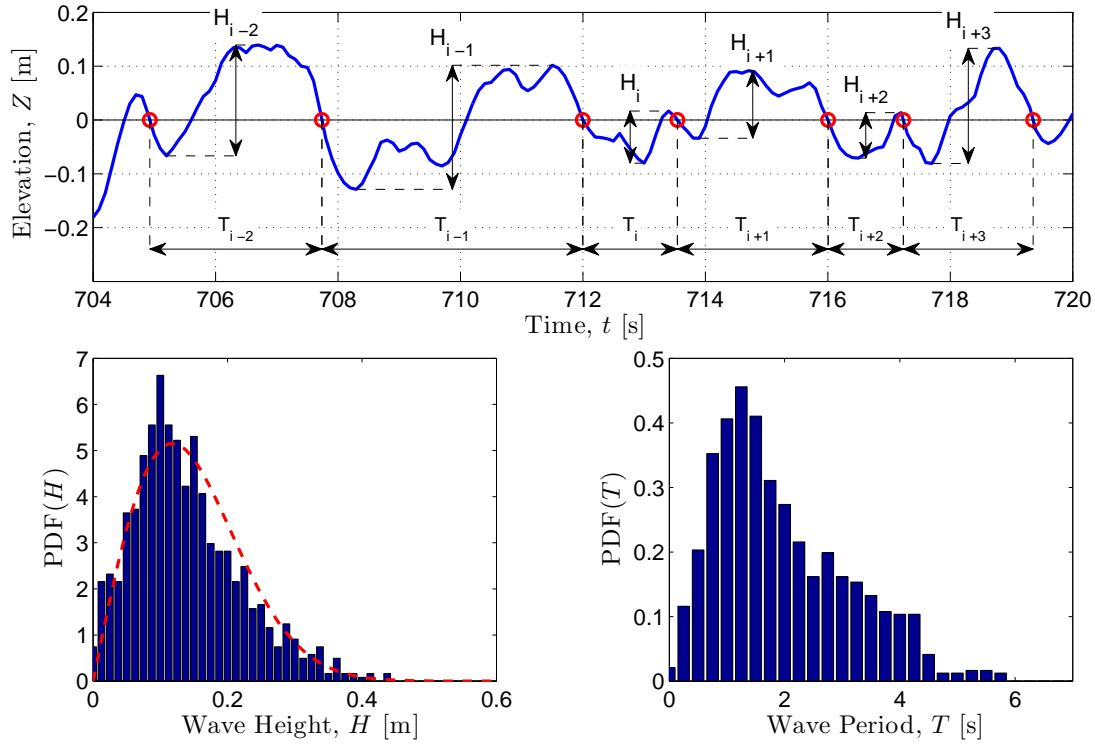


Figure 1.1: Illustration of wave-by-wave analysis for a sea surface elevation time series obtained from capacitance wave gauge in the Black Sea on 1/10/2013. The wave field is composed only by a developing wind sea. Top panel: Measured sea surface elevation (blue line) and decomposition into individual waves using zero down-crossing method (red circle). H_i and T_i respectively represent the wave height and the wave period of the individual wave i . Lower panels : Probability Density Function of wave height H (left) and wave period T (right). Red dashed line represent the Rayleigh distribution that describes the statistical distribution of the individual wave heights for linear gaussian waves and stationary sea state. The average of the one-third of highest individual waves is $H_{1/3} = 0.24$ m.

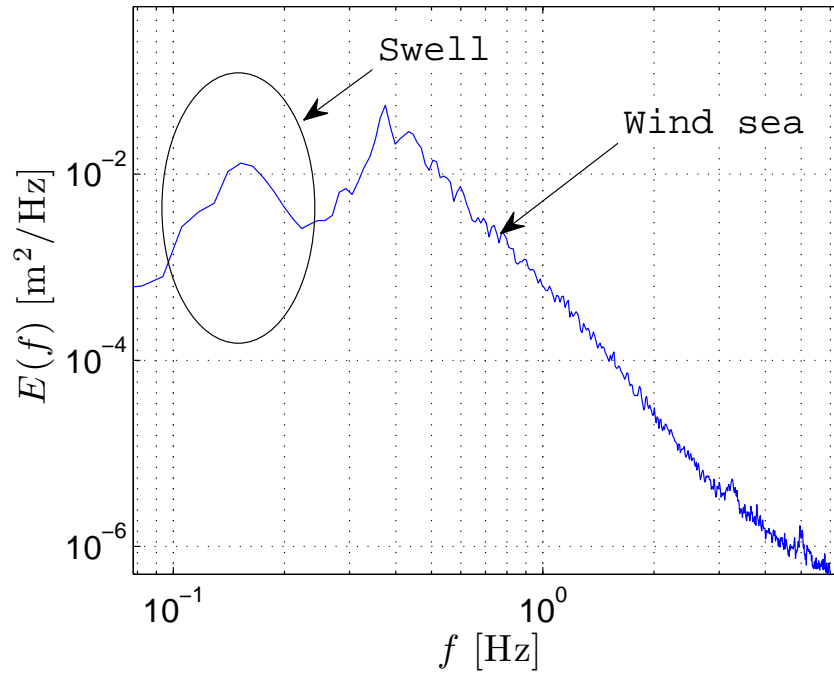


Figure 1.2: Frequency analysis of a sea surface elevation time series obtained from capacitance wave gauge in the Black Sea on 3/10/2013. The wave field is composed by both variance from the developing wind sea (right part of the spectrum) and from swell wave (left part of the spectrum).

The global significant wave height is:

$$H_{\text{sig}} = 4\sqrt{\int_0^{\infty} E(f)df} = 0.35\text{m}.$$

The significant wave height of swell waves is:

$$H_{\text{sig,swell}} = 4\sqrt{\int_0^{0.23} E(f)df} = 0.12\text{m}.$$

The significant wave height of wind sea waves is:

$$H_{\text{sig,wind sea}} = 4\sqrt{\int_{0.23}^{\infty} E(f)df} = 0.33\text{m}.$$

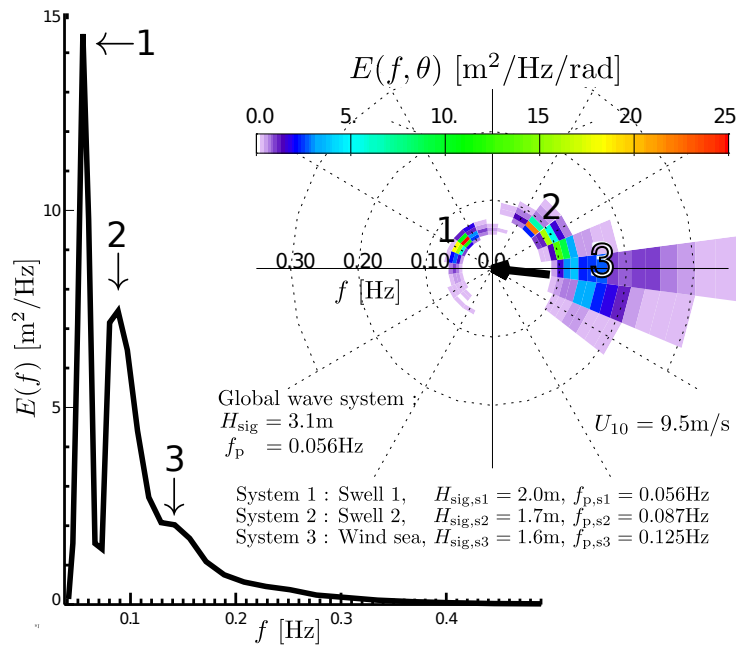


Figure 1.3: Typical example of directional frequency wave spectrum in the tropical zone, measured with buoy 51001, 350km north-west of Kauai island, on January, 11th 2007.

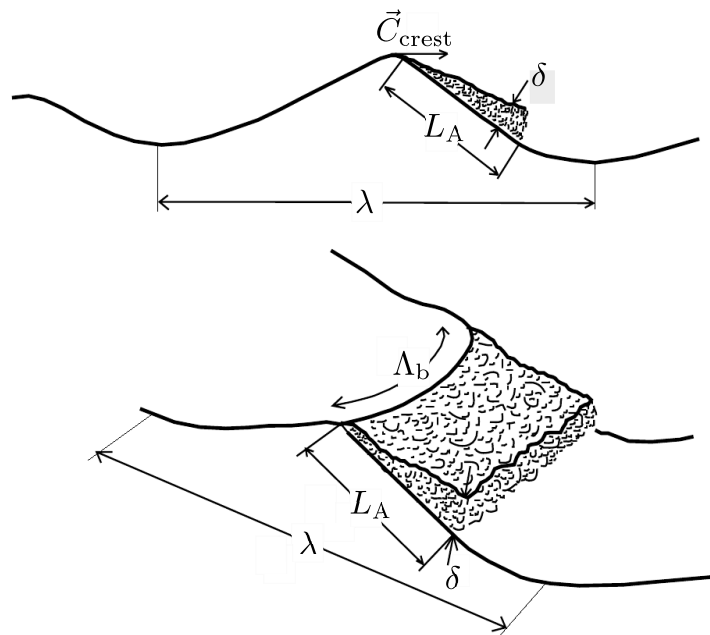


Figure 1.4: Sketch showing the features of a spilling breaker. The waves is moving from left to right and has a whitecap on its forward face. The figure is extracted from Reul and Chapron (2003), the notation are modified to agree the present thesis.



Figure 1.5: Typical example of depth-induced wave breaking occurring on sandy beach of the Atlantic French coast (La Piste, Capbreton).



Figure 1.6: Picture of deep-water wave breaking taken by the author from a boat off the north coast of Bretagne.

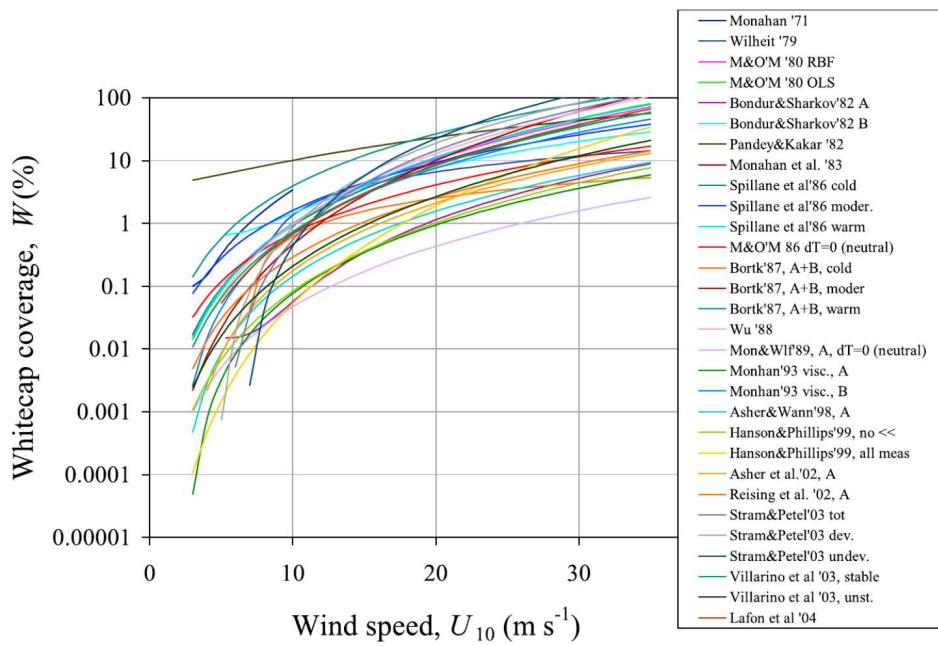


Figure 1.7: Various published wind-driven whitecap coverage formula. Figure extracted from Anguelova and Webster (2006).

Chapter 2

Wave breaking parameterization and whitecap properties modeling

Note

The major part of the results presented in this chapter have been published in the journal *Ocean Modelling* in October 2013 (Leckler et al., 2013).

2.1 Introduction

Phase-averaged wave models consider the spectral decomposition of the sea surface elevation across wavenumbers k (or frequencies f) and directions θ at point (x, y) and time t . The evolution of spectral density $F(k, \theta, x, y, t)$ is resolved using the wave energy balance equation proposed by Gelci et al. (1957):

$$\frac{dF}{dt} = S_{\text{atm}} + S_{\text{nl}} + S_{\text{oc}} + S_{\text{bt}} + \dots \quad (2.1)$$

where the Lagrangian derivative of spectral density on the left-hand side includes the local time evolution and advection in both physical and spectral spaces (e.g. WISE Group, 2007). The source terms on the right-hand side include an atmospheric source term S_{atm} which includes the classical input of energy S_{in} from wind to waves, and the energy output S_{out} from waves to wind¹, associated with friction at air-sea interface (Ardhuin et al., 2009). The nonlinear source term S_{nl} represents energy transfers in the spectral domain due to wave-wave interactions. S_{bt} is the sink of energy due to bottom friction. Other effects may also be included (WISE Group, 2007). Finally, the oceanic source term S_{oc} , usually negative, represents dissipation due to wave breaking, S_{bk} , and wave-turbulence interactions, S_{turb} (e.g. Ardhuin and Jenkins, 2006). The latter effect will be ignored here, because it typically represents at most a 10% fraction of the breaking-induced dissipation (Rascle et al., 2008; Kantha et al., 2009), and here we focus on wave breaking. The

¹The transfer of energy from waves to wind (S_{out}) is responsible for the swell dissipation over long distances. A modification of the formulation of Ardhuin et al. (2010) is provided in paragraph 2.2.2.

goal of the present chapter is to evaluate the ability of the breaking-induced dissipation parameterization to model the associated whitecap properties.

Early parameterizations of dissipation were adjusted to close the energy balance of waves, with no explicit link to breaking and dissipation observations. This, in particular, was the basis of the parameterizations of Komen et al. (1984). Following Hasselmann (1974), they proposed a dissipation quasi-linear in the wave spectrum adjusted on Pierson-Moskowitz spectrum (Pierson and Moskowitz, 1964) such that

$$S_{oc}(k, \theta) = S_{ds}(k, \theta) = -\psi_d(k)F(k, \theta), \quad (2.2)$$

with ψ_d depends only on the wavenumber and integrated parameters. Various forms had been proposed for the quasi-linear coefficient ψ_d . One of the most successful forms of ψ_d , used for a long time as dissipation source term in WAM, was proposed by Komen et al. (1994)

$$\psi_d(k) = -C_{ds} \left(\frac{\hat{\alpha}}{\hat{\alpha}_{PM}} \right)^m \left[(1 - \delta) \frac{k}{\bar{k}} + \delta \left(\frac{k}{\bar{k}} \right)^{n/2} \bar{\omega} \right], \quad (2.3)$$

where $\hat{\alpha} = E_{tot} \bar{k}^2$ is an integral steepness parameter, $\hat{\alpha}_{PM} = 4.57 \cdot 10^{-3}$ is the integrated steepness of a fully developed Pierson–Moskowitz spectrum (Pierson and Moskowitz, 1964), k is the mean wavenumber, $\bar{\omega}$ is the mean angular frequency, δ is a weighting factor that controls the magnitude of linear and quadratic functions of the ratio k/\bar{k} and E_{tot} is the total wave energy obtained by integrating the directional wavenumber spectrum $F(k, \theta)$. δ , n and m are tuning parameters. We note that this dissipation aims to produce spectra close to the empirical Pierson–Moskowitz spectrum, and not to reproduce dissipation due to wave breaking.

Thereafter, following Phillips (1984)'s analysis, breaking probabilities have been related to the nondimensional saturation spectrum B ,

$$B(k) = k^3 F(k) = k^3 \int_{-\pi}^{\pi} F(k, \theta) d\theta. \quad (2.4)$$

This approach was extended to the parametrization of breaking probabilities for dominant waves (Banner et al., 2000). In particular, it was found that breaking probabilities become significant when the saturation exceeds a constant threshold B_r . A similar threshold may also be applied to waves shorter than the dominant waves (Banner et al., 2002).

A preliminary modeling effort based on these observations was made by Alves and Banner (2003) who modified the Komen et al. (1994) dissipation to include a further dependence on the ratio $B(k, \theta)/B_r$, such that

$$S_{ds}(k, \theta) = -C_{ds} \left[\frac{B(k)}{B_r} \right]^{p/2} \left(E_{tot} k_p^2 \right)^m \left(\frac{k}{\bar{k}} \right)^n \omega F(k, \theta), \quad (2.5)$$

where $B(k)$ is the local saturation parameter defined by equation 2.4, $(E_{tot} k_p^2)$ is an integral spectral steepness parameter, with k_p is the peak wavenumber. Following Banner et al. (2002), wave breaking occurs when $B(k) > B_r$, and whitecapping dissipation should become negligible. Nevertheless, to take in account for the other dissipation processes

(straining of shorter waves and wave–turbulence interactions), they assumed that term $[B(k)/B_r]^{p/2}$ asymptotically approaches unity instead of zero with

$$p = \frac{p_0}{2} + \frac{p_0}{2} \tanh \left(10 \left\{ \left[\frac{B(k)}{B_r} \right]^{1/2} - 1 \right\} \right) \quad (2.6)$$

Therefore, we note that the primary dissipation mechanism is supplemented with two multiplication factors $A = (E_{\text{tot}} k_p^2)^m$ and $B = (k/\bar{k})^n$, inherited from Komen et al. (1994)’s parameterisation, in order to represent dissipation due to general background turbulence. The threshold saturation level B_r and the coefficient C_{ds} and p_0 , m and n are constants determined numerically to provide modeled spectra which match the observations. From numerical tuning, they obtained B_r about double of the threshold saturation found from observations by Banner et al. (2002). Furthermore, numerically found high value of p_0 implies a dependence of dissipation on the variance density of up to a power of 5, difficult to reconcile with the conventional wind input expression (van der Westhuysen et al., 2007).

Considering this, van der Westhuysen et al. (2007) built another parameterization, implemented in SWAN, where the dissipation rate is a function of $B(k, \theta)/B_r$ to a power that varies with the wave age. They also removed the multiplication factors A and B considering that general background turbulence cannot be simplified to a simple multiplication factor but must be considered as an independent additional source term. They proposed a whitecapping dissipation in frequency space², except for saturation parameter B kept in wavenumber space, such that

$$S_{\text{ds}}(\sigma, \theta) = -C_{\text{ds}} \left[\frac{B(k)}{B_r} \right]^{p/2} \sigma E(\sigma, \theta), \quad (2.7)$$

where exponent p is a function of the wave age which scales it from 4 to 2, taking into consideration the balance with the wind input (see details on appendix A in van der Westhuysen et al. (2007)).

That type of dependency to wave age was then abandoned in the recent parameterizations by Banner and Morison (2010), Ardhuin et al. (2010), and Babanin et al. (2010). Ardhuin et al. (2010) introduced a directional dependence of the dissipation rate, with much strong dissipation in the mean direction, consistent with observed higher probabilities of breaking waves propagating in the mean direction (Mironov and Dulov, 2008). Conversely, the parameterization by Babanin et al. (2010) assumes a stronger dissipation in oblique directions. More importantly these last three parameterizations also include some suppression of the short wave energy due to the breaking of longer waves. This so-called cumulative effect is consistent with many observations (Banner et al., 1989; Melville et al., 2002; Young and Babanin, 2006).

In his analysis, Phillips (1984) had warned that the use of the saturation spectrum was only meaningful if the spectrum was relatively smooth. Indeed, monochromatic waves of very small amplitude have an infinite saturation level but do not produce any breaking. The saturation-based parameterization of Ardhuin et al. (2010), hereinafter referred to as

²The model SWAN resolves the wave energy balance equation (Eq. 2.1) in frequency space.

TEST451³, does not use a smoothed saturation spectrum. In practice the wave spectrum is most saturated at the peak of the wind sea. As a result, that parameterization gives an abnormal lower dissipation rate on frequencies just above the peak, which is difficult to reconcile with the relatively broad spectral signature expected from the short lifetime of each breaking event. For this reason, Banner and Morison (2010) use a smoothed saturation spectrum.

A different smoothing procedure is used in the parameterization by Filipot and Ardhuin (2012), hereinafter referred to as TEST500. They defined wave steepnesses for different scales based on a moving-window integration of the spectrum. This parameterization has two benefits. Firstly, it allows the estimation of breaking probabilities for different scales, in a way consistent with observations (Filipot et al., 2010). Secondly, it provides a natural way of combining deep and shallow water breaking in a single formulation, extending the work of Thornton and Guza (1983) and Chawla and Kirby (2002). One inconsistency of TEST500 is that it uses the cumulative effect of Ardhuin et al. (2010) which is based on different breaking probabilities. For this reason a modification of TEST500 is proposed. Parameters for all parameterizations discussed in this chapter are given in table 2.1 in paragraph 2.2.4.

Furthermore, mixing air into water, breaking waves form clouds of bubbles beneath the sea surface and foamy patches on the surface. This surface signature makes breaking easily observable with simple visible video or photo camera (Mironov and Dulov, 2008; Thomson and Jessup, 2008; Kleiss and Melville, 2011). The video observations collected at small scales, traditionally from research platforms, ships, or aircraft give information about breaking probability and breaking crest length density as functions of wavenumber (or wave scale). Another source of whitecap measurement is given by the very clear signature of bubbles and foam on the emissivity and brightness of sea surface temperature (Droppleman, 1970). This property was particularly exploited by Anguelova and Webster (2006). Using satellite radiometric measurements, they gave the first global dataset of whitecap coverage.

Many investigations have resulted in relationships between the whitecap coverage and the wind speed at 10m above the sea surface, U_{10} . These relationships exhibit a large variability which cannot be predicted only with the wind speed. Although the measurement conditions, in particular the view geometry and lighting conditions are an inherent source of scatter in video measurements, there are also environmental and meteorological factors besides the wind speed that may explain some of this scatter. These include air-sea temperature difference ΔT , water salinity, but also sea state parameters such as the significant wave height H_s or wave age (Monahan and Muirheart, 1981). Indeed, Hanson and Phillips (1999) found that observed wave age explained a large part of the scatter in the whitecap coverage measurements that they analyzed. Recent measurement campaigns have focused on the estimation of the spectral distribution of breaking crest lengths, introduced by Phillips (1985). Banner and Morison (2010) have shown that their parameterization of wave dissipation was indeed able of reproducing the variability in dominant breaking wave crest lengths. In order to investigate the general applicability

³Compared to the version TEST441b described in that paper, we have introduced a minor swell dissipation modification described in paragraph 2.2.2. This modification has no impact on the breaking statistics.

of our wave model for such a task, we confront here our model to the global radiometric data of Anguelova et al. (2009).

In section 2.2 the two parameterizations by Ardhuin et al. (2010) and Filipot and Ardhuin (2012) are fully described, with a minor update to the latter to make the cumulative effect consistent. This updated parameterization is called TEST570. The resulting dissipation and breaking crest length density are analyzed in section 2.3 with an academic test case and an hindcast of the SHOWEX experiment. In the next section, we interpret whitecap coverage W and mean foam thickness $\bar{\Delta}$ compared to radiometer data over the world ocean. Conclusions and perspectives follow in section 2.5.

2.2 Investigated dissipation parameterizations

From now on, we focus the investigation on the parameterizations by Ardhuin et al. (2010), used for operational ocean wave forecasting at NOAA/NCEP since May 2012, and the parameterizations by Filipot and Ardhuin (2012), now used operationally at NOAA/NCEP for the Great Lakes since 2013, because of their better performance at short fetches. Results with the parameterization of Bidlot et al. (2005) (hereinafter BJA) are given as references, because this parameterization has been used operationally at European Center for Medium-Range Weather Forecasts (hereinafter ECMWF) since 2005, with a few minor adjustments (Bidlot, 2012). However, this parameterization is not investigated because of its poor link to breaking and dissipation observations.

2.2.1 Description of the parameterizations

The two parameterizations by Ardhuin et al. (2010) and Filipot and Ardhuin (2012) here investigated split the swell dissipation and the dissipation of the wind-sea into independent negative source terms, S_{out} and S_{bk} . As stated in the introduction, the swell dissipation due to air-sea friction is added to the wind input in the atmospheric source term such that

$$S_{\text{atm}} = S_{\text{in}} + S_{\text{out}} \quad (2.8)$$

and the oceanic source term includes the dissipation due to wave breaking and wave-turbulence interactions, such that

$$S_{\text{oc}} = S_{\text{bk}} + S_{\text{turb}}. \quad (2.9)$$

Following observations by Banner et al. (1989), Melville et al. (2002), and Young and Babanin (2006), both parameterizations split the wave breaking dissipation source term S_{bk} into a spontaneous dissipation source term $S_{\text{bk,sp}}$ due to wave crest collapsing and another source term $S_{\text{bk,cu}}$ which represents the dissipation of the shorter underlying waves wiped out by the larger breaking waves (cumulative effect). Therefore, the wave breaking source terms is

$$S_{\text{bk}} = S_{\text{bk,sp}} + S_{\text{bk,cu}}. \quad (2.10)$$

The cumulative effect can be observed on the photograph 2.1. We note that, by definition, these two source terms should depend on the same breaking quantities, in particular the breaking probability.

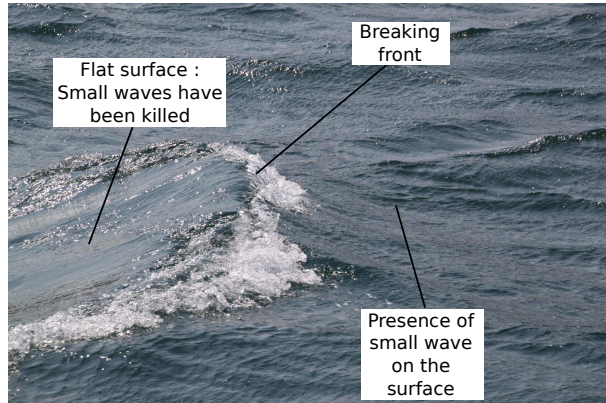


Figure 2.1: Picture of deep-water wave breaking taken by the author from a boat off the north coast of Bretagne. Before the passage of the breaking front, sea surface is covered by ripples waves whereas, in the breaking front wake, sea surface is smoothed. Same process is observed for all wave scales.

Ardhuin et al. (2010) defined⁴ a directional saturation spectrum $B'(k, \theta)$, partially integrated over directions between $\theta - \Delta_\theta$ and $\theta + \Delta_\theta$,

$$B'(k, \theta) = \int_{\theta - \Delta_\theta}^{\theta + \Delta_\theta} k^3 \cos^2(\theta - \theta') F(k, \theta') d\theta', \quad (2.11)$$

with $\Delta_\theta = 80^\circ$. This directional sector of plus or minus 80° , combined with the cosine-square weighting is there to limit the integration of wave trains that actually have enough time to merge together so that individual waves can evolve to breaking (e.g. Banner and Tian, 1998). Because the high frequency gravity waves are generally distributed more broadly over directions, this parameterization also reduces the breaking probability at high frequencies, in a way similar to the directional normalization used by Banner and Morison (2010) or Rogers et al. (2012). Varying $\Delta_\theta = 80^\circ$ from 50 to 120° has very little influence on the model results. This reduction of breaking probability with directional spreading is also consistent with a smaller whitecap coverage in crossing seas (Holthuijsen et al., 2012), although the physical processes involved may be different.

The actual estimation of the dissipation induced by spontaneous breaking $S_{\text{bk,sp}}$ is a weighted average of a dissipation given by the directional saturation $B'(k, \theta)$ and an isotropic dissipation given by the non-directional saturation spectrum $B(k)$, such that

$$B(k) = \max\{B'(k, \theta'), \theta' \in [0, 2\pi]\}. \quad (2.12)$$

Therefore, they proposed a spontaneous breaking dissipation source term

$$S_{\text{bk,sp}} = \sigma \frac{C_{\text{ds}}}{B_r^2} \left(\begin{array}{l} \delta_d \max[\sqrt{B(k, \theta)} - \sqrt{B_r}, 0]^2 + \\ (1 - \delta_d) \max[\sqrt{B'(k, \theta)} - \sqrt{B_r}, 0]^2 \end{array} \right) F(k, \theta). \quad (2.13)$$

⁴We corrected the typographic error in equation (12) of Ardhuin et al. (2010) by removing the erroneous factor $df/dk = C_g/(2\pi)$.

This combination of $B'(k, \theta)$ and $B(k)$ allowed a control of the dissipation directionality. δ_d was adjusted to reproduce observed directional spreads, and also provided good estimates of the energy levels in opposing wave directions (Ardhuin and Roland, 2012).

For the cumulative dissipation, the breaking probability is estimated from the directional saturation spectrum B' , extrapolating the empirical expression given by Banner et al. (2000) for dominant waves on the entire spectrum, and assuming that for the dominant waves the steepness is given by $B'/1.6$. This gives a spectral breaking probability P_b

$$P_b(k, \theta) = 28.4 \max[\sqrt{B'(k, \theta)} - \sqrt{B_r}, 0]^2. \quad (2.14)$$

For each breaking wave with phase speed \mathbf{C}_b , relative crest velocities of underlying short waves are defined by $\Delta_{\mathbf{C}} = |\mathbf{C} - \mathbf{C}_b|$. Then, the dissipation rate due to cumulative effect is simply defined by the rate of passage of the long breaking waves over the short underlying waves $\Delta_{\mathbf{C}} \Lambda(\mathbf{C}) d\mathbf{C}$ where $\Lambda(\mathbf{C}) d\mathbf{C}$ is the breaking crests length density of wave with phase speed in range $[\mathbf{C}, \mathbf{C} + d\mathbf{C}]$ introduced by Phillips (1985). $\Lambda(k, \theta) dk d\theta$ is estimated using the length density of crest (breaking or not) $l(k, \theta) \simeq 1/(2\pi^2)$ (defined by Ardhuin et al., 2010) with

$$\Lambda(k, \theta) = P_b(k, \theta) l(k, \theta). \quad (2.15)$$

This yields the cumulative dissipation

$$S_{\text{bk,cu}}(k, \theta) = C_{\text{cu}} F(k, \theta) \int_{k' < r_{\text{cu}}^2 k} \int_0^{2\pi} \Delta_{\mathbf{C}} \Lambda(k', \theta) d\theta dk', \quad (2.16)$$

where r_{cu} defines the maximum ratio between the frequency of the underlying waves wiped out by the breaker and the breaker frequency. This whitecapping dissipation added to the wind-wave generation and swell dissipation is called TEST441b and is fully described by Ardhuin et al. (2010). A minor adjustment of the swell dissipation is described in paragraph 2.2.2, giving a parameterization TEST451.

The parameterization of Filipot and Ardhuin (2012) is built on the Breaking Wave Height Distribution (hereinafter BWHD) per wave scale, as parameterized by Filipot et al. (2010). As stated in the introduction, Filipot and Ardhuin (2012) filtered the spectrum $E(k)$ with a sliding rectangular windows R_{f_i} , similar to the range used used by Banner et al. (2000), such that

$$R_{f_i}(f) = \begin{cases} 1 & \text{if } 0.7f_i < f < 1.3f_i \\ 0 & \text{elsewhere.} \end{cases} \quad (2.17)$$

Then for each wave scale f_i , wave steepness is defined from representative wave height H_{f_i} and mean wavenumber \bar{k}_{f_i} , with

$$H_{f_i} = \frac{4}{\sqrt{2}} \sqrt{E_{f_i}} \quad (2.18)$$

and

$$\bar{k}_{f_i} = \frac{\int_0^\infty R_{f_i}(f) k(f) E(f) df}{E_{f_i}}, \quad (2.19)$$

with

$$E_{f_i} = \int_0^\infty R_{f_i}(f)E(f)df. \quad (2.20)$$

Following Thornton and Guza (1983), the BWHD is given in each wave scale f_i by the product of the Rayleigh distribution of wave heights (breaking or not) P_{R,f_i} times a weight function W . Filipot and Ardhuin (2012) used the weight function W_{FAB} introduced and fully described by Filipot et al. (2010). Then integration of BWHD over wave heights gives the breaking probability of the wave field, so breaking probability of the wave scale f_i is then given by

$$P_{b,f_i} = \int_0^\infty P_{R,f_i}(H)W_{\text{FAB},f_i}(H)dH, \quad (2.21)$$

with

$$P_{R,f_i}(H) = \frac{2H}{H_{f_i}^2} \exp\left(-\left(\frac{H}{H_{f_i}}\right)^2\right) \quad (2.22)$$

and

$$W_{\text{FAB},f_i}(H) = a \left[\frac{\beta_{f_i}}{\beta_{t,\text{lin}}}\right]^2 \left\{1 - \exp\left(-\left(\frac{\beta}{\beta_{t,\text{lin}}}\right)^p\right)\right\} \quad (2.23)$$

where $\beta_{t,\text{lin}}$ is a breaking threshold similar to the one defined by Miche (1944) but taking the linearization of the waves into account, and, with D is the water depth,

$$\beta = \frac{\bar{k}_{f_i}H}{\tanh(\bar{k}_{f_i}D)} \quad (2.24)$$

$$\beta_{f_i} = \frac{\bar{k}_{f_i}H_{f_i}}{\tanh(\bar{k}_{f_i}D)}. \quad (2.25)$$

From their observations, Filipot et al. (2010) gave a in range $[1 - 2]$ and p in range $[2 - 4]$. The parameterization of Filipot and Ardhuin (2012) uses $a = 1.5$ and $p = 4$.

The authors also estimated the energy dissipation by unit of breaking crest length $\epsilon(H)$ of breakers with height H , adjusting the bore model to all water depths (full details in Filipot et al., 2010). Defining $\Pi_{f_i} = \bar{k}_{f_i}/(2\pi)$ as the crest length (breaking or not) of unidirectional waves per square meter in wave scale f_i , they obtained dissipated energy Q_{f_i} with

$$Q_{f_i} = \int_0^\infty P_{R,f_i}(H)W_{\text{FAB},f_i}(H)\Pi_{f_i}\epsilon(H)dH. \quad (2.26)$$

The dissipated energy quantity Q_{f_i} is then distributed over the wavenumber contained in the wave scale f_i using a weight function of the energy such that

$$Q_{f_i}(k) = Q_{f_i} \frac{E(k)dk}{E_{f_i}}, \quad (2.27)$$

where E_{f_i} is the energy in the wave scale f_i . Due to overlap of the filtering windows, each spectral component participates in several scales. Energy lost by spontaneous breaking $Q_{\text{bk,sp}}$ is then given by

$$Q_{\text{bk,sp}}(k) = \frac{1}{N} \sum_{i=1}^N Q_{f_i}(k) \quad (2.28)$$

where $f_{i \in [1, N]}$ are the wave scales involving k .

$Q_{\text{bk,sp}}(k)$ is then distributed over direction with

$$Q_{\text{bk,sp}}(k, \theta) = Q_{\text{bk,sp}}(k) \frac{E(k, \theta) d\theta}{E(k)}, \quad (2.29)$$

Finally, dissipation $S_{\text{bk,sp}}$ is given by $S_{\text{bk,sp}}(k, \theta) dk d\theta = Q_{\text{bk,sp}}(k, \theta)$. Compared to the original algorithm, we now compute P_{b, f_i} by extrapolating the wave spectrum to unresolved high frequencies, assuming a f^{-5} roll-off of the energy spectrum. The bottom panel of figure 2.3 shows the breaking probabilities obtained with this spectral extrapolation.

Because there may be inconsistencies in combining breaking probabilities derived from saturation spectrum (Ardhuin et al., 2010) for cumulative dissipation, and breaking probabilities derived from wave scale analysis (Filipot and Ardhuin, 2012) for spontaneous dissipation, a consistent combination, resulting in TEST570 parameterization, is presented and validated in paragraph 2.2.3. Despite the fact that this new parameterization does not clearly provide better results, the inconsistency of the dissipation term S_{bk} in TEST500 does not allow the modelisation and the investigation of the breaking properties which are derived from it.

2.2.2 Correction of swell dissipation

The essence of that modification is a smoothing of the swell dissipation function around the threshold for transition between laminar and turbulent conditions. This was done by introducing a weighted average of the laminar $S_{\text{out,l}}(f, \theta)$ and turbulent $S_{\text{out,t}}(f, \theta)$ dissipation source terms respectively given by equations (8) and (9) of Ardhuin et al. (2010),

$$S_{\text{out}}(f, \theta) = (0.5 + \alpha) S_{\text{out,l}}(f, \theta) + (0.5 - \alpha) S_{\text{out,t}}(f, \theta) \quad (2.30)$$

where the smoothing parameter is defined by,

$$\alpha = 0.5 \tanh \left[(\pi H_s^3 / (4\nu T_{m0,2}) - s_4) / s_7 \right], \quad (2.31)$$

where $\nu = 1.4 \times 10^{-5} \text{ m}^2 \text{ s}^{-1}$ is the air viscosity, $T_{m0,2}$ is the mean wave period and $s_4 = 10^5 \text{ m}$ and $s_7 = 2.3 \times 10^5 \text{ m}$ are fitting parameters.

The new parameterization of swell dissipation reduced the global errors on wave height by 4% on average (Fig. 2.2). More importantly it corrected the abnormal distribution of significant wave heights. Implemented in both TEST441b and TEST500, parameterizations are respectively renamed TEST451 and TEST510.

2.2.3 Adaptation of TEST500 into TEST570

The parameterization TEST500 by Filipot and Ardhuin (2012) is now modified by including both a correction of swell dissipation described above, and a cumulative effect now consistent with the spontaneous breaking dissipation term. These aspects are implemented in WAVEWATCH III[®] (hereinafter WWATCH), and we refer to the modified parameterization as TEST570.

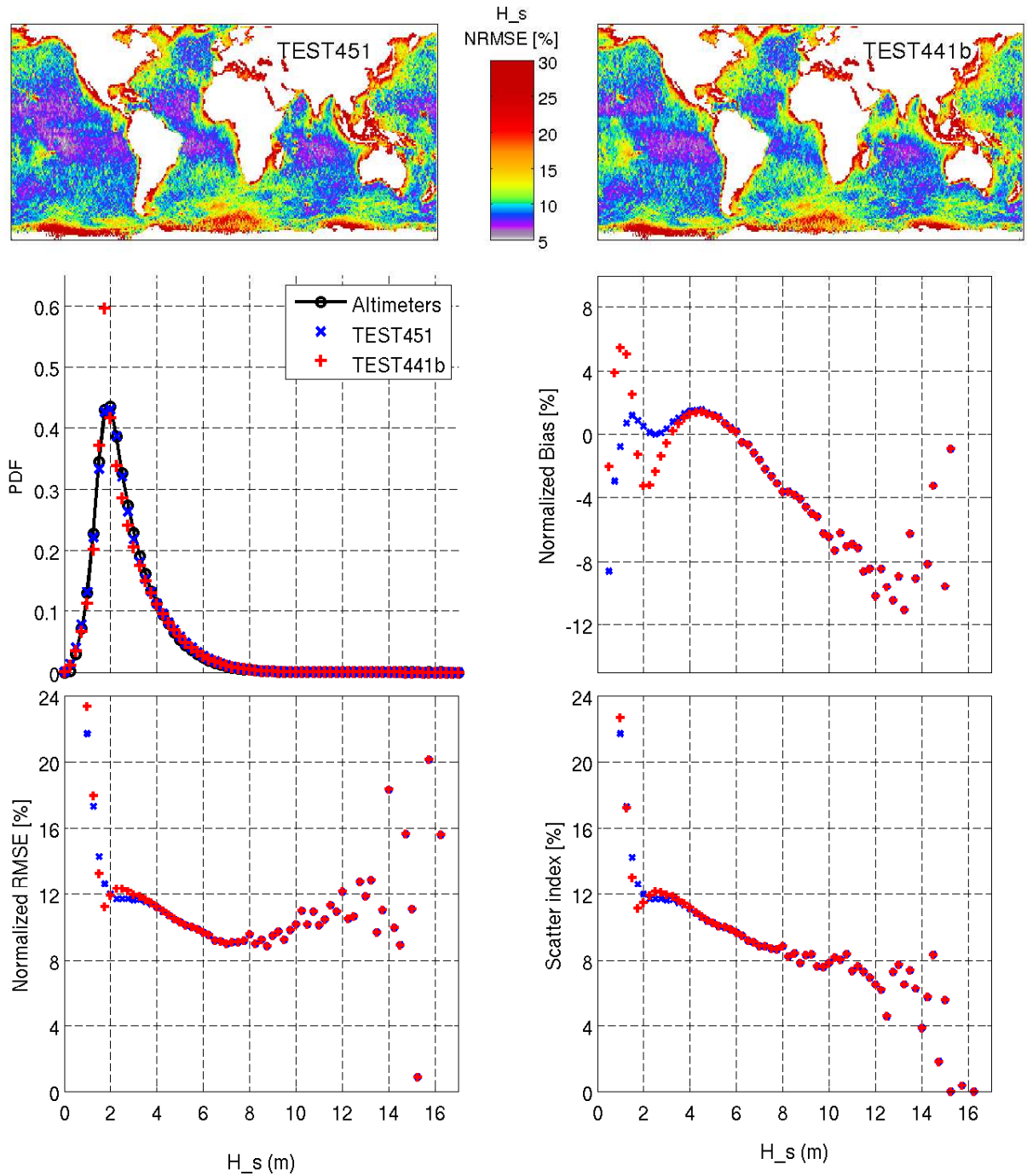


Figure 2.2: Top: Global NRMS Error for parameterizations TEST441b (left) and TEST451 (right). Middle: Comparison of PDF of wave heights (left) and Normalized bias vs wave height (right). Bottom: Comparison of Normalized RMS Error (left) and Scatter Index vs wave height (right).

From breaking probabilities P_{b,f_i} estimated by equation (2.21), breaking probabilities $P_b(k)$ at wave wavenumber k is then estimated averaging the P_{b,f_i} of the N wave scales $f_{i \in [1,N]}$ involving k ,

$$P_b(k) = \frac{1}{N} \sum_{i=1}^N P_{b,f_i}. \quad (2.32)$$

The breaking probability is distributed over different directions proportionally to the spectral energy

$$P_b(k, \theta) = P_b(k) \frac{E(k, \theta)}{\int_0^{2\pi} E(k, \theta) d\theta}. \quad (2.33)$$

Then, $\Lambda(k, \theta)$ is obtained with equation (2.15) and is now used in equation (2.16) to provide the cumulative dissipation.

The parameters for spontaneous dissipation are kept equal to those proposed by Filipot and Ardhuin (2012) and parameters for cumulative effect dissipation, r_{cu} and C_{cu} in equation (2.16) are kept equal to those proposed by Ardhuin et al. (2010) (see §2.2.4). As a result, the only differences with TEST500 are the breaking probabilities used in the cumulative term.

We note that $C_{cu} = 0.6$ is kept whereas it is expected to be close to 1 (Ardhuin et al., 2010). There can be two explanations. First, the crest lengths of all waves, breaking or not, is larger by a factor of two in Ardhuin et al. (2010) compared to Banner and Morison (2010). Using the expression in Banner and Morison (2010), we would arrive at the same model results with $C_{cu} = 1.2$. Second, it appears likely that the wind input for the shortest waves is underestimated in the parameterizations described here (see Rascle and Ardhuin, *A global wave parameter database for geophysical applications. Part 2: model validation with improved source term parameterization*, submitted to Ocean Modelling). This low input requires an underestimation of the dissipation rate to produce a correct spectral level. Calibration of the new parameterization leads us to reduce the global swell dissipation factor from 0.70 to 0.65. The wind input coefficient β_{max} is also decreased from 1.52 to 1.50 (see 2.2.4 for further details).

Validation of the updated (TEST570) parameterization

Global validation for all of 2006 The model performance in terms of significant wave height H_s and mean square slope (mss) is now given. The model uses a 0.5-degree regular resolution in longitude and latitude. ECMWF operational analyses for the wind and sea ice concentration are used as forcing fields, with the addition of sub-grid blocking of waves by small icebergs in the Southern Ocean, using the method and iceberg dataset described by Ardhuin et al. (2011b). The validation uses altimeter data from ERS2, ENVISAT, Jason-1 and GFO-Sat, assembled in the Globwave database (Queffeulou and Croizé-Fillon, 2010). The model results from three-hourly gridded output are interpolated on the satellite track position every second. Both model and satellite data are then averaged over 1 degree in latitude along the track. These averaged parameters are then binned geographically or according to the wind speed and wave height.

Figure 2.4 shows the similar biases and random errors of the TEST570 and TEST451 parameterizations. These are also close to the results of TEST500 (not shown, see Filipot

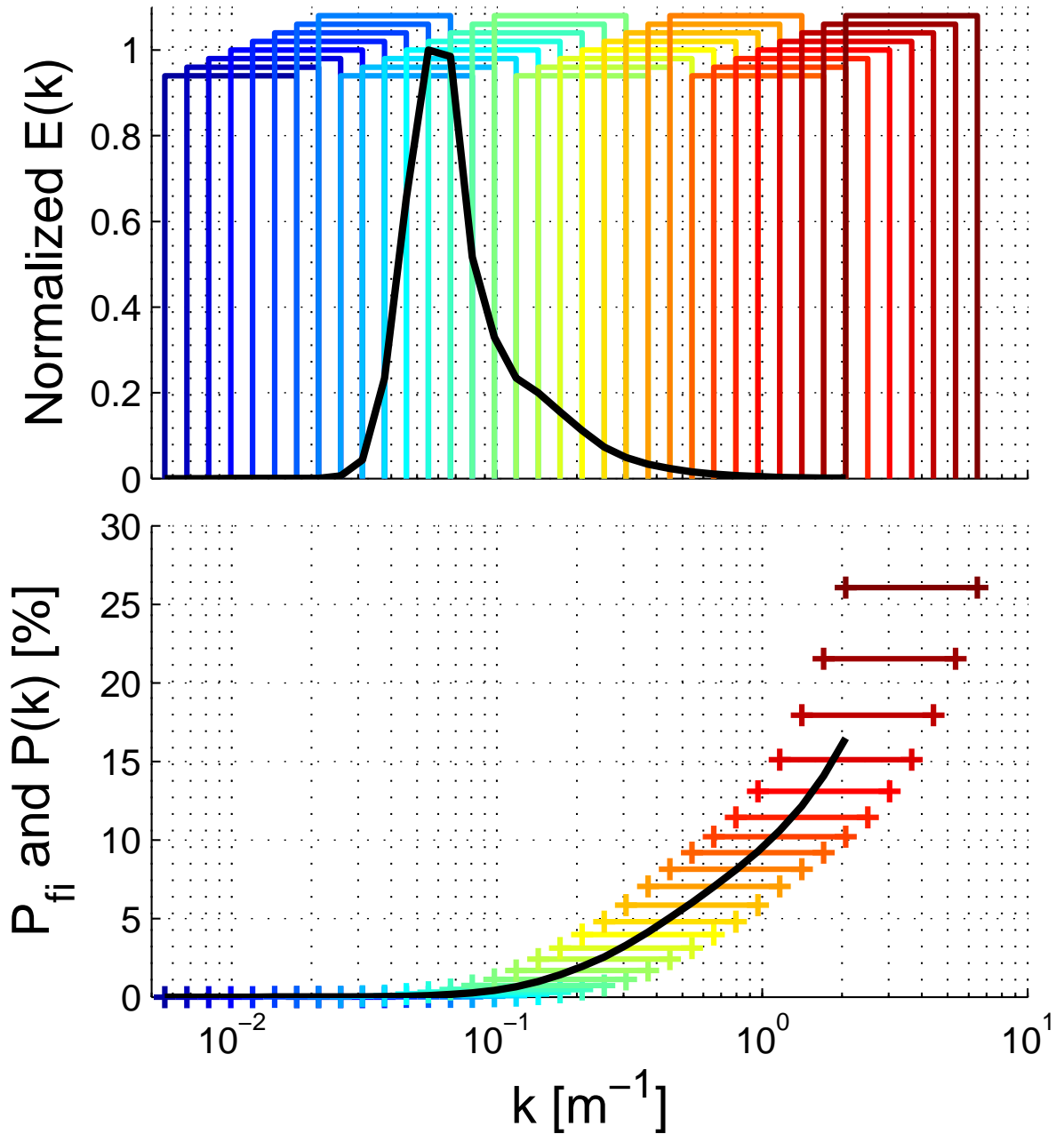


Figure 2.3: Top: Rectangular filtering windows W_{f_i} (colors) over integrated spectrum (black line). Bottom: Breaking probabilities P_{b,f_i} obtained for each wave scale f_i (colors) and breaking probability $P_b(k)$ obtained with averaging (Black line).

and Ardhuin 2012). These results contrast with the very different error pattern obtained with the BJA parameterization by Bidlot et al. (2005), which is shown for reference. BJA produces larger normalized errors, with large biases for low wave heights, due to an underestimation of swell dissipation, in particular in the Pacific Ocean. That effect is generally well corrected in the operational ECMWF by the assimilation of altimeter data. Other aspects of these differences are discussed by Ardhuin et al. (2010). TEST570 generally

yields slightly larger random errors compared to TEST451 but, similar to TEST500 (Filipot and Ardhuin, 2012), it also has less bias for the significant wave height in enclosed seas such as the Gulf of Mexico, the Mediterranean Sea or Hudson Bay, giving smaller overall errors there.

When the data is binned according to wave height, as shown on figure 2.5, we see that the swell dissipation correction of TEST451 has removed most of the strange biases in TEST441b for heights between 1 and 3 m (Ardhuin et al., 2011a, Fig. 1). Because they share the same swell treatment, the same benefits are found in TEST570 compared to TEST500. For larger wave heights, the negative bias with TEST451 is greatly reduced in TEST570. However, this reduced bias for the highest wave ranges should be considered with caution, given the general underestimation of high winds in the ECMWF analyses (Ardhuin et al., 2011a; Hanafin et al., 2012). It is likely that, for these phenomenal seas, an overestimation of the wave growth is compensating for a low bias in the ECMWF wind speeds. Results are also given using CFSR wind as forcing wind fields. In this case, wind input coefficients are reduced to $\beta_{\max, \text{CFSR}} = 1.33$ (Ardhuin et al., 2011a) for TEST451 and we consistently fix $\beta_{\max, \text{CFSR}}$ to 1.30 for TEST570.

A complementary and interesting diagnostic of the model performance is provided by the altimeter normalized radar cross sections (NRCS) that can be interpreted as the mean square slope of the sea surface (Barrick, 1968; Vandemark et al., 2004). Although the absolute calibrations of the NRCS and thus the mean square slope estimation are difficult, their relative variations with wave height, for a fixed wind speed, should follow the variations of the true mean square slope. Ardhuin et al. (2010) showed that, in wave model estimates, this variation is strongly modified by the cumulative parameterization and the sheltering effect in the wind-wave generation term.

The TEST451 parameterization inherits the tuning performed for TEST441b and generally gives a realistic spread in mean square slope for a fixed wind speed, in particular for low wind speeds (Fig. 2.6). Using same cumulative term, TEST500 (not shown here) gives a similar spread. In contrast the distribution $m_{\text{SS}_{\text{ku}}}(U_{10}, H_s)$ shown for TEST570 is narrower than the observed distribution and biases to relatively high values. This behavior suggests that the cumulative effect may be overestimated in TEST570, i.e. the short waves that contribute strongly to the mean square slope are not energetic enough. This could be caused by an overestimation of the breaking probabilities at the largest wave scales. The other possibility is that the sheltering effect is exaggerated, giving a too strong reduction of wave generation at high frequencies. That latter hypothesis is consistent with the nearly inexistent variability of wave-supported stress with wave age in both TEST451 and TEST570.

Fetch-limited case: SHOWEX hindcast Due to its important effect on the spectral shape, wave breaking dissipation also influences the wind input source term, which controls the wave field growth. This wave growth and associated spectral shape, is evaluated with a hindcast of a fetch-limited case measured during SHOWEX, on November 3, 1999 (Ardhuin et al., 2007). The 1 m high swell present with a peak frequency of 0.1 Hz during the experiment is included in the model offshore boundary from the X6 buoy measurements. Details on buoy location and observed data analysis are given by Ardhuin et al. (2007). The model configuration uses the same model grid as the one used

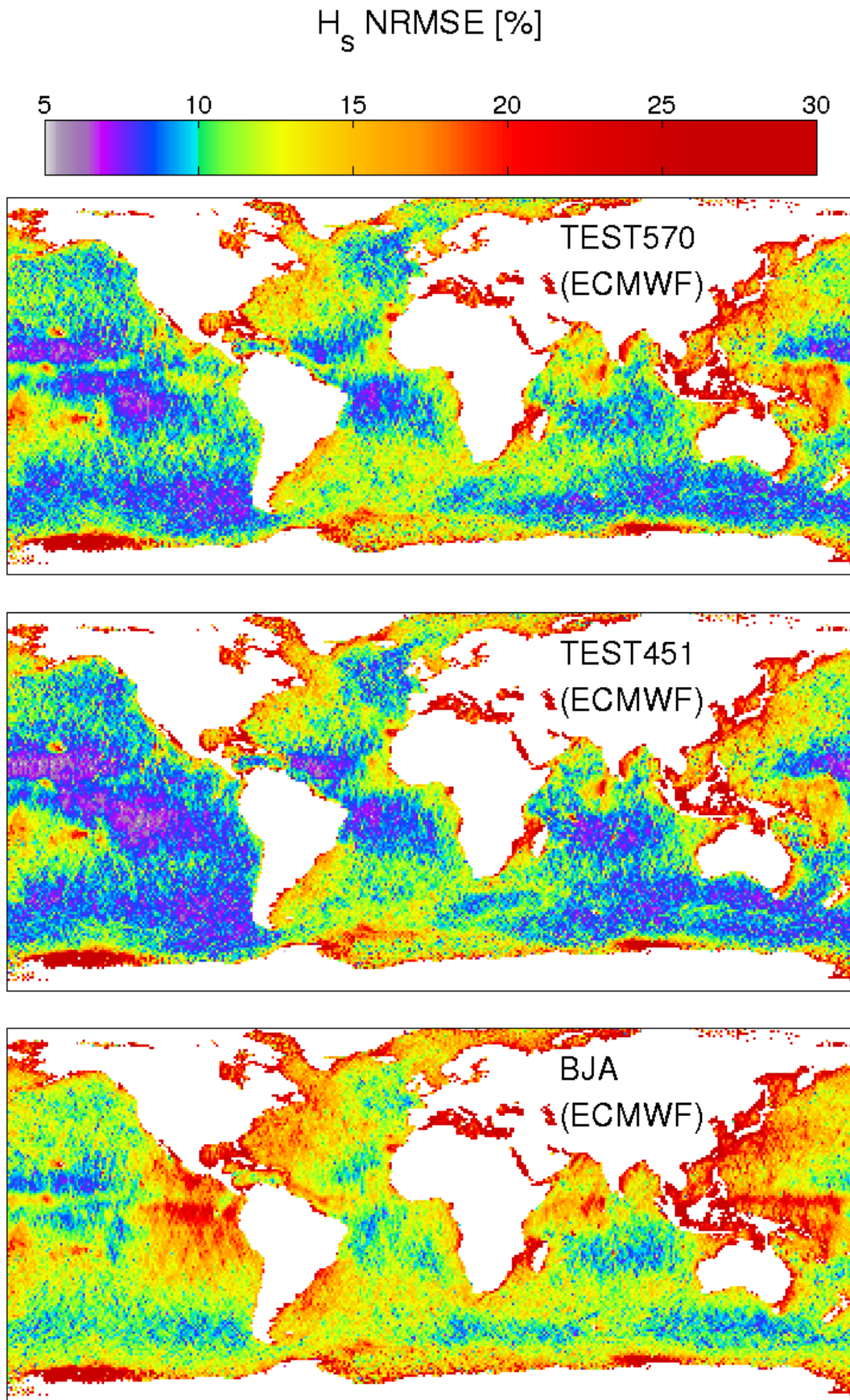


Figure 2.4: Normalized RMS Error for new parameterization TEST570 compared to TEST451 (Ardhuin et al., 2010) and BJA⁶(Bidlot et al., 2005) parameterizations for whole 2006 year. In all three cases the model is driven by ECMWF operational wind analyses.

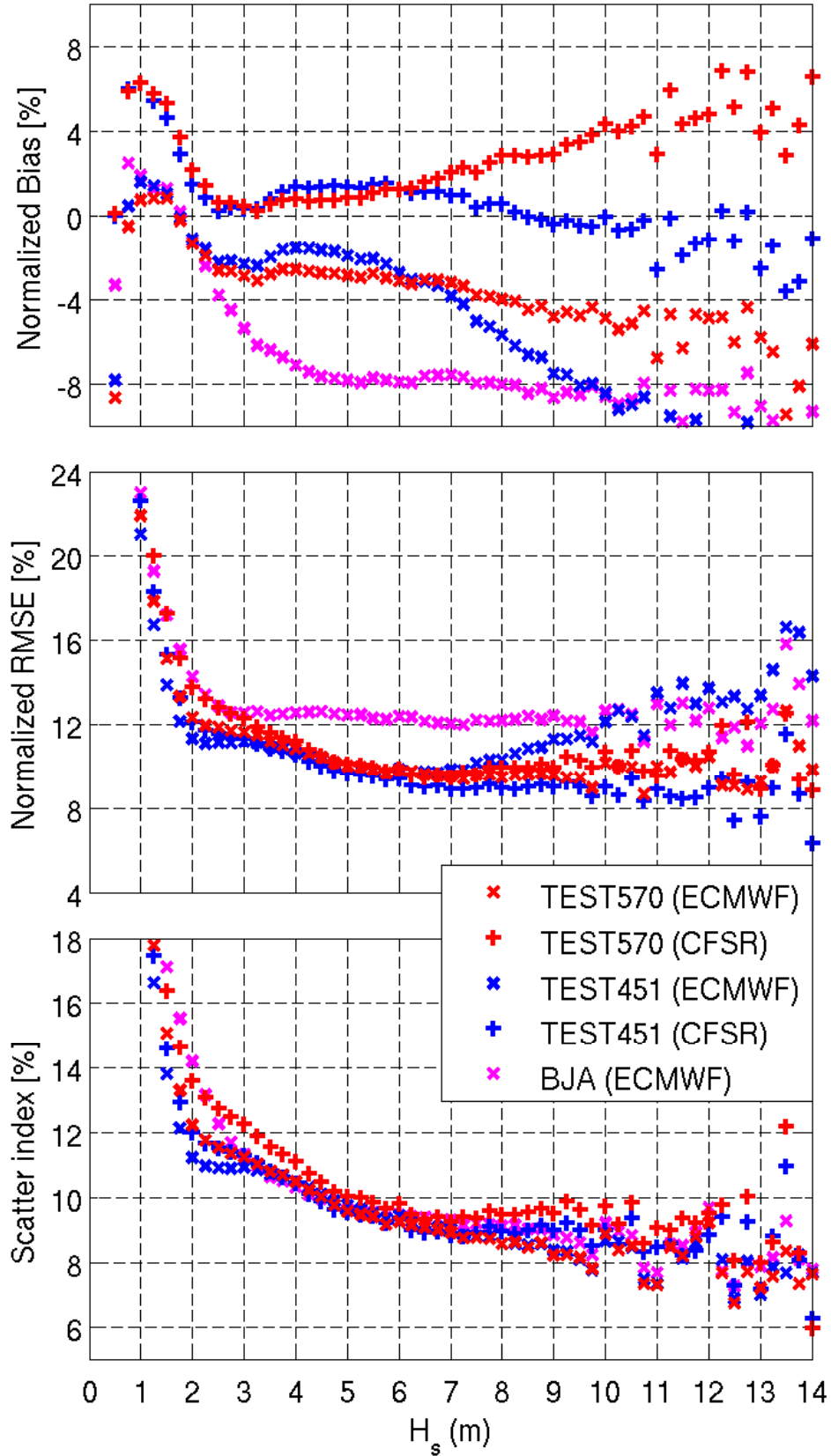


Figure 2.5: Normalized Bias, RMS Error and Scatter Index on H_s for new parameterization TEST570 compared to TEST451 and BJA parameterizations.

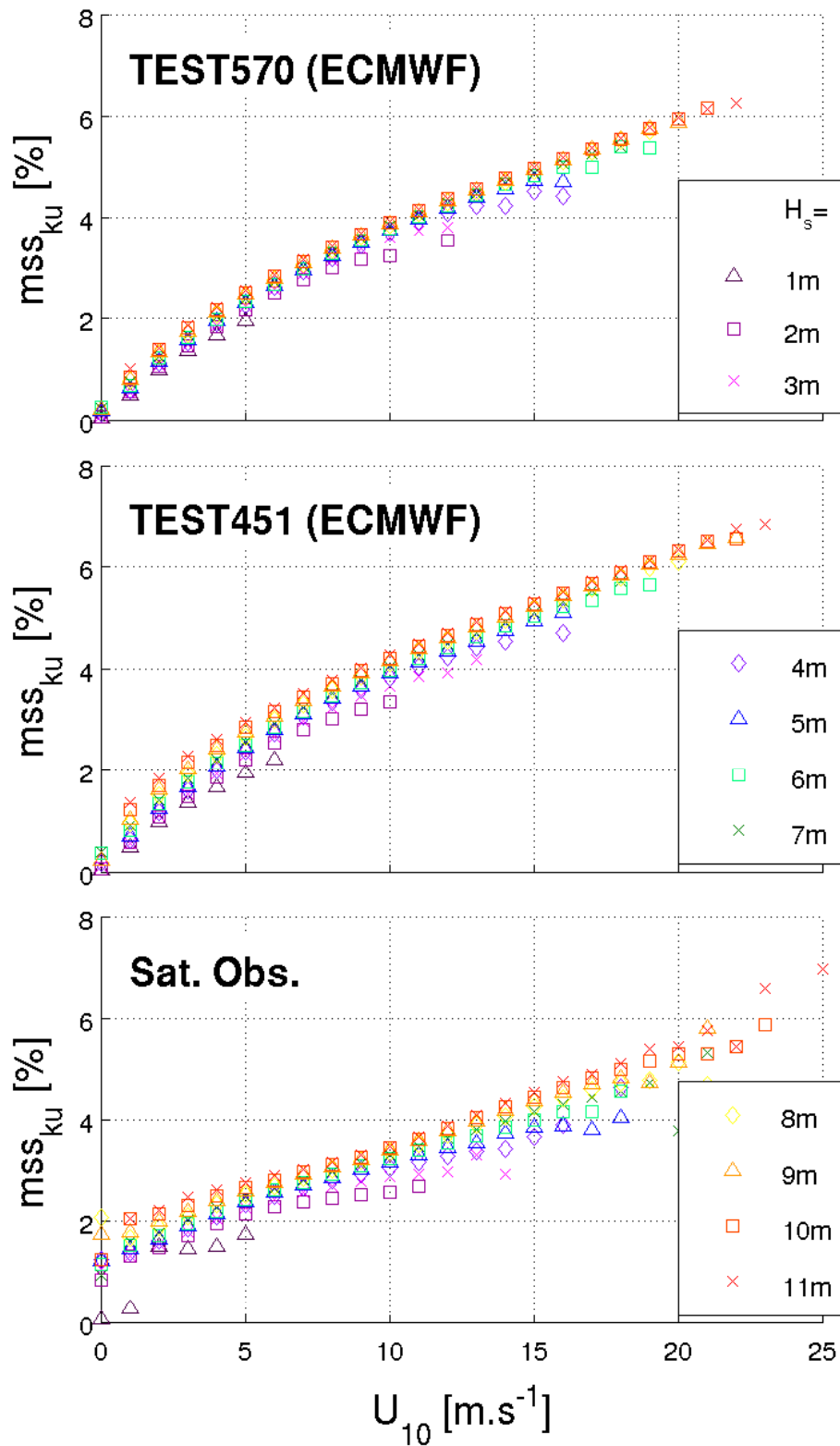


Figure 2.6: Mean values of mss_{ku} binned as a function of H_s (x-axis) and U_{10} (y-axis) for TEST570 and TEST451 parameterizations and satellite observations.

in Ardhuin et al. (2010) with a resolution of 0.016 deg (≈ 1.6 km). Wind forcing is taken from the Climate Forecast System Reanalysis (Saha et al., 2010).

The wind blows offshore with a direction 20 degrees from shore-normal, which results in a particular slanting fetch wind sea for buoys such as X2, located 25 km from shore. Ardhuin et al. (2007) showed how the strength of the input and dissipation source term influence the mean direction in these slanting fetch conditions. Wave directions align with the wind for strong forcing, and wave directions align in the longest fetch (alongshore) for the longer and more weakly forced components. As they also strongly control the spectral shape, non-linear interactions also influence the wave field growth, as reported by Gagnaire-Renou et al. (2010). Here, both DIA and XNL methods are used to estimate the non-linear source term.

Overall, we find a good agreement between model and measurements in terms of energy and mean directions (Fig. 2.7, top and middle panels). The shift in mean direction at the location of buoy X2, from the wind direction at high frequency to the alongshore direction at low frequency, occurs at a slightly lower frequency in TEST570 compared to TEST451, due to a faster development of the wind sea with the new parameterization. Modeled directional spreads are more problematic (Fig. 2.7, bottom panels). They are underestimated for all parameterizations, especially for TEST570, due to a stronger cumulative effect, because short waves in oblique directions are more easily taken over by the large breakers in the main direction. That narrowing effect is partly compensated in TEST451 by the broadening associated with the stronger spontaneous breaking in the mean direction, but in the case of an isotropic dissipation term such as used in TEST570 or by van der Westhuysen et al. (2007), the produced spectra are too narrow.

2.2.4 Model settings for the different parameterizations

Table 2.1 gives the values of the different namelist parameters to reproduce the present results. They can be used in version 4.04 to 4.08 of WWATCH.

Parameters :	β_{\max} [1]	s_7 (Eq. 2.31)	B_{dw} [2]		κ (Eq. 2.34)
WWATCH var. :	BETAMAX	SWELLF7	SDSBCK	SDSC1	WHITECAPWIDTH
namelist :	SIN4	SIN4	SDS4	SDS4	SDS4
TEST441b	1.52	0.0	0	0	0.3
TEST451	1.52	$2.3 \cdot 10^6$	0	0	0.3
TEST500	1.52	0.0	0.185	1	0.3
TEST510	1.52	$2.3 \cdot 10^6$	0.185	1	0.3
TEST570	1.50	$2.3 \cdot 10^6$	0.185	0	0.18

Table 2.1: Wave model settings for parameterizations discussed in the thesis. TEST510 is the updated version of TEST500 (Filipot and Ardhuin, 2012) including minor swell dissipation modification (§2.2.2). Bold values are non-default values, which need to be reset via the SIN4 and SDS4 namelist (see manual of WWATCH) to switch from the default parameterization (TEST451) to another. [1], see Ardhuin et al. (2010). [2], see Filipot and Ardhuin (2012).

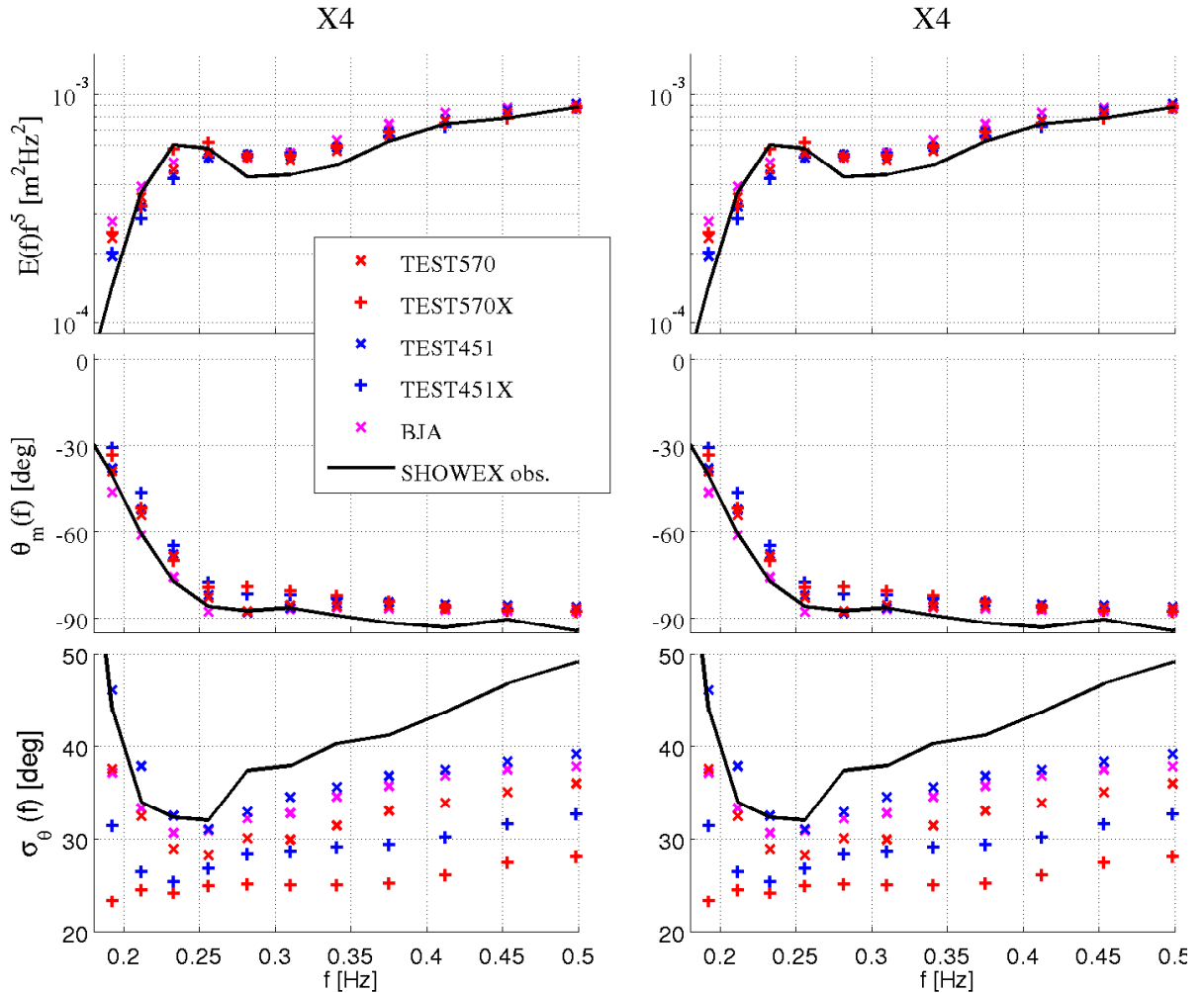


Figure 2.7: Wave spectra (top panels), mean direction (middle panels) and directional spread (bottom panels) on 3 November 1999 at buoy X2 and X4, averaged over the time window 12:00-17:00 EST, from observations and model runs with T451 , TEST510 and T570 parameterizations. The swell is excluded due to the frequency range used in the figure.

2.3 Dissipation source terms and breaking crest length densities

All model results described here use the same spectral grid with 24 directions and 32 frequencies exponentially spaced between 0.037 and 0.7 Hz. In this section, different parameterizations are both used to compute nonlinear interactions between spectral components. Runs named TESTNNN use the Discrete Interaction Approximation (hereinafter DIA) proposed by Hasselmann et al. (1985). Runs noted TESTNNNX use the Webb-Tracy-Resio algorithm for the exact nonlinear interactions (hereinafter XNL), as coded by van Vledder (2006). A diagnostic tail proportional to f^{-5} is imposed at a cut-off frequency $f_c = r_{\text{FM}} f_m$, with $f_m = 1/T_{m,0.1}$. In TEST500X, Filipot and Ardhuin (2012) reduced the value of r_{FM} to 4.5, to maintain a reasonable energy level in the spectral tail. In the new parameterization TEST570X, as in TEST441bX (Ardhuin et al., 2010), the diagnostic tail is imposed only above $r_{\text{FM}} = 9.9$ times the mean frequency, which generally falls outside the model frequency range.

2.3.1 Academic case: Uniform infinite deep ocean

The first model calculations are performed for a single point domain, corresponding to uniform deep ocean conditions. First, the wave evolution is started from rest with a constant wind of 10 m s^{-1} . Figure 2.8 shows breaking probabilities and the associated dissipations obtained after 3 days of simulation, when the wave field is fully developed.

Both parameterizations, TEST570 and TEST451, give similar breaking probability distributions but with a higher level for TEST570. However, the abnormal lower breaking probabilities on frequencies just above the peak observed with saturation-based parameterization (TEST451) disappears with wave scale analysis (TEST570), which provides smooth breaking probability distribution over frequencies. As a result, the higher breaking of waves just above the peak leads to a stronger cumulative dissipation ($S_{\text{bk,cu}}$) at high frequencies.

All source terms and spectra are presented in figures 2.9 (DIA) and 2.10 (XNL). The net dissipation induced by breaking $S_{\text{oc}} = S_{\text{bk,sp}} + S_{\text{bk,cu}}$ is shifted to lower frequencies in the new parameterization TEST570 compared to the result given by TEST451.

With the more accurate estimation of the non-linear source term S_{nl} , the spectral level is artificially higher in the highest two spectral bins. This artefact is due to a kink in the spectrum between the resolved spectral range and the assumed tail shape beyond the highest resolved frequency. However, the breaking probability distribution is not much affected, as shown on figure 2.11.

We now compare the two parameterizations in terms of breaking crest length distribution $\Lambda(\mathbf{C})$ defined by equation 2.15. Here we use the linear dispersion relation to estimate the crest velocities C from the wavenumbers k .

Model calculations are performed for the single point (uniform ocean) started from rest, described above with uniform winds ($U_{10} = 5, 10, \text{ and } 15 \text{ m.s}^{-1}$), during 48 hours (Fig. 2.11). We note that observations show a maximum of the Λ -distribution (Gemrich et al., 2008; Thomson and Jessup, 2008), which is not reproduced by either parameterization. This could be partially explained by the absence of bubble generation in the breaking of

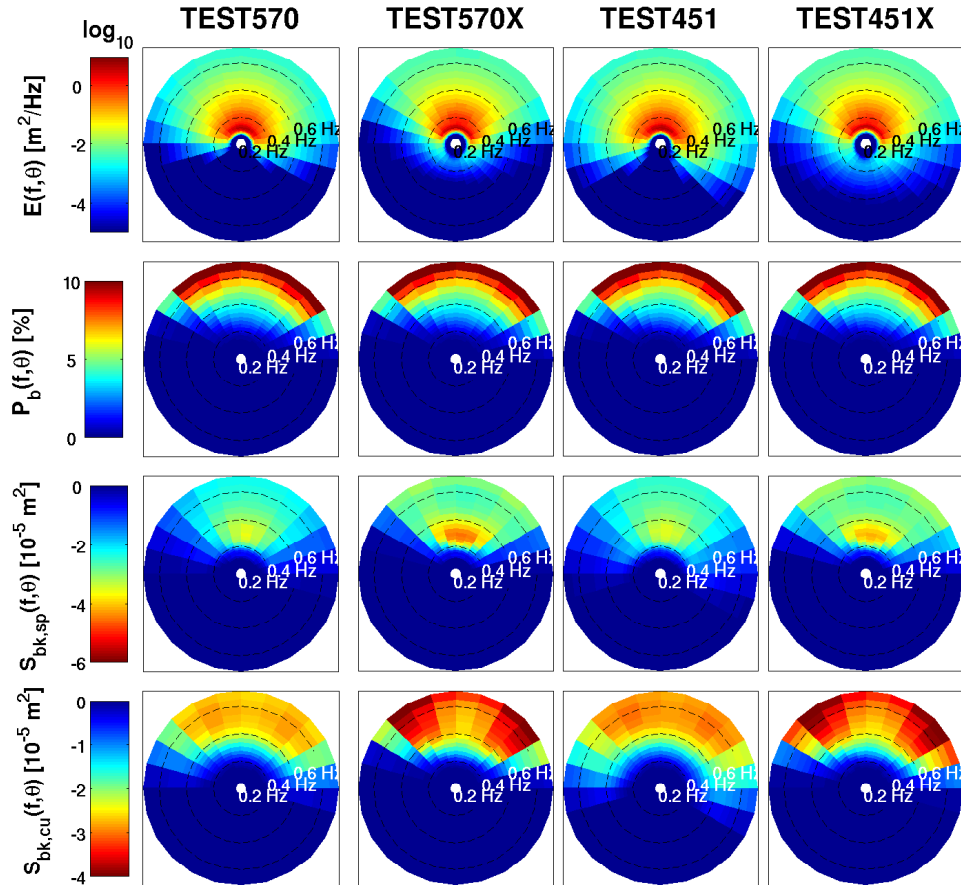


Figure 2.8: Breaking probabilities and associated dissipations obtained for a fully developed sea state (3 days of simulation) for TEST570 (left) and TEST451 (right).

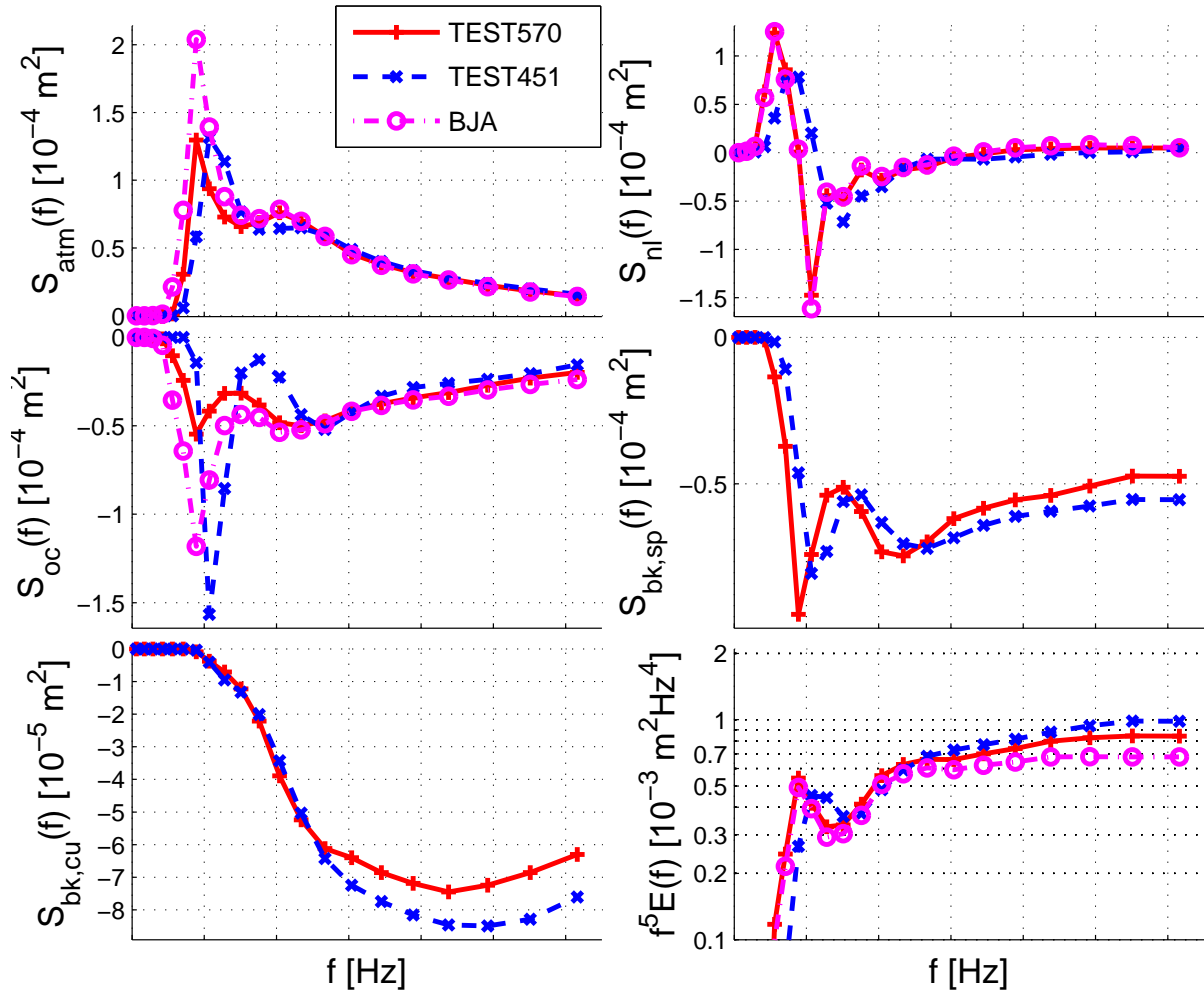


Figure 2.9: Source terms for TEST570, TEST451 and BJA parameterizations using DIA for non-linear interactions after 8 hours of run. The considered model is a uniform infinite deep ocean with a uniform 10 ms^{-1} wind, starting from rest.

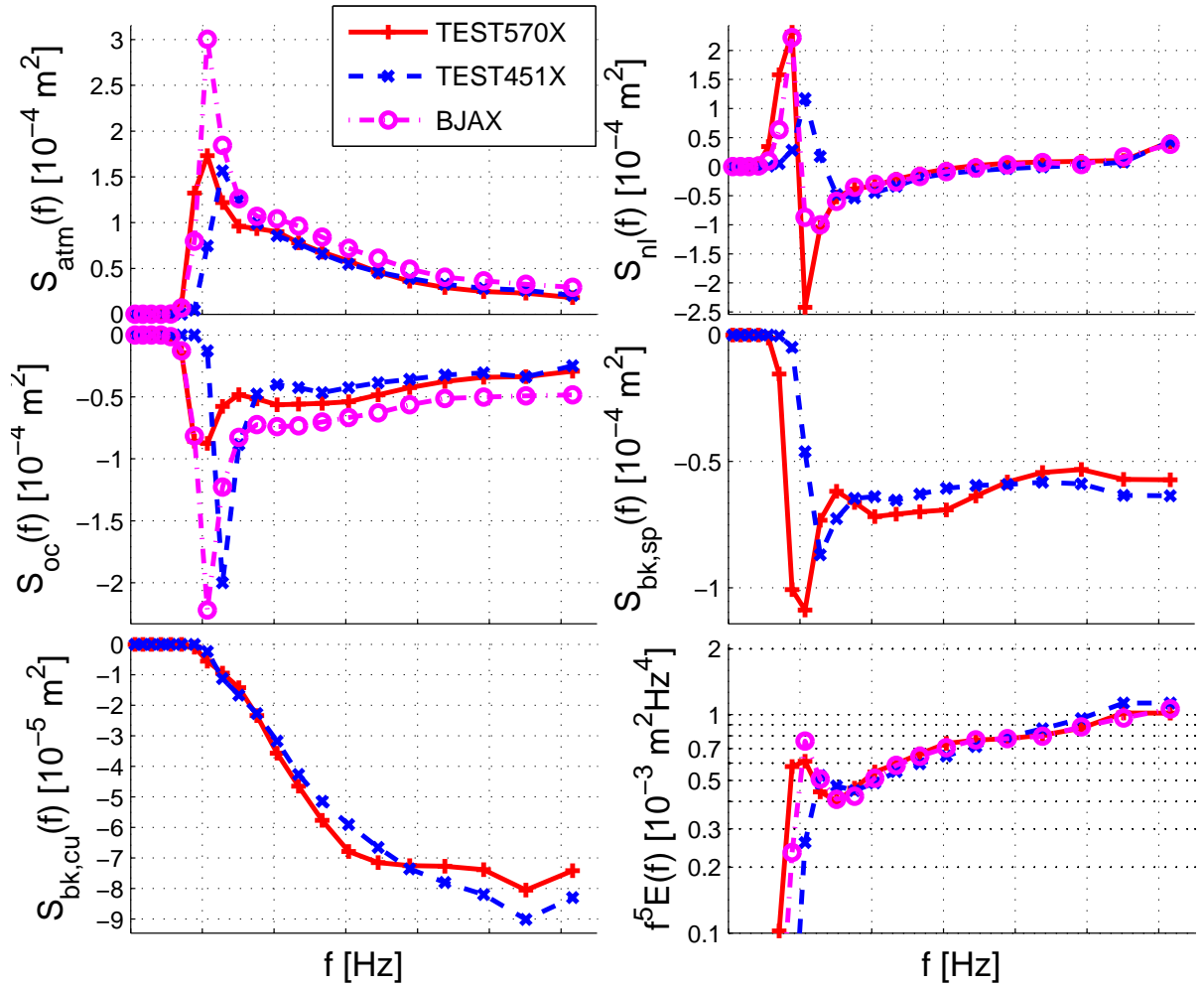


Figure 2.10: Source terms after 8 hours of run for TEST570X, TEST451X and BJAX parameterizations using XNL for non-linear interactions. The considered model is a uniform infinite deep ocean with a uniform 10 ms^{-1} wind, starting from rest.

short waves ($C < 1.5\text{--}2$ m/s). However, infrared observations show that such a maximum also occurs for short gravity waves (Jessup and Phadnis, 2005). In TEST451, the increase in directional spreading towards high frequencies tends to reduce the direction-dependent saturation, but this reduction is not sufficiently pronounced to make $\Lambda(\mathbf{C})$ decrease for small values of C . We have tried a similar generalization of TEST570 in which the spectrum would only be integrated over an angular sector to give the wave steepness from which breaking probabilities are derived. In this case $\Lambda(\mathbf{C})$ can also be reduced but it would also take a very steep spectral decay, close to f^{-6} to produce a maximum in $\Lambda(\mathbf{C})$. Such a spectral variation is not supported by observations (e.g. Banner et al., 1989; Kosnik and Dulov, 2011).

The smooth shape of $\Lambda(C)$ around the peak given by TEST570 is in accordance with the C^{-6} asymptote proposed by Phillips (1985) from the generation and dissipation balance, and observed in experiments by Gemmrich et al. (2008), Melville and Matusov (2002), Mironov (2009), and Kleiss and Melville (2011). However, the level of this asymptote is lower by a factor ≈ 4 than in the observations of Gemmrich et al. (2008) and could be again reduced by a factor of 2 using the expression of the crest lengths of all waves, breaking or not, given by Banner and Morison (2010). In contrast, Λ distributions given by TEST451, with a clear minimum for phase speeds just below those of dominant waves, are not consistent with the observed distributions.

The top panels in figure 2.12 show the evolution of the wave spectrum (left) and the associated Λ -distribution (right). The bottom panel shows the evolution of the Λ -distribution value at the frequency peak (Λ_p) for the various parameterizations. We have used $U_{10} = 12$ m s⁻¹, allowing a direct comparison with the model results of (Banner and Morison, 2010, their figure 8b). Both parameterizations tested here provide values of Λ_p in good agreement with this other model. Nevertheless, we remark that using the DIA or XNL methods for the nonlinear interactions slightly modifies values of Λ_p , with higher levels obtained when using XNL, compared to results obtained with the DIA parameterization.

2.3.2 Wave-breaking experiment: FAIRS hindcast

Hindcasts were run from September 24 to October 10, 2000 offshore of the central Californian coast corresponding to FAIRS (Fluxes, Air-sea Interaction and Remote Sensing) experiment aboard the research platform FLIP in the open ocean 150 km offshore of the central Californian coast (Gemmrich and Farmer, 2004). A global model using a regular grid (0.5 deg resolution) provides input boundary condition for a high resolution domain using an unstructured grid. That particular grid covers the entire U.S. West coast with a resolution of about 500 m along the shoreline and was already used by Ardhuin and Roland (2012). The spectral grid considers 24 directions and 32 frequencies exponentially spaced between 0.037 and 0.7 Hz. Input wind fields are taken from the Climate Forecast System Reanalysis (Saha et al., 2010). Figure 2.13 shows that modeled $\Lambda(C)$ using TEST570 parameterization are consistent with observed one by Gemmrich et al. (2008). The measured and modeled distributions differ for the slowest waves because these waves break without forming bubbles and thus are not detected in the measurements. However, the figure show clearly that shapes of Λ given by TEST570 are in better agreement than

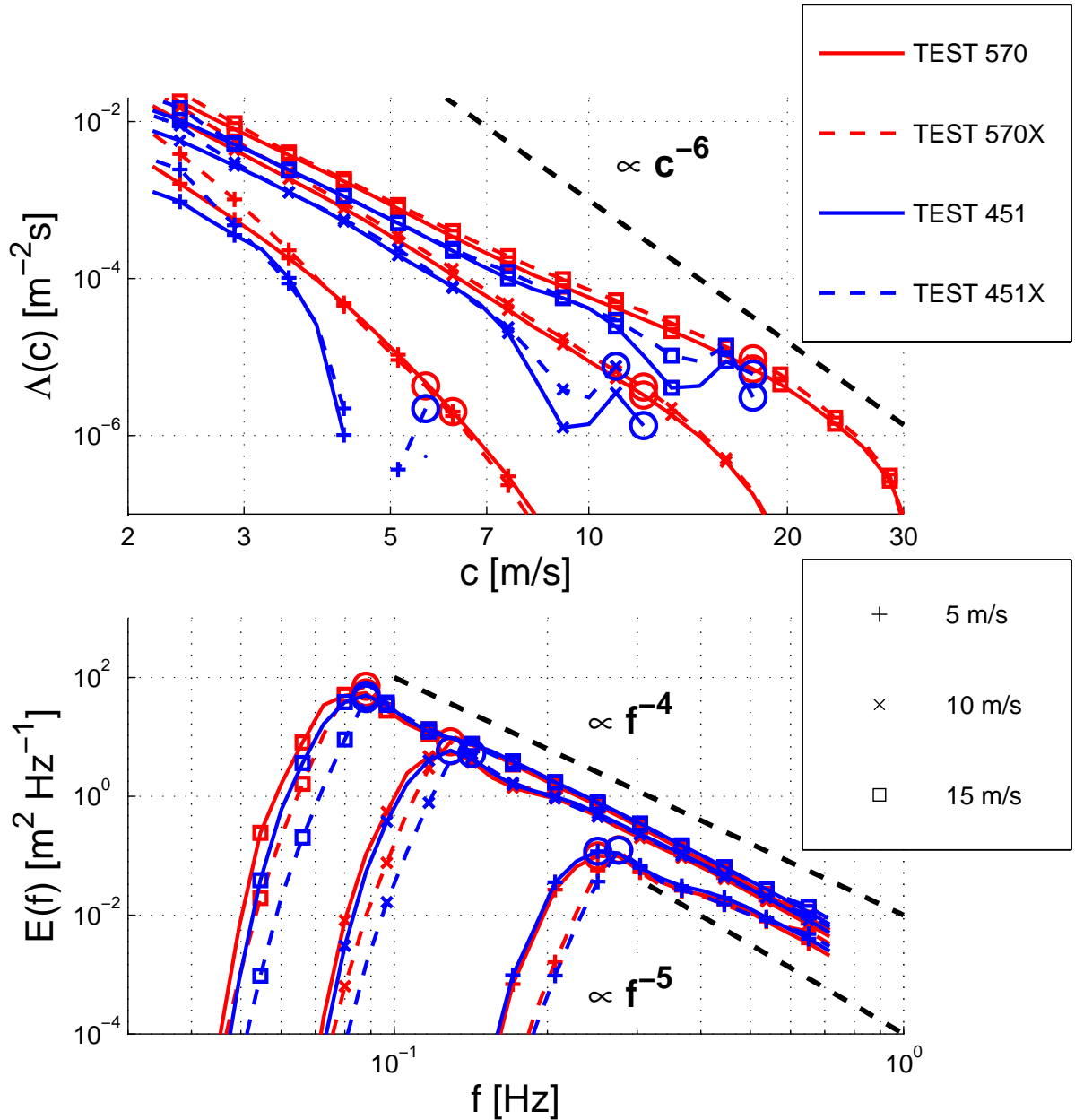


Figure 2.11: Spectra (left) and direction-integrated breaking crest length distribution (right) obtained with TEST570 and TEST451 parameterizations for a uniform infinite deep ocean after 3 days of run, when $C_p/U_{10} > 1.2$, with $U_{10} = 5, 10,$ and 15 m s^{-1} . Energy peaks are marked by circles.

those given by TEST451 which provides too small values at peak scale.

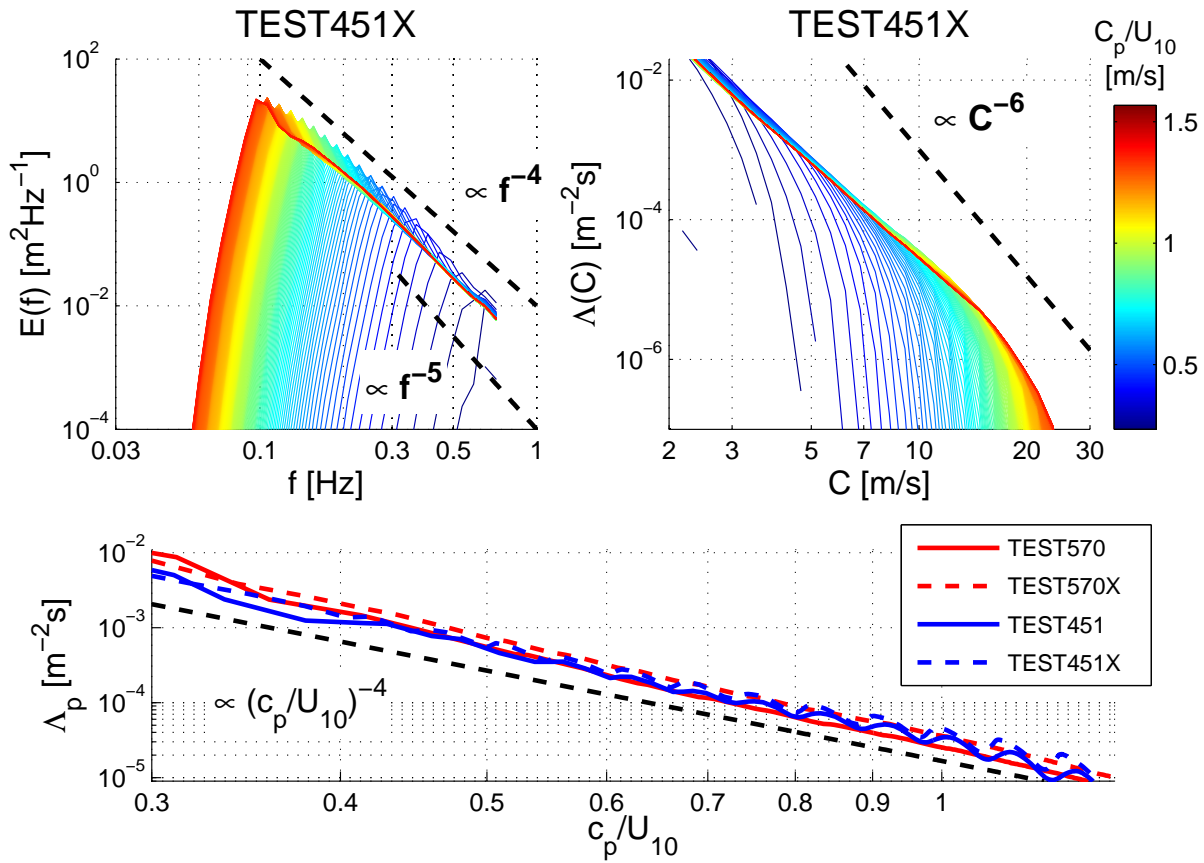


Figure 2.12: Top: Evolution of spectra (left) and direction-integrated breaking crest length distribution (right) for TEST570 (XNL) with increasing wave age (colors), for $U_{10} = 12 \text{ m s}^{-1}$. Bottom: Evolution of $\Lambda(C_p)$ as function of C_p/U_{10} , with TEST570 and TEST451 parameterizations

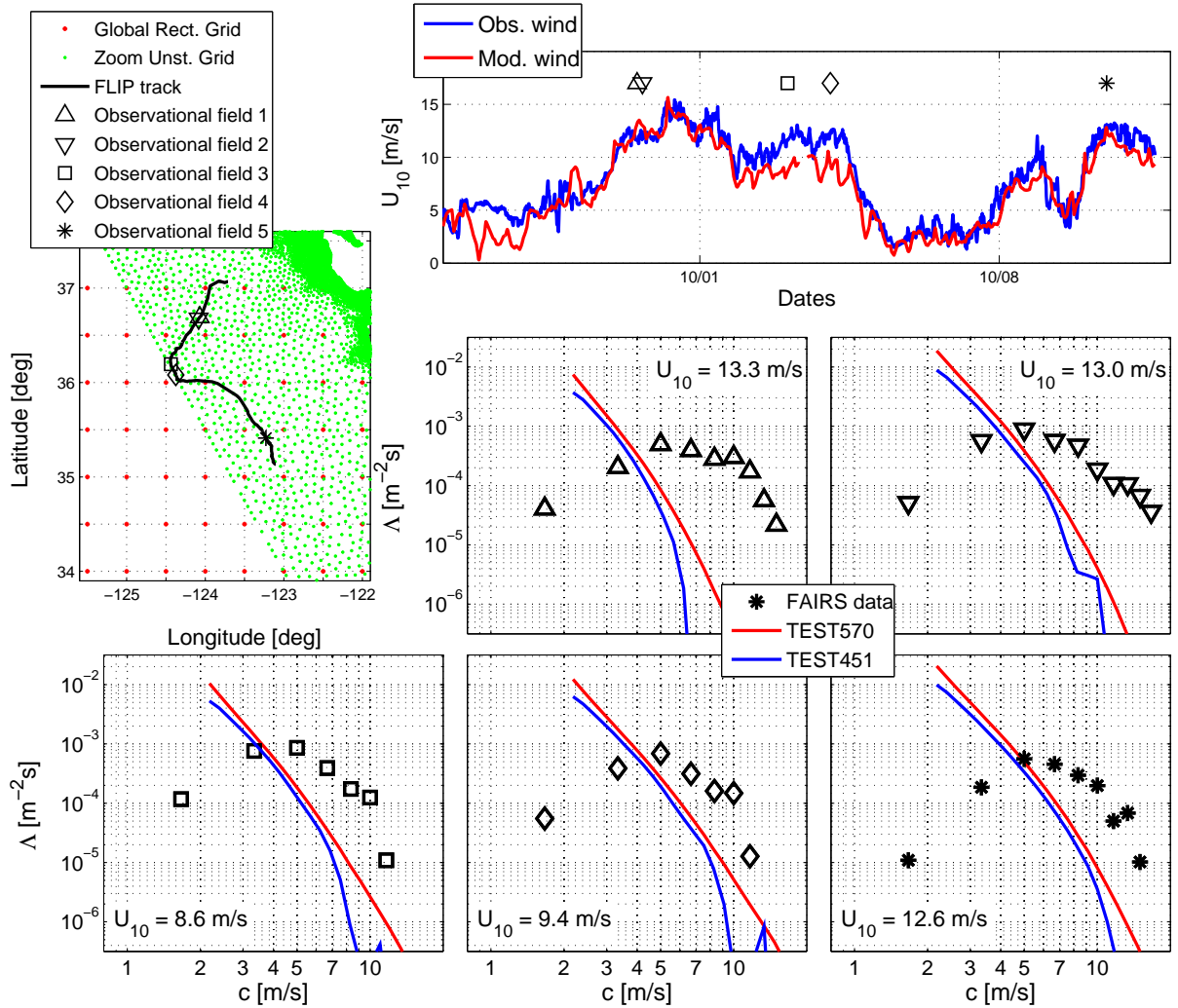


Figure 2.13: Direction-integrated Breaking Crest Length Distribution $\Lambda(C)$ from BWHD integration (TEST570, red) and from directional saturation spectrum (TEST451, blue) extracted from hindcast of FAIRS experiment. Squares are observed $\Lambda(C)$ by Gemmrich et al. (2008).

2.4 Whitecap coverage and mean foam thickness at the global scale

In this section, we consider the global hindcast of the year 2006, for which we obtained the WindSat radiometer data interpreted by Anguelova and Webster (2006). The model uses the same 0.5-degree regular resolution in longitude and latitude, ECMWF operational analyses for the wind and sea ice and iceberg concentrations than used in previous described global validation of the TEST570 parameterization. The non-linear source term is now computed using only the DIA (Hasselmann et al., 1985). This same model is validated in terms of wave height and mean square slope in 2.2.3. The low error levels for both parameters, typically 10% of the observed RMS values, indicate a generally good representation of the frequency spectrum. We now consider our estimations of whitecap coverage in relation to the radiometer data of Anguelova et al. (2009).

In order to be consistent with radiometer data, we define the whitecap coverage (WCC) as the fraction of sea surface covered by both active breaking (stage A) and residual foam (stage B). Although stage A is more closely related to breaking fronts, which is what we model, these two stages are difficult to separate in microwave radiometric data. This combination with stage B introduces a large variability due to other factors, such as water temperature and salinity, which we have not introduced in our model.

For a single breaker, the area covered by foam is obtained by multiplying the breaking crest length by a mean whitecap width parameterized as the constant fraction $\kappa = \kappa_A + \kappa_B$ of breaker wavelength λ . Mironov (2009) has found that the geometry of phase A is well represented by ellipses of almost constant eccentricity with breaking crest lengths distributed as a power-law. These observations are consistent with the use of a constant κ_A . Reul and Chapron (2003) also proposed a κ_A constant to represent stage A. Based on laboratory observations of Duncan (1981), they used $\kappa_A = 0.3$. Our parameterization for both stages A and B is based on the fact that, for constant environmental parameters, stage B is related to stage A.

The whitecap coverage, corresponding to the fraction of sea surface covered by both stages, is here estimated as

$$W = \int_0^\infty \kappa \lambda_C \Lambda(C) dC, \quad (2.34)$$

where λ_C is the wavelength of breaking waves with phase speed C . In deep water, the wavelength is proportional to the squared phase speed ($\lambda_C = 2\pi C^2/g$). Therefore, whitecap coverage from breaking wave with velocities in range C to $C + dC$ in deep water is proportional to the second moment of λ_C (Reul and Chapron, 2003) and the total whitecap coverage, in deep water, is given by

$$W = \int_0^\infty \kappa 2\pi \cdot \frac{C^2}{g} \Lambda(C) dC. \quad (2.35)$$

We have adjusted the constant κ for each parameterization, to provide whitecap coverage consistent with empirical wind-driven fit by Monahan and Woolf (1989) and the global whitecap coverage database of Anguelova et al. (2009). κ is adjusted to 0.30 for TEST451 and 0.18 for TEST570.

The figure 2.14 shows W binned as a function of U_{10} for both model parameterizations using ECMWF forcing wind and satellite observations of whitecap coverage by Anguelova et al. (2009) for the month of March 2006. The blue line corresponds to the empirical wind-dependent expression by Monahan and Woolf (1989), based on video data analysis. The whitecap coverages were derived from WindSat observations by Anguelova et al. (2009), using the methodology of Anguelova and Webster (2006). They used 10 GHz and 37 GHz radiometric measurements in horizontal polarization across the WindSat swath, giving respectively W_{10H} and W_{37H} . The model and observed W are then interpolated on the satellite measurements, and then averaged over 1 degree in latitude along the satellite track. The general dependence of W on the wind speed is relatively well reproduced with a good correlation between modeled whitecap coverage and formula by Monahan and Woolf (1989), mainly for $U_{10} < 15$ m/s. For higher winds ($U_{10} > 15$ m/s), both parameterizations provide a linear dependence of WCC to wind speed, which is consistent with satellite observations. We remember here that the absolute level of W is controlled by κ . Using model wind field, independent of wind observation, by Anguelova et al. (2009), differences between observed wind under satellite track and collocated ECMWF winds leads to a large spread of W_{obs} for a given wind speed. However, this spread shrinks when satellite winds are used, because the wind speed is then estimated from the same brightness temperature used to derive the WCC. Direct comparison between values of modeled and observed WCC on collocated points is shown in figure 2.15. Modeled whitecap coverages are slightly better correlated than an empirical estimate using Monahan and Woolf (1989) and model wind speeds ($R^2 = 0.53$ instead of 0.5), but this improvement is very far from the impact reported by Hanson and Phillips (1999) who used measured wind trends in addition to measured wind speeds. Although geophysical and measurement factors contribute to the scatter, we expect that both the wave modelling and the modelled ECMWF winds are responsible for the larger errors in our model results.

We finally attempted to estimate the mean vertical foam thickness. For this purpose, we modeled the average vertical thickness of foam-layers following Reul and Chapron (2003) (Fig.3, Eq.5), who considered stage A and B of breaking separately. During active breaking (stage A), vertical thickness grows linearly (equation 2.36) to reach a maximum value $\overline{\delta_{\text{max}}} = 0.4 \tau^*/k$. Then, foam thickness decreases exponentially with a time constant τ' (stage B) (equation 2.37). Following Reul and Chapron (2003), the persistence time of active breaking is set to $\tau^* = 0.8T$ and global persistence of a foam-layer, including stage A and B is set to $\tau_{\text{max}} = 5T$ with T the period of the breaking wave. τ_{max} represents the duration between the beginning of the breaking event and the time at which the foam thickness is practically zero. Time evolution of foam thickness $\overline{\delta}(C, t)$ for a wave with phase speed C is estimated for $0 < t < \tau^*$ using:

$$\overline{\delta}(C, t) = \frac{\overline{\delta_{\text{max}}}(C)}{\tau^*} t \quad (2.36)$$

and for $\tau^* < t < \tau_{\text{max}}$ using

$$\overline{\delta}(C, t) = \overline{\delta_{\text{max}}}(C) \exp\left(-\frac{t - \tau^*}{\tau'}\right) \quad (2.37)$$

where the relaxation time τ' is equal to 3.8 s (salt water). Time evolution of vertical thickness is integrated over the foam time persistence to obtain mean foam thickness

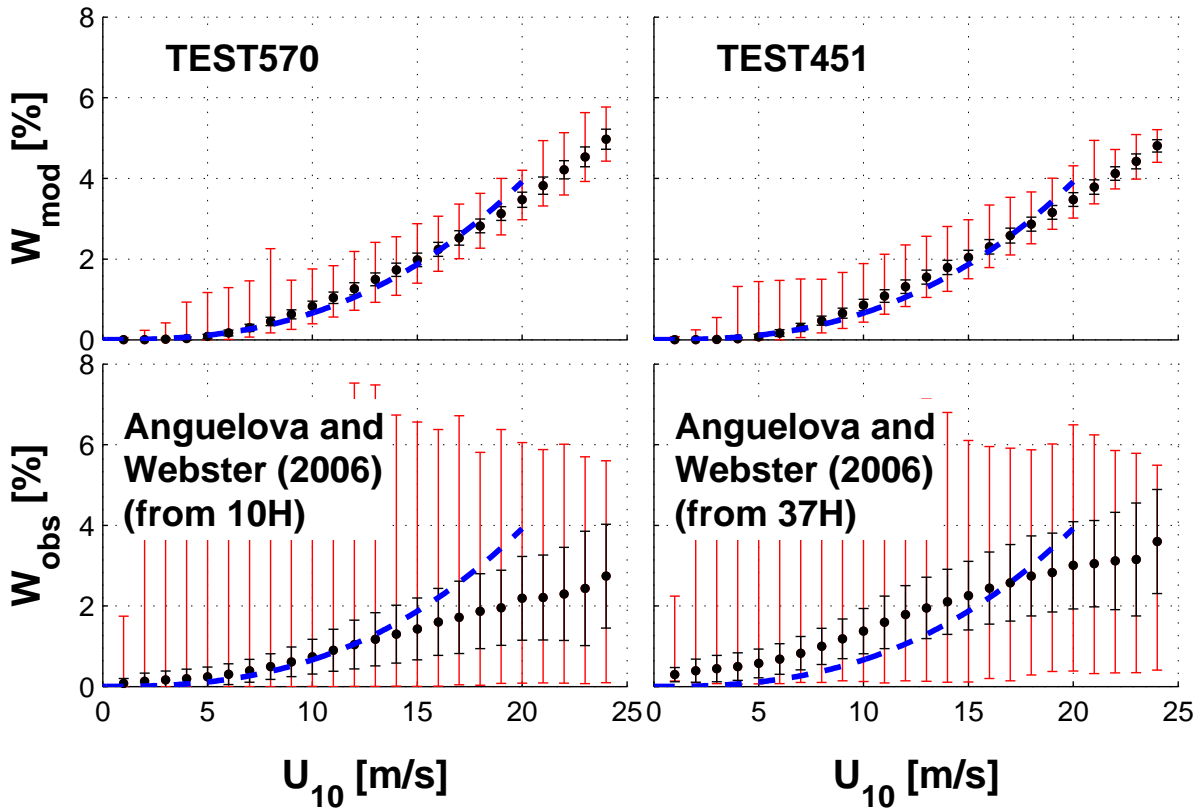


Figure 2.14: Mean values of W binned under the WindSat track as a function of U_{10} for new parameterization (TEST570) and modified Ardhuin et al. (2010)’s parameterization (TEST451) compared to March 2006 satellite observations by Anguelova et al. (2009). Wind used for binning is the collocated CFSR data, which is independent of the WindSat data until September 2008. Red bars represent minimum and maximum values, black bars are the standard deviations and the blue line represents the empirical fit by Monahan and Woolf (1989).

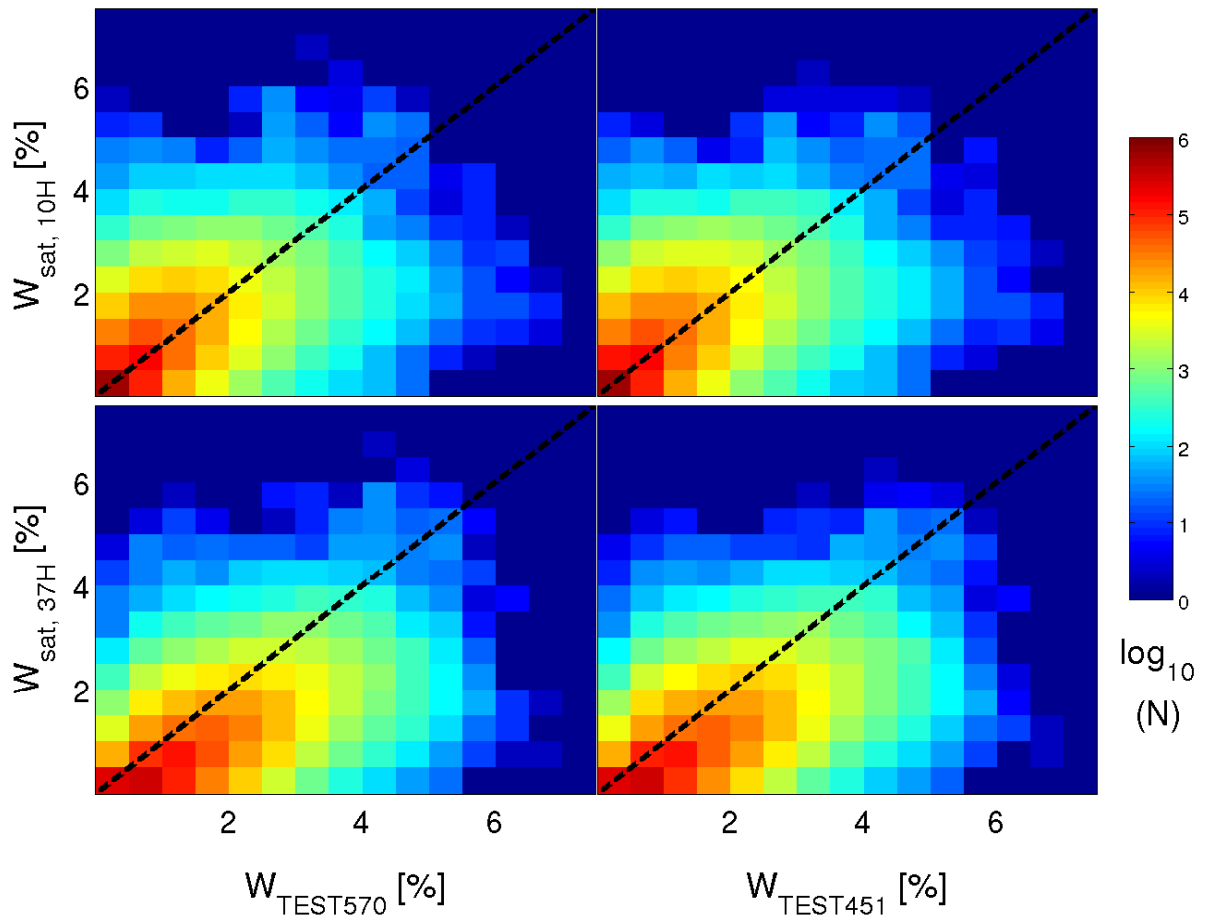


Figure 2.15: Q-Q plot of WCC given by TEST570 and TEST451 and satellite observations (Anguelova et al., 2009) on March 2006. Compared values are collocated under WindSat swath. Colors give the values of $\log(N_{\text{val}})$.

$\overline{\Delta}(C)$ of individual breaking events:

$$\overline{\Delta}(C) = \frac{\overline{\delta_{\max}}(C)}{\tau_{\max}} \left(\frac{1}{2} + 3.8 \left(1 - \exp \left(-\frac{\tau_{\max} - \tau^*}{3.8} \right) \right) \right) \quad (2.38)$$

Integration of the whitecap coverage produced by each scale times its mean foam thickness over all wave scales gives a global mean foam thickness

$$\overline{\Delta} = \int_0^{\infty} \overline{\Delta}(C) \kappa \lambda(C) \Lambda(C) dC, \quad (2.39)$$

The figure 2.16 shows the dependence between the mean foam thickness and the wind speed for the two parameterizations. Higher breaking probabilities just above the peak in TEST570 than ones in TEST451 lead to a slightly higher level of mean foam thickness. This difference increases with wind speed due to displacement of the peak to longer waves which produce higher foam layers. More importantly, for a fixed wind speed, the relative variability of foam thickness is much larger than the variability observed in whitecap coverage values. This suggests that radiometric data at larger wavelengths, which are more sensitive to foam thickness, may be a good indicator of breaking activity beyond the usual wind-whitecap coverage relation of which the Beaufort scale for wind speeds is a perfect example.

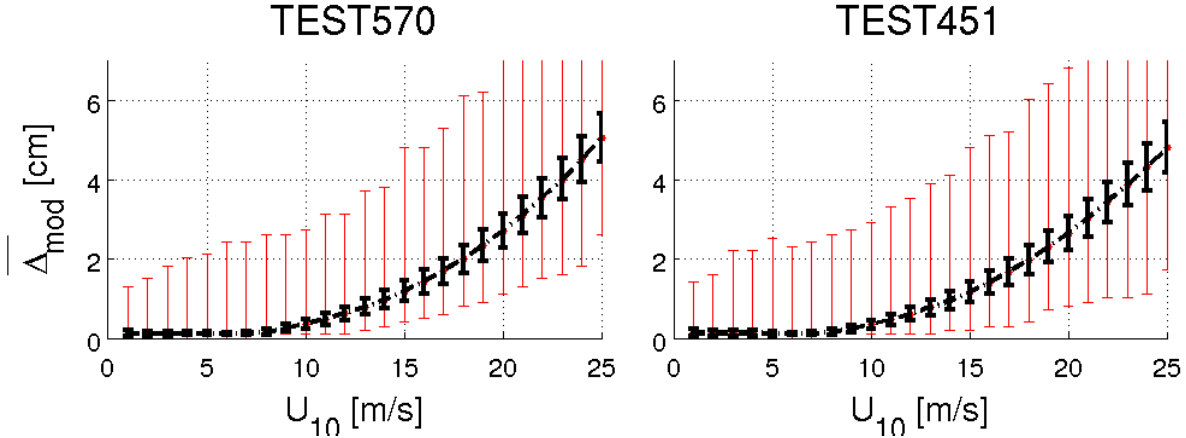


Figure 2.16: Mean values of mean foam thickness ($\overline{\Delta}$) binned as a function of U_{10} for new parameterization (TEST570) and modified Ardhuin et al. (2010)'s parameterization (TEST451). Wind used for binning is the collocated CFSR data, which is independent of the WindSat data until September 2008. Red bars represent minimum and maximum values, black bars are the standard deviations.

2.5 Conclusion and Perspectives

The TEST570 parameterization presented here accounts for the physical relationship that intrinsically links spontaneous breaking dissipation and dissipation induced by breaking waves (cumulative term) and thereby extends the work of Filipot and Ardhuin (2012). The cumulative dissipation term was adjusted so that the model could reproduce observed spectral evolution and global wave heights distributions. It is found that this TEST570 parameterization produces breaking crest lengths distributions that are in better qualitative agreement with observations, contrary to TEST451 which fails to produce smooth Λ -distributions. This difference is clearly associated with the integration over frequencies in TEST570 compared to the local saturation used in TEST451. Banner and Morison (2010) have shown that estimating breaking parameters after smoothing the local saturations over frequencies has the same effect.

Overall, as already shown by Banner and Morison (2010), an explicit modeling of whitecap properties provides a new constraint on the model dissipation source terms, and a more detailed use of global observations from satellite radiometers, such as interpreted by Anguelova and Webster (2006), can be used for this. In particular, we find that joint estimates of the whitecap coverage and foam thickness could be an interesting way to discriminate between different sea states or parameterizations. This can be achieved by combining radiometric measurements from different bands. Recent results by Reul et al. (2006) with L -band radiometric measurements in Hurricanes using the Soil Moisture and Ocean Salinity space mission can be combined with the Ku and X band data to provide the necessary information.

Further work on the parameterization remains, in particular on the method to attribute breaking probabilities and dissipation rates to different directions, and in the physical processes represented in the cumulative term. Indeed, the cumulative effect parameterization of Ardhuin et al. (2010) used with isotropic breaking probability tends to reduce the width of the directional spectrum. All the parameterizations tested here produce directional spectra which are too narrow at high frequencies ($f > 0.6$ Hz in typical oceanic conditions). We attribute this deficiency to a lack of physical processes in the model. In particular the splash of breakers has been shown to transfer energy to high frequencies by creating small waves (Rozenberg and Ritter, 2005, e.g.), and short waves are known to break mostly at the crest of longer waves, due to hydrodynamic and aerodynamic modulations (e.g. Smith, 1986).

The analysis of the recent wave breaking dissipation parameterizations provided in this chapter showed that such parameterizations are able to provide an energy dissipation that properly equilibrate the wave energy balance equation providing spectra in good agreement with observation in terms of shape and energy level, but without guarantee for the underlying physics. In particular, we showed that modeled breaking crest length densities are inconsistent with observations. Moreover, models are currently not able to reproduce the large disparity in observations. We also note that the parameterizations

combine results from different studies, from different areas, from both laboratory and field experiments. The large sensibility of the results to a misunderstood number of external parameters, makes the combination of these studies uncertain.

We here highlights the need of observations that provide in same time information on wave spectrum, directional breaking parameters and directional breaking dissipation. In the next chapter, we propose a field experiment using stereo video system to observe time-space evolution of sea surface wave evolving towards breaking or not. Such observations provide simultaneously directional breaking parameters and directional wave spectrum including non-linear contributions. These observation can also be used to observe the evolution of the wave shapes induced by breaking, and thus, to estimate dissipation induced by breaking.

Chapter 3

Reconstruction of 3D oceanic surface waves

3.1 Introduction

Water wave elevations can be measured with different methods. Usually, 1-D elevation is obtained using a pressure sensor in the water or a capacitive wave gauge crossing the surface. By multiplying the number of instruments, several 1-D surface elevations can be obtained and 2-D surfaces can be approached. Direct 2-D surface elevation can also be obtained using 2-D radar-based systems installed on either fixed positions (Dankert et al., 2003) and aircrafts (Hwang et al., 2000) or using stereo video systems. These last systems provide 3-D elevation maps of water waves by using a spatial-widespread and non-intrusive optical system. Video imagery has another significant advantage with a low-cost system in both installation and maintenance (Holland et al., 1997; Holland and Holman, 1997). A stereo camera view provides spatial and temporal data whose statistical content is richer than that of a time series retrieved from a buoy, which is expensive to install and maintain (Benetazzo, 2006; Gallego et al., 2008). Moreover, extending image processing from static individual images to image sequences of stereo-pairs opens a new world of information. Indeed, stereo image sequences contain both the temporal and spatial structure of the phenomena observed. Except for limitations in resolution in time and space and the size of the images, image sequences capture the events as completely as possible.

Stereoscopy regroups all the methods which reproduce relief effect from a pair of 2D images. Long before its application to recent computer vision, humans have exploited the ability of their brain to create a 3D illusion starting from a pair of 2D images. Therefore, in 1550's, painter Jacopo Chimenti made two drawings representing a slightly different point of view of a same scene to produce a relief effect within the brain of viewer. The first stereoscopic camera appeared in the 1850's, soon after the first simple camera and their evolution is still underway. Taken with a spacing of a few centimeters, pairs of photographs present a slightly different image to each eye and reproduce the relief of the scene. A rich literature on the subject exists on the subject. Stereoscopy appeared in scientific literature from the middle of the 18th century (Wheatstone, 1853; Claudet, 1856, 1857, and many others.) with large scope of application, such as for example, topography

(Galton and Galton, 1865) or medicine (Mach, 1896). Nevertheless, 3D reconstruction of the scene was only a brain process, and no quantitative access to the 3rd dimension was possible.

Further, the development of the epipolar geometry (see §3.3.3) sets the basis of the recent computer vision, where the shape of the scene can be extracted from the stereo pairs of photographs. In spite of the relatively simple procedures involved by the stereo vision, its application to oceanic surface waves is rather limited. Therefore, before the 1950's, only one published study used it (Dankert et al., 1939). In the early 1950's, the desirability of obtaining the two-dimensional sea spectra appeared in the literature (Pierson, 1952; St Denis and Pierson Jr, 1953). The stereo-photography of the wavy surface for determining the vertical displacement of the water surface was initiated by Marks (1954) to determine the wave number spectrum. By taking photographs from a bridge, he was able to get useful data on the two-dimensional wave spectrum, but on a much reduced scale. Moreover, Cruset (1953) also showed feasibility of photogrammetric measurements of the sea swell from synchronized cameras driven by separated aircrafts. These two studies among others motivated the launching of the Stereo Wave Observation Project (Chase et al., 1957; Cote et al., 1960). Latter, Banner et al. (1989) also used the stereo-photography for the measurement of the spectrum directionality. Recently, with the development of the numerical photography, some investigators concerned themselves with wave measurements from stereo photography (Kosnik and Dulov, 2011) or stereo-video (Benetazzo, 2006; Gallego et al., 2008).

In this chapter, the first section gives a description of the experiment. Then, the section 3.3 deals with the theoretical background and the mathematical definitions of the relations between a 3D scene and its camera image projection. The epipolar geometry describing the relations existing between the projection of a same scene on multiple camera images is also considered. Then, the section 3.5 describes methodology of the stereo reconstruction of sea surfaces. Finally the section 3.6 deals with the validation of reconstructed surfaces and the analysis of their corresponding spectra.

3.2 Experiment description

The experiment was conducted on September and October 2011 from the research platform of the Marine Hydrophysical Institute of the Academy of Sciences of Ukraine. The platform is located 500 meters off the coast next to Katsiveli in the Black Sea. The depth at the observation area is at least 30m. The measurements consider synchronized acquisition of wind speed and direction, sea surface elevation and stereo video acquisitions. The positions of the instruments are shown in the figure 3.1. The wind measurements, speed and direction, are obtained using a 23 meter height anemometer. The sea surface elevation is measured at a 10Hz sampling frequency and 2mm accuracy with an array of six wave gauges. Finally, the Wave Acquisition Stereo System (hereinafter WASS) acquires image sequences of the sea surface.

The WASS is a couple of synchronized 5 Megapixel BM-500GE JAI cameras encapsulated in waterproof cases (Fig. 3.2) with the following specifications

- Sensor 2/3" progressive scan CCD (8 bit)



Figure 3.1: Platform of Katsiveli, Crimea, Ukraine. Location of anemometer, wave gauge array and Wave Acquisition Stereo System (WASS).

- Pixel Clock 60 MHz
- Active area 8.45 (h) x 7.07 (v)
- Cell size 3.45 (h) x 3.45 (v)
- Active pixels 2456 (h) x 2058 (v). (Cell size = $3.45\mu\text{m}$ x $3.45\mu\text{m}$)
- Read-out modes
- GigE Vision interface with 12, 10 or 8-bit output

Each camera was coupled to a 5-mm focal length low distortion lens and linked to the workstation with RJ45 Ethernet cable for data transfer and a power cable, also used for trigger, ensuring synchronization of pictures taken by each camera. Due to the hard disk writing speed limitation, the maximum frame rate is 15 frames per second. In addition to ensure trigger and picture storage, the software allows parameterization of the exposure time of each camera by the user before acquisition and an automatic adjustment of the gain is done by the system during the acquisition to compensate for the brightness variations. For all the acquisitions described further, the exposure time is set for the both cameras to $6000\mu\text{s}$. Such a large value is set to keep a small analogical gain, but it implies some blurring on the image borders.

The acquisitions were done for wind direction established to West-South-West, with speed up to 10m/s. The figure 3.3 and the table 3.1 resume the wind and wave conditions during the 4 video acquisitions selected for this study. The wind speeds and directions are averaged over the duration of the record. The significant wave heights and the wind sea peak frequencies are get from wave gauge records.

3.3 Theoretical background

The video cameras capture the light reflected from the objects on the observed scene using a Charge-Coupled Device (CCD). During the exposure time, each cell of the CCD measures the received light quantity. Then, this quantity is discretized to give the value of the corresponding pixel. The number of possible discretized values is the image depth. To maintain the values between the range of the possible values, an analogical gain is generally applied on the measured raw light quantities before discretization. Repeating the process at high frequency, the result is a N frame-per-second (fps) sequence of pictures capturing the evolution of the scene, with a resolution (i.e. a number of pixels) given by the number of CCD cells. The aim of the camera calibration is to find the parameters which link a 3D object to its projection on the bit-mapped image. Usually used in computer vision, the pinhole camera model, described in paragraph 3.3.1, provides this link. Nevertheless, this simple model does not take in account that the coordinates are generally expressed in a reference system independent of camera position and orientation nor the discretization of the image plane into pixels and the distortion induced by the optical lenses. The complete equations that relates a 3D point to its projection are discussed in the paragraphs 3.3.2. Finally, the last paragraph 3.3.2 describes the epipolar geometry which links the two pinhole cameras.



Figure 3.2: Top: Waterproof camera case. Bottom, left: 5-mm focal length low distortion lens. Bottom, right: 5 Megapixel BM-500GE JAI cameras.

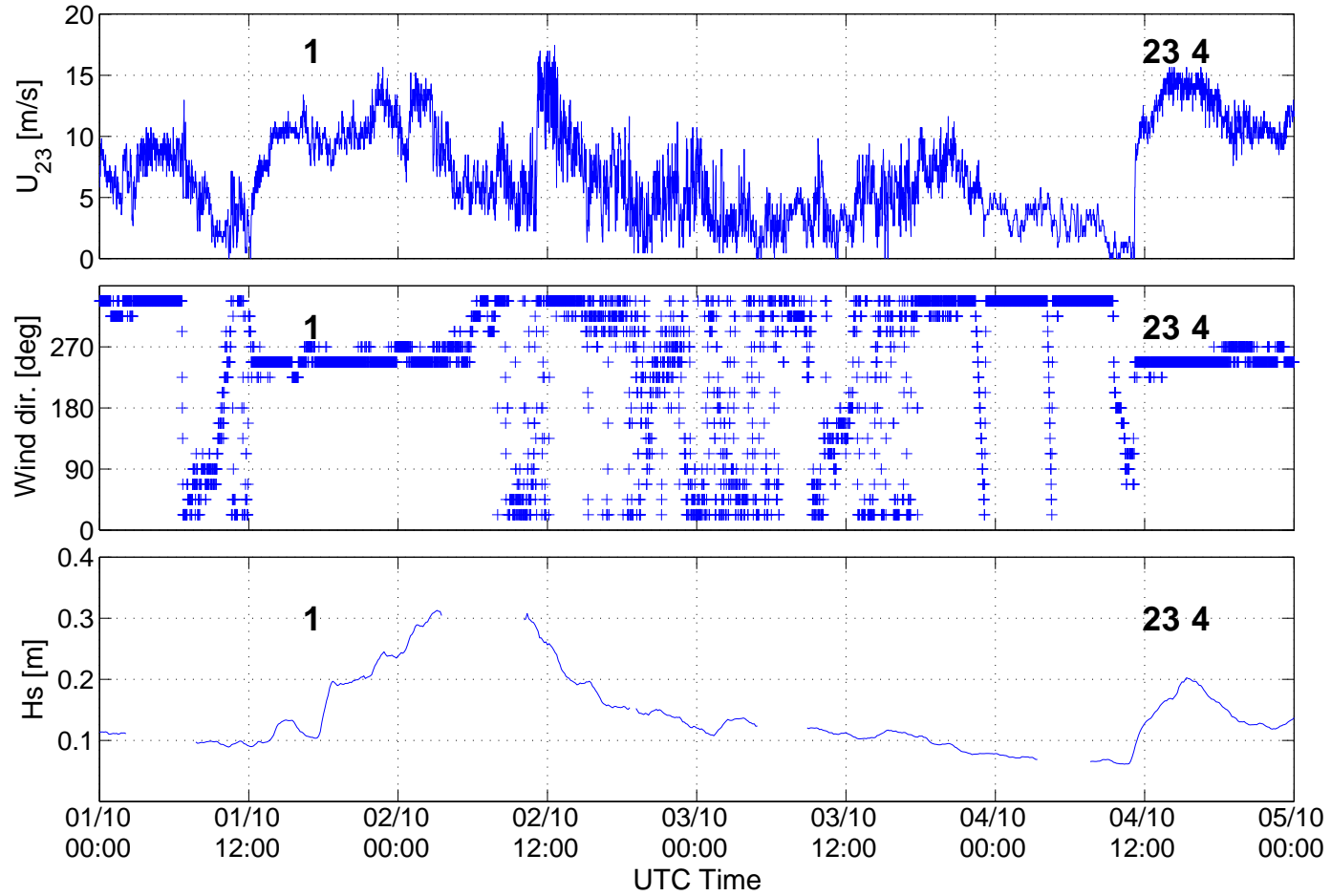


Figure 3.3: Evolution of wind and wave conditions during the experiment. Acquisitions were done for wind direction established to West-South-West, with speed up to 10m/s.

Acq. #	Acq. freq.	# of images	Acq. duration	Mean wind speed	Mean wind direction	H_{sig}	Wind sea peak freq.	Wave Age C_p/U_{23}
1	15Hz	5689	$\approx 7\text{min}$	11.5ms^{-1}	W-S-W	0.30m	0.33Hz	0.41
2	12Hz	14376	$\approx 20\text{min}$	10.9ms^{-1}	W-S-W	0.36m	0.38Hz	0.38
3	12Hz	21575	$\approx 30\text{min}$	13.2ms^{-1}	W-S-W	0.45m	0.33Hz	0.35
4	12Hz	21576	$\approx 30\text{min}$	13.9ms^{-1}	W-S-W	0.55m	0.27Hz	0.42

Table 3.1: Conditions during video acquisitions. Wind speeds and directions are averaged over the duration of the record. Significant wave heights and wind sea frequencies are obtained from wave gauges records.

3.3.1 Pinhole camera model

The pinhole camera model is the simplest model which relates a point of the scene to its projection on the image plane. It assumes a rectilinear projection in which the straight lines in a scene are projected into straight lines in the image. In other words, it assumes that all rays from the 3D scene straightly crosses the image plane and focus on the projection center, at a distance f , so-called the focal length, such as shown on figure 3.4. A metric image coordinate system is defined such that origin o is the intersection between the optical axis and the image plane and the vectors \vec{u}' and \vec{v}' are orthogonal and parallel to the image plane. The camera coordinate system is defined such that the origin O_c is the projection center, the axis \vec{Z}_c is collinear to the optical axis and the vectors \vec{X}_c and \vec{Y}_c are respectively collinear to \vec{u}' and \vec{v}' . Therefore, a 3D point $P(X_c, Y_c, Z_c)$ of the scene is related to its projection point $p(u', v')$ on image plane with

$$\begin{bmatrix} u' \\ v' \end{bmatrix} = \frac{f}{Z_c} \begin{bmatrix} X_c \\ Y_c \end{bmatrix}. \quad (3.1)$$

3.3.2 From 3D coordinates to 2D pixel coordinates

This paragraph, illustrated by the figure 3.5, describes links between a 3D point P of the scene expressed in 3D world reference and its projection in the undistorted bit-mapped image. Generally, the coordinates of the 3D point P in the scene are not known in the camera reference system $(O_c, \vec{X}_c, \vec{Y}_c, \vec{Z}_c)$, but in an external system, usually called world system, $(O_w, \vec{X}_w, \vec{Y}_w, \vec{Z}_w)$. Assuming that both the camera axes and the world axes are orthogonal and isotropic, the unique Euclidean 3D transformation between the two coordinate systems can be defined by a 3×3 rotation matrix R and a 3-dimensional translation vector T , such that

$$\begin{bmatrix} X_c \\ Y_c \\ Z_c \end{bmatrix} = R * \begin{bmatrix} X_w \\ Y_w \\ Z_w \end{bmatrix} + T, \quad (3.2)$$

where R transforms axes $(\vec{X}_w, \vec{Y}_w, \vec{Z}_w)$ into axes $(\vec{X}_c, \vec{Y}_c, \vec{Z}_c)$ and T moves origin from O_w to O_c . We note that the rotation matrix R is related to the 3 angles parameters, the roll θ (counterclockwise rotation of the camera around X -axis), the pitch ϕ (Y -axis), and the yaw ψ (Z -axis). These three angles with the three components of T are called the extrinsic (or external) camera parameters.

We now define two different coordinate systems on the image plane. The first one is the metric system defined by the camera pinhole model which the origin is the intersection of the optical axis with the image plane and the axis (\vec{u}', \vec{v}') are collinear to the camera reference system (see Fig. 3.4). The second system, called pixel coordinates system, is defined such that the origin is the center of the upper-left pixel and the axis (\vec{u}, \vec{v}) respectively follow rows and columns of the pixel matrix, such as shown on figure 3.5. We note here that due to the manufacturing defects on camera sensor, these axis are generally not perfectly orthogonal.

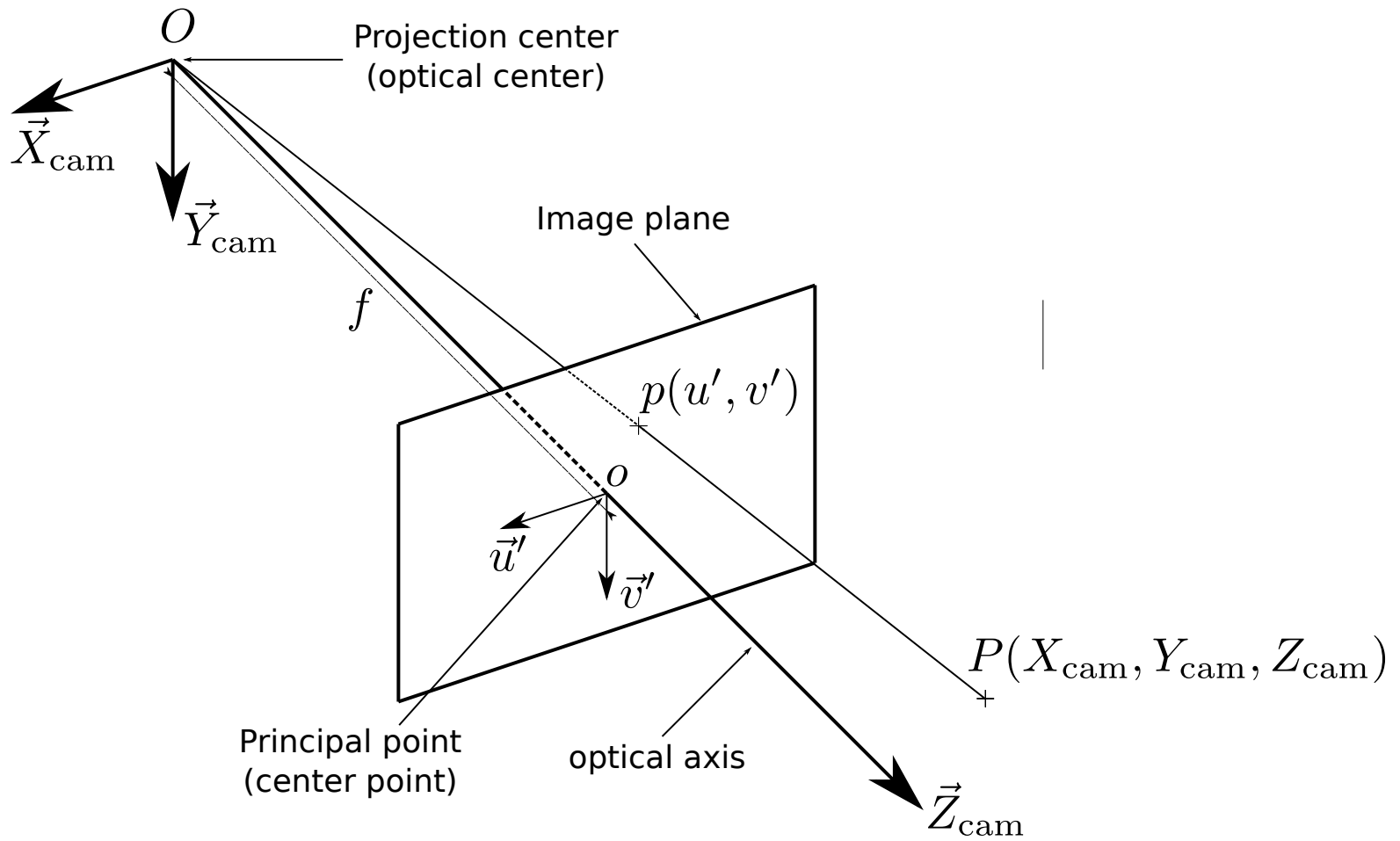


Figure 3.4: Schema of the pinhole camera model.

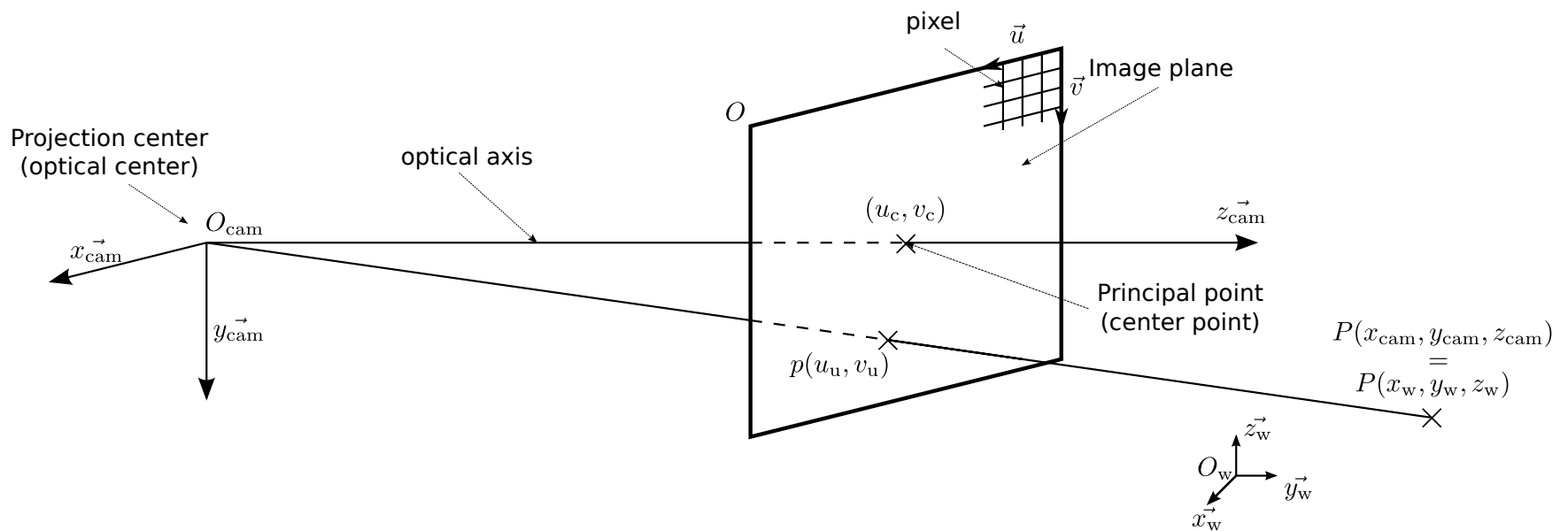


Figure 3.5: Schema of the links between 3D points of the scene and their projection on undistorted bit-mapped image.

Many transformations can be found in the literature, implying different parameters adapted to type and quality of the sensor. Consistently with calibration described further, and accordingly with the used CCD sensor, the set of intrinsic (or internal) parameters used to link point coordinates expressed in camera reference system to pixel coordinates of its projections on bit-mapped image consists of :

- the focal length f as defined in pinhole camera model,
- the distortion coefficient, K_n and P_n , which correct for the optical lens distortion,
- the pixel coordinates of the principal (or center) point, (u_c, v_c)
- the coefficients, D_u and D_v , which change metric into values to pixel (Stated otherwise $1/D_u$ and $1/D_v$ are the center-to-center distance between two consecutive CCD cells in respectively u and v axis.),
- an uncertainty scale factor on u -axis, s_u (Typically, such an uncertainty scale factor also exist on v -axis. However, one of these uncertainty factors can be absorbed by focal length. Calibration used for this work, as usually done in the literature, keeps s_u and adapt focal length to obtain $s_v = 1$),
- and the skew coefficient, γ , which corrects for error on the orthogonality of CCD cells.

All these internal parameters are linked to the use of a given optical lens with a given CCD in a given configuration, so they generally differ from left to right camera. The calibration of these parameters is discussed in section 3.4.

We note that the projection of the 3D scene on an image plane reduces the dimensions from three to two. Following the pinhole camera model, the coordinates (u', v') of the projection on the image plane of a given 3D scene point expressed in camera reference system by (X_c, Y_c, Z_c) is fully determined by the equation 3.1. On the contrary, given the image projection coordinates, the position of the scene point is only defined with an ignoring factor. Indeed, the ensemble of the possible coordinates of the scene point is a line, called line of sight or ray. Following the 3D camera geometry given by the pinhole camera model, the orientation vector r of the ray is defined such that

$$r \sim \begin{bmatrix} u' \\ v' \\ f \end{bmatrix} \quad (3.3)$$

Usually, the orientation vector r is normalized such that its third component is the unity. Therefore

$$r = \left[\frac{u'}{f}, \frac{v'}{f}, 1 \right]^T = [\tilde{u}', \tilde{v}', 1]^T, \quad (3.4)$$

where (\tilde{u}', \tilde{v}') are normalized metric image coordinates.

The pinhole camera model considers the rectilinear projection. Nevertheless, the use of real optical lens entails distortion, which corresponds to a deviation from the rectilinear projection. Indeed, seen through optical lens the straight lines can appear curved.

The resulting image deformation is nonlinear. Assuming a rectilinear projection, the pin-hole camera model described above cannot take into account such an optical aberration. Therefore, a correction for lens distortion must be apply independently (§3.4.4).

The lens distortion is split into radial and tangential distortions. The radial distortion, also called centering distortion, corresponds to an inhomogeneous image magnification. When the image magnification decreases with the distance from the optical axis, we talk about barrel distortion. Contrary, an increasing of the magnification with the distance from the optical axis is called pincushion distortion. As example, the barrel distortion is used in fish-eye lenses as a way to map an infinitely wide object plane (hemispherical view) into a finite image area. In contrast, the pincushion distortion is used for the visual optical instruments to limit the globe effect induced by a long focal length. A mixture of the both types could also be used and is referred to as mustache distortion or complex distortion. The radial distortion is usually predominant but is often coupled with a tangential distortion, also known as decentering distortion. This latter is caused by the physical elements in the lens not perfectly aligned. Its effect is weak for high-quality lenses. Brown (1966) proposed a distortion model based on work of Conrady (1919), which corrects for the both radial and tangential distortion. To be consistent with the calibration procedure described in the next section, Brown's model is here adapted to normalized images coordinates $(\tilde{u}', \tilde{v}') = (\tilde{u}', \tilde{v}')/f$. Then, the displacement due to the radial and tangential distortion are respectively given by

$$\begin{cases} \delta^{(r)}(\tilde{u}') &= \tilde{u}' (K_1 r^2 + K_2 r^4 + \dots) \\ \delta^{(r)}(\tilde{v}') &= \tilde{v}' (K_1 r^2 + K_2 r^4 + \dots) \end{cases} \quad (3.5)$$

and

$$\begin{cases} \delta^{(t)}(\tilde{u}') &= 2P_1 \tilde{u}' \tilde{v}' + P_2 (r^2 + 2\tilde{u}'^2) \\ \delta^{(t)}(\tilde{v}') &= P_1 (r^2 + 2\tilde{v}'^2) + 2P_2 \tilde{u}' \tilde{v}' \end{cases} \quad (3.6)$$

where $r = \sqrt{\tilde{u}'^2 + \tilde{v}'^2}$ and K_n and P_n are respectively the coefficients for the radial and tangential distortion. Therefore, the projection on image plane taking into account for the lens distortion is given using normalized metric image coordinates by

$$\begin{cases} \tilde{u}'_d &= \tilde{u}' + \delta^{(r)}(\tilde{u}') + \delta^{(t)}(\tilde{u}') \\ \tilde{v}'_d &= \tilde{v}' + \delta^{(r)}(\tilde{v}') + \delta^{(t)}(\tilde{v}') \end{cases} \quad (3.7)$$

We note that by adding distortion into the projection model, it becomes strongly non-linear. As a result, the reverse mapping which consists in recover the ray from the image coordinates does not have a direct solution. However, few solutions for inverse mapping exist in the literature (Melen, 1994; Wei and Ma, 1993; Heikkila and Silven, 1997).

Finally, the image coordinate (u'_d, v'_d) must be expressed in the pixel reference system. With the notations described above, the pixel coordinates (u, v) are linked to the metric image coordinates (u', v') with

$$\begin{aligned} u_d &= f D_u s_u (\tilde{u}'_d + \gamma \tilde{v}'_d) + u_c \\ &= f_u (\tilde{u}'_d + \gamma \tilde{v}'_d) + u_c \end{aligned} \quad (3.8)$$

$$\begin{aligned} v_d &= f D_v \tilde{v}'_d + v_c \\ &= f_v \tilde{v}'_d + v_c, \end{aligned} \quad (3.9)$$

where $f_u = D_u s_u f$ and $f_v = D_v f$ are the unique focal metric distance f expressed in term of pixels in each direction. When the pixels in the CCD sensor are not perfectly square, the aspect ratio, $D_v/(s_u D_u) = f_v/f_u$, differs from 1. Nevertheless, the recent high quality CCD manufacturing leads to an aspect ratio close to 1 (f_u and f_v are usually very similar). Moreover, the high quality manufacturing also leads to skew factor close to 0.

The computer vision science usually used the homogeneous coordinates, which consists in the expression of the coordinates with an additional dimension, such that the homogeneous 3D points coordinates in world reference system (resp. in camera reference system) are given by vector $[X_w, Y_w, Z_w, 1]^T$ (resp. $[X_c, Y_c, Z_c, 1]^T$). Then, neglecting the distortion, the projection of a scene points into the bit-mapped image can be represented with a 3×4 matrix C , called the camera matrix such that

$$Z_c \begin{bmatrix} u \\ v \\ 1 \end{bmatrix} = C * \begin{bmatrix} X_w \\ Y_w \\ Z_w \\ 1 \end{bmatrix} = A \begin{bmatrix} R & T \end{bmatrix} \begin{bmatrix} X_w \\ Y_w \\ Z_w \\ 1 \end{bmatrix} \quad (3.10)$$

where R and T are the external parameters (see Eq. 3.2) and A is the matrix containing the intrinsic parameters such that

$$Z_c \begin{bmatrix} u \\ v \\ 1 \end{bmatrix} = A \begin{bmatrix} X_c \\ Y_c \\ Z_c \end{bmatrix}, \quad (3.11)$$

with

$$A = \begin{bmatrix} D_u s_u f & D_u s_u f \gamma & u_c \\ 0 & D_v f & v_c \\ 0 & 0 & 1 \end{bmatrix} = \begin{bmatrix} f_u & f_u \gamma & u_c \\ 0 & f_v & v_c \\ 0 & 0 & 1 \end{bmatrix}, \quad (3.12)$$

As previously discussed, the coordinates of a points, given coordinates of its projection, are given by

$$\begin{bmatrix} X_c \\ Y_c \\ Z_c \end{bmatrix} = \alpha C^{-1} \begin{bmatrix} u \\ v \\ 1 \end{bmatrix}. \quad (3.13)$$

We note that the ray where are all the possible positions of the point is then given by varying α , and coordinates of the 3D point are given by $\alpha = Z_c$, which is generally unknown. The equation 3.13 is the linear solution for the inverse mapping usually used in computer vision. Nevertheless, as noted, by including distortion, the projection becomes non-linear ($C = C(u, v)$). As a result, the camera matrix C cannot be inverted and the equation 3.13 cannot be applied. A way around the problem is to use the equation on a rectified image corrected for the lens distortion (see §3.4.4).

3.3.3 Epipolar geometry and stereo triangulation

Given two (or more) cameras with distinct projection centers, the epipolar geometry describes geometric constraints existing between the cameras. This geometry is based on the pinhole camera model, so the distortion must be neglected or previously corrected

(see §3.4.4). The example for two cameras is shown on the figure 3.6, where the centers of projection of the cameras are the points C_1 and C_2 . We suppose the external parameters (R_1, T_1) and (R_2, T_2) . We note that the world reference system can be defined as equal to the reference system of the first camera. Therefore, $R_1 = I_3$ and $T_1 = [0, 0, 0]^T$, and (R_2, T_2) represent the relative positions of the cameras. We define the epipolar points (e_1, e_2) as the intersection of the line (C_1C_2) with the image planes. These epipolar points generally fall out of the bit-mapped image. For each point P of the scene, the corresponding epipolar plane is defined by the three points (C_1, C_2, P) . This plane intersects the left and right image planes in lines, called epipolar lines.

Projecting on the first image plane onto p_1 , the corresponding scene point P must be on the ray (C_1, p_1) . Therefore, its projection on the second image must be on the epipolar line, which corresponds to the projection of the ray. This property is used in the point matching step of the reconstruction processing, described further, to reduce search area of the corresponding points (see §3.5.1). Inversely, given p_1 and p_2 the projections of a same scene points P into the image 1 and 2 respectively, the 3D location of the point P is fully determined by the intersection of the rays (C_1, p_1) and (C_2, p_2) . The determination of the 3D coordinates of a point from its projections onto two images is called stereo triangulation (see §3.5.2).

3.4 Camera calibration and image rectification

The aim of the camera calibration is to compute the intrinsic and extrinsic camera parameters disused in paragraph 3.3. The performances of the WASS are inevitably related to the camera calibration accuracy which is described in this paragraph. After a short history on the evolution of calibration methods, a detailed description of the calibration procedures, for the intrinsic and extrinsic calibration, used in this work for WASS calibration are given.

3.4.1 Short historical of camera calibrations

Throughout the years, many authors proposed many methods following the growing need of accuracy and image sensor evolution. We must note the strong influence of the works of Tsai (1987) on the recent camera calibration methods. The previous methods could be simply classified into two categories. The first category involves full scale nonlinear optimization, allowing easy adaptation of any arbitrarily complex model for imaging, including obviously the lens distortion. Nevertheless, this adaptability is made at the cost of a large set of non-physical implicit parameters. Moreover, these implicit methods require a good initial guess to start computing. In contrast, the second category regroups the computationally efficient explicit methods that solve only linear equations related to physical parameters. These methods have generally a number of unknowns much larger than the degrees of freedom. Moreover, no nonlinear search entails that the effect of the lens distortion cannot be considered. These linear solutions do not provide as good results as nonlinear minimization.

Mixing these two approaches, Tsai (1987) proposed an autonomous, accurate, reason-

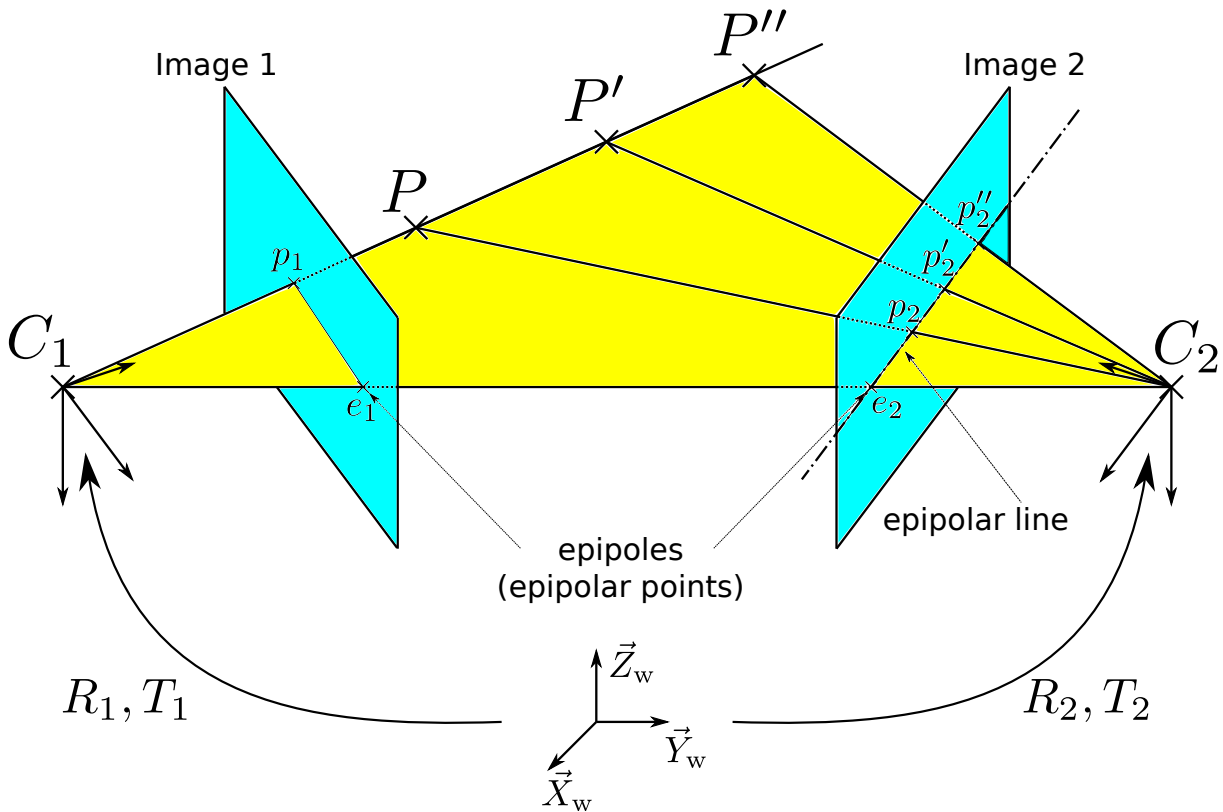


Figure 3.6: Illustration of epipolar geometry for a pair of cameras. The points C_1 and C_2 are the center of projection. The image points e_1 and e_2 are epipolar points. The epipolar plane corresponding to scene point P is represented in yellow. The intersection between the epipolar plane and the image planes defined the epipolar line.

ably efficient and versatile two-step method applicable to any type of camera, whereas most of previous methods require professional cameras and processing equipment. Approximating the intrinsic parameters to the manufacturing given values, the first stage consists in a linear approximation of the parameters. In the second stage, the optimized solution is computed with a standard optimization scheme, using as guess null distortion ($K_1 = 0$) and the parameter approximations previously computed in the first step. Even if a reduction of the lens effect to this first radial component limits the method accuracy, this kind of two-step method (the linear approximation is the guess for the nonlinear optimization) still today the groundwork of most of the recent calibration procedures. Heikkila and Silven (1997) further improved calibration by including the asymmetric projection correction. We note that the historical development of camera calibration techniques with an exhaustive literature survey can be found in Clarke and Fryer (1998).

Numerous calibration tools are available today (Heikkila and Silven, 1997; Vezhnevets, 2005; Strobl et al., 2006; Scaramuzza et al., 2006; Stoyanov, 2010, and many others). For this work, the WASS calibration was done using the *Camera Calibration Toolbox for Matlab*[®] written by Jean-Yves Bouguet which proposes interesting additional tools, such as corner extraction and visual check routines. As the overall accuracy of the surface reconstruction is interconnected with the accuracy of the camera calibration, the details on both operator procedure and calibration code as written by Jean-Yves Bouguet are given.

3.4.2 Camera intrinsic calibration

The intrinsic parameters, which link a 3D point in the camera reference system to its projection in the bit-mapped image reference system, must be firstly defined. Driven by the association of a given Charge-Coupled Device (CCD) with a given lens, the intrinsic calibration is done independently for each camera with an identical processing. A large set of calibration images containing a square-chessboard at various distances are taken (see Fig. 3.7). Precisely, more than 1000 images are selected for each camera. Two chessboards with 30mm and 80mm square size were used. We note that chessboard corners correspond to a coplanar set of points.

Since the coordinates of the chessboards are not initially known in the camera reference system, the extrinsic parameters must be also estimated. The intrinsic parameters do not depend on the extrinsic ones. This allows us to define an independent world coordinate system for each image. Conveniently, the world systems are fixed such that the X_w -axis and Y_w -axis are collinear to the square sides of the chessboard and the origin is the center of the up-left corner (see Fig. 3.7, up-left panel). Therefore, the corner world coordinates are well known in its corresponding reference system and depend only on the chessboard square size, dX . In a second step, the coordinates of the corner projections must be extracted from images. The human influence on the processing is limited to a rough estimation of the four extreme corners of the chessboard. An automatic mechanism then counts squares in each direction and deduces approximate locations of the projected corners. Finally, the sub-pixel corner coordinates are computed using gradients. A visual check is done by the operator. At the end, for each image, a set of coplanar 3D points and their projection on the images are stored. Following the previous notations, a corner point

is defined by its coordinates (X_w, Y_w, Z_w) in the world reference system and its projection on bit-mapped image coordinate system is defined by (u, v) .

Heikkila and Silven (1997) proposed a first linear estimation of the 12 elements of the camera matrix C (Eq. 3.10) using Direct Linear Transformation (DLT) initially developed by Aziz and Karara (1971), from which can be then extract the focal length, the principal point coordinates and the coefficients for linear distortion. In the procedure used here, recently developed for high quality CCD and lens, the first estimation of the internal camera parameters considers the skew factor γ and the distortion coefficients K_n and P_n are null, and the center point (u_c, v_c) is the center of the pixel matrix. Moreover, using a planar target (the corners on the chessboard are coplanar), the procedure can be simplified compared to one proposed by Heikkila and Silven (1997) by using homography, which reduces number of unknowns to 9. Indeed, using the world reference such as defined previously, it follows that for all points i , $Z_{w,i} = 0$, therefore equation 3.10 becomes

$$Z_c \begin{bmatrix} u \\ v \\ 1 \end{bmatrix} = A \begin{bmatrix} R & T \end{bmatrix} \begin{bmatrix} X_w \\ Y_w \\ 0 \\ 1 \end{bmatrix} = A \begin{bmatrix} r_1 & r_2 & T \end{bmatrix} \begin{bmatrix} X_w \\ Y_w \\ 1 \end{bmatrix}, \quad (3.14)$$

where r_i is the i^{th} column of rotation matrix R . In other hand, chessboard and image planes (respectively Π' and Π on figure 3.8) can also be seen as projective planes. Therefore, there exists a projective transformation, also called homography, which links chessboard points to their corresponding image points. Let us define homogeneous coordinates of point i on plane Π' with $P_i = [X_{w,i}, Y_{w,i}, 1]^T$ and on plane Π with $p_i = [u_i, v_i, 1]^T$. Homography is defined using 3×3 matrix H such that

$$\begin{aligned} \forall i, \quad p_i &\sim A[r_1, r_2, T]P_i \\ &\sim HP_i \\ &\sim [h_1, h_2, h_3]P_i \end{aligned} \quad (3.15)$$

where \sim means equality up to a non-zero scale factor, and h_i is the i^{th} column of homography matrix H . This implies that the vector p_i and HP_i are collinear, so $p_i \times HP_i = 0$, with \times is the vector cross product. Applying DLT to the N chessboard points of a same image, H can be defined as the solution of the following system

$$Lh = 0 \quad (3.16)$$

with

$$L = \begin{bmatrix} P_1(1) & P_1(2) & 1 & 0 & 0 & 0 & P_1(1)p_1(1) & P_1(2)p_1(1) & p_1(1) \\ 0 & 0 & 0 & P_1(1) & P_1(2) & 1 & P_1(1)p_1(2) & P_1(2)p_1(2) & p_1(2) \\ \vdots & \vdots \\ P_i(1) & P_i(2) & 1 & 0 & 0 & 0 & P_i(1)p_i(1) & P_i(2)p_i(1) & p_i(1) \\ 0 & 0 & 0 & P_i(1) & P_i(2) & 1 & P_i(1)p_i(2) & P_i(2)p_i(2) & p_i(2) \\ \vdots & \vdots \\ P_N(1) & P_N(2) & 1 & 0 & 0 & 0 & P_N(1)p_N(1) & P_N(2)p_N(1) & p_N(1) \\ 0 & 0 & 0 & P_N(1) & P_N(2) & 1 & P_N(1)p_N(2) & P_N(2)p_N(2) & p_N(2) \end{bmatrix}$$

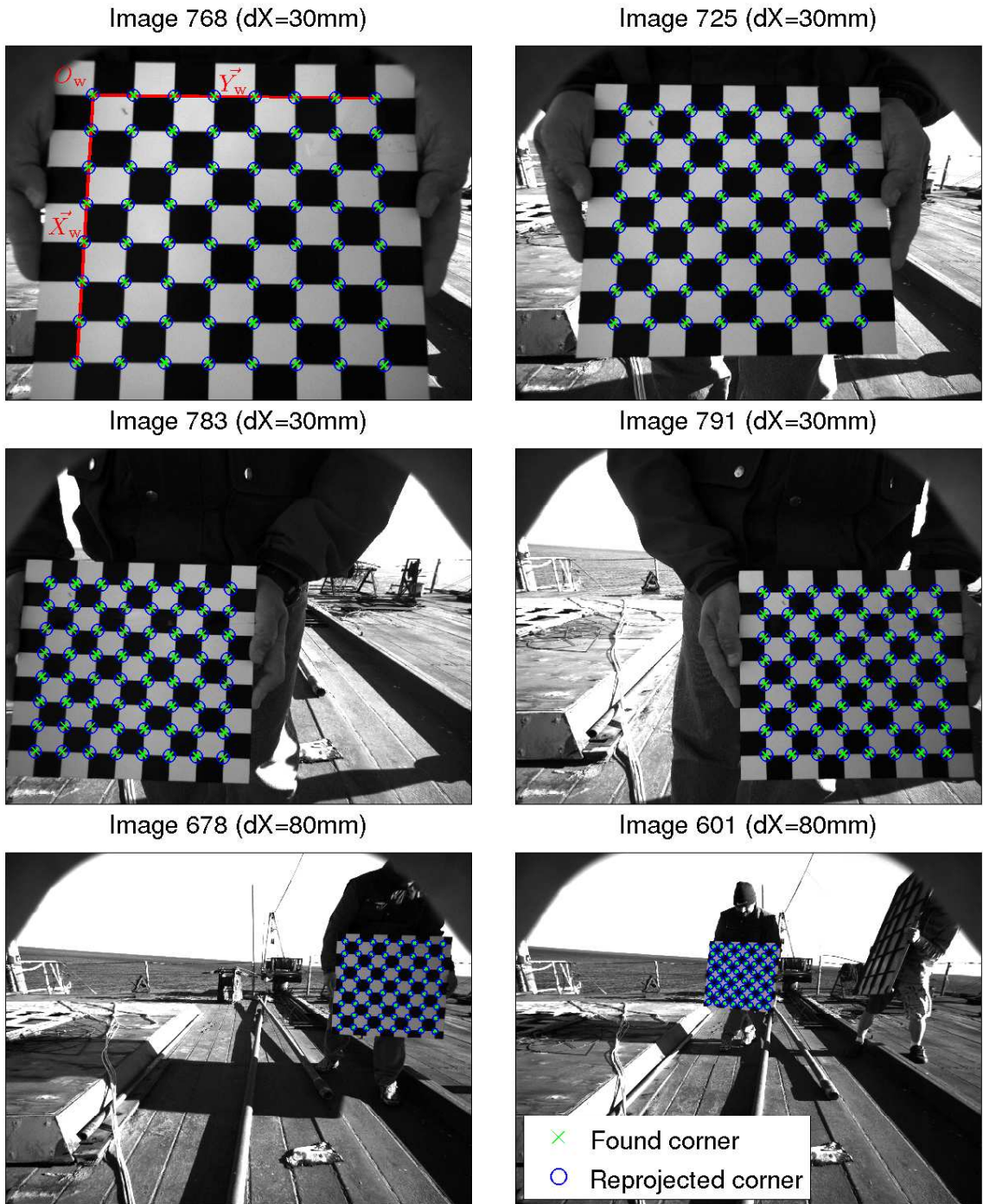


Figure 3.7: Example of images using for left intrinsic camera calibration. Green crosses represent corner detected on the images whereas blue circle are reprojections of 3D points using with calibrated intrinsic and extrinsic parameters. On upper-left panel, red lines represent definition of the world coordinate system. Chessboard square size is 30mm on the four upper images, and 80mm on the two lower ones.

and

$$h = [H_{1,1}, H_{1,2}, H_{1,3}, H_{2,1}, H_{2,2}, H_{2,3}, H_{3,1}, H_{3,2}, H_{3,3}]^T.$$

The solution is defined at the least square sense using Singular Value Decomposition (Golub and Reinsch, 1970, among others). Then the focal length f is extracted from the homography matrix following Zhang (1999), with some simplifications due to the previous estimations. As R (Eq. 3.10) is a rotation matrix, the vectors r_i (Eq. 3.15) are orthonormal. Therefore, the equation (3.15) gives two constraints (verifying the two basic constraints given one homography), which are

$$h_1^T (A^{-1})^T A^{-1} h_2 = 0 \quad (3.17)$$

$$h_1^T (A^{-1})^T A^{-1} h_1 = h_2^T (A^{-1})^T A^{-1} h_2. \quad (3.18)$$

By using the parameter estimations given above and assuming the aspect ratio is 1, the matrix A (Eq. 3.12) becomes

$$A = \begin{bmatrix} f_{u,v} & 0 & u_c \\ 0 & f_{u,v} & v_c \\ 0 & 0 & 1 \end{bmatrix}. \quad (3.19)$$

Finally, we define the matrix M , which translates the origin of the pixel coordinate system to the center point (u_c, v_c) such that

$$M = \begin{bmatrix} 1 & 0 & -u_c \\ 0 & 1 & -v_c \\ 0 & 0 & 1 \end{bmatrix}. \quad (3.20)$$

Therefore, the equation 3.15 becomes

$$\tilde{H} = [\tilde{h}_1, \tilde{h}_2, \tilde{h}_3] \sim \tilde{A}[r_1, r_2, T], \quad (3.21)$$

with $\tilde{H} = MH$ and

$$\tilde{A} = MA = f_{u,v} \begin{bmatrix} 1 & 0 & 0 \\ 0 & 1 & 0 \\ 0 & 0 & 1/f_{u,v} \end{bmatrix}. \quad (3.22)$$

Therefore, the constraint (3.17) gives

$$f_{u,v} = \sqrt{\frac{h_{1,1}\tilde{h}_{2,1} + h_{1,2}\tilde{h}_{2,2}}{h_{1,3}\tilde{h}_{2,3}}}, \quad (3.23)$$

with $[h_{i,1}, h_{i,2}, h_{i,3}]^T = \tilde{h}_i$, the i^{th} column of the homography matrix \tilde{H} . We note that h_1 and h_2 represent the vanishing points of the lines parallel to square sides of the chessboard. Indeed, following the definition of the world reference system, these lines have direction vectors respectively given by $[t, 0, 1]^T$ and $[0, t, 1]^T$. Therefore, the equations of their projection into the image plane are $h_1 t + h_3$ and $h_2 t + h_3$, so their director vectors are h_1 and h_2 . As shown in Caprile and Torre (1990), the vanishing points of parallel lines are given by their director vector. So, the equation 3.23 corresponds to the estimation

of the focal length from the vanishing points of lines vertically and horizontally parallel to square side of the chessboard. A similar estimation can be done using diagonal lines ($[t/2, t/2, 1]^T$ and $[t/2, -t/2, 1]^T$), so

$$f_{u,v} = \sqrt{\frac{h'_{1,1}h'_{2,1} + h'_{1,2}h'_{2,2}}{h'_{1,3}h'_{2,3}}}, \quad (3.24)$$

with $h'_1 = (h_1 + h_2)/2$ and $h'_2 = (h_1 - h_2)/2$. In practice, $f_{u,v}$ is computed over the whole set of the M calibration images as the least square solution of the following system

$$\left\{ \begin{array}{l} 0 = h_{1,1}h_{2,1} + h_{1,2}h_{2,2} + Xh_{1,3}h_{2,3} \\ 0 = h'_{1,1}h'_{2,1} + h'_{1,2}h'_{2,2} + Xh'_{1,3}h'_{2,3} \\ \vdots \\ 0 = h_{1,1}h_{2,1} + h_{1,2}h_{2,2} + Xh_{1,3}h_{2,3} \\ 0 = h'_{1,1}h'_{2,1} + h'_{1,2}h'_{2,2} + Xh'_{1,3}h'_{2,3} \\ \vdots \\ 0 = h_{1,1}h_{2,1} + h_{1,2}h_{2,2} + Xh_{1,3}h_{2,3} \\ 0 = h'_{1,1}h'_{2,1} + h'_{1,2}h'_{2,2} + Xh'_{1,3}h'_{2,3} \end{array} \right\} \begin{array}{l} \text{Image 1} \\ \\ \\ \text{Image } I \\ \\ \\ \text{Image } M \end{array} \quad (3.25)$$

where $h_{i,j}$ and $h'_{i,j}$ are extracted from M -set of homography matrices $\tilde{H} = CH$ computed over the M -set of calibration images and $f_{u,v} = \sqrt{X}$.

We note that numerous linear estimations of the intrinsic parameters given in the literature leads to a better estimations of a larger number of intrinsic parameters. Indeed, the homography matrix contained 8 coefficients (9 – 1 for scale factor) that can be used to evaluate elements of $A[r_1, r_2, T]$ (Eq. 3.14). As $[r_1, r_2, T]$ is defined by 6 parameters (3 for rotation + 3 for translation), two parameters can be estimated in A , whereas our processing extracts only the focal length. Moreover, other methods proposed a direct estimation of $A[R, T]$ (Tsai, 1987; Heikkila and Silven, 1997, among others) from which more intrinsic parameters can be extracted. Nevertheless, the present processing considers a computationally fast and simple way to provide enough accurate guess for the following nonlinear estimation - thanks to the use of recent well manufactured camera and lenses. Indeed, even when using more complicated direct methods, nonlinear estimation is still necessary to fully take into account the lens distortion¹. Another disadvantage of linear methods is highlighted by Heikkila and Silven (1997). Considering non perfect data - the 3D coordinates (X_w, Y_w, Z_w) can be disturbed by non-perfectly planar chessboard and the image coordinates of the projected corners (u, v) can contain some noise - linear solution does not provide best estimation.

Estimating the data errors as a white Gaussian noise, the best estimation is found with an iterative non-linear process, starting from the previously estimated parameters, which minimize the residual between the projection model and the N -observations. As the model (Eq. 3.10) considers also the extrinsic parameters, their estimations are required

¹We note that some lens effect can nevertheless be estimated using linear methods (Shih et al., 1993, as example), but accuracy is less than that expected with non-linear methods.

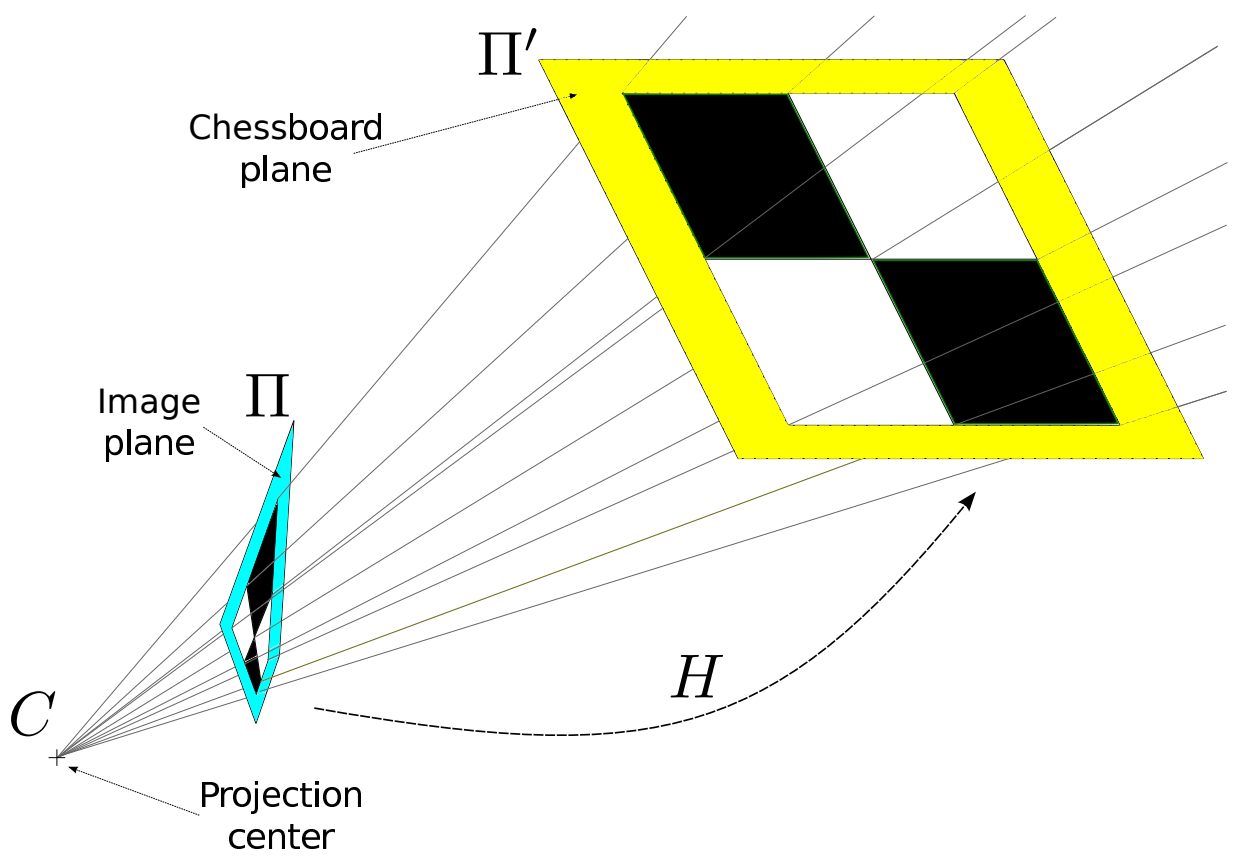


Figure 3.8: Chessboard and image planes seen as projective planes, so linked by a homography matrix H .

to start the non-linear error minimization. The extrinsic parameters differs between the calibration images (world system depends on chessboard position), and so are estimated independently for each image. As the intrinsic parameters are now estimated, the image coordinates can be normalized with

$$\begin{cases} \tilde{u}' &= (u - u_c)/f_{u,v} \\ \tilde{v}' &= (v - v_c)/f_{u,v}. \end{cases} \quad (3.26)$$

The origin of the world coordinate system is translated to the barycenter of points with

$$\begin{cases} \tilde{X}_w &= X_w - \overline{X_w} \\ \tilde{Y}_w &= Y_w - \overline{Y_w} \\ \tilde{Z}_w &= Z_w = 0. \end{cases} \quad (3.27)$$

Then the homography \tilde{H} between normalized coordinates is computed using same method as previously. Using the normalized pixel coordinates, the equation 3.15 becomes $\alpha\tilde{H} = [r_1, r_2, T]$, with α an ignoring factor. An approximation of this factor is given by $\alpha = 1/2(\|r_1\| + \|r_2\|)$ where $\|X\|$ means the norm of the column vector X . Therefore, the approximated extrinsic parameters R and T are get using

$$r_1 = \alpha\tilde{h}_1 \quad (3.28)$$

$$\tilde{r}_1 = r_1/\|r_1\| \quad (3.29)$$

$$r_2 = \tilde{h}_2 - (\tilde{r}_1 \cdot \tilde{h}_2)\tilde{r}_1 \text{ (ensures orthogonality)} \quad (3.30)$$

$$\tilde{r}_2 = r_2/\|r_2\| \quad (3.31)$$

$$\tilde{r}_3 = \tilde{r}_1 \times \tilde{r}_2 \text{ (\tilde{r}_3 finishes orthonormal basis).} \quad (3.32)$$

$$R = [\tilde{r}_1, \tilde{r}_2, \tilde{r}_3] \quad (3.33)$$

$$T = \tilde{h}_3 \quad (3.34)$$

where \cdot and \times are respectively vector dot and cross product. Theses estimations being very poor due to poor approximation of factor α , a refinement is done using minimization of the reprojection error. The iterative non-linear least square optimization processing is now described in detail using the external parameter refinements as example. A similar processing will be used further for the intrinsic parameter refinements. Remember that the rotation matrix is defined by the 3 angles: θ (roll), ϕ (pitch), ψ (yaw) and $T = [t_1, t_2, t_3]^T$. From the world coordinates $(X_{w,i}, Y_{w,i}, Z_{w,i})$ of each point i , the coordinates $(u_{p,i}, v_{p,i})$ of the corresponding projection are computed using equation 3.10. So, the residual (error) r can be estimated for each point i with $r_i = (u_i - u_{p,i}, v_i - v_{p,i})$. The solution in the least squares sense, is the set of n parameters $\beta_{j=1,\dots,n}$ (here there are n parameters: $\theta, \phi, \psi, t_1, t_2, t_3$) which minimize the sum S of the squares residuals,

$$S = \sum_{i=1}^N \|r_i\|^2. \quad (3.35)$$

The minimum value of S occurs when all its partial derivatives with respect to the 6 external parameters are zero: $\forall i \in [1, n]$,

$$\frac{\partial S}{\partial \beta_j} = 2 \sum_{i=1}^N r_i \frac{\partial r_i}{\partial \beta_j} = 0 \quad (3.36)$$

In a non-linear system, the derivatives $\partial r_i / \partial \beta_j$ are functions of both the independent variables and the model parameters, so these gradient equations do not have a closed solution. Nevertheless, an iterative optimization can be implemented as follows. At each iteration, the parameters β_j are refined with $\beta_j + \Delta\beta_j$, where $\Delta\beta_j$ is the approximation to a first-order Taylor series expansion about β_j . The convergence is given by all $\Delta\beta_{j=1,\dots,n}$ are 0. We note $\beta_{j=1,\dots,n}$ (respectively $r_i, u_{p,i}, v_{p,i}$) the values at convergence, whereas $\beta_{j=1,\dots,n}^{(k)}$ (respectively $r_i^{(k)}, u_{p,i}^{(k)}, v_{p,i}^{(k)}$) are the values at iteration (k). The projection function is noted P such that $P_{\text{Re}^3 \rightarrow \text{Re}^2} : (X_{w,i}, Y_{w,i}, Z_{w,i}) \rightarrow (u_{p,i}, v_{p,i})$. The first-order Taylor series expansion about β_j gives

$$P(X_{w,i}, Y_{w,i}, Z_{w,i}, \beta_{j=1,\dots,n}^{(k+1)}) \approx P(X_{w,i}, Y_{w,i}, Z_{w,i}, \beta_{j=1,\dots,n}^{(k)}) + \sum_{j'=1}^n J_{ij'}^{(k)} \Delta\beta_{j'} \quad (3.37)$$

where $\Delta\beta_{j'} = (\beta_{j'}^{(k+1)} - \beta_{j'}^{(k)})$, and

$$J_{ij'}^{(k)} = \frac{\partial P(X_{w,i}, Y_{w,i}, Z_{w,i}, \beta_{j=1,\dots,n}^{(k)})}{\partial \beta_{j'}}. \quad (3.38)$$

So, in terms of the linearized model,

$$\begin{aligned} r_i^{(k+1)} &= (u_i, v_i) - P(X_{w,i}, Y_{w,i}, Z_{w,i}, \beta_{j=1,\dots,n}^{(k+1)}) \\ &= (u_i, v_i) - P(X_{w,i}, Y_{w,i}, Z_{w,i}, \beta_{j=1,\dots,n}^{(k)}) + \sum_{j'=1}^n J_{ij'} \Delta\beta_{j'}^{(k)} \\ &= r_i^{(k)} - \sum_{j'=1}^n J_{ij'}^{(k)} \Delta\beta_{j'}^{(k)} \\ &= r_i^{(k)} + \sum_{j'=1}^n \frac{\partial r_i^{(k)}}{\partial \beta_{j'}^{(k)}} \Delta\beta_{j'}^{(k)}, \end{aligned} \quad (3.39)$$

with $\partial r_i^{(k)} / \partial \beta_{j'}^{(k)} = -J_{ij'}$. From gradient equation 3.36, convergence is found when

$$-2 \sum_{i=1}^N J_{ij} \left(r_i - \sum_{j'=1}^n J_{ij'} \Delta\beta_{j'} \right) = 0. \quad (3.40)$$

This gives the normal equations, $\forall j = 1, \dots, n$,

$$\sum_{i=1}^N \sum_{j'=1}^n J_{ij} J_{ij'} \Delta\beta_{j'} = \sum_{i=1}^N J_{ij} r_i. \quad (3.41)$$

The matrix notation is adopted. The set of parameters $\beta_{j=1,\dots,n}$ defines the vector β , and residuals $r_{i=1,\dots,N}$ defines the vector r . The Jacobian matrix J , storing all the derivatives J_{ij} for the whole set of $2N$ calibration point coordinates with respect to the n set of

parameters, is defined such that

$$J = \begin{bmatrix} \partial_\theta u_{p,1} & \partial_\phi u_{p,1} & \partial_\psi u_{p,1} & \partial_{t_1} u_{p,1} & \partial_{t_2} u_{p,1} & \partial_{t_3} u_{p,1} \\ \partial_\theta v_{p,1} & \partial_\phi v_{p,1} & \partial_\psi v_{p,1} & \partial_{t_1} v_{p,1} & \partial_{t_2} v_{p,1} & \partial_{t_3} v_{p,1} \\ \vdots & \vdots & \vdots & \vdots & \vdots & \vdots \\ \partial_\theta u_{p,i} & \partial_\phi u_{p,i} & \partial_\psi u_{p,i} & \partial_{t_1} u_{p,i} & \partial_{t_2} u_{p,i} & \partial_{t_3} u_{p,i} \\ \partial_\theta v_{p,i} & \partial_\phi v_{p,i} & \partial_\psi v_{p,i} & \partial_{t_1} v_{p,i} & \partial_{t_2} v_{p,i} & \partial_{t_3} v_{p,i} \\ \vdots & \vdots & \vdots & \vdots & \vdots & \vdots \\ \partial_\theta u_{p,N} & \partial_\phi u_{p,N} & \partial_\psi u_{p,N} & \partial_{t_1} u_{p,N} & \partial_{t_2} u_{p,N} & \partial_{t_3} u_{p,N} \\ \partial_\theta v_{p,N} & \partial_\phi v_{p,N} & \partial_\psi v_{p,N} & \partial_{t_1} v_{p,N} & \partial_{t_2} v_{p,N} & \partial_{t_3} v_{p,N} \end{bmatrix}. \quad (3.42)$$

The normal equations are therefore written

$$(J^T J)\Delta\beta = J^T r. \quad (3.43)$$

In the procedure, the convergence is considered reached when $\|\Delta\beta\|$ becomes smaller than a fixed threshold, with the iterative procedure given with

$$\beta^{(k+1)} = \beta^{(k)} + \Delta\beta, \text{ with } \Delta\beta = (J^T J)^{-1} J^T r^{(k)}. \quad (3.44)$$

We note that an additional condition, related with the sensitivity of the solution of the linearized system to errors in the data, is required to validate convergence. Indeed, the condition number of the Jacobian matrix J (corresponding to the ratio of the largest singular value of J to the smallest) must be under a fixed threshold, else the corresponding calibration image is disable for the further intrinsic parameter optimization.

So, the external parameters R_i and T_i are now known for each calibration image and can be used as guess for the global intrinsic-extrinsic calibration optimization over the whole set of M calibration images. The new set of parameters (intrinsic + extrinsic) to optimize is

$$\beta = [f_u, f_v, u_c, v_c, \gamma, K_1, P_1, K_2, P_2, \theta_I, \phi_I, \psi_I, t_{1,I}, t_{2,I}, t_{3,I}]_{I=1,\dots,M}^T \quad (3.45)$$

where $(\theta_I, \phi_I, \psi_I, t_{1,I}, t_{2,I}, t_{3,I})$ are the external parameters of the I^{th} calibration image. The non-linear optimization procedure is similar as one described previously. Nevertheless, the new optimization considers $n = 9 + 6 * M$ parameters to optimize over all calibration images. For obvious memory reasons, the very large matrix J is not explicitly computed. The $n \times n$ matrix $(J^T J)$ and the n vector $J^T r$ are directly computed, using a loop over calibration images. We note that, the external parameters depend only on the point set of their corresponding image. As a result, the matrix $(J^T J)$ is sparse and so easily invertible. Contrary to the external parameter optimization described further, $\Delta\beta$ is now computed using a smoothing coefficient α , increasing with iteration such that,

$$\Delta\beta = \alpha_k (J^T J)^{-1} J^T r^{(k)}, \text{ with } \alpha_k = 1 - (0.9)^k. \quad (3.46)$$

This provides an optimization of both internal and external parameters. Nevertheless, the convergence condition only takes in account the focal length and center point accuracies such that convergence is considered reached when

$$\frac{\|[\Delta f_u, \Delta f_v, \Delta u_c, \Delta v_c]^T\|}{\|[f_u, f_v, u_c, v_c]^T\|} < 10^{-9}. \quad (3.47)$$

Finally, the intrinsic and extrinsic parameters are extracted from the optimized vector β and an estimation of the uncertainties is get from the matrix $(J^T J)^{-1}$, such that

$$U(\beta_j) = 3D_j E, \quad (3.48)$$

with $D = D_{j=1,\dots,n}$ the vector formed with the diagonal values of $(J^T J)^{-1}$ and E is the standard deviation between the observed corner projection (u, v) and the reprojection (u_p, v_p) for all points of all images. The deviation of the pixels from rectilinear projection due to distortion is shown on figure 3.9.

Some tools are included in the calibration toolbox helping the operator to manage the calibration. In particular, the difference between the found image corners and the reprojected points can help to quickly identify bad corner detection, and remove the image or the point from the calibration set. However, the errors on the images extremities can be large despite of good corner matching. In this case, it is difficult to define if the image (or the point) must be removed or not. In our calibration, we decided to use a very large number of calibration images (compared to the number usually used) so that the influence of such points on the calibration results is very limited. Therefore, all points, except for the visual bad corner matching are kept for the calibration procedure. The figure 3.10 shows these errors. We note that the skew coefficient γ was found to be equal to zero within its uncertainty (as computed by equation 3.48) for the left camera. Its computation was disabled (i.e. γ is removed from the vector β), and the calibration was run again. The representation of the chessboard positions used for the left camera intrinsic calibration computed from the optimized external parameters, are presented in figure 3.11, in the camera reference system. The calibration results for the intrinsic parameters are presented in table 3.2 for the two cameras.

3.4.3 Camera extrinsic calibration

The second step of the WASS calibration, usually called extrinsic calibration, consists in get the relative positions of the cameras. This calibration required a set of stereo image pairs, with the calibration pattern (chessboard) taken at same time by each camera in their rigid position. Therefore, the absolute calibration pattern position is the same for each camera and the different projections obtained on each image are only due to the different points of view. In practice, this stereo image set have been respectively merged with left and right image set used for the intrinsic calibration. In the following, the extrinsic calibration considers only the set of stereo image pairs. The calibrated positions of the chessboard in each camera reference system are thus already given by the intrinsic calibration. We note (R_L, T_L) and (R_R, T_R) the external parameters that respectively relates the chessboard (i.e. world) reference system to the left and right camera reference systems. Therefore, the equation 3.2 applied to each camera gives

$$\vec{X}_w = R_L^{-1} (\vec{X}_{c,L} - T_L) \quad (3.49)$$

$$\vec{X}_w = R_R^{-1} (\vec{X}_{c,R} - T_R) \quad (3.50)$$

where $\vec{X}_w = [X_w, Y_w, Z_w]^T$ $\vec{X}_{c,L} = [X_{c,L}, Y_{c,L}, Z_{c,L}]^T$ and $\vec{X}_{c,R} = [X_{c,R}, Y_{c,R}, Z_{c,R}]^T$ are respectively coordinates in world, left camera and right camera reference systems. It

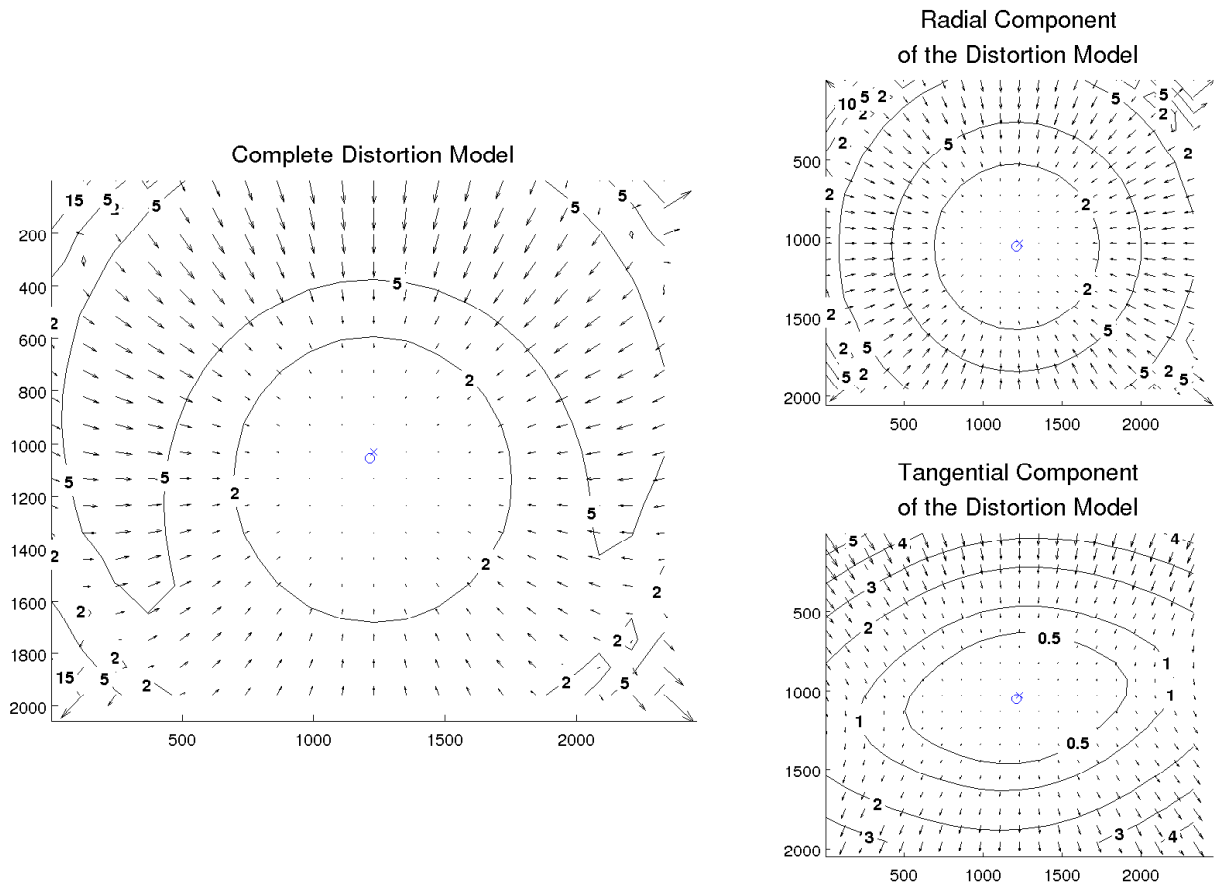


Figure 3.9: Deviation of pixels from rectilinear projection due to distortion for right camera.

	Left cam.	Right cam.
f_u	(1457.95300 \pm 0.37922) pix	(1456.05048 \pm 0.49248) pix
f_v	(1458.25791 \pm 0.38494) pix	(1456.16652 \pm 0.48999) pix
u_c	(1211.97340 \pm 0.24963) pix	(1240.00987 \pm 0.30611) pix
v_c	(1051.17932 \pm 0.28919) pix	(1043.86046 \pm 0.31326) pix
γ	0	(-0.00017 \pm 0.00004)
K_1	(-0.03499 \pm 0.00021)	(-0.02265 \pm 0.00024)
K_2	(0.04543 \pm 0.00026)	(0.03179 \pm 0.00025)
P_1	(0.00141 \pm 0.00005)	(0.00157 \pm 0.00006)
P_2	(0.00021 \pm 0.00005)	(-0.00143 \pm 0.00006)

Table 3.2: Calibrated internal parameters as returned by the calibration tool. Skew coefficient γ was found to be equal to zero within its uncertainty for left camera, so its computation was disable, and calibration was run again. We note that uncertainties on left camera are lower, despite of greater error on reprojection, than ones on right camera.

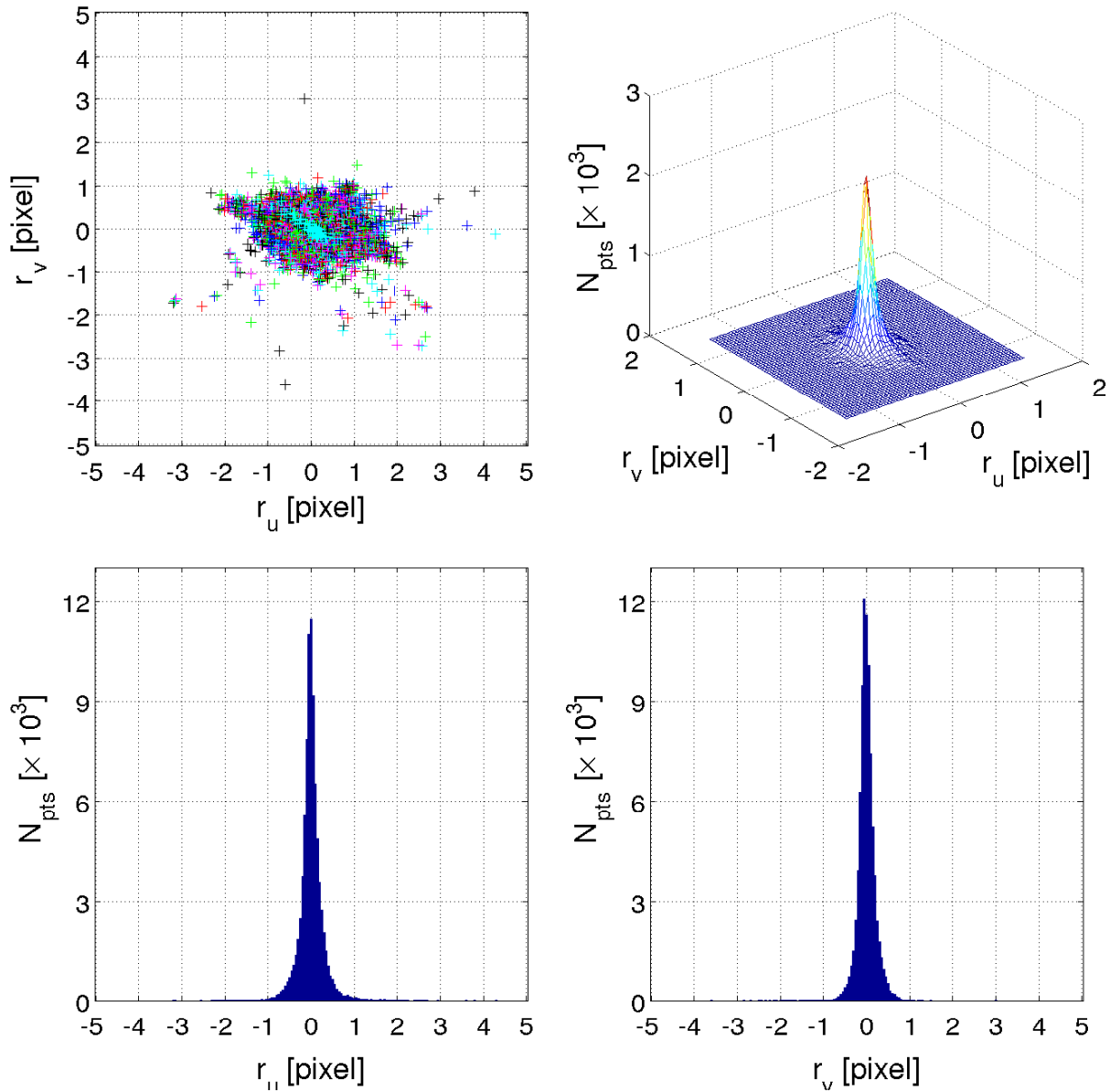


Figure 3.10: Error of reprojection (residual after optimization) for the right camera : $r_u = u - u_p$ and $r_v = v - v_p$. Upper-left panel shows that some reprojections are far from observed corner, nevertheless, these points have small influence on global calibration results, given large number of calibration points. Upper-right panel shows disparity in reprojection errors in both u and v pixel axis. Lower panel gives disparity in reprojection errors for each axis. We note that assumption of error assimilated to a white Gaussian noise looks fine. Directional RMS errors of reprojection are $(0.28, 0.20)$ for left camera and $(0.26, 0.18)$ for right one.

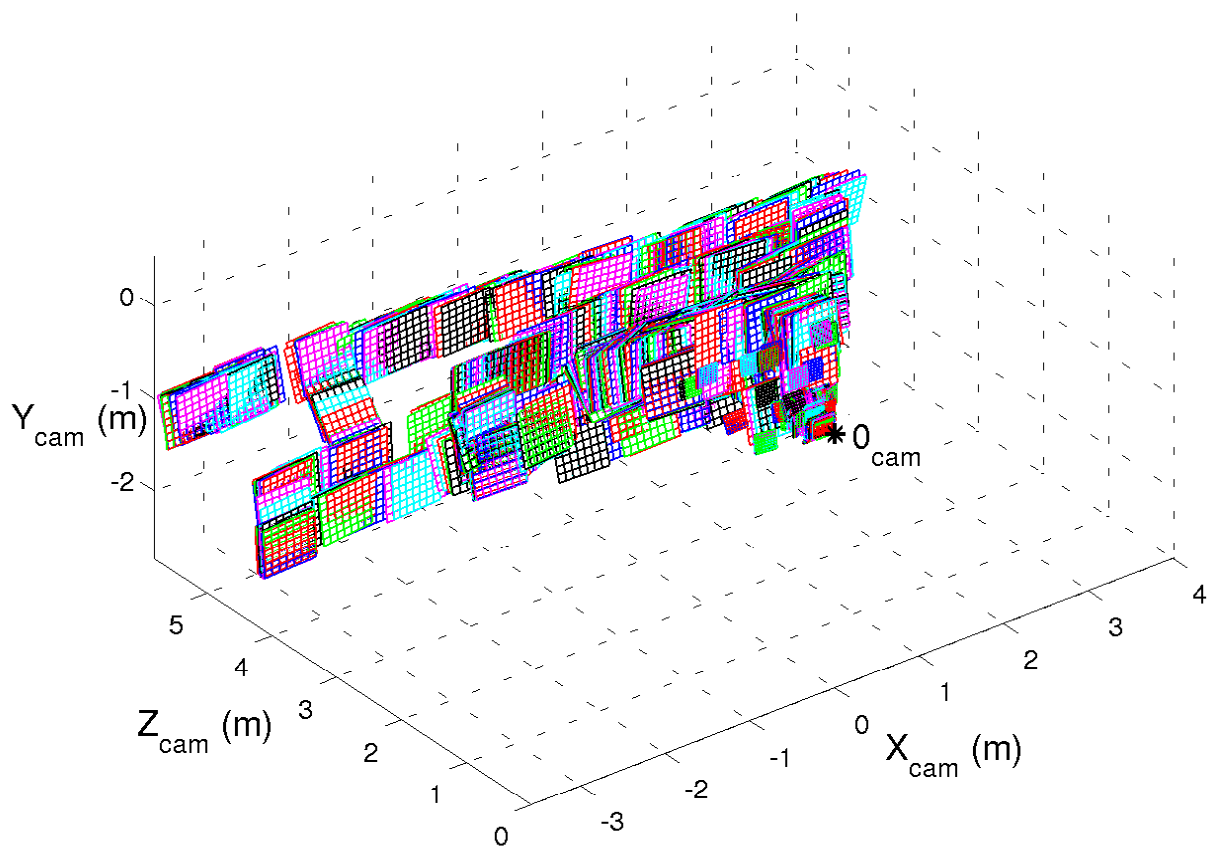


Figure 3.11: Distribution of intrinsic calibration chessboards in camera reference system for right camera.

follows

$$\vec{X}_{c,R} = R_{L \rightarrow R} \vec{X}_{c,L} + T_{L \rightarrow R}, \quad (3.51)$$

where $R_{L \rightarrow R}$ and $T_{L \rightarrow R}$ described rotation matrix and translation vector from left to right camera reference systems, such that

$$R_{L \rightarrow R} = R_R R_L^{-1} = R_R R_L^T \quad (3.52)$$

$$T_{L \rightarrow R} = T_R - R_R R_L^{-1} T_L = T_R - R_{L \rightarrow R} T_L. \quad (3.53)$$

Using these equations (3.52,3.53), the rotation matrix $R_{L \rightarrow R}$ (or angles $\theta_{L \rightarrow R}$, $\phi_{L \rightarrow R}$ and $\psi_{L \rightarrow R}$) and the translation vector $T_{L \rightarrow R}$ are computed independently for each stereo image pair. The first estimation for the rotation and the translation between the two views are given by the median values over the set. Then, as in the intrinsic calibration, an iterative non-linear optimization refines the values minimizing the reprojection errors on both left and right images. The optimization considers the relative angles $\theta_{L \rightarrow R}$, $\phi_{L \rightarrow R}$, and $\psi_{L \rightarrow R}$, the three components of relative translation vector $T_{L \rightarrow R}$ and the sets of the left extrinsic parameters for all stereo image pairs. We note that the set of right extrinsic parameters are now considers rigidly liked to left ones with $R_{L \rightarrow R}$ and $T_{L \rightarrow R}$, and do not have to be included in list of parameters to optimize. The stereo calibration tool also proposed a refinement of the left and right intrinsic parameters. However, the set of stereo calibration images does not cover properly the whole field of view of each camera. So, despite a better minimizing of the global reprojection errors, such a refinement leads to non-real intrinsic values, and is hereby disabled. The vector β of parameters to optimize is so

$$\beta = [\theta_{L \rightarrow R}, \phi_{L \rightarrow R}, \psi_{L \rightarrow R}, t_{L \rightarrow R,1}, t_{L \rightarrow R,2}, t_{L \rightarrow R,3}, \dots \quad (3.54)$$

$$\theta_{L,I}, \phi_{L,I}, \psi_{L,I}, t_{L,1,I}, t_{L,2,I}, t_{L,3,I}]_{I=1,\dots,M}^T, \quad (3.55)$$

where M is now the number of stereo image pairs. The non-linear optimization procedure is similar as one used previously, with the direct computation of the matrix $(J^T J)$ and the vector $J^T r$ to save memory, but without the smoothing coefficient ($\alpha = 1$). The convergence condition is considered reached when

$$\|[\Delta\theta_{L \rightarrow R}, \Delta\phi_{L \rightarrow R}, \Delta\psi_{L \rightarrow R}, \Delta t_{L \rightarrow R,1}, \Delta t_{L \rightarrow R,2}, \Delta t_{L \rightarrow R,3}]^T\| \quad (3.56)$$

$$- \|[\theta_{L \rightarrow R}, \phi_{L \rightarrow R}, \psi_{L \rightarrow R}, t_{L \rightarrow R,1}, t_{L \rightarrow R,2}, t_{L \rightarrow R,3}]^T\| < 5 \cdot 10^{-6} \quad (3.57)$$

Finally, the optimization procedure returns the relative camera position $(\theta_{L \rightarrow R}, \phi_{L \rightarrow R}, \psi_{L \rightarrow R}, t_{L \rightarrow R,1}, t_{L \rightarrow R,2}, t_{L \rightarrow R,3})$ with their uncertainties computed with the equation 3.48.

This kind of external calibration, using a chessboard pattern, generally provides very nice results. Nevertheless, the calibration and the acquisitions were not done in the same place and it appears that the mounting of the camera bar on the platform modified the relative positions of the cameras. A solution was found thanks to a recent calibration code developed by at the *Dipartimento di Scienze Ambientali, Informatica e Statistica* of the university *Ca' Foscari Venezia* in Italy and run by Filippo Bergamasco. The code is not yet published and so will not be fully detailed here. For each acquisition, the code is run over 30 sea surface images extracted from the acquisition, and returns relative position of the camera. Nevertheless, the absolute translation vector between the cameras cannot be

extracted from sea surface images, and is returned normalized by the absolute distance between camera. Compared to the results obtained with the chessboard calibration, the relative rotation (around $X_{c,L}$) between the cameras is increased by a few degrees. These few degrees have a strong influence on the final results, providing a magnification of the 3-dimensions by a factor about 2. Nevertheless, they do not significantly affect distance between the cameras. The distance between the cameras is obtained by the chessboard calibration and is the applied to the normalized translation vector to obtain the absolute translation vector later used for reconstruction.

3.4.4 Image rectification

The image rectification is an important step of the stereo reconstruction made in this work. First, it permits the correction for distortion for left and right images. As a result, the linear inverse mapping given by the equation 3.13 can be applied on the rectified images. The second rectification, named stereo rectification, brings the epipolar lines aligned with the horizontal pixel lines, and in correspondence between left and right images. As a result, a point which projects on the left image into pixel (u_L, v_L) must project on the right image on the epipolar line defined by $u_R = u_L$, and vice versa. The stereo rectification is not fundamental for stereo reconstruction itself, nevertheless, it simplifies the matching points processing described further (§3.5.1).

The image rectification consists in an image transformation such that the rectified image corresponds to the projection of the same scene taken by an hypothetical camera with the same optical center, but with another orientation and/or another set of intrinsic parameters. The image rectification processing consists in the following steps. First, all pixels of the rectified image are associated to their 3D ray using rectified set of intrinsic parameter and new orientation. As no distortion effects are wanted on the rectified images (i.e. $K_n = 0$ and $P_n = 0$ for rectified images), the rays are linearly expressed in the a hypothetical camera reference system by

$$\begin{bmatrix} X_c \\ Y_c \\ Z_c \end{bmatrix}_{(r)} = tA^{-1} \begin{bmatrix} u \\ v \\ 1 \end{bmatrix}_{(r)}, \quad (3.58)$$

with $t \in [0, \infty[$. The subscript (r) means that coordinates are given in rectified image or hypothetical camera system, whereas the subscript (i) means that coordinates are given in initial image or camera system. Then defining R_{rect} the rotation matrix between hypothetical and real camera optical axis, the rays are expressed in real camera reference system (r) by

$$\begin{bmatrix} X_c \\ Y_c \\ Z_c \end{bmatrix}_{(i)} = R_{\text{rect}} \begin{bmatrix} X_c \\ Y_c \\ Z_c \end{bmatrix}_{(r)} = \alpha R_{\text{rect}} A^{-1} \begin{bmatrix} u \\ v \\ 1 \end{bmatrix}_{(r)}. \quad (3.59)$$

Then, the projections $(u_{(i)}, v_{(i)})$ of the rays, from rectified image, onto the initial image plane are given by the equation 3.8 using the real calibrated intrinsic parameters. We note that the distortion of the initial image is taken into account. Finally, for rays that intersect the initial image (i.e. $u_{(i)}$ and $v_{(i)}$ are respectively in range $[0, N_{u,(i)} - 1]$ and $[0, N_{v,(i)} - 1]$, with $(N_{u,(i)}, N_{v,(i)})$ the size of the initial image), a bilinear interpolation of the pixel values at $(u_{(i)}, v_{(i)})$ on the initial image gives the pixel value at $(u_{(r)}, v_{(r)})$ on the rectified image. In practice, the pixel index and the interpolation coefficients are computed to be applied quickly on the whole set of acquisition images.

Using $R_{\text{rect}} = I_3$ and identical initial and rectified intrinsic parameters, except the rectified distortion parameters that are set to zero, the process returns images only corrected for distortion. However, the stereo rectification implies both a modification of the camera orientation, through R_{rect} , and the modification of some intrinsic parameters. First, making epipolar lines parallel implies bringing the epipolar point at infinity. This corresponds

to parallel left and right image planes, and so parallel optical axis ($RL \rightarrow R = I_3$). This is obtained by rotating each camera minimally such that

$$R_{1,L} = F_{\text{rodrigues}}(-\theta_{L \rightarrow R}/2, -\phi_{L \rightarrow R}/2, -\psi_{L \rightarrow R}/2) = R_L^{-1} = R_L^T \quad (3.60)$$

$$R_{1,R} = F_{\text{rodrigues}}(\theta_{L \rightarrow R}/2, \phi_{L \rightarrow R}/2, \psi_{L \rightarrow R}/2) = R_R^{-1} = R_R^T. \quad (3.61)$$

where $F_{\text{rodrigues}}$ returns the rotation matrix corresponding to roll, pitch, and yaw angles (Rodrigues formula). This implies that the new translation vector between the cameras is $T_1 = R_{1,R}T$. Then, the epipolar lines aligned with the horizontal pixel lines are given by the rotation R_2 which makes the horizontal pixel lines parallel to T_1 . Finally, the rotations to be applied to each camera are

$$R_{\text{rect},L} = R_2 R_{1,L} \quad (3.62)$$

$$R_{\text{rect},R} = R_2 R_{1,R}. \quad (3.63)$$

The rectified set of external parameters that links left to right camera is

$$\begin{aligned} R_{\text{rect},L \rightarrow R} &= I_3 \\ T_{\text{rect},L \rightarrow R} &= R_{\text{rect},R}T. \end{aligned} \quad (3.64)$$

Finally, epipolar lines in correspondence are obtained by coplanar left and right image planes and a same vertical pixel discretization ($f_{v,\text{rect}}$ identical for both each image). In order to retain the maximum information from initial image (i.e. a maximum of rays from the rectified image intersect the initial image), the common rectified focal length is defined such that

$$f_{\text{rect},v} = \min(f_1, f_2) \quad (3.65)$$

where

$$f_1 = f_{v,L} \left[1 + P_{1,L}(N_u^2 + N_v^2)/(4P_{2,L}^2) \right] \quad (3.66)$$

$$f_2 = f_{v,R} \left[1 + P_{1,R}(N_u^2 + N_v^2)/(4P_{2,R}^2) \right] \quad (3.67)$$

Therefore, the rectified set of intrinsic parameters for each camera is only modified by setting distortion parameters to zero and vertical pixel focal length to $f_{v,\text{rect}}$ and the rectified relative position of the cameras are given by equations 3.64

3.5 Sea surface reconstruction

The stereo analysis to obtain the 3-D shape of a scene is one of the first and most popular problems in Computer Vision. As discussed above in paragraph 3.3.3, using two projections of the same scene from different points of view restores the third dimension lost by single projection. Thanks to the camera calibration described in the previous paragraph 3.4, links between 3D scene and each projection are now well-known. Moreover, using rectified images (with rectified camera parameters), the inverse mapping has now a simple linear solution given by equation 3.13. For the continuation of the chapter, only rectified images with their rectified intrinsic and extrinsic parameters are now considered

and, subscript *rect* is removed to simplify the notation. Surface reconstruction is in theory trivial. Since projection in each image of a same scene point is found, intersection of corresponding rays gives its 3D position (see paragraphs 3.3.3 and 3.5.2). In practice, the main problem in stereo analysis is how to find, given a point in the first image, the corresponding point in the second image. This problem, commonly known as the correspondence problem is discussed in the section 3.5.1. Then, the triangulation process which computes the 3D coordinates in the camera reference system from the matched projections is given in the section 3.5.2. The definition of the mean sea surface plane in the camera reference system is discussed in the paragraph 3.5.3. The section 3.5.4 deals with the expression of the 3D coordinates of the points in the world reference system. Then, the paragraph 3.5.5 investigates the correction of asymmetric projection. Finally, the section 3.5.6 describes gridding and smoothing of the sea surfaces. The main steps of the processing are illustrated on the figure 3.12.

3.5.1 Point matching processing

Usually, in computer vision, when the dynamic of the scene is acquired (i.e. movie of the scene is taken), motion can be used to help the research of correspondences and correspondences can be used to infer the motion of rigid bodies in the scene (Kanade and Morris, 1998). Since water waves are definitely far from rigid bodies, an ad-hoc algorithm must be implemented and each image pairs is processed independently (Benetazzo, 2006).

Point matching processing used here is an adaptation of the work of Benetazzo (2006). Given a point in a right image, process consists in search the corresponding point on the corresponding left image. A rectangular area is defined around the point in right image as template. Then similar templates are searched in right image using cross-correlation. Also known as sliding dot product, cross-correlation determines a correlation coefficient for each part of the left image that quantifies the similarity with the right template. Similarity of the templates is then assimilated to similarity of the points. Correlation coefficient can be computed over various algorithm. Here, the normalized correlation coefficient, $C_{u_R, v_R}(u_L, v_L)$, which measures similarity between right point (u_R, v_R) and left point (u_L, v_L) is given by

$$C_{u_R, v_R}(u_L, v_L) = \frac{\sum_{u', v'} (T_R(u', v') - T_L(u', v'))^2}{\sqrt{(\sum_{u', v'} T_R(u', v')^2) (\sum_{u', v'} T_L(u', v')^2)}} \quad (3.68)$$

where T_L and T_R are respectively left and right template defined around (u_L, v_L) and (u_R, v_R) and $\sum_{u', v'}$ is the sum over all element of the templates. Therefore, C_{u_R, v_R} defined the correlation map on left image of right point (u_R, v_R) . The best matching is then get as point providing greater correlation coefficient and pairs of corresponding points $[(u_L, v_L), (u_R, v_R)]$ are defined. Horizontal and vertical disparity maps are respectively given by $u_R - u_L$ and $v_R - v_L$. As discussed in Benetazzo et al. (2012), discretization of the continuous world by CCD cell implies that correspondence are fit to the closest integer-pixel, forcing the reconstructed 3D points to lie only on a certain discrete collection of depth planes from the cameras after triangulation (§3.5.2). In this work, sub-pixel

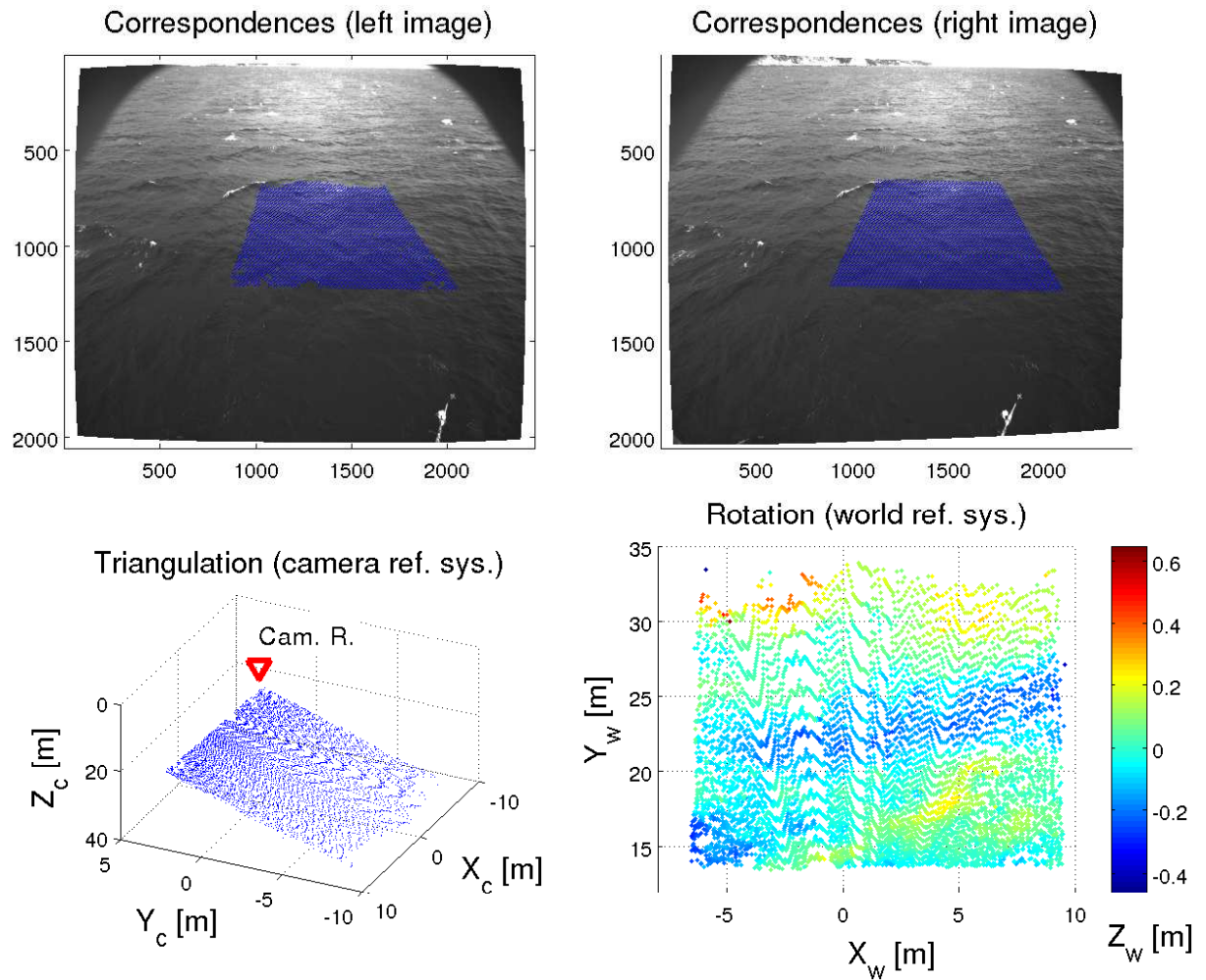


Figure 3.12: Main steps of stereo reconstruction processing: Top panels show set of corresponding points returned by matching point processing. Bottom left panel corresponds to the stereo-triangulation processing. Finally, bottom-right panel represents the sea surface obtained in world coordinate system. Figure presented here shows results obtained for first image pair of the 4th acquisition.

matching algorithm proposed by Benetazzo et al. (2012) is implemented, reducing discontinuous transitions in disparity map.

Following epipolar geometry, corresponding point must be on left epipolar line, limiting the searching of correspondence to this line. In practice, a search area of some pixel width Δ_v around epipolar line is chosen to avert for errors in calibration and image stereo rectification. Using stereo rectified images, search area corresponding to right point (u_R, v_R) is defined on left image by $v_L - v_R < \Delta_v$. In addition to save computational time, this restricted search area limits for multiple matching which comes from pseudo-fractal aspect of the sea surface. We note that using rectified images, epipolar line are supposed to be horizontal and in correspondence. Therefore, non-zero vertical disparity maps are an indicator of errors in calibration. This will be discussed further and focus is now on horizontal disparity map, linked to the 3D scene.

To reject bad matching, Benetazzo (2006) proposed that the pairs of matched points are kept when texture (variance) in templates and obtained maximum correlation coefficient exceeds predefined thresholds. However, experience showed that in the presence of breaking waves, these conditions are not adapted. Breaking waves form bright patches over darker surface water², resulting in strong brightness gradients. The presence of these strong gradients in correlation templates strongly disturbs matching processing, particularly if the gradients are on extremities of the templates, by providing large variance and correlation coefficients but non corresponding points. Indeed, strong gradients in templates give too much weight on the corresponding zone of the template. As a result, best matching is obtained for templates that provide best fit only on strong gradient parts. The figure 3.13 shows aberrant surfaces provided by this spurious effect around a breaking wave. Typically, extension around bright part of the images of such effects is subdued by defining smaller correlation templates. Nevertheless, smaller correlation templates also increase probability of multiple and bad matching. Therefore, improvements on the processing of Benetazzo (2006) were implemented for reconstruction of sea surface in presence of breaking waves.

A first improvement consists in a simple equalization of the pixel value histogram applied on both left and right images, resulting in a homogenization correlation weight within templates. Histogram equalization is a gray scale transformation T which minimizes $|c_1(T(i)) - c_0(i)|$ where $c_0(i)$ is the cumulative histogram of the image, $c_1(i)$ is the cumulative sum of an ideal flat histogram for all intensities i . This minimization is subject to the constraints that T must be monotonic and $c_1(T(i))$ cannot overshoot $c_0(i)$ by more than half the distance between the histogram counts at intensity i . Another good way to homogenize template correlation weight is to apply histogram pixel equalization independently over each pair of right correlation template and left search area. Such an implementation was tested. The slight results improvement costs an increase of the computational time of about a factor 3, and was so not retained in our processing algorithm.

A second improvement consists in reducing of the correlation template size. To avoid increasing probability of bad matching, search areas must be reduced. Therefore, the pyramidal search, implemented by Benetazzo (2006) to save computational time, now

²This particularity is used for the breaking detection discussed in next chapter.

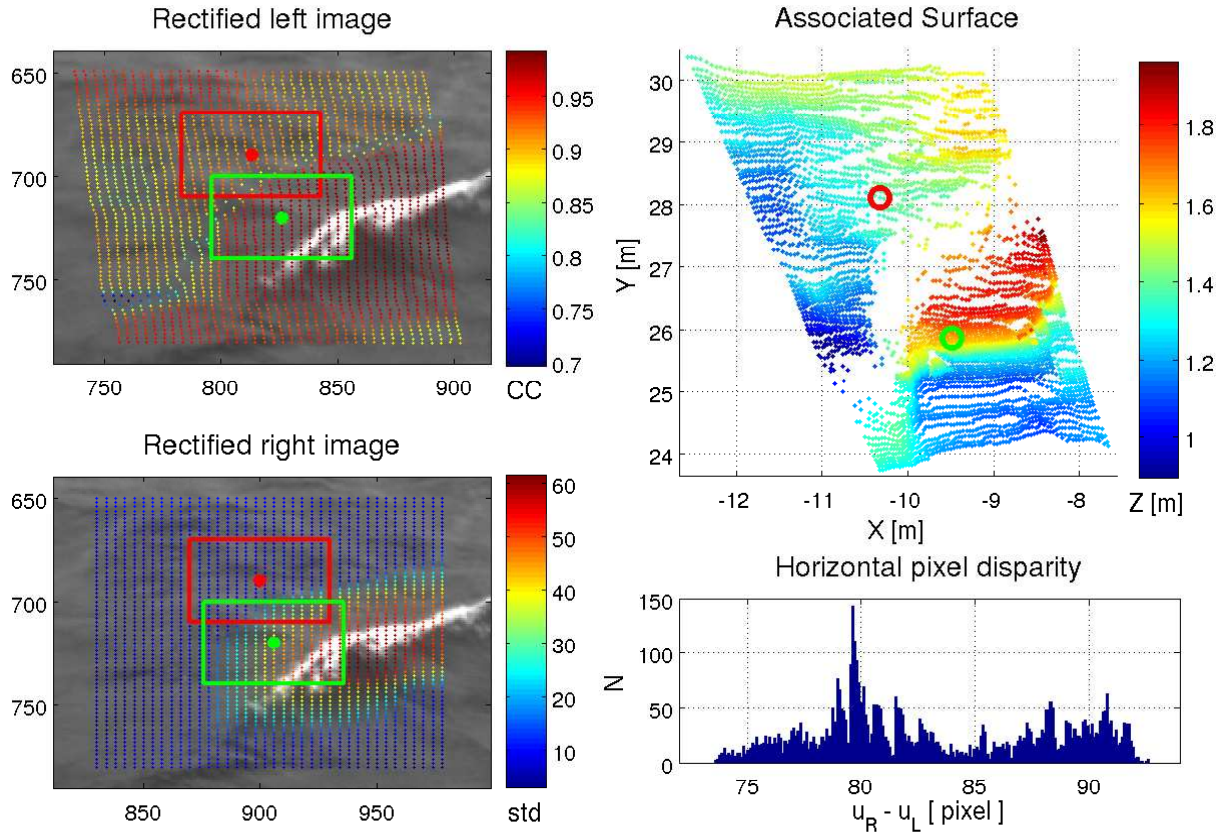


Figure 3.13: Example of bad point matching due to foam patch. Size of correlation templates is purposefully increased to 121×61 pixels to exaggerate this phenomenon. Left panels: Matching points obtained between left (top) and right (bottom) images. Color of points are correlation coefficient of matching (top) and standard deviation of pixel values in right correlation window. Green point matching is not disturbed by foam patch whereas red point matching is fully driven by small part of foam patch in correlation window. Top-right: resulting surface after stereo triangulation (§3.5.2) and rotation to world coordinates (§3.5.4). Green point falls on reconstruction in back of wave crest whereas images show that it is in front of the crest. Bad matching leads to unrealistic step around foam patch. Bottom-right: histogram of pixel vertical coordinates disparity between left and right images, with abnormal peak observed around pixel value 101 due to bad matching.

includes a decreasing of correlation template size with increasing iterations. A 3-step corresponding point search is implemented. In the first step, we get disparity map corresponding to the mean surface plane. A few number of corresponding points distributed over reconstruction area are given by highest correlation coefficient computed using a large correlation template (121×61 pixels), which increases the probability of good matching. A simple standard deviation filtering rejects uncertain matching. Then, 2D linear functions are fit at the least square sense on kept correspondence, such that

$$u_L = A_u u_R + B_u v_R + C_u \tag{3.69}$$

$$v_L = A_v u_R + B_v v_R + C_v. \tag{3.70}$$

These functions are then assimilated at pixel displacement between right and left corresponding point, due to mean sea surface plane of the considered area. Then, second step is to approximate disparity map due to long signal waves in images. A denser grid is defined on the right image and corresponding left points are searched using smaller correlation template (41×41 pixels). Estimating location of corresponding left points thanks to linear functions 3.69 and 3.70, search areas can be reduced and bad matching probability decreased. A standard deviation filtering is then applied on the difference between predicted and found left points to rejects uncertain matching. Finally, the last step is to find a very dense set of corresponding points, with a 2×2 pixel resolution grid defined on the right image. Once again, predictive locations of correspondences on left image are estimated using linear interpolation of the previous results. Finally, a fine disparity map is obtained using a small correlation template (21×21 pixels), and sub-pixel fit. Again, a standard deviation filtering is then applied on the difference between predicted and found left points.

We note that due to the projective transformation between left and right images, the rectangular template in the right image must corresponds to a parallelogram on the left image. Therefore, the processing is slightly modified by taking into account for this fact. Following methods of Kosnik and Dulov (2011), results at each step are now used to transform the left image, such that disparity map computed over transformed image is null. In a similar way as described above, a projective transformation fitted on the first step filtered results is applied on the left image. The rectified left image is used in the second step search, where predictive positions of correspondences are $(u_L, v_L) = (u_R, v_R)$. Reverse transformation then recover correspondences in the initial left image. A piecewise linear transformed image is computed by these results and used in the last step search. Reverse transformation gives fine disparity map. Correlation template sizes are kept equal. We note that with this method variant, matching should be better, because rectangle pattern in right image correspond to rectangular pattern in transformed left one. We note that image transformation also induces a smoothing of pixel values, so a loss of texture in the images, which slightly increases the number of unmatched points.

Experience shows that direct triangulation of these results leads to spiky surfaces. Therefore, the disparity map is smoothed using a 10×10 point (i.e. 20×20 pixel) median filter, resulting in the figure 3.15. The figure 3.14 shows corresponding points obtained with this modified matching processing.

We note that Benetazzo (2006) proposed to approximate locally the water surface by a planar surface to limit the possible location of the corresponding points on the

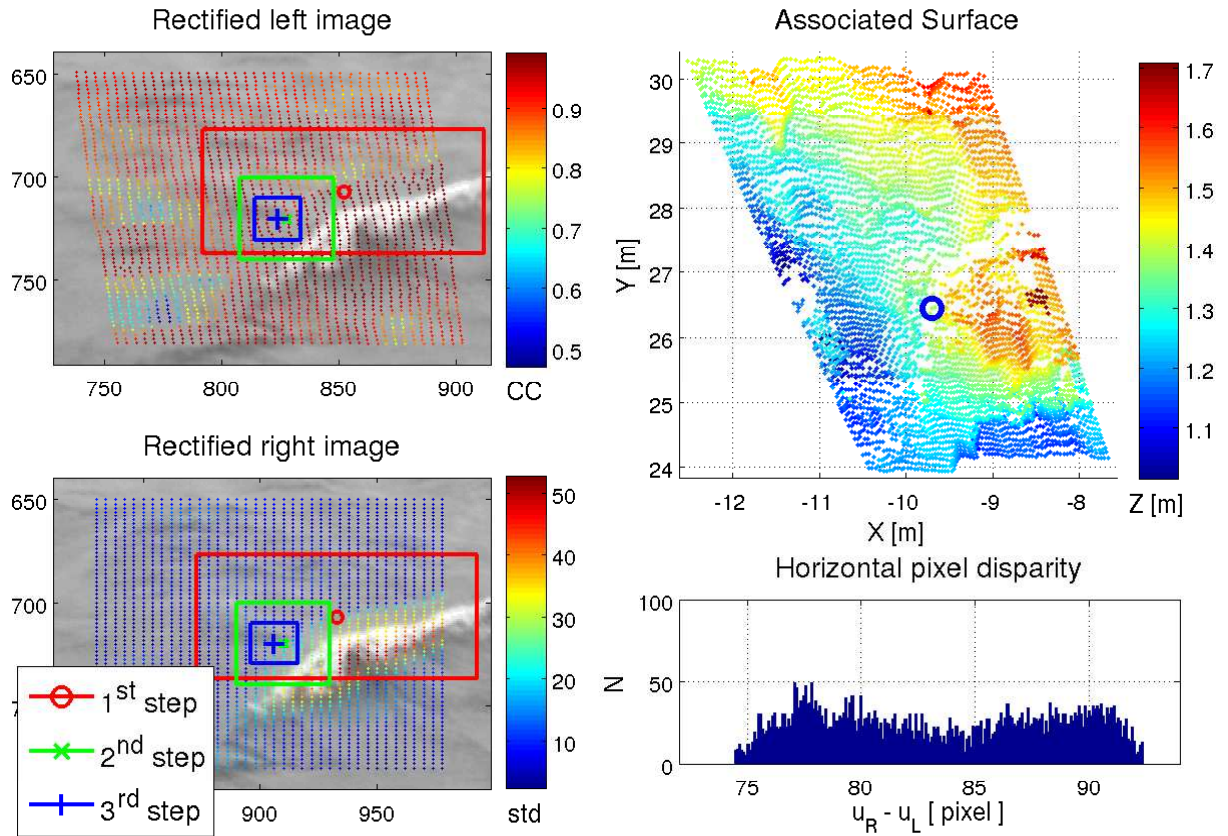


Figure 3.14: Same figure as 3.13, but matched points are now obtained with decreasing correlation template size, pixel histogram equalization, and left image rectification. Sizes of correlation templates are 121×61 pixels, 41×41 pixels, and 21×21 pixels in subsequent searching steps. Left panels: Matching points obtained between left (top) and right (bottom) images. The point colors represent correlation coefficient of matching (top) and standard deviation of pixel values in right correlation window. Top-right: resulting surface after stereo triangulation (§3.5.2) and rotation to world coordinates (§3.5.4). Bottom-right: histogram of pixel vertical coordinates disparity between left and right images. The abnormal peak observed around pixel value 79 in figure 3.13 is not present here.

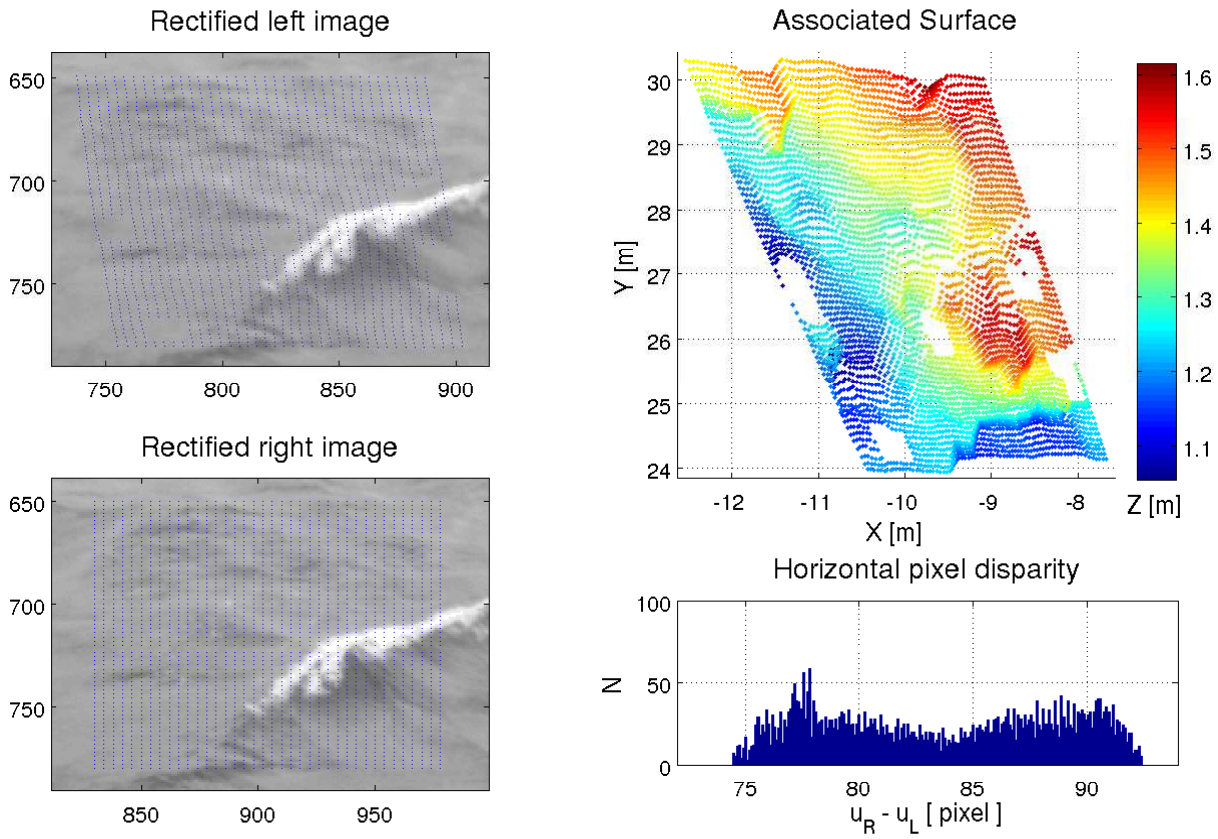


Figure 3.15: Same figure as 3.15, after the smoothing of the disparity map with a 10×10 point (i.e. 20×20 pixel) median filter. Top-right: resulting surface after stereo triangulation (§3.5.2) and rotation to world coordinates (§3.5.4). Bottom-right: histogram of pixel vertical coordinates disparity between left and right images.

epipolar line in subsequent steps. Here, the reasoning is different. Indeed, Benetazzo (2006) use a same correlation template size for all its steps, and so subsequent steps only search for new correspondences, with the aim of refining the disparity map. Therefore, a non-iterative search should lead to the same disparity map, and iterative-processing only saves computational time. In the method described here, the previous steps predict the approximative locations of the correspondences and so reduces the search areas in the next step. This helps to reduce the correlation template size, with a limited increase in the probability of bad matching. Therefore, each step refines correspondences location.

The size of the correlation template footprints on the sea surface greatly increase away from the cameras. Therefore, the use of a fixed template size over the whole image must be interpreted with care. Indeed, on upper part of images, disparity is obtained over sea surface areas of a few square meters whereas disparity on the lower part of the images is obtained over sea surface areas of a few square centimeters. At this stage, absolute position and orientation of cameras are not known³. Nevertheless, they can be estimated from triangulation (see §3.5.2) of the points taken in the first step. Therefore, an adaptive correlation template size can be implemented to keep a constant footprint on the sea surface. Such processing should leads to more homogeneous disparity map. However, in a same way, informations on small waves far from cameras (i.e. in the upper part of the images) is lost due to the larger footprints of pixels. Because the correspondence search needs enough texture within the correlation templates, such a processing was not implemented.

The figure 3.16 show the zone on images selected for reconstruction. The zone shapes are computed using an approximation of the mean sea surface plane to provide reconstructed surfaces approximatevely rectangular.

Figure 3.17 shows the time-mean horizontal and vertical disparity maps obtained for the acquisition 4. The non-null vertical disparity map means that correspondences were found out of calibrated epipolar lines, and so reveals errors in calibration results. Nevertheless, we note that the vertical disparity maps are typically less than one pixel. This indicates that the intrinsic and extrinsic camera parameters are correct and can be used for next reconstruction steps.

The matching process is the more expensive process of reconstruction in term of computational time. Matching process takes more than 6 minutes to search for the about 100000 correspondence, corresponding to previous shown figures. As reference, the fixed correlation template size (61×41 pixels) process takes about 30% more time, and rejecting process applying pixel histogram to each correlation template and search areas takes more than 300% more time for same reconstruction area. Written in Matlab[®], codes were compiled and matching processes, independent for each image pairs, were then distributed in a few hundred parallel jobs.

3.5.2 Triangulation processing

Following the epipolar geometry discussed in paragraph 3.3.3, the triangulation provides the 3D coordinates of the intersection of rays corresponding to left and right corre-

³Only relative positions and orientations of camera compared to each other are given by calibration.

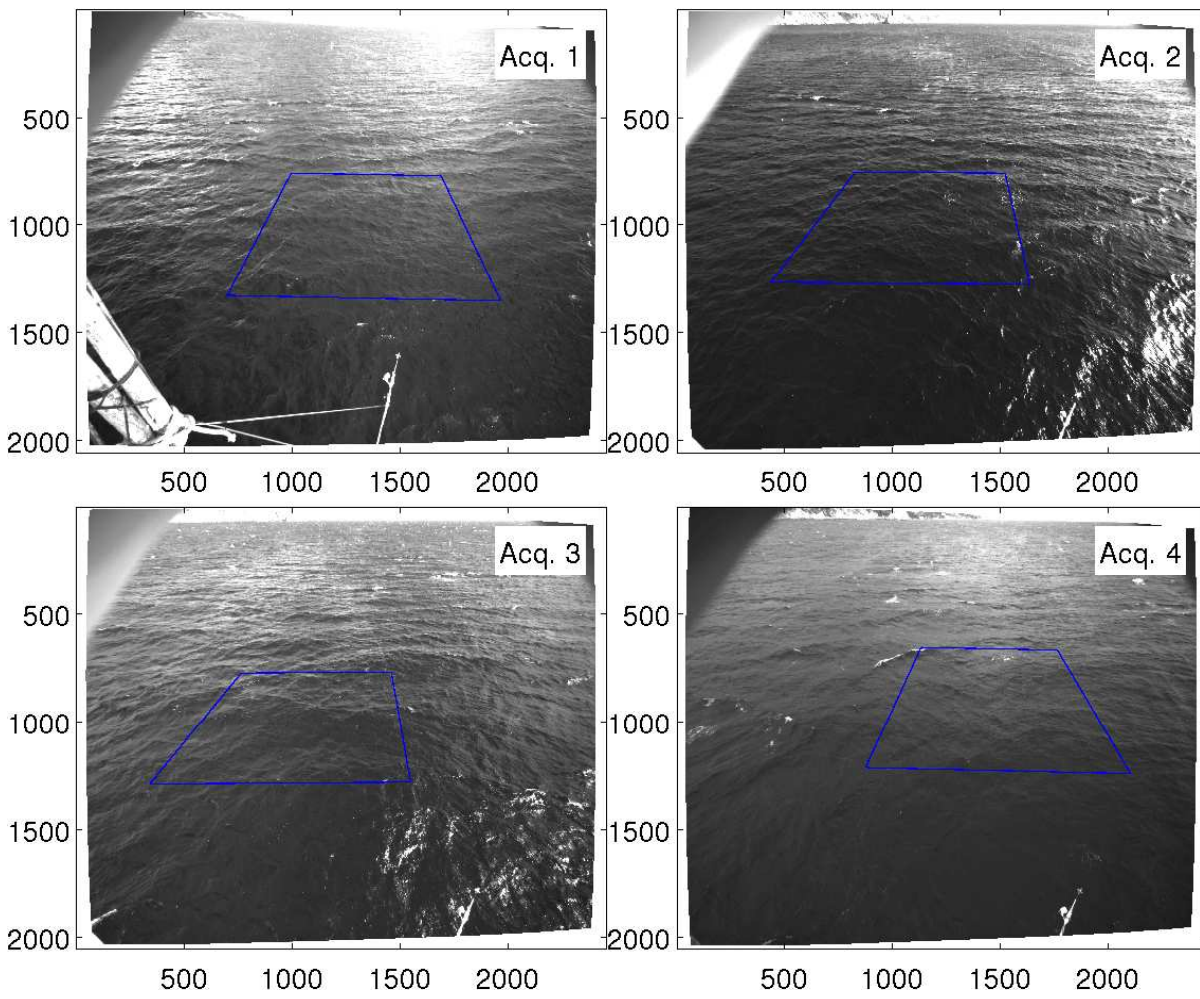


Figure 3.16: Reconstruction zone in which matching processing is done. Results are approximately rectangular reconstructed sea surface.

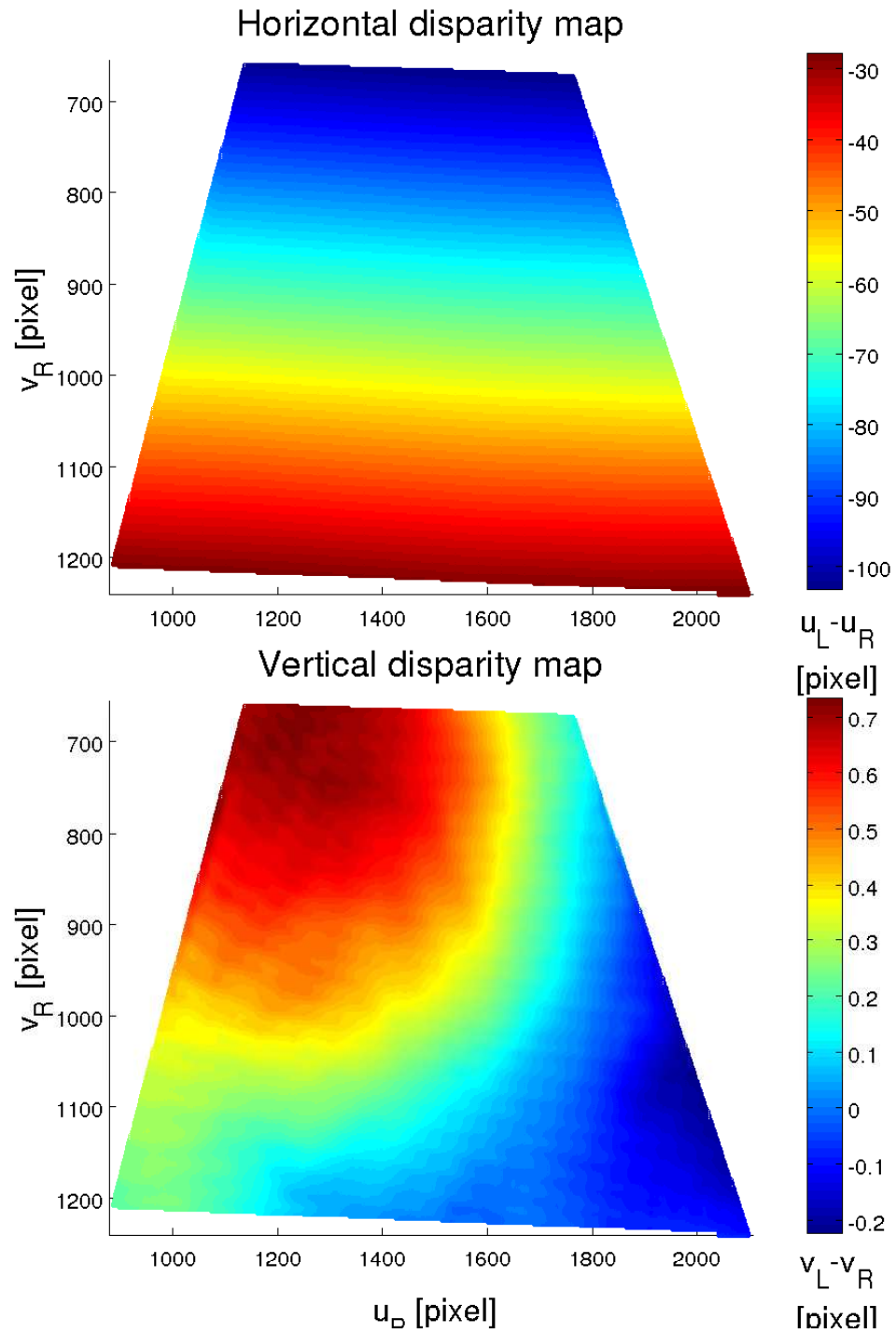


Figure 3.17: Mean vertical (left) and horizontal (right) disparity maps obtained from the average of the 21576 disparity maps of the 4th acquisition.

sponding points using equation (3.13),

$$\begin{bmatrix} X_c \\ Y_c \\ Z_c \end{bmatrix} = \alpha_L C_L^{-1} \begin{bmatrix} u_L \\ v_L \\ 1 \end{bmatrix} = \alpha_R C_R^{-1} \begin{bmatrix} u_R \\ v_R \\ 1 \end{bmatrix}. \quad (3.71)$$

As the earth system is not defined at this stage, the world system is defined as the left camera system. Then, using relative camera position (Eq. 3.51) with intrinsic camera matrix (Eq. 3.12), triangulation searches for α_L and α_R which are solution of

$$\begin{bmatrix} X_c \\ Y_c \\ Z_c \end{bmatrix} = \alpha_L A_L^{-1} \begin{bmatrix} u_L \\ v_L \\ 1 \end{bmatrix} = \alpha_R R A_R^{-1} \begin{bmatrix} u_R \\ v_R \\ 1 \end{bmatrix} + T, \quad (3.72)$$

where $R = R_{L \rightarrow R}$ and $T = T_{L \rightarrow R}$, such as defined by external camera calibration. As undistorted images are used, $\tilde{v}'_L = \tilde{v}'_R = \tilde{v}'$ and $[\tilde{u}', \tilde{v}', 1]^T = A^{-1}[u, v, 1]^T$, with $\alpha[\tilde{u}', \tilde{v}', 1]^T$ is equation of the 3D ray corresponding to pixel (u, v) . Moreover, the stereo rectification of images implies $R = I_3$ and $T = [d, 0, 0]^T$. Therefore, equation 3.72 can be written

$$\alpha_L \begin{bmatrix} \tilde{u}'_L \\ \tilde{v}' \\ 1 \end{bmatrix} = \alpha_R \begin{bmatrix} \tilde{u}'_R \\ \tilde{v}' \\ 1 \end{bmatrix} + \begin{bmatrix} d \\ 0 \\ 0 \end{bmatrix}. \quad (3.73)$$

Then, the equation 3.73 gives

$$\begin{cases} Z_c &= Z_{c,L} = Z_{c,R} = d / (\tilde{u}'_R - \tilde{u}'_L) \\ Y_c &= Y_{c,L} = Y_{c,R} = Z_c \tilde{v}' \\ X_{c,L} &= Z_c \tilde{u}'_L = X_{c,R} + d \\ X_{c,R} &= Z_c \tilde{u}'_R = X_{c,L} - d \end{cases} \quad (3.74)$$

This verifies definition of image stereo rectification, with third dimension fully given by horizontal disparity map. Nevertheless, in practice, calibration errors and non-perfect accuracy of matching points lead to $v_L \neq v_R$. As a result, left and right rays computed by equation 3.13 do not intersect in the 3D space. The problem, then, is to find a 3D point which optimally fits the measured image points. Literature proposes multiple methods to define this optimal point. Based on different optimality criteria, the various methods produce different estimates when noise (error) is involved. A description of triangulation processing used in this work is now given. Usually called mid-point method, the algorithm first computes independently the point $[X'_L, Y'_L, Z'_L]^T = \alpha_L[\tilde{u}'_L, \tilde{v}'_L, 1]^T$ on left ray closest to right ray and inversely, the point $[X'_R, Y'_R, Z'_R]^T = \alpha_R[\tilde{u}'_R, \tilde{v}'_R, 1]^T$ on right ray closest to left ray with

$$\alpha_L = \frac{1}{D} \left[(r_R \cdot (Rr_L))(r_R \cdot T) - \|r_R\|^2 (Rr_L \cdot T) \right] \quad (3.75)$$

$$\alpha_R = \frac{1}{D} \left[\|r_L\|^2 (r_R \cdot T) - (Rr_L \cdot T)(r_R \cdot Rr_L) \right] \quad (3.76)$$

where $(x \cdot y)$ means dot product of vectors x and y , $r_L = [\tilde{u}'_L, \tilde{v}'_L, 1]^T$, $r_R = [\tilde{u}'_R, \tilde{v}'_R, 1]^T$ are respectively left and right rays, and

$$D = \|r_L\|^2 \|r_R\|^2 - (Rr_L \cdot r_R)^2. \quad (3.77)$$

Obviously, if the left and right rays intersect, these two points are directly linked by rigid transformation between camera. In general case, the two different points are expressed in the same reference system (here left camera one) and mid-point is computed, in both left and right camera reference system with

$$\begin{bmatrix} X_L \\ Y_L \\ Z_L \end{bmatrix} = \frac{1}{2} \left(\begin{bmatrix} X'_L \\ Y'_L \\ Z'_L \end{bmatrix} + R^{-1} \left(\begin{bmatrix} X'_R \\ Y'_R \\ Z'_R \end{bmatrix} - T \right) \right), \quad (3.78)$$

and

$$\begin{bmatrix} X_R \\ Y_R \\ Z_R \end{bmatrix} = R \begin{bmatrix} X_L \\ Y_L \\ Z_L \end{bmatrix} + T. \quad (3.79)$$

We note that the following triangulation algorithm does not need image stereo rectification. Nevertheless, it is implicitly assumed that a previous correction of images for distortion was done, which allows a linear link between pixel $p = (u, v)$ to its corresponding ray $[\tilde{u}', \tilde{v}', 1]^T$. From each stereo image pair, triangulation returns a scattered set of 3D surface point positions expressed in left and right camera reference system. Bottom left panel of figure 3.12 shows an example of 3D surface point coordinates returned by triangulation processing, expressed in right camera reference system.

3.5.3 Mean surface plane definition

This process consists in the expression of the scattered surface points in world coordinate system, where axis \vec{X}_w and \vec{Y}_w are horizontal and \vec{Z}_w is aligned with gravity, looking up. As position of cameras in such a reference system is not known, information must be extracted from the set of 3D points. Only right coordinates are now used, but similar process can be done over left ones. Following Benetazzo (2006), gravity direction in right camera reference system is obtained using time-averaged water surface elevation. Indeed, considering a long period, the time-average surface is assumed to be a horizontal plane. Benetazzo (2006) proposed to fit a plane ($aX_c + bY_c + cZ_c + d = 0$, with $a^2 + b^2 + c^2 = 1$ and $c \geq 0$) over all scattered points using a least square solution. In practice, solution can be found directly over the whole set of 4D (space + time) scattered points. Therefore, the mean plane is obtained by averaging all the a , b , c , and d parameters of planes fitted for each stereo image pairs. We note here that triangulation applied on time-mean disparity map gives 3D positions of 3D scattered points on mean sea surface plane. Mean plane can then be extracted directly from this set of points. The two methods were implemented, and they give similar results. The effect on final reconstruction is negligible.

3.5.4 Surfaces in world reference system

The rigid transformation between right camera reference system and world system is defined by consecutive rotation $R_{c \rightarrow w}$ which makes the mean surface plane horizontal and vertical translation $T_{c \rightarrow w}$ which moves mean sea surface plane to $Z_w = 0$. In other words, the world system is defined by \vec{Z}_w is aligned with gravity, looking upwards, and the origin is on mean sea surface plane, vertically below right camera. We define the unit normal vector of plane $\vec{n}_p = [-a, -b, -c]^T$, looking out water (camera looks down and plane parameters are defined such that $c \geq 0$). Rotation must transform \vec{n}_p into $[0, 0, 1]^T$. Therefore, $R_{c \rightarrow w} = [\vec{u}, \vec{v}, \vec{n}_p]^T$ with $(\vec{u}, \vec{v}, \vec{n}_p)$ forms an orthonormal basis, here defined with

$$\vec{u} = \frac{[b, -a, 0]^T}{\sqrt{a^2 + b^2}} \quad (3.80)$$

$$\vec{v} = \vec{n}_p \times \vec{u}. \quad (3.81)$$

where \times means cross product. We note that any couple of vectors (\vec{u}, \vec{v}) which form orthonormal basis with \vec{n}_p makes mean sea surface plane horizontal with \vec{Z}_w looking up. Nevertheless, defining the third component of \vec{u} null, the obtained \vec{Y}_w is aligned with camera reference (i.e. rotation around Z -axis (yaw) is null). The proper direction of \vec{u} then gives positive values of Y_w . Finally, translation vector is simply defined with $T_{c \rightarrow w} = [0, 0, -d]^T$. Therefore, coordinates of surface points in world coordinates are

$$\begin{bmatrix} X_w \\ Y_w \\ Z_w \end{bmatrix} = R_{c \rightarrow w} \begin{bmatrix} X_c \\ Y_c \\ Z_c \end{bmatrix} + T_{c \rightarrow w}. \quad (3.82)$$

3.5.5 Correction for the asymmetric projection

Inspired from works of Heikkila and Silven (1997) (§2.3), a correction for the asymmetric projection was implemented. In our experimentation, image and sea surface planes are not parallel. So, projective geometry does not preserve shape. In other words, the image rectangular correlation template projects on the mean sea surface plane in a quadrilateral polygon. Considering a real sea surface deformed by waves, projection is a complex surface. Generally, the barycenter of this surface does not project on center of the corresponding image template. This problem is commonly called asymmetric projection. Using a five-step iterative processing, template corners of each left and right camera are projected on sea surface plane, as defined in the previous paragraph. The template barycenter is then reprojected on left and right images respectively, giving a new disparity map. A new triangulation is done, giving a new mean plane. The process is reiterated to obtain both the mean plane and a set of triangulated points corrected for the asymmetric projection. We note that this processing does not take in account the local sea surface slope due to waves. Nevertheless, experience shows that such a correction provides a minor modification of the results. Figure 3.18 shows deviation of triangulated points due to correction for the asymmetric projection.

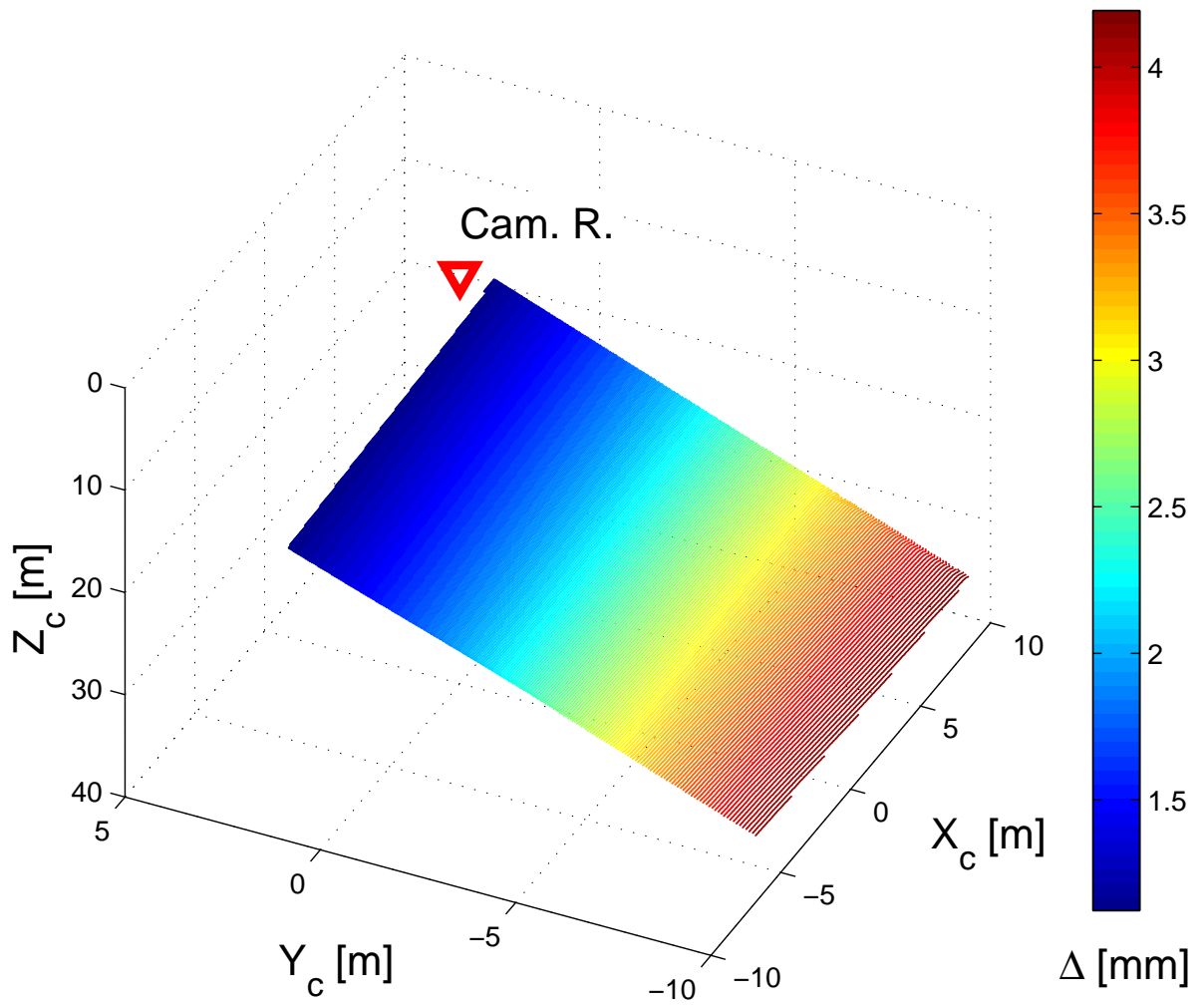


Figure 3.18: Triangulated point deviation due to correction for asymmetric projection, applied on the mean disparity map of acquisition 4 (Fig. 3.17)

3.5.6 Griding and smoothing of the surfaces

As scattered point sets are difficult to manipulate, the surface at each time step (i.e. for each stereo image pair) is then gridded, using a bi-linear interpolation. Three different grids are defined. First, two grids, shown in blue and red on figure 3.16, are used for the 3D spectra (frequency-wavenumber) described in the next section. A third large grid, shown in black on the figure is used in next chapter to analyze breaking events.

To reduce noise in the data, a slight smoothing is applied on the gridded surface, using a time-space low-pass filter. The 2D space filter is defined by the matrix F_s such that

$$F_s = \frac{1}{16} \begin{bmatrix} 1 & 2 & 1 \\ 2 & 4 & 2 \\ 1 & 2 & 1 \end{bmatrix}, \quad (3.83)$$

and the time filter is a 5-point hann window. This time-space filtering reduces noise for frequencies up to 1Hz.

3.6 Analyses of sea surface reconstructions

The reconstruction results here analyzed correspond to the matching processing including both equalization of pixel intensity histogram and decreasing correlation template size as discussed in paragraph 3.5.1, with the correction for asymmetric projection described in paragraph 3.5.5. If it is not specified, the smoothed surfaces are analyzed (see §3.5.6). After the reconstruction processing and the data gridding, the time-evolving elevation map are $Z(x, y, t)$ for a regular x, y grid.

Unfortunately, the wave elevation could not be measured in the reconstruction areas. Indeed, the above-water part of the capacitance wave gauges would have affected the images, making reconstruction impossible and due to the water depth (30m), the pressure sensors could not measure the short waves. Nevertheless, the capacitance wave gauges were about 20-30 meters away from reconstruction areas. At this distance, wave shapes are strongly disturbed, and the direct comparison of water elevation cannot be done, however, the wave statistics are comparable. Therefore, Probability Density Function (PDF) of elevation and the frequency spectra obtained with reconstruction are compared to those obtained with wave gauges in the respective sections 3.6.1 and 3.6.2. Another way to validate our reconstruction is the 3D wavenumber-frequency-direction spectra discussed in the section 3.6.3. The directional wavenumber spectra are then analyzed in the section 3.6.4. Finally, the mean square slopes (mss) are compared to the observations of Cox and Munk (1954) in the section 3.6.5.

3.6.1 Probability density function of the elevation

For each acquisition, the Probability Density Function (hereinafter PDF) of the elevation is computed over the whole set of 3D reconstructed surfaces. The PDF are compared to those those obtained with the wave gauges time series on the figure 3.19. The obtained PDF are in line with the wave gauge observations. Nevertheless, we note that the

reconstruction for the fourth acquisition disagree with wave gauges data. Same disagreement is observed on the comparison of frequency spectra given further. We also note an unrealistic step in the PDF obtained with the wave gauges around $Z = -0.5\text{m}$.

3.6.2 Non directional frequency spectra

For each (x, y) of the grid, the time series of surface elevations, $Z_{x,y}(t)$, are exacted. For each time series, the frequency spectra are computed in the sliding sub-time series of 1024 elevation, and averaged. We note that no spatial variation of spectra on the grid appears up to 2Hz. The same processing is applied on the 6 wave gauges time series. For both reconstruction and wave gauge data, all the frequency spectra obtained in different location are finally averaged and plotted on figure 3.20. The spectra from the reconstructions are globally in line with wave gauges observations, and well followed the expecting f^{-5} decreasing asymptote. We note however that a bad fit is observed for the small swell present during the first acquisition. This bad fit could be relied to the short time-series observations for the first acquisition, in which statistics on longer waves can not be well represented.

3.6.3 Frequency-wavenumber directional spectra

For the acquisition 1 (resp. 2, 3 and 4), 11 (resp 28, 42 and 42) elevation matrix $Z(x, y, t)$ with size $128 \times 128 \times 1024$ (resp. $200 \times 200 \times 1024$, $240 \times 240 \times 1024$ and $256 \times 256 \times 1024$) are extracted from smoothed surfaces, and the corresponding 3D spectra $E(k_x, k_y, f)$ are computed and averaged. Hann-windows are applied in each axis (x , y and t), before the spectrum calculation. We note that an ambiguity in direction of 180° on the 2D wavenumber spectra cannot be resolved using an individual elevation map. Nevertheless, the time evolution of the elevation maps resolves this direction ambiguity through the 3D frequency-wavenumber spectra. Therefore, the spectrum part corresponding to the negative frequencies is removed. Due to the symmetry of the Fourier spectrum, the energy is conserved with a multiplication of the energy spectrum part corresponding to the positive frequencies by 2. The 3D spectra $E(k_x, k_y, f)$ are converted to frequency-wavenumber-direction spectra $E(k, \theta, f)$ and respectively plotted on the figures 3.21-3.24, for the 4 acquisitions.

The figures show that the energy integrated over directions follows the dispersion relation up to 1.6Hz. We however note that the phase speeds of the small waves is slightly greater than ones expected by the dispersion relation. The small wave are modulated and drifted by the longer underlying wave orbital velocity, resulting in absolute greater apparent phase speed. We note also the presence of the energy corresponding to the second order. The directional energy spreading is discussed in the next paragraph.

3.6.4 Wavenumber spectra

The wavenumber spectrum considers the spatial Fourier analysis. From a square sub-area is extracted from each elevation map, the wavenumber spectra $E(k_x, k_y)$ can be computed, then averaged over the whole set of images. As stated before, this Fourier

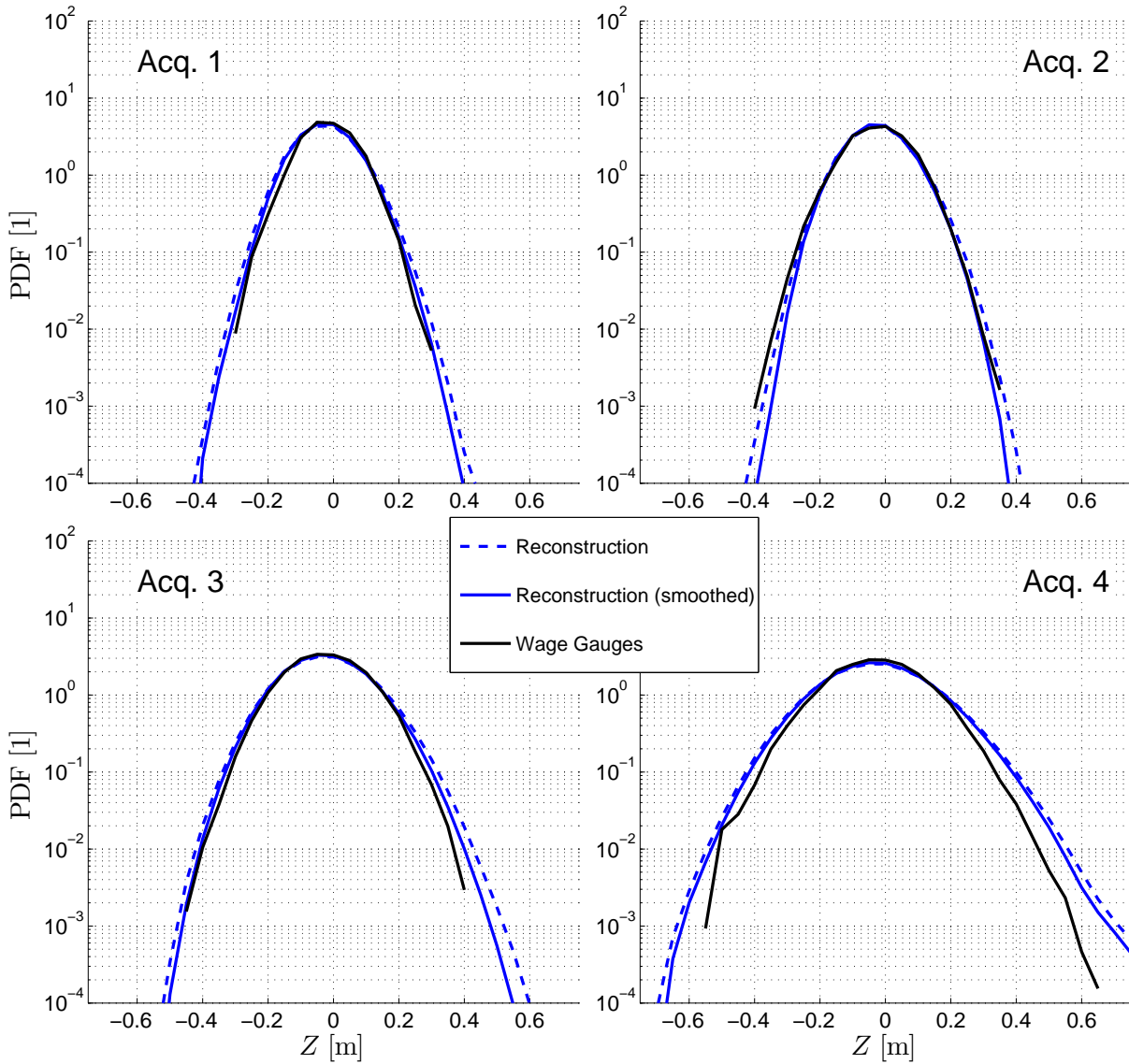


Figure 3.19: Probability Density Function (PDF) of the surface elevation. Black lines correspond to the PDF obtained with wave gauges time series. The blue lines correspond to the PDF of the reconstructions obtained with the new processing, including both equalization of pixel intensity histogram and decreasing correlation template size in the matching point processing, and the correction for asymmetric projection.

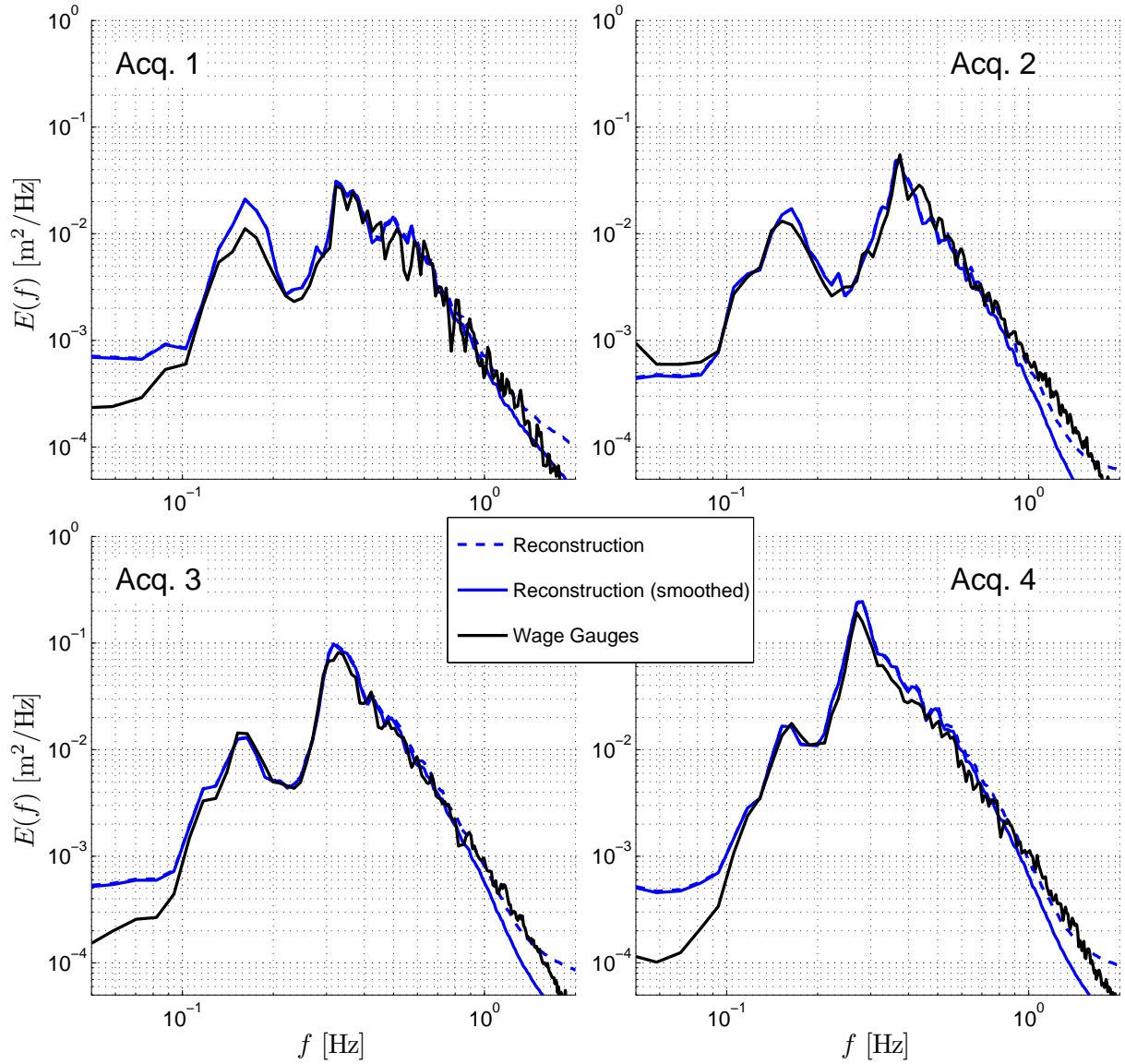


Figure 3.20: Frequency Spectra (FS) of the surface elevation. Black lines correspond to the PDF obtained with wave gauges time series. The blue lines correspond to the FS of the reconstructions obtained with the new processing, including both equalization of pixel intensity histogram and decreasing correlation template size in the matching point processing, and the correction for asymmetric projection.

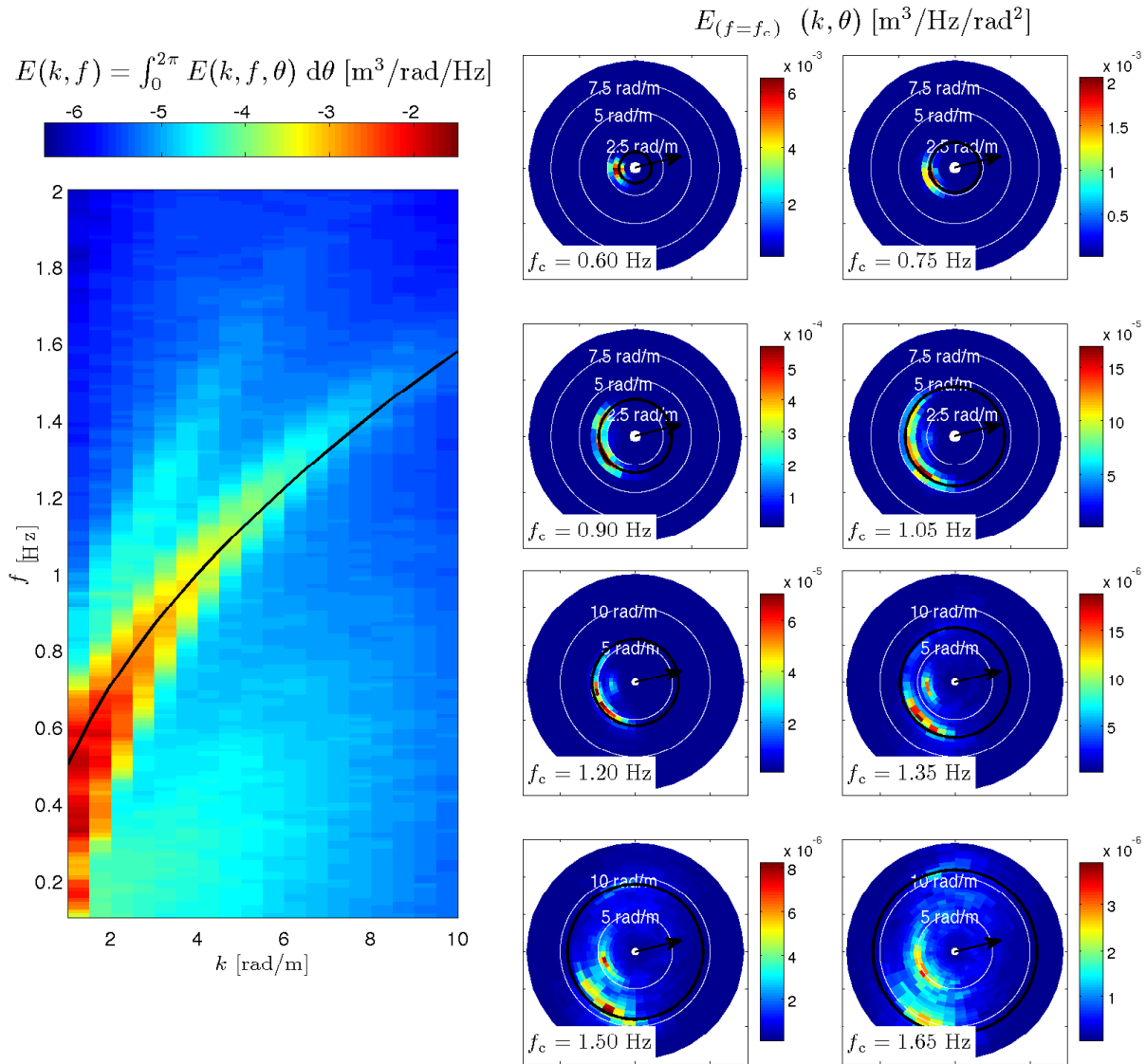


Figure 3.21: Wave spectrum over wavenumbers and frequencies (i.e. 3D spectrum integrated over directions) on the left panel and cross-sections in the 3D frequency-wavenumber-direction spectrum at fixed frequencies on right panels, for acquisition 1 ($U_{23} = 11.5$ m/s, $H_s = 0.30$ m, $f_p = 0.33$ Hz). The white arrow indicates the wind direction.

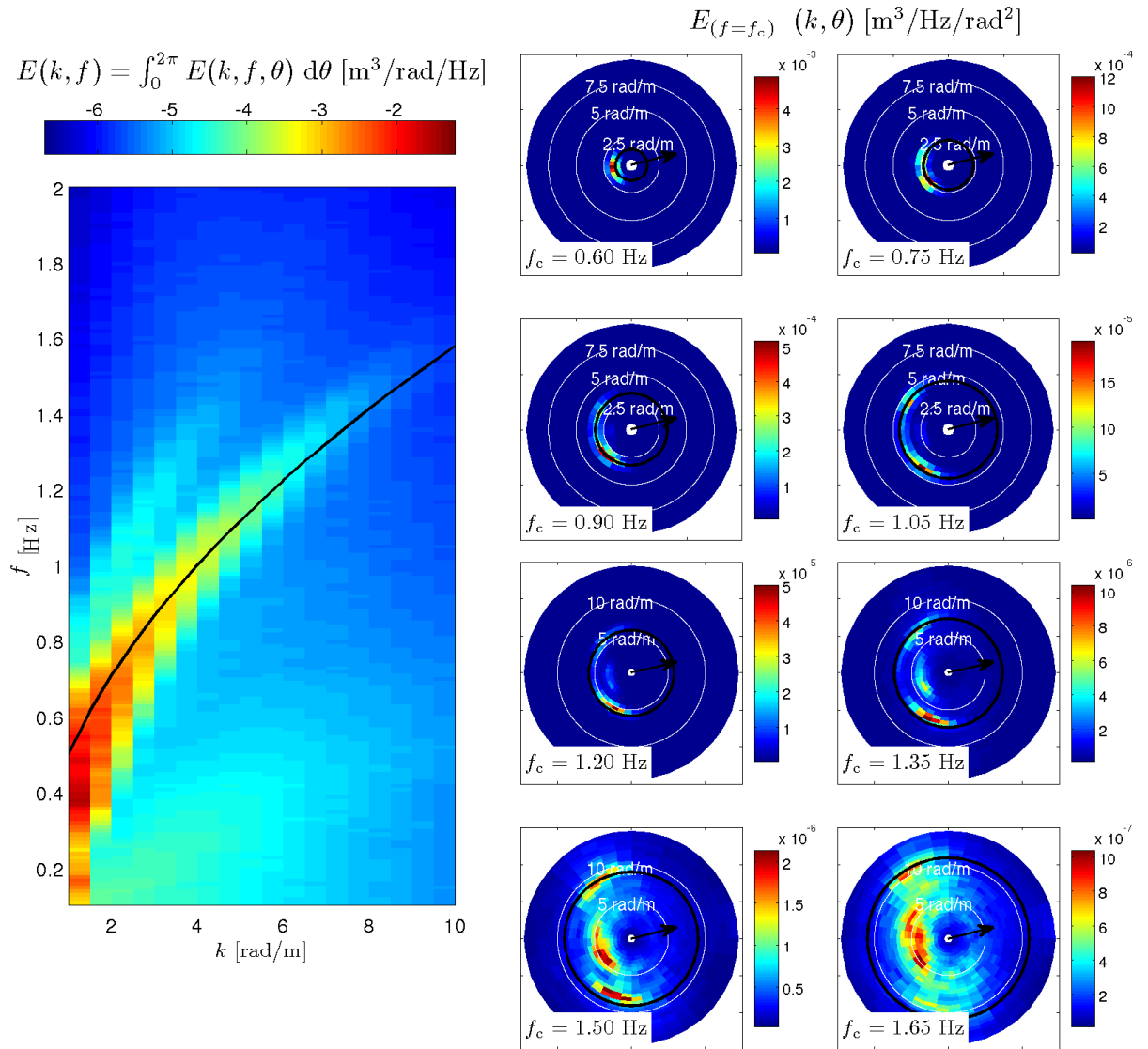


Figure 3.22: Same figure as Fig. 3.21 for acquisition 2 ($U_{23} = 10.9$ m/s, $H_s = 0.36$ m, $f_p = 0.38$ Hz).

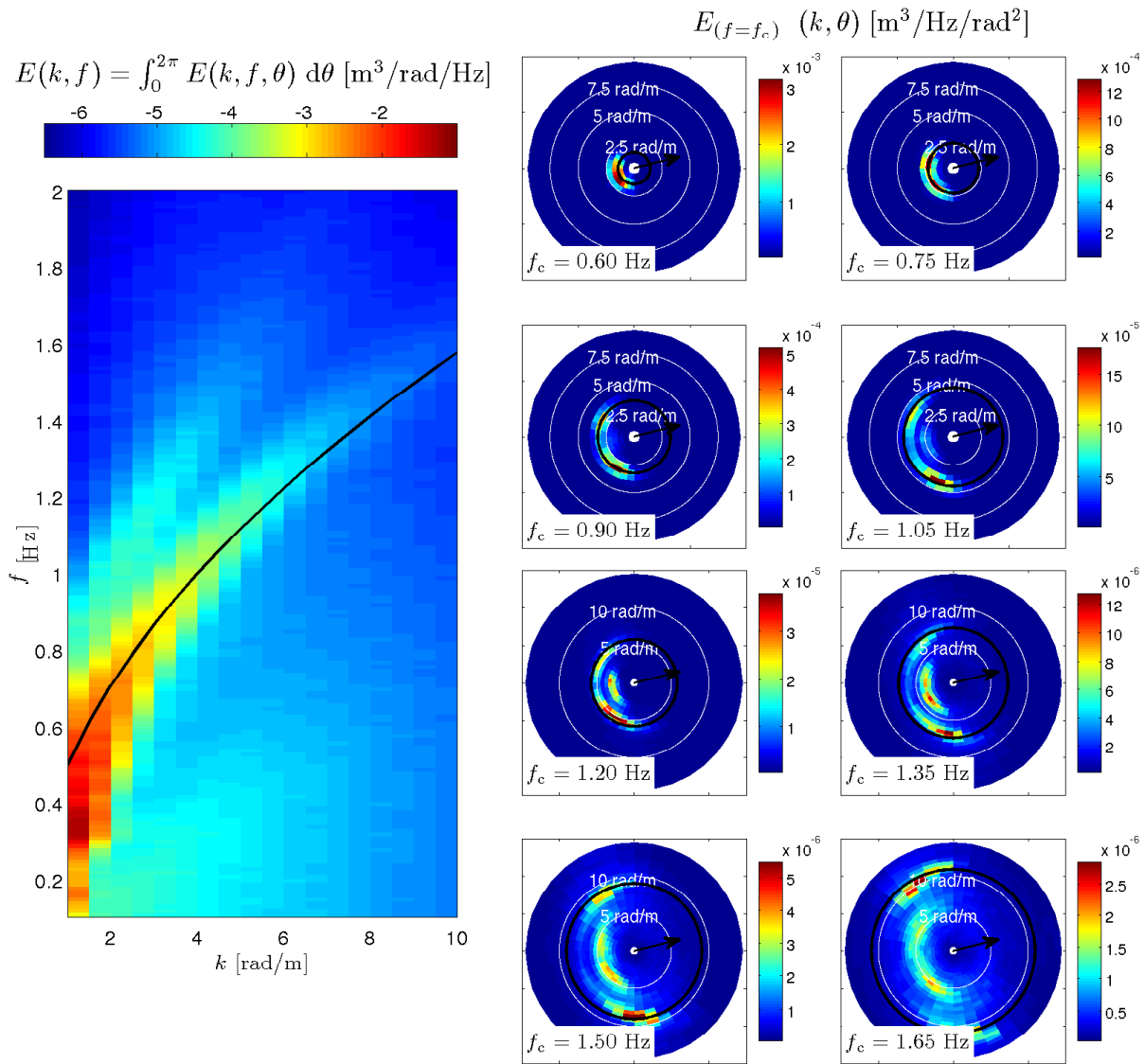


Figure 3.23: Same figure as Fig. 3.21 for acquisition 3 ($U_{23} = 13.2$ m/s, $H_s = 0.45$ m, $f_p = 0.33$ Hz).

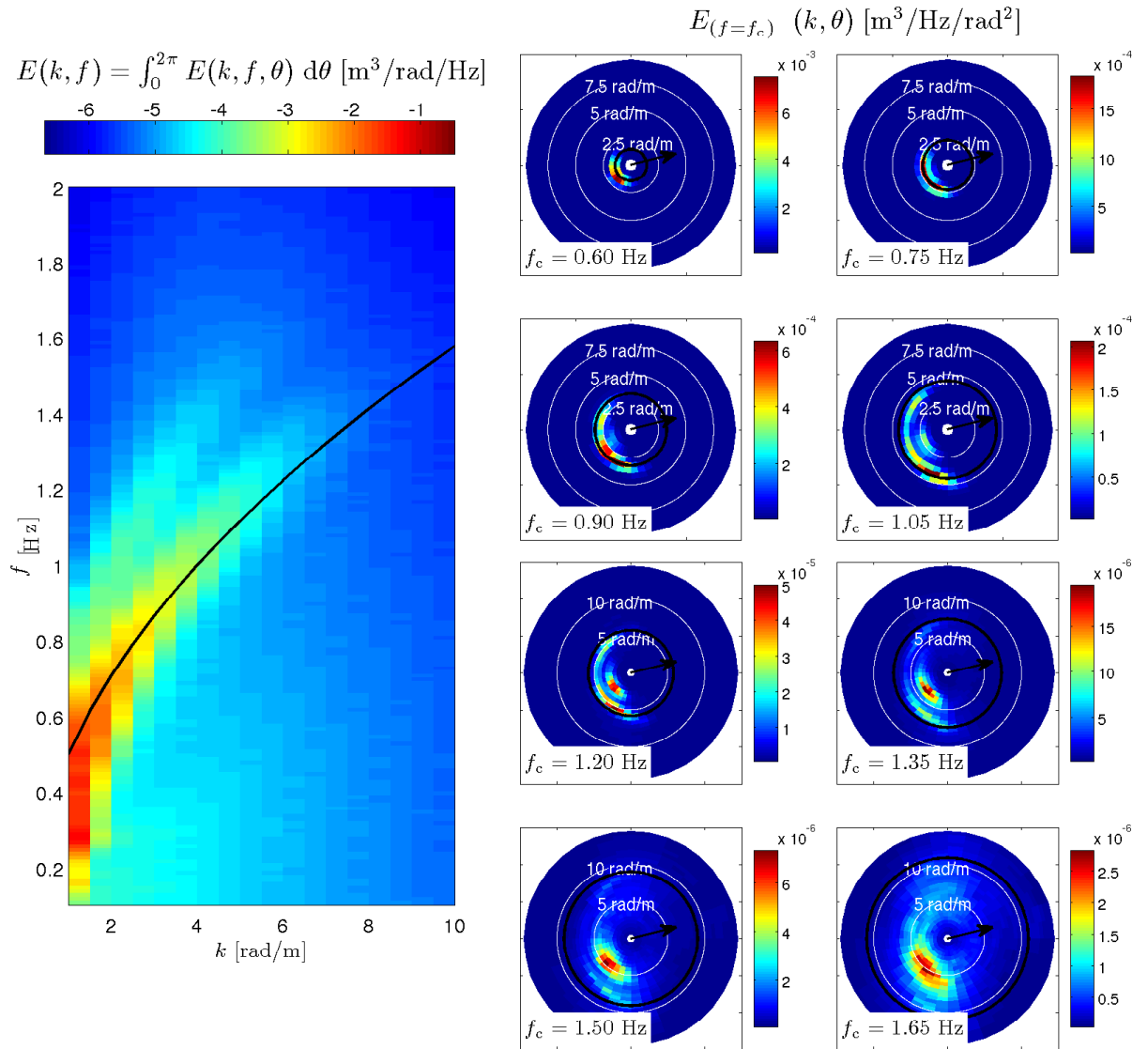


Figure 3.24: Same figure as Fig. 3.21 for acquisition 4 ($U_{23} = 13.9$ m/s, $H_s = 0.55$ m, $f_p = 0.27$ Hz).

analysis is ambiguous in the direction of 180° , and the directional spreading can be properly extracted. Using stereo reconstruction of the sea surface using photograph, the observations of Banner et al. (1989) are altered by this directional ambiguity. The integration of the spectra over direction is nevertheless analyzable. $E(k) = \int_0^{2\pi} E(k, \theta) d\theta$ is plotted on figure 3.25 and saturated spectra $S(k) = E(k)k^3$ is plotted on 3.26. The energy level, and so the saturation, becomes higher with the development of wave field (i.e. with increasing wave age). The saturation level is compared to the analytic spectra for fully developed sea state of of Bjerkaas and Riedel (1979), Apel (1994), Donelan and Pierson (1987) and Elfouhaily et al. (1997). In the wavenumber range given by the surface areas considered, these analytical spectra have large disparity in the saturation levels, from $4 \cdot 10^{-3}$ for spectrum of Bjerkaas and Riedel (1979) and one of Elfouhaily et al. (1997) to $42 \cdot 10^{-2}$ for Donelan and Pierson (1987) spectrum. The Apel (1994) spectrum is saturated at $8 \cdot 10^{-3}$. We note also that the peak wavenumbers are respectively 0.44, 0.58, 0.44, and 0.29rad/m. An oscillation of the saturated spectra at $10k_p$ is also observed by Leykin and Rozenberg (1984).

To study the directional spreading of the 2D wavenumber spreading, the ambiguity on the direction must be removed. Here, the time evolution of the elevation maps is acquired thanks to the use of high frequency cameras. The directional ambiguity can so be resolved using the 3D spectra (see §3.6.3). Therefore, the 3D spectrum is integrated over positive frequencies and the obtained wavenumber spectrum $E(k_x, k_y)$ is thus unambiguous in direction. The mean directional wavenumber $E(k_x, k_y)$ are plotted on the figure 3.27. The directional spreading over wavenumbers,

$$M_k(k) = \frac{E(k, \theta)}{\int_0^{2\pi} E(k, \theta) d\theta} \quad (3.84)$$

is plotted on figure 3.28 for each acquisition, and the spreading integral $I(k)$ such that

$$I_k(k) = \int_0^{2\pi} M(k, \theta)M(k, \theta + \pi) d\theta, \quad (3.85)$$

is shown on the figure 3.29. $I(k)$ is cut for wavenumber smaller than 2rad/m due to the lack of directional information on the wave with wavelengths close to the size of the elevation maps used to compute the spectra.

First, note that the spreading function $I(k)$, coming from the directional spreading is a fundamental property of the surface wave spectrum. There is a large theoretical and experimental literature on the spreading function for long gravity waves. Nevertheless, very little is known about the spreading function for the short gravity waves, here observed (Munk, 2008). Webb and Cox (1986) have demonstrated that plausible estimates of the spreading integral could be inferred from deep ocean pressure data. Wilson et al. (2003) followed a different strategy, using deep sea pressure data in the band between 0.1 and 1 Hz to confirm a spreading integral calculated from surface measurements. Here, the range of observed wavenumber ($k = [2, 10]$, $\lambda = [0.6, 3.1]$) is about 10 times the peak wavenumber. The present observations show that the two broad lobes in the directional spectrum of the gravity wave spectrum become nearly perpendicular to the wind direction, leading in the increasing of the spreading integral $I(k)$. Duennebier et al. (2012) proposed that the spreading integral decrease with higher frequency to get the value of $1/(2\pi)$ (the value for

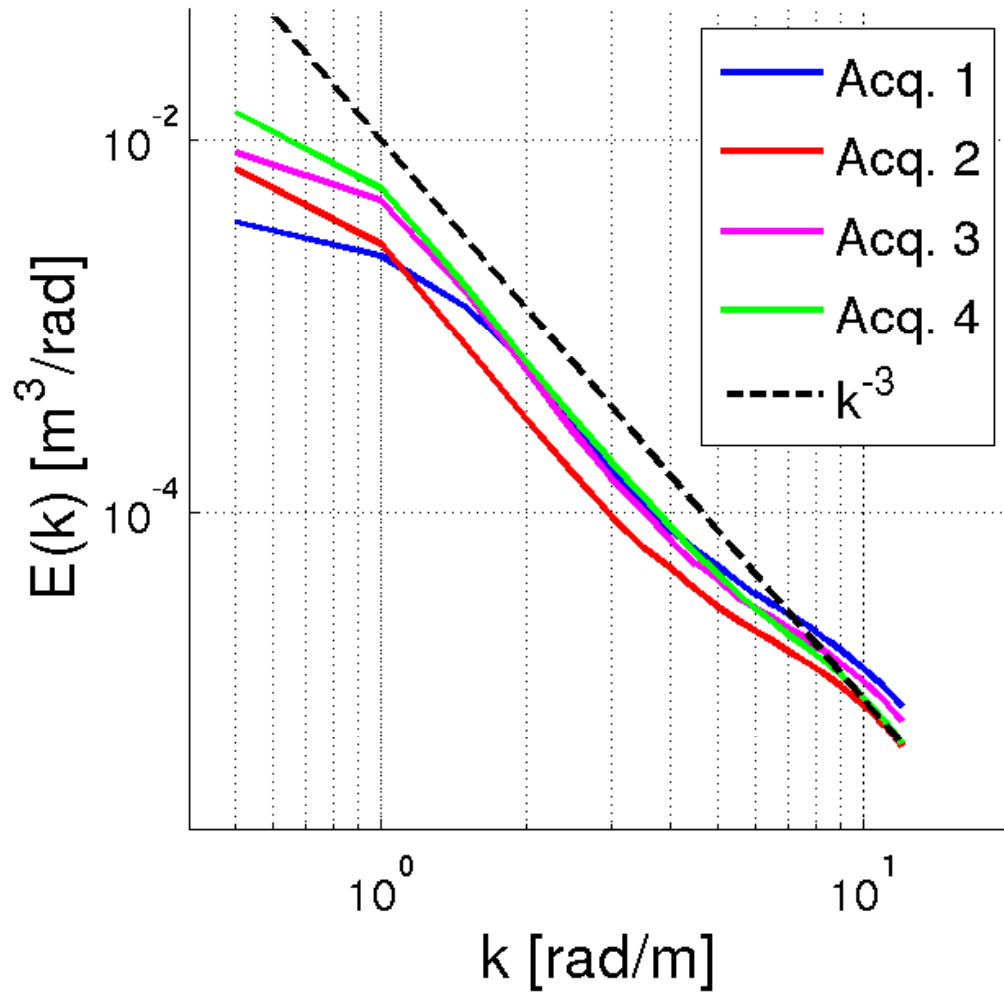


Figure 3.25: Non directional wavenumber spectra $E(k)$ for the 4 acquisition. The black dashed line is the k^{-3} asymptote.

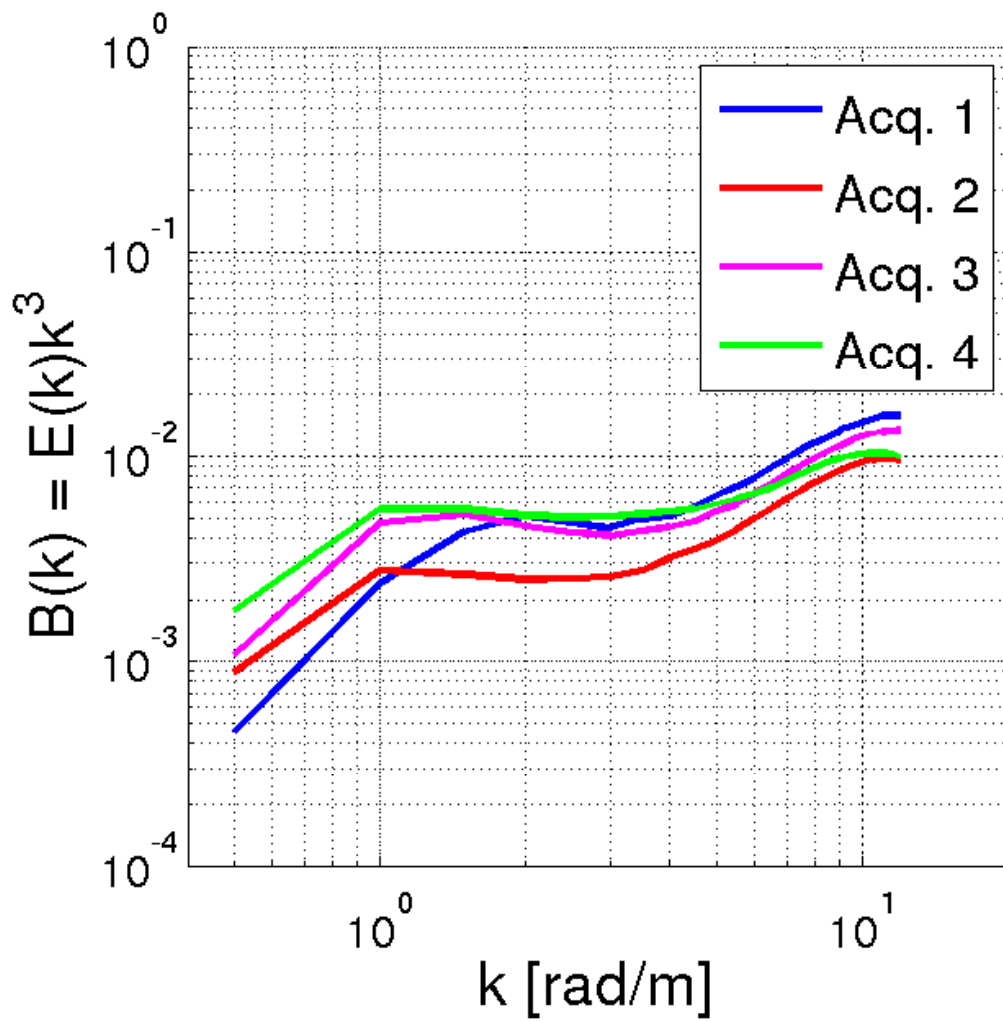


Figure 3.26: Saturated directional wavenumber spectra $S(k) = E(k)k^3$ for the 4 acquisition.

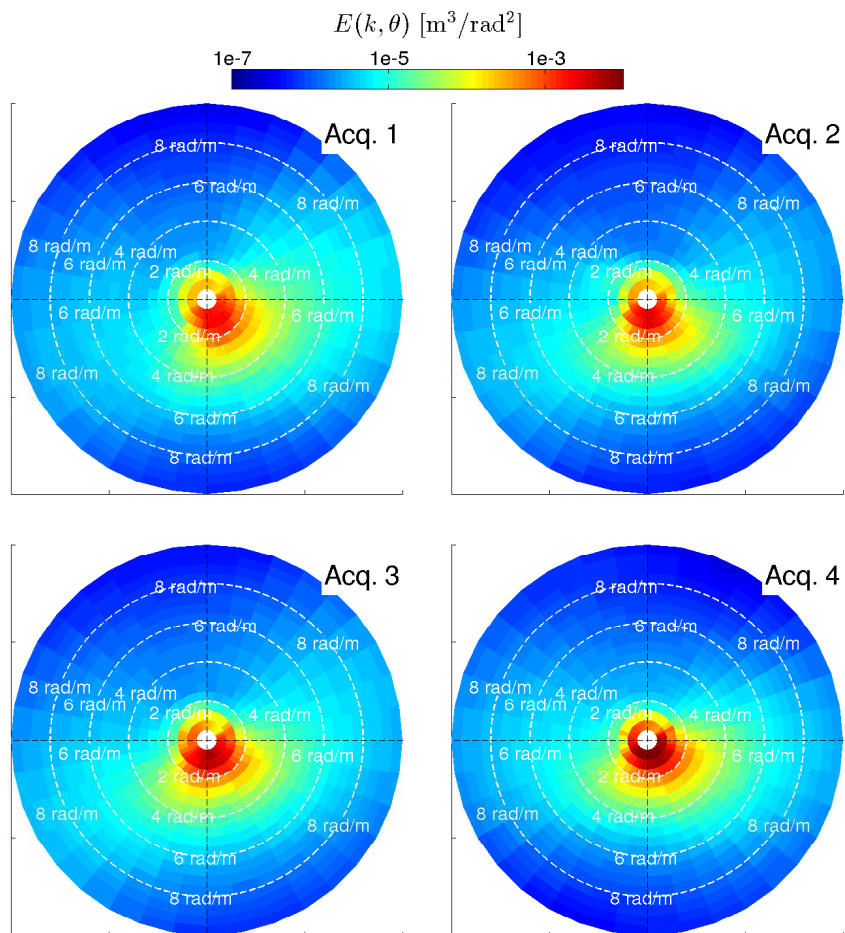


Figure 3.27: Wavenumber spectra obtained with the integration over positive frequencies of the 3D spectra presented on the figures 3.21-3.24. The obtained wavenumber spectrum $E(k, \theta)$ is so unambiguous in direction.

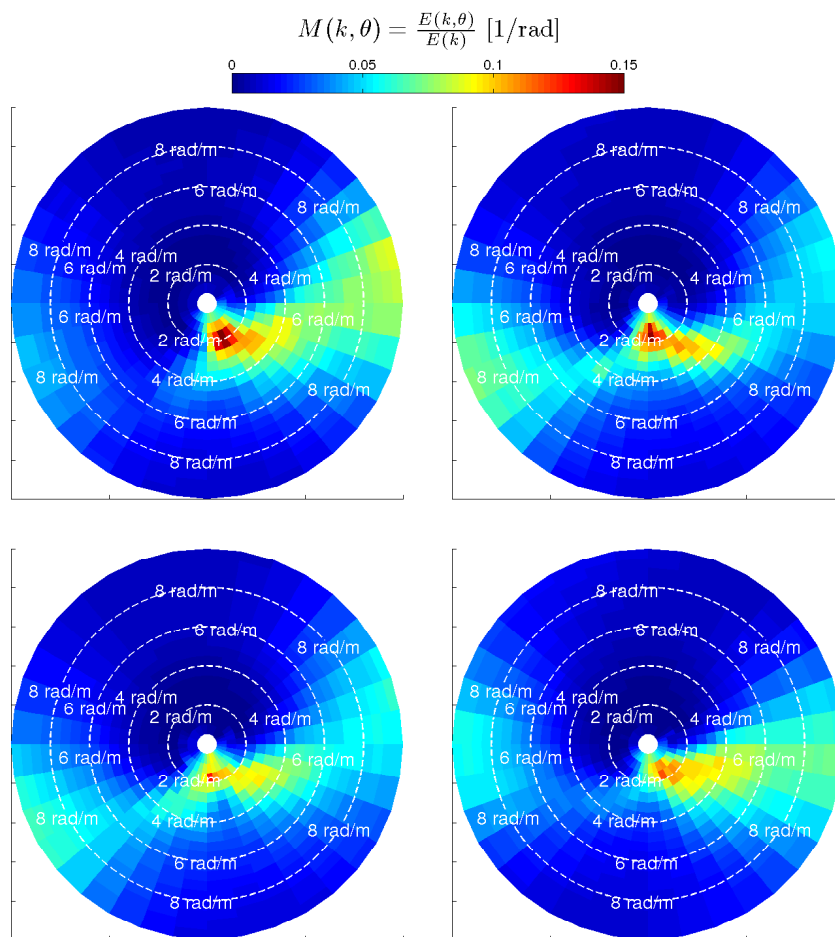


Figure 3.28: Directional spreading (Eq. 3.6.4) computed from the spectra presented in figure 3.27.

a near isotropic spreading) at the wave frequency of 1Hz. Our observations clearly show a non isotropic spreading up to 1.6Hz.

3.6.5 Mean Square Slopes of elevation maps

Another interesting parameter generally observed is the Mean Square Slopes (hereinafter *mss*). As the whole range of wave scale is not given by the reconstruction, the standard comparison with the *mss* computed from sunlight reflection by Cox and Munk (1954) cannot be done directly. However, Vandemark et al. (2004) proposed to add the $mss_{<1m} = 0.019 \ln(U_{10})$ to 1m-*mss*. At each point (x, y, t) of the elevation maps, the slope s_x and s_y are computed mss_x and mss_y are so computed with

$$s_{x,>1m}(x, y, t) = (Z(x - 0.5, y, t) - Z(x + 0.5, y, t)) / 1 \quad (3.86)$$

$$s_{y,>1m}(x, y, t) = (Z(x, y - 0.5, t) - Z(x, y + 0.5, t)) / 1. \quad (3.87)$$

Therefore, 1m-*mss* is given with

$$mss_{x,>1m}(x, y) = \frac{1}{T} \int_0^T s_x^2(x, y, t) dt \quad (3.88)$$

$$mss_{y,>1m}(x, y) = \frac{1}{T} \int_0^T s_y^2(x, y, t) dt \quad (3.89)$$

$$mss_{>1m}(x, y) = mss_x(x, y) + mss_y(x, y) \quad (3.90)$$

The figure 3.30 shows the slope variance mss_{1m} (left panels), and the slope variance along x -axis, $mss_{x,1m}$ (center panels) and y -axis, $mss_{y,1m}$ (right panels) for each acquisition. We note that the spatial disparity of the *mss* over the reconstructed area does not have a physical sense. In particular, the inhomogeneous mss_y obtained for acquisition 4 is linked to the errors in the matching processing due to inhomogeneous illumination of the sea surface. The spatial-averaged mss_{1m} are respectively 0.65%, 0.55%, 0.84% and 0.97 for the four acquisitions. Then, the *mss* given by the smaller scales than 1m are added following Vandemark et al. (2004) with $mss = mss_{>1m} + mss_{<1m}$. To a function of the wind speed, 11.5m/s, 10.9m/s, 13.2m/s and 13.9m/s, the *mss* are 5.29%, 5.09%, 5.74.% and 5.87%, where Cox and Munk (1954)'s formula gives respectively 6.19%, 5.88%, 7.06% and 7.42%, with a standard deviation estimated to 0.004. Our *mss* are strongly under the Cox and Munk (1954)'s ones. However, note that the acquisitions correspond to young wave field, and Vandemark et al. (2004) show that *mss* given by wave scale greater than 1m wavelength, here not fully developed, strongly influence the global *mss*.

3.7 Conclusion

The existing methods of sea surface reconstruction provide good results in term of sea elevation statistics and spectra. Nevertheless, it was shown that the presence of foam patches on the sea surface strongly disturbs the local shape of the surface. Particularly, these methods provide unrealistic breaking wave shapes. In this chapter, a complete method for the reconstruction of sea surface in presence of foam patches is proposed

and validated. Compared to the existing reconstruction methods, the main improvement concerns the matching point processing. The implementation of an iterative corresponding point search with a correlation template which size decreases with increasing iteration greatly increases the accuracy of the reconstructed surface, particularly in the presence of foam patches. A correction for the asymmetric projection is also proposed.

Four stereo video acquisitions are investigated. A first validation of the reconstructed surfaces obtained with the improved method is given by comparison with wave gauge data. Then the observation of the 3D direction-wavenumber-frequency spectra obtained from the time-space evolution of the surface shows the coherence of the surfaces up to $f = 1.6\text{Hz}$ ($\lambda \approx 60\text{cm}$). The observed directional wavenumber spectra directly computed over the elevation maps and the directional frequency spectra computed over extraction of several times series are also discussed. Finally, the mean square slope are computed and compared to the classical observations by Cox and Munk (1954). After the validation provided, the reconstructed sea surfaces are considered accurate enough to be used in the breaking wave study proposed in the next chapter.

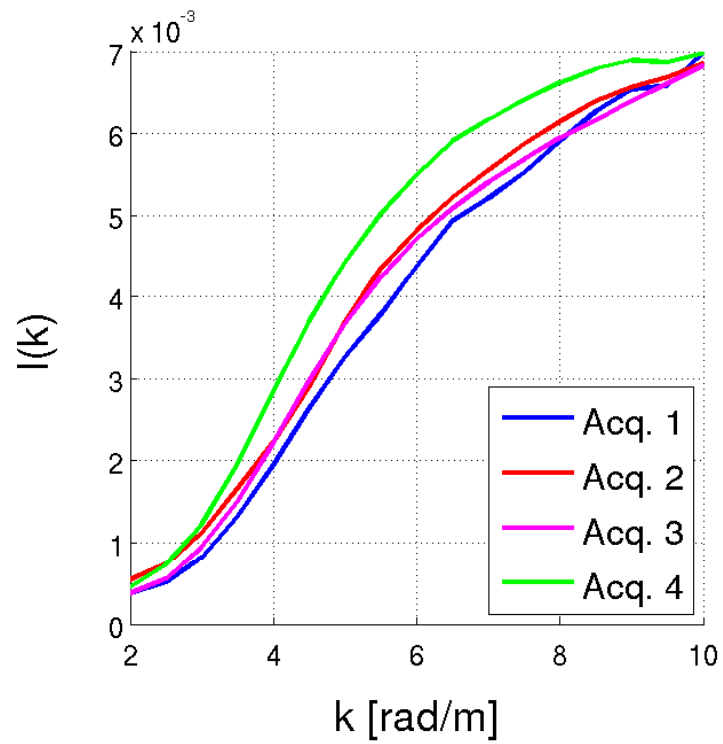


Figure 3.29: Spreading integral (Eq. 3.85) computed from the directional spreading presented in figure 3.28.

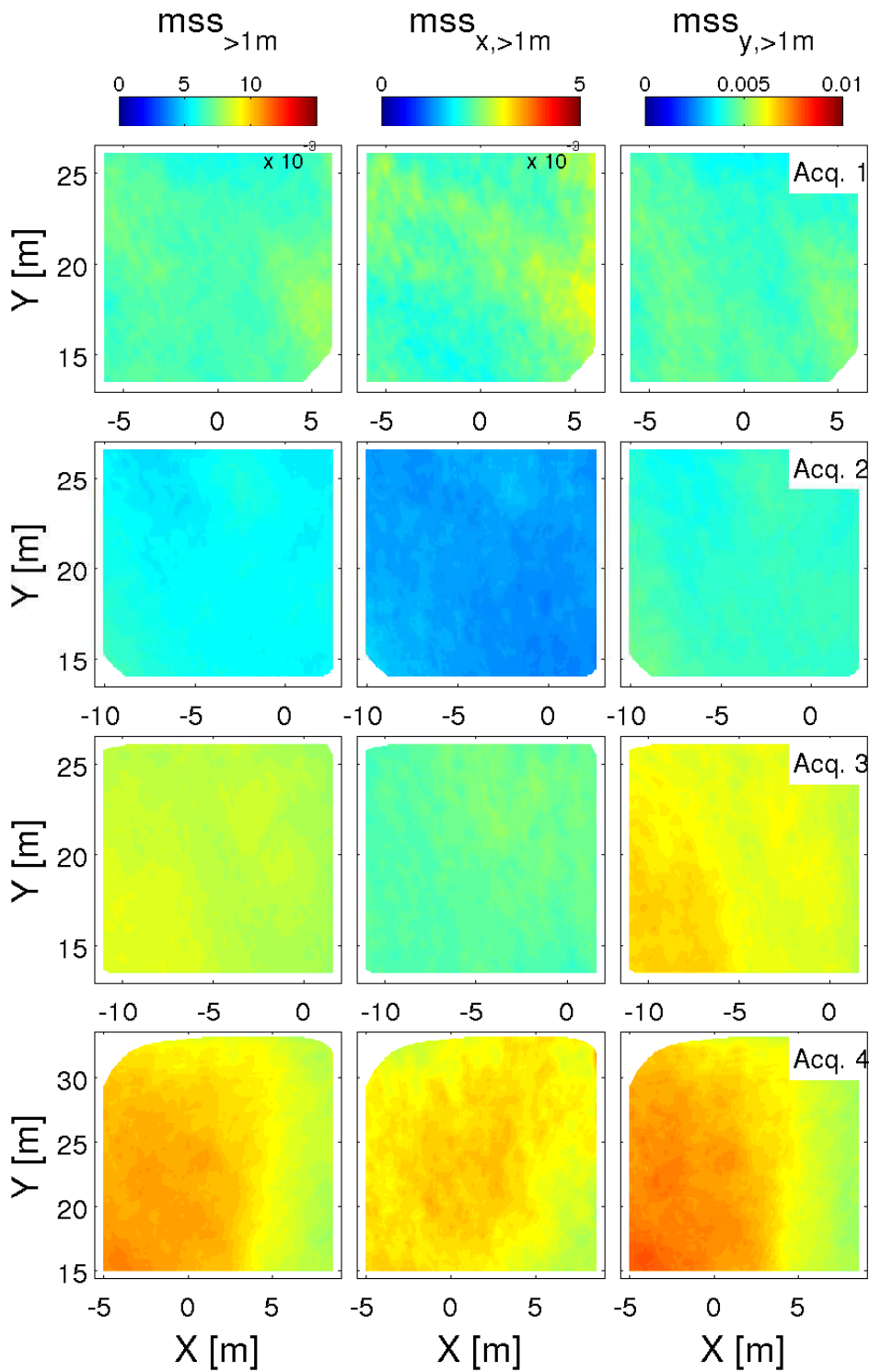


Figure 3.30: Mean Square Slope given by waves longer than 1m computed over the whole set of images for the 4 acquisitions. $mss_{>1m}$ is the global slope variance (left panels), $mss_{>1m}$ is the slope variance along x -axis (center panels) and $mss_{>1m}$ is the slope variance along y -axis (right panels).

Chapter 4

Observation of breaking waves

4.1 Introduction

Breaking waves occur everywhere on the world's oceans and affect almost all sea surfaces. Today, the breaking phenomena are still misunderstood. Nevertheless, it is clear that breaking is the dominant process for wind wave energy dissipation. Therefore, a good understanding of wave breaking is necessary to understand wave energy balances and wave spectra characteristics. Moreover, breaking waves also influence many processes. Inducing a turbulence increasing in the upper sea layer and an active air entrainment into water, they play an important role in air-sea gas transfers and biochemical processes. Wave breaking process is also associated to the production of sea sprays. In addition, the breaking-induced foam strongly influences many ocean electromagnetic measurements. In particular, whitecaps increase surface reflectance in visible frequencies and strongly impact on radar backscattered signal and brightness temperatures measured by radiometers, such as those used on Windsat, SMOS and Aquarius. Thus, the whitecap coverage variability must be taken into consideration for the sea surface albedo or ocean color estimations, but also for retrieving sea surface properties. These electromagnetic properties are used in this work to detect breaking wave in visible spectrum range. Indeed, generated white foam areas contrast with a dark sea surface, and are easily observable signatures of the breaking waves.

Wave breaking is a complex non-linear process with various intense physical phenomena in it. Different terminology can be found in the literature to describe evolution of breaking waves. Wave breaking event is usually decomposed into two parts. The first one is the active breaking usually called stage A (Bondur and Sharkov, 1982; Monahan and Woolf, 1989). It results from an instability which develops from the wave crest, when water particle velocities approach the wave phase speed (Longuet-Higgins, 1978; Longuet-Higgins and Fox, 1978; Tanaka, 1983, 1985). The wave crest thus collapses on the front size of the wave, resulting in wave energy dissipation. The breaking phenomenon occurs at all wave scales once they are energetic enough.

For waves shorter than one meter in wavelength, breaking occurs without air entrainment, and so without signature in the visible spectrum range. Nevertheless, laboratory measurements of Jessup et al. (1997) show that microscale wave breaking associated with evolving wind waves disturbs the thermal boundary layer at the air-water interface,

producing signatures that can be detected with infrared imagery. Their laboratory observations, under the moderate wind speed conditions, showed a substantial frequency of occurrence and an important areal coverage of the phenomenon. Therefore, microscale breaking is undoubtedly widespread over the oceans and may prove to be a significant mechanism for enhancing the transfer of heat and gas across the air-sea interface (Jessup and Phadnis, 2005; Sutherland and Melville, 2013). These microwave scales are not resolved in the global ocean spectral wave model, and microwave breaking is not studied in this work.

The present thesis focuses on longer breaking waves as modeled in spectral wave models. These waves, more energetic, are attended with air entrainment and bubble formation. Formation of foam needs a large quantity of energy, corresponding to the surface tension multiplied with surface excess. Thus, when breaking waves are energetic enough, they generate white bubble clouds which form whitecaps that contrast with the darker sea surface. This signature in the visible frequency spectrum makes the phenomenon easily observable.

Persistence of the foam on sea surface in the wake of the breaking wave is usually referred as stage B of the breaking, also called passive breaking. Passive foam, in contrast with active foam produced by active crest breaking, does not imply wave dissipation. Nevertheless, the lifetime of the foam persistence is of interest to many investigators due to the previously discussed strong influence on electromagnetic measurements and air-sea gas exchanges. Foam lifetime has been related to environmental and meteorological parameters, including air-sea temperature difference, salinity or even biological content, which directly influence surface tension. Focusing on whitecap dissipation, this work does not investigate the passive breaking.

Despite wave breaking being an important phenomenon with many authors interested in this subject, it is still misunderstood for many reasons. Wave breaking is generally studied with laboratory or field measurements. Laboratory measurement provides very interesting and complete data. Indeed, experimental tanks are manageable environment where a complete instrumentation can be easily deployed. Moreover, laboratory experiments allow a quasi complete control of the various factors which influence wave breaking, and thus provide reproducible experiments in well defined conditions. Numerous laboratory experiments have quantified the breaking occurrence and the wave dissipation. However, these experiments fail to reproduce all the conditions observed *in situ*. Indeed, wave age have a strong influence on breaking ; for young wind-sea, intensive breaking is observed around a spectral peak whereas breaking seems to be absent at the peak wave scale for mature sea ($C_p/U_{10} \simeq 1$), and whitecaps are observed on smaller wave scales. Tank experiments succeed in reproducing very young wind sea (with wave age C_p/U_{10} less than 0.15), but fail to reproduce more developed sea due to limited fetches (Donelan et al., 1993). However, *in situ* measurements sample a wave age from 0.2 for young sea to 0.83 for fully developed wave field. These considerations make the results obtained in laboratory difficult to apply in the wave models. In contrast, field measurements deal with real external conditions. But such investigations also have their limits. Firstly, the deployment of complex measuring equipment is difficult in real sea condition. Secondly, the large number of non manageable external parameters makes experiments non reproducible and results difficult to analyze. Here again, application of observation results to

model parameterization seems difficult, due to dependence of results to very particular conditions.

Two approaches are usually used to study breaking in field measurements. Generated white foam areas contrasting with the dark sea surface, breaking wave can be easily detected on photo (Monahan et al., 1983; Stramska and Petelski, 2003; Callaghan et al., 2008) or on image sequences from video camera (Melville and Matusov, 2002; Mironov and Dulov, 2008). Various acoustic methods can also be used to measure breaking intensity. On one hand, breaking wave characteristics can be retrieved from reflection of the acoustic sonar signal on breaking wave (Loewen and Melville, 1991). On the other hand, sound produced by breaker crest collapsing can be measured using hydrophones (Babanin et al., 2001). This last method provides direct information on the occurrence and intensity of breaking, but is not able to define neither precise location of the breaking nor breaking direction. In contrast, optical methods based on breaking foam detection at sea surface, are generally used to investigate shape, speed, direction and other characteristics of the breaking waves. Nevertheless results are strongly dependent on the threshold used for foam patch detection and on the discrimination of stage A and B.

In this study, an optical system is used. As in majority of the optical methods published in the literature, foam patches of breaking waves are here detected using a threshold method. In large number of studies, the threshold is defined by the investigator. These methods have two main disadvantages. Firstly, results depend on the investigator subjectivity. Secondly, these methods are difficult to apply automatically on different data sets. Discrimination of phases A (active breaking) and stage B (passive foam) is also problematic. Many studies proposed a discrimination using two different thresholds. Active breaking entrains air into water, and so actively produce new bubbles, associated with brighter foam. Passive foam corresponds to the decreasing of the foam density and is related to darker foam. Therefore, high level selects bright whitecaps and marks them as active breaking, whereas a lower value discriminates passive foam. Results of whitecap measurements vary in different works; often, the problem of threshold selection is among the causes of such variations (Mironov and Dulov, 2008).

Mironov and Dulov (2008) developed a processing algorithm to define threshold and discriminates stage A and B based on physical prerequisites and statistical properties of the studied phenomenon that maximally eliminates human influence, and so that can be applied in a same way on different data sets. They applied their processing on large data set, providing very interesting speed and direction distribution. Nevertheless, their study does not include the elevation of the surface and shape of breaking waves. Indeed, using only one camera, they linked pixel coordinates to sea surface coordinates by a simple projection on the mean sea plane, losing sea surface elevation information. Originality of the present work is that, using surface stereo reconstruction discussed in previous chapter, the breaking waves are observed together with sea surface elevation maps, providing an alternative source of information.

The vast majority of the wave breaking studies discuss the breaking probability. On the classical 1D studies, the breaking probability P_b is defined with

$$P_b = \frac{N_b}{N_w}, \quad (4.1)$$

where N_b is the number of breaking waves and N_w is the total number of waves. In an elevation time series, the individual waves are generally defined between successive points where the water surface crosses downwards (zero down-crossing) or upwards (zero up-crossing) the mean water level. For each individual wave, the period is the time lag separating the two zero down-crossing (or up-crossing) and the height is the difference between minimum and maximum elevation. This wave-by-wave analysis is applied for the study of the dominant wave breaking (Banner et al., 1989). By construction, this analysis can be applied to the study of the smaller waves, which may be riding on the crest of the large waves (Banner et al., 2002). Nevertheless, this wave counting method can be applied to frequency filtered elevation time-series to analyze breaking of smaller wave scales (Banner et al., 2000; Babanin et al., 2001; Filipot et al., 2010). The difficulty is to choose a frequency bandwidth narrow enough in order to discriminate the energy of waves with different frequencies but also large enough so that the filtered surface has a representative steepness. Indeed, the narrower bandwidth, reduced to a unique frequency would lead to a small monochromatic wave not representative of the observed surface elevation. Banner et al. (2000) and Babanin et al. (2001) assumed that the components contributing to the dominant waves were contained between $(1 - \delta_{\text{BBY}})f_p$ and $(1 + \delta_{\text{BBY}})f_p$, with $\delta_{\text{BBY}} = 0.3$. For deep water waves, this frequency interval corresponds to wavenumbers from $0.5k_p$ to $1.7k_p$. Further, Filipot et al. (2010) re-use this frequency bandwidth for their wave-scaled analysis of breaking.

As disused in the chapter 2, these breaking probabilities were then related to the spectrum saturation (Banner et al., 2002), leading to the breaking parameterization of Ardhuin et al. (2010) (TEST451) or to the wave steepness (Filipot et al., 2010), leading to the breaking parameterization of Filipot and Ardhuin (2012) (TEST500), improved to TEST570 (see chapter 2). The work presented here proposed a comparison of our observations with these two parameterization of breaking probability and a critical analysis of the assumptions used in the breaking parameterizations. Indeed, it must be noted that in the wave model, the assumption is made for the length of crest calculation, and so for the cumulative effect estimation, that the breaking probability thus calculated can be applied on the wave crest (breaking or not) length density to obtain the breaking crest length density. Another severe assumption is made for the definition of the wave crest length density.

The breaking detection processing used in this work, greatly inspired from the algorithm of Mironov and Dulov (2008), is described in the section 4.2, with a description of the results in terms of speed and direction distributions of the detected breaking. The next section (4.3) discussed a definition of the crest length density. Then, observed breaking probabilities are shown in section 4.4. These observations are compared to the model of Filipot et al. (2010) used in the parameterization of Filipot and Ardhuin (2012) in the section 4.5, then rely to the partially integrated saturation spectrum used in the parameterization of Ardhuin et al. (2010) in the section 4.6. The conclusion follows in the last section.

4.2 Automatic detection of breaking events

Detection of breaking events used for this study is now described. The processed image parts of the 4 records correspond to the reconstruction areas shown on figure 3.16. The process is split into two steps. First step consists in removing of all unnecessary information not connected with breaking wave properties, to simplify processing. An evident way of such simplification is binarization of whitecaps from the sea surface video records using brightness threshold criterion (Mironov and Dulov, 2008). A binary data array with only whitecap information is the result of this procedure. The main difficulty of this step is the selection of the threshold which discriminates foam patches. The method of Mironov and Dulov (2008) is used here, as described in section 4.2.1. Second step consists in the discrimination of the binarized foam patches into active and passive foam. This second step is also adapted from works of Mironov and Dulov (2008). Using physical properties, the binarized data are then discriminated into active and passive foam. The discrimination is described in section 4.2.2. The automatic detection of breaking events is applied to the four acquisition already described in the chapter 3 (see §3.2, Tab. 3.1).

4.2.1 Image binarization

Pixel brightness arises from various parameters. Basically, brightness levels depend on the position of the Sun and sea surface slope. Nevertheless, many other parameters can strongly influence it: the presence of clouds, the sky reflection and air scattering and absorption (which is a problem in airborne imagery. Note that in our case, there can also be a strong reflection from the coastal mountains. Moreover, the automatic gain adjustment also affects pixel brightness. Finally, the presence of foam on the sea surface also strongly increases brightness level. The aim of the present algorithm is to define a threshold which discriminates high pixel brightness level due to presence of foam.

Long-lasting brightness removing

Mironov and Dulov (2008) proposed an algorithm, independent of human influence and based on physical principles of brightness field formation, which ensures satisfactory threshold for such a wide range of conditions. Brightness variance at a fixed point of sea surface, I , is the sum of an instant brightness, I_g , due to surface slope and of a long-lasting brightness component, I_{avg} , resulting from background conditions. Generally, the values of I_{avg} widely vary on the frame, making the selection of a common threshold impossible. The first step so consists in the removing of this brightness trend. This trend is evaluated by averaging a sequence of consecutive images. In this work, average is done over 2000 images, corresponding to about 2.2 min sequence for the 15 Hz acquisition 1 and 2.7 min sequence for the 12 Hz acquisitions 2, 3, and 4. The evolution of the automatic gain is smoothed, and the gain is assumed constant during the averaged image sequence. Spatial brightness distribution permanently evolves along the frame (sun displacement, cloud moving, ...) and I_{avg} is computed for every 2000 image sequence of the record. Then, all brightness trends and heterogeneity can be removed by the subtraction of the calculated I_{avg} values from each frame of the processed video record.

On the figure 4.1, the panel A shows the original 1028th image, I_{1028} , of the 4th acquisition and the panel B is the corresponding long-lasting brightness component, I_{avg} , given by the average of the first 2000 images :

$$I_{\text{avg}} = \frac{1}{2000} \sum_{i=0}^{1999} I_i \quad (4.2)$$

Therefore, I_{avg} corresponds to the brightness obtained with a flat horizontal sea surface.

The panel C (= panel A - panel B) is then the instant brightness $I_g = I - I_{\text{avg}}$, supposed to be due only to sea surface slopes ζ_x and ζ_y , respectively in x and y direction, such that :

$$I_g = c_x \zeta_x + c_y \zeta_y. \quad (4.3)$$

With x -axis and y -axis respectively along and across wind direction, ζ_x and ζ_y are independent, with a normal distribution (Cox and Munk, 1954) :

$$p(\zeta_x) = \frac{1}{\sqrt{2\pi}\sigma_x} \exp\left(-\frac{\zeta_x^2}{2\sigma_x^2}\right) \quad (4.4)$$

$$p(\zeta_y) = \frac{1}{\sqrt{2\pi}\sigma_y} \exp\left(-\frac{\zeta_y^2}{2\sigma_y^2}\right), \quad (4.5)$$

where σ_x and σ_y are surface slope variance in each direction. Therefore, defining $\sigma_I^2 = c_x^2 \sigma_x^2 + c_y^2 \sigma_y^2$, it follows that distribution of I_g is close to Gaussian :

$$p(I) = \frac{1}{\sqrt{2\pi}\sigma_I} \exp\left(-\frac{I^2}{2\sigma_I^2}\right), \quad (4.6)$$

if c_x and c_y are constant. In a strict physical sense, c_x and c_y depend on viewing and sun angles. Mironov and Dulov (2008) proposed to neglect spatial variation of c_x and c_y , due to variation of viewing angle in the whole frame. Nevertheless, they avoid variation of sun angles by computing σ_I values for short record segments. Compared to their study, the image part processed here is smaller so the variations of the viewing angles (i.e. spacial variation of c_x and c_y are also smaller). Nevertheless, σ_I is here computed over the whole record.

Threshold finding algorithm and data binarization

First, for each acquisition, the observed $p(I)$ (blue solid thin lines on figure 4.2) are computed for the positive values I_g using the whole whole set of trend-free image. Following Mironov and Dulov (2008), we now define the probability function F of excess of the brightness I (green solid thick line on the figure 4.2) with

$$F(I) = \int_I^{\infty} p(I') dI'. \quad (4.7)$$

In absence of foam patches (i.e. brightness I only depends on sea surface slope), the normal brightness distribution F_0 meets the relation

$$F(I) = \frac{1 - \text{erf}(Y)}{2}, \quad (4.8)$$

where erf is the error function defined as

$$\operatorname{erf}(Y) = \frac{2}{\sqrt{\pi}} \int_0^Y \exp(-t^2) dt, \quad (4.9)$$

and

$$Y = \frac{I_g - I_m}{\sqrt{I} \sigma_I}, \quad (4.10)$$

with I_m a likely average error. Therefore, defining erf^{-1} as the inverse function of erf, it follows

$$Y(I) = \operatorname{erf}^{-1}(1 - 2F(I)). \quad (4.11)$$

Note that for a normal distribution $F_0(I)$, $Y_0(I) = \operatorname{erf}^{-1}(1 - 2F_0(I))$ must be linear. Using observed distribution $F(I)$, this linearity is found only for low brightness values, but is strongly disturbed for higher brightness values due to presence of the bright foam patches. The Y_0 function is fitted on the low brightness value part of $Y(I)$ and is linearly extrapolated to higher brightness. Then, the extrapolated normal distribution F_0 (i.e. the presumed distribution in absence of foam patches, the red dashed line on the figure 4.2) is obtained with equation 4.8 applied on Y_0 . Further, the threshold I_T is get when observed distribution $F(I)$ becomes 10 times higher than the normal distribution $F_0(I)$. The thresholds found with this method are marked with blue crosses on the figure 4.2. Finally, data are binarized in the reconstruction areas (panel D of the figure 4.1) with

$$M(u, v) = \begin{cases} 1 & \text{if } I_g(u, v) \geq I_T \\ 0 & \text{if } I_g(u, v) < I_T, \end{cases} \quad (4.12)$$

such that $M(u, v) = 1$ corresponds to the pixel (u, v) is detected as abnormal too white point and so considered as foam point. Visual check shows that all the active whitecaps are well detected. Note that the points where the sun light reflects onto the camera, called specular points, are also detected as foam points by the method and must be removed in the next step. A few points corresponding the right part of the Gaussian distribution can also be detected as foam. Using the reconstructed 3D surfaces, it should be possible to compute a threshold depending on the slope. Such an improved method could reduce the number of the detected points corresponding to the right part of the Gaussian distribution and not to foam. A visual check shows that part of the passive foam is not detected.

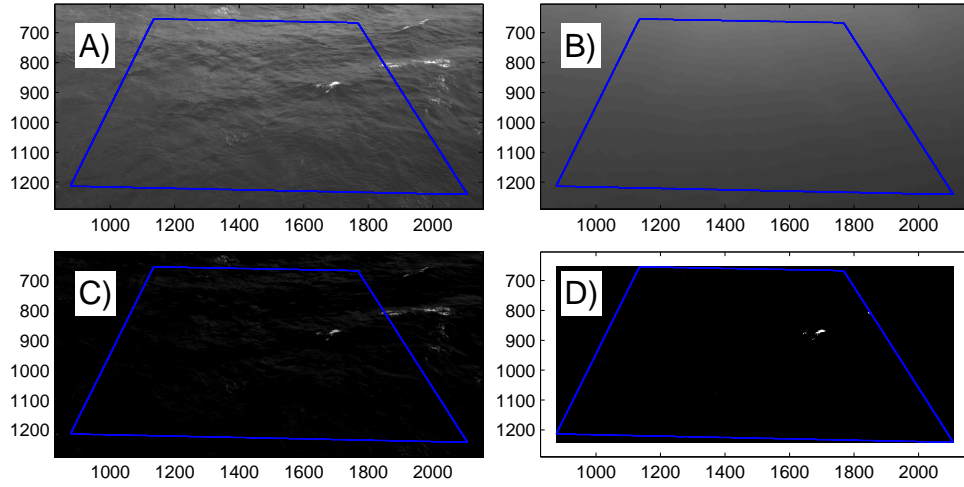


Figure 4.1: A) Image 001028 of acquisition 4 (I). B) Long-lasting brightness component (I_{avg}) resulting from background conditions. C) Instant brightness ($I_g = I - I_{\text{avg}}$) due to surface slope. D) Binarized Images ($I_g > T$).

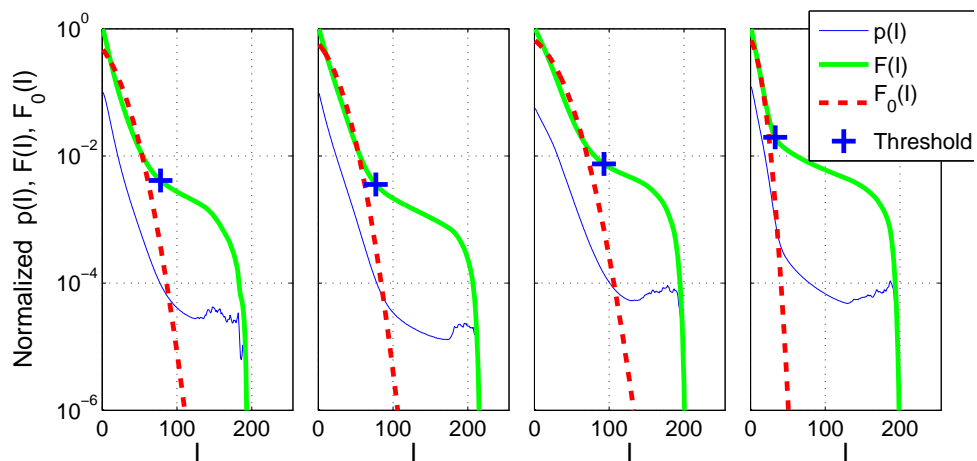


Figure 4.2: Brightness variance distribution and probability function obtained for the 4 acquisitions. The blue solid thin line corresponds to the observed $p(I)$ function. The green solid thick line is its corresponding $F(I)$ function. The red dashed line corresponds to $F_0(I)$. The computed threshold value I_T is marked with a blue cross.

4.2.2 Event filtering method

For each acquisition, binarized data are organized in a large 3D binary matrix $M = M(u, v, f)$ where u and v are pixel coordinates in reconstruction area and f is the frame number. The foam points directly connected in time and connected in space within a length of 10 pixels are grouped. Generally, the set of foam points in each group includes active and passive foam, but also mirror points which must be discriminated. High sunglint on wave crest can also imply additional white point detection. This problem is difficult to resolve because corresponding detected white points follow the wave evolution and so have dynamic properties very close to breaking detected white points. To avoid this problem, the processed image areas have been chosen in the image part dark enough to visually distinguish the breaking. However, specular points can appear in the reconstruction areas. These points have short lifetime and a small area. The acquisition time was chosen so that most of the specular points are in the lower part of the image, where they disturb only small number of connected pixel. These points are removed by a filtering of smallest white point groups in time and space. Typically, groups which contain less than 200 white points, or which time duration is less than 0.4 seconds are removed. All non-removed white points are now called foam points. Note that this filtering also removed small breaking event. Nevertheless, the reconstructed surface resolution is also not adapted, due to insufficient pixel resolution, to study the small events. Higher pixel resolution and/or using of zoom lenses should allow for smaller breaking event study.

As stated in the introduction, many investigators discriminate active foam by brighter pixels. In this work, a discrimination algorithm based on physical properties, inspired from work of Mironov and Dulov (2008), is implemented. Focusing on active breaking and wave dissipation, the present algorithm is adjusted to mainly detect the start of the breaking event, and as far as possible the complete active breaking. Each foam point group is the analyzed separately.

The group is first analyzed in the pixel-frame reference system. Let's note $M_i(u, v, f)$ the binary sub-matrix containing the foam points of group i . The time evolution of number of foam points $N_i(f)$ is first computed with

$$N_i(f) = \sum_u \sum_v M_i(u, v, f). \quad (4.13)$$

The sea surface footprint of pixels depends on both surface shape and coordinates of the pixel on the image. Nevertheless, foam pixels of a same group stretch on a small and localized image part. Therefore, the time evolution of pixel number $N_i(f)$ is in first approximation assimilated to the time evolution of foam patch surface. Active breaking actively produces new bubbles, faster than passive foam disappears. Typically, $N_i(f)$ increases to a maximum during active wave breaking and then decreases as a function of the foam lifetime. However, a new active breaking can occur in the same zone, before the residual foam of the previous one completely disappears. In this case, the two active breaking events are contained in the same group, and must be split. If the second breaking wave is not too small compared to the first one, it implies a second increase of $N_i(f)$ and so can be detected. In practice, each group is split into independent events such that previous an event ends when its number of foam points N becomes smaller than 25% of its maximum and a new event starts further if N becomes higher by 25% of the previous

minimum of N (since the defined end of previous event), and so on. Each separated event is then processed separately. Again, short events are removed.

For each active breaking event, the foam points are then projected on the 3D surfaces to obtain the set of N_{pt} 4D surface foam point $P_j = (x_j, y_j, z_j, t_j)$, with $t = f/\text{fps}$. Therefore, speed in each direction of the point set is computed as the least square solution of

$$x_1 - \bar{x} = V_x(t_1 - \bar{t}) \quad (4.14)$$

$$y_1 - \bar{y} = V_y(t_1 - \bar{t}) \quad (4.15)$$

$$\vdots \quad (4.16)$$

$$x_j - \bar{x} = V_x(t_1 - \bar{t}) \quad (4.17)$$

$$y_j - \bar{y} = V_y(t_1 - \bar{t}) \quad (4.18)$$

$$\vdots \quad (4.19)$$

$$x_{N_{\text{pt}}} - \bar{x} = V_x(t_1 - \bar{t}) \quad (4.20)$$

$$y_{N_{\text{pt}}} - \bar{y} = V_y(t_1 - \bar{t}), \quad (4.21)$$

with

$$\bar{X} = \frac{1}{N_{\text{pt}}} \sum_{j=1}^{N_{\text{pt}}} X_j. \quad (4.22)$$

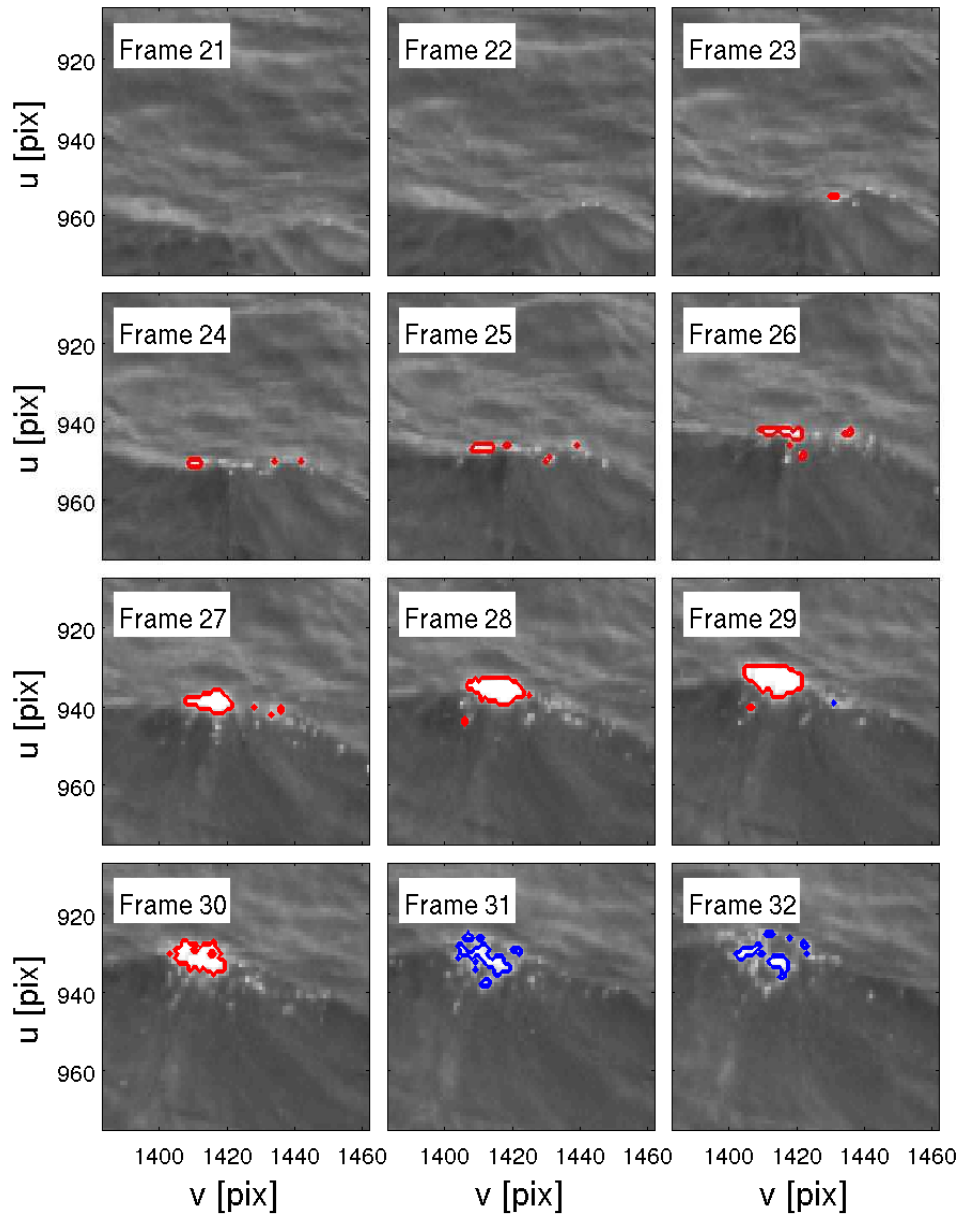


Figure 4.3: Example 1: 1st detected active breaking event on acquisition 1. The blue contours are white patches detected by threshold method. The red contour is the filtered active breaking.

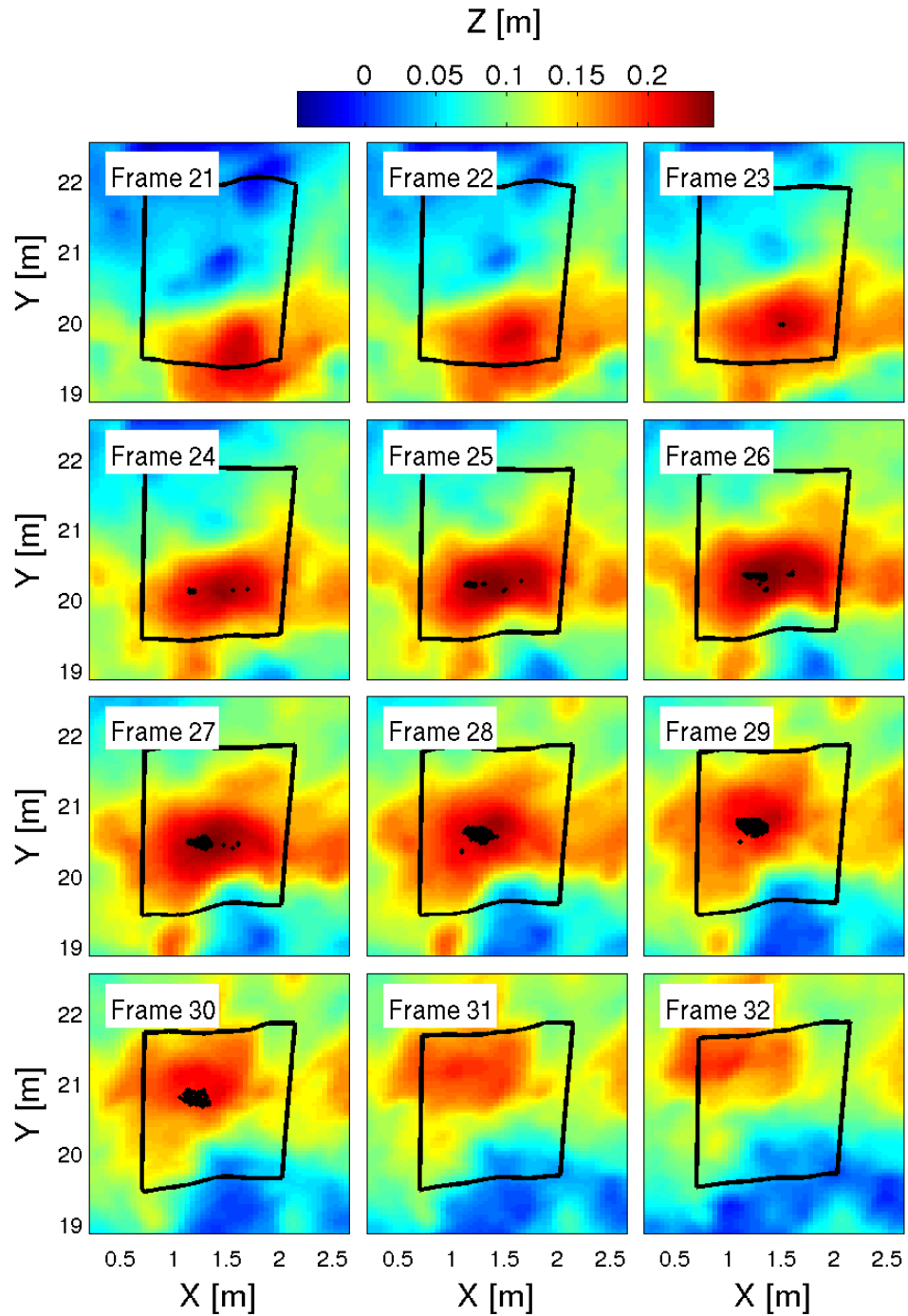


Figure 4.4: Example 1: 1st detected active breaking event on acquisition 1. The black points correspond to the projection of the active foam points (red contour of the figure 4.3) on 3D surfaces. Black contours are the footprint of the images shown on figure 4.3.

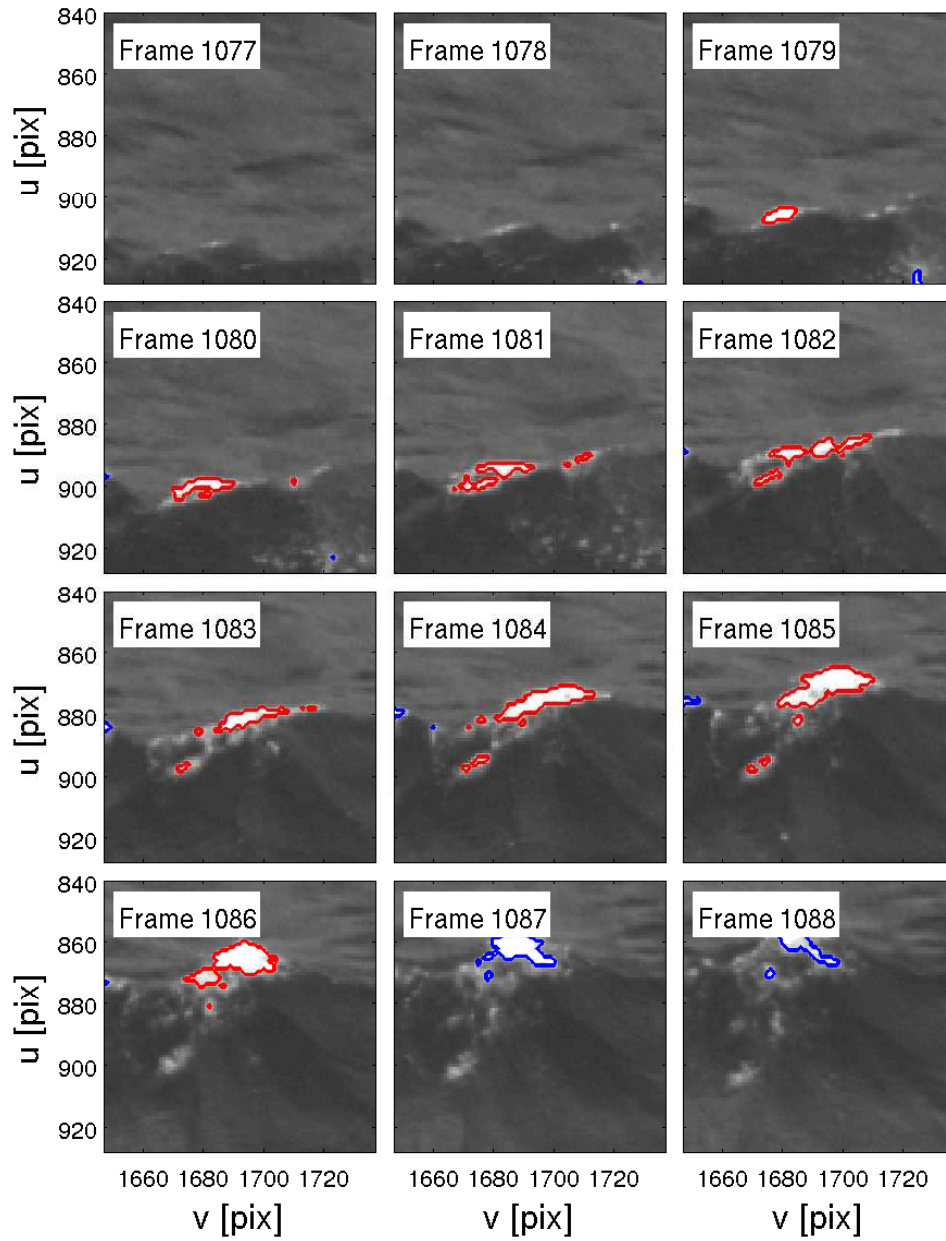


Figure 4.5: Example 2: 54th detected active breaking event on acquisition 4. The blue contours are white patches detected by threshold method. The red contour is the filtered active breaking.

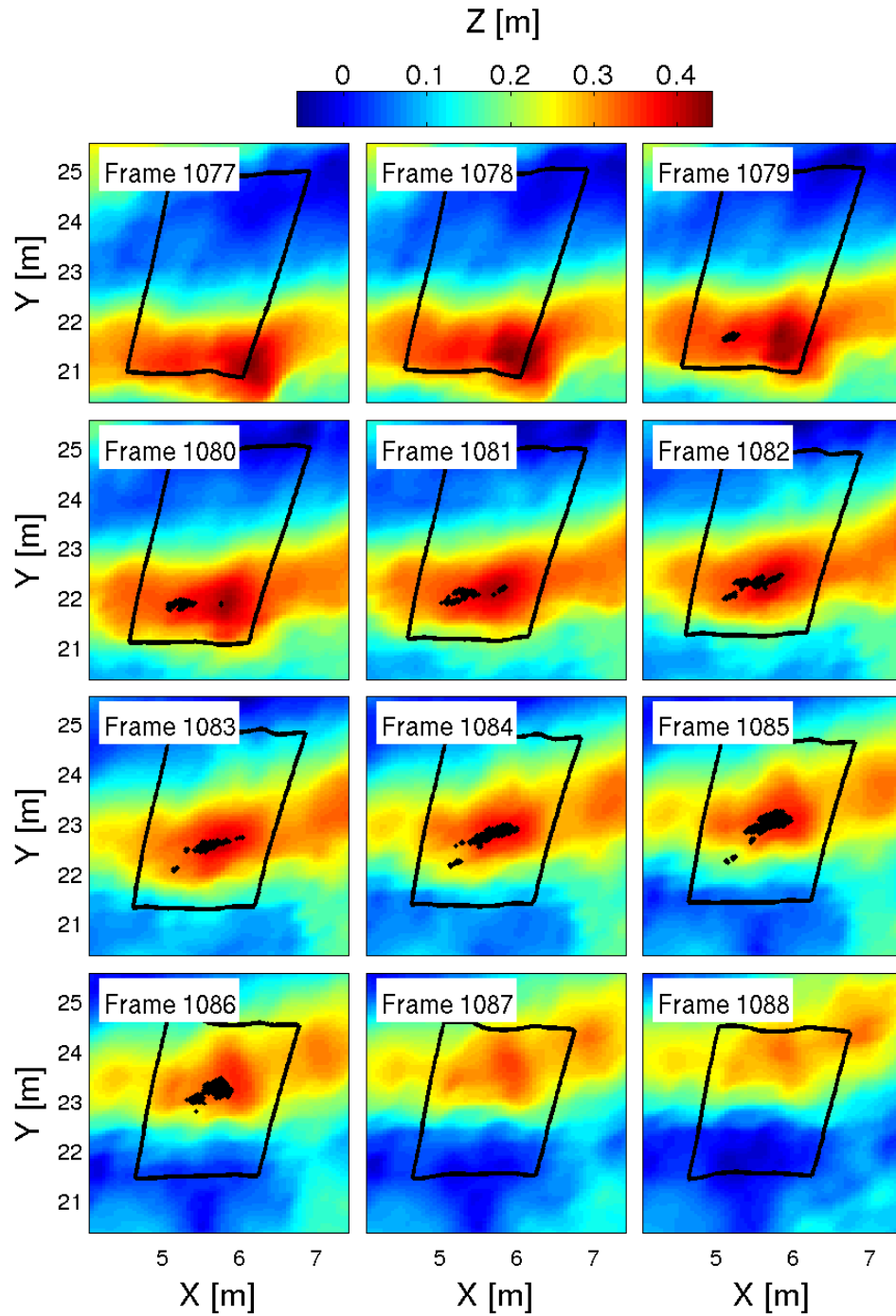


Figure 4.6: Example 2: 54th detected active breaking event on acquisition 4. The black points correspond to the projection of the active foam points (red contour of the figure 4.5) on 3D surfaces. Black contours are the footprint of the images shown on figure 4.5.

Therefore, absolute speed and direction are

$$V_b = \sqrt{V_x^2 + V_y^2} \quad (4.23)$$

$$\theta_b = \arctan\left(\frac{V_y}{V_x}\right). \quad (4.24)$$

Visual observations of breaking waves show that active breaking foam move around the main direction of wind surface waves and passive foam drift on a sea surface with rather slow velocity modulated by orbital velocities of the surface waves. Therefore, all events with computed speed less than 1m/s are assimilated to small events or passive foam and are removed. The figures 4.3 and 4.5 show two examples of detected active breaking events on images. The figure 4.4 and 4.6 show their respective projection on 3D surfaces.

With this algorithm, 276, 795, 1669 and 1390 active breaking events are respectively found for the 4 acquisitions. The probability density functions of breaking waves to breaking speed and directions are respectively shown on the figures 4.7 and 4.8. The observations show a maximum in the breaking speed distribution, which could be related to the maximum of the Λ -distribution observed by Gemmrich et al. (2008) and Thomson and Jessup (2008). The maximum seems to move to the higher breaking speeds with wind speed increasing. The breaking wave direction distribution show a Gaussian centered on the wind direction, in line with the observations of Mironov and Dulov (2008). The 2D probability density function of breaking to breaking speeds and directions is given on figure 4.9.

4.3 Crest length density

We define wave crest as the locations where one slope component is zero, with a negative curvature. In other words, the crests are defined by the points such that ($dz/dx = 0$ and $d^2z/d^2x < 0$) or ($dz/dy = 0$ and $d^2z/d^2y < 0$). Note that this method also considers the crests corresponding to the smaller riding waves, generally not taken into account by wave-by-wave zero-crossing analysis. Consecutive points in the elevation map matrix are grouped to form the wave crests. Finally the crest length is measured and divided by the sea surface area to obtained the crest length density of the waves, breaking or not, for the considered wave scale f_c . Note that the obtained crest length densities are linked to the frequency bandwidth $\Delta k = 2\delta_{\text{BBY}}k = 0.6k$.

Following Filipot et al. (2010), the crest are detected on frequency-filtered surfaces, at various scales, with frequency filter defined by a 2δ wide Hann window $U_{f_c}(f)$, centered at f_c such that

$$U_{f_c}(f) = 0.5 - 0.5 \cos \left[\frac{\pi}{\delta} \left(\frac{f}{f_c} - 1 - \delta \right) \right], \quad (4.25)$$

with $\delta = \delta_{\text{BBY}} = 0.3$. The 3D spectra presented on the figures 3.21-3.24 in the chapter 3 show that the frequency-filtered surfaces also contain energy associated with nonlinear harmonics of other wave scales. As the wave models only takes into account linear waves energy, Filipot et al. (2010) proposed to remove the nonlinear contribution using an iterative removing of the harmonic coming from the other wave scales estimated using the

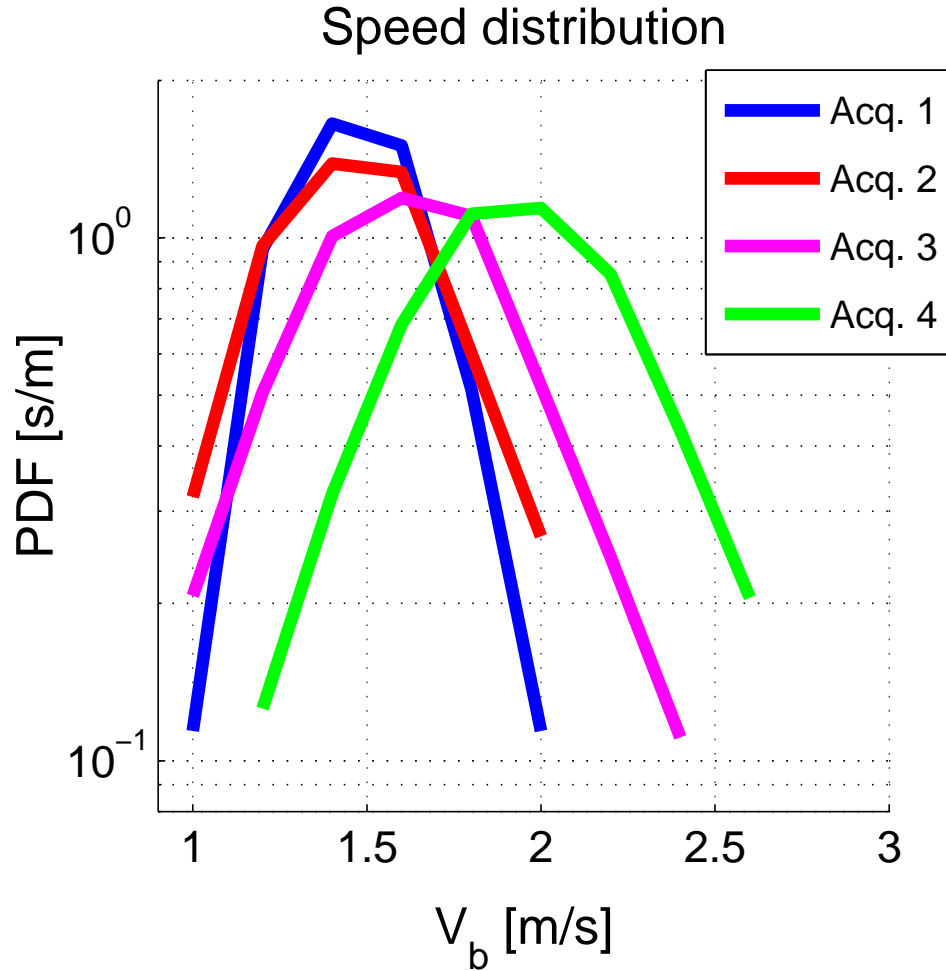


Figure 4.7: Probability density function of breaking to breaking speeds for the 4 acquisitions.

second order theory by Sharma and Dean (1993). Here, the non-linear wave removal is done using a wavenumber-filtering applied on the frequency-filtered surfaces. Consistently with the frequency filtering, the wavenumber filter is defined using the linear dispersion in deep water such that

$$U_{k_c}(k) = 0.5 - 0.5 \cos \left[\frac{\pi}{\delta_k} \left(\frac{k}{k_c} - 1 - \delta_k \right) \right], \quad (4.26)$$

with $\delta_k = \sqrt{\delta}$. The figure 4.10 shows on the left panels the frequency-filtered surfaces which contain non-linear contribution from the larger scale and the wavenumber-frequency-filtered surfaces (corresponding to the linear waves) on right panels, for different 3 wave scales, $\lambda = 1\text{m}$ (i.e. $f_c = 1.25\text{Hz}$, $k_c = 2\pi\text{rad/m}$), $\lambda = 3\text{m}$ (i.e. $f_c = 0.72\text{Hz}$, $k_c = 2\pi/3\text{rad/m}$) and $\lambda = 5\text{m}$ (i.e. $f_c = 0.56\text{Hz}$, $k_c = 2\pi/5\text{rad/m}$). We note the strong influence of nonlinear contribution particularly for the wave scale $\lambda = 1\text{m}$.

The crest length densities are then computed on each surfaces for five wave scale ($\lambda = 1\text{m}$, 2m , 3m , 4m , 5m) over the wavenumber-frequency-filtered surfaces, then averaged

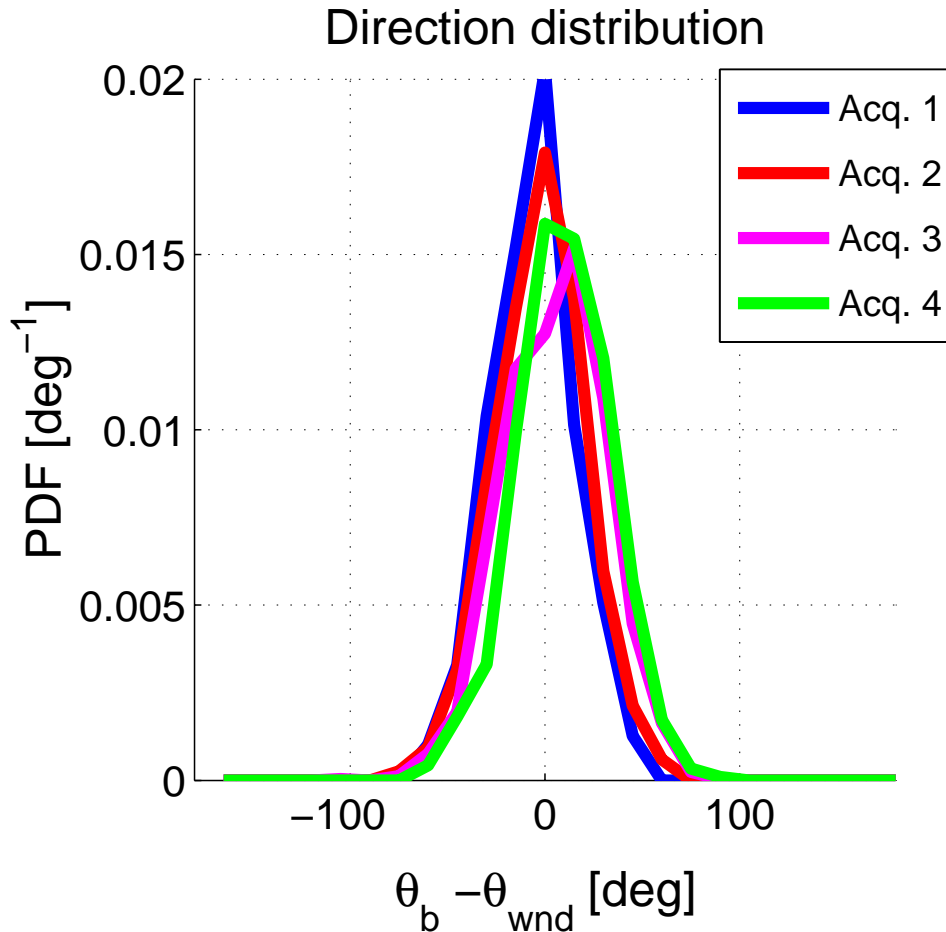


Figure 4.8: Probability density function of breaking direction relative to the wind direction for the 4 acquisitions.

over the whole image sequence of each acquisitions. The obtained crest length densities are plotted on the figure 4.11.

4.4 Breaking probabilities

The breaking probabilities are computed in the seven overlapped wave scale defined by equation 4.25 with $f_c = 0.55f_p, 0.74f_p, f_p, 1.37f_p, 1.86f_p, 2.45f_p$ and, $3.45f_p$. The detected breaking events are then distributed in various wave scales such that a breaking event belongs to the wave scale f_c if the frequency f_b of the breaking wave is in the range $[(1 - \delta_{\text{BBY}})f_c, (1 + \delta_{\text{BBY}})f_c]$. Note that with this wave scale, major breaking belongs in two wave scales. As discussed in the previous paragraph, the smallest wave scales (in order of some meters wavelength) are strongly influenced by nonlinear contribution, but nonlinear contribution strongly decreases for the longer wave scale. Therefore, the nonlinear contributions are removed by applying the wavenumber filtering discussed in the previous paragraph for the estimation of the crest length and the breaking crest length for

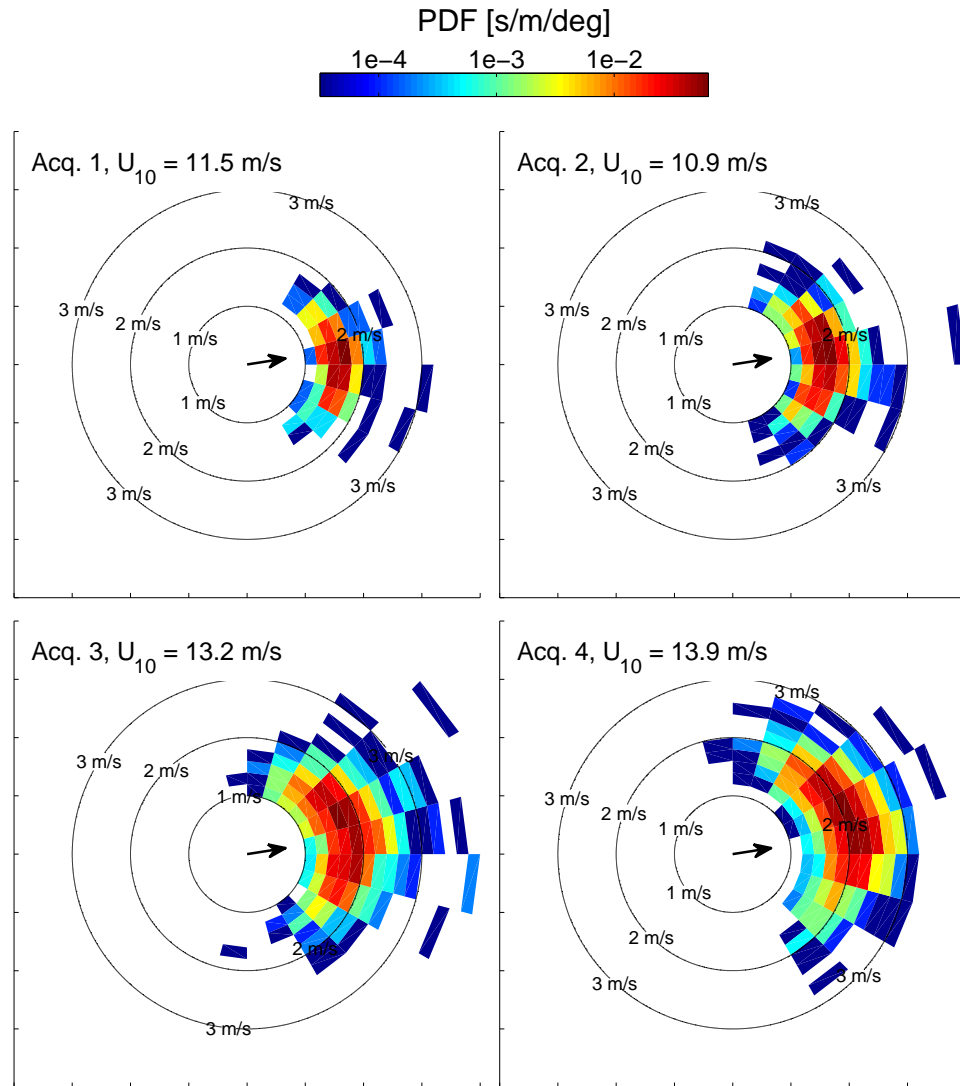


Figure 4.9: Probability density function of breaking to breaking speeds and directions for the 4 acquisitions. The black arrows give the wing direction.

the wave scale in which the wavelengths are included in the surface areas and are neglected for the other wave scales. Moreover, with the reconstructed surface areas greater than the half size of the peak wavelength, the non-linear contribution is only neglected in the wave scale $f_c = 0.55f_p, 0.74f_p, f_p, 1.37f_p$, in which non-linear contribution from the harmonics of the peak waves do not have strong influence.

As stated in the introduction, the breaking probability is generally the ratio between the number of breaking waves and the total number of waves (breaking or not). The number of waves is generally computed using a zero up-crossing (or zero down-crossing) processing of the elevation time series. On a 2D real sea surface, the definition of an individual wave is more difficult. Therefore, two methods for the probability estimation

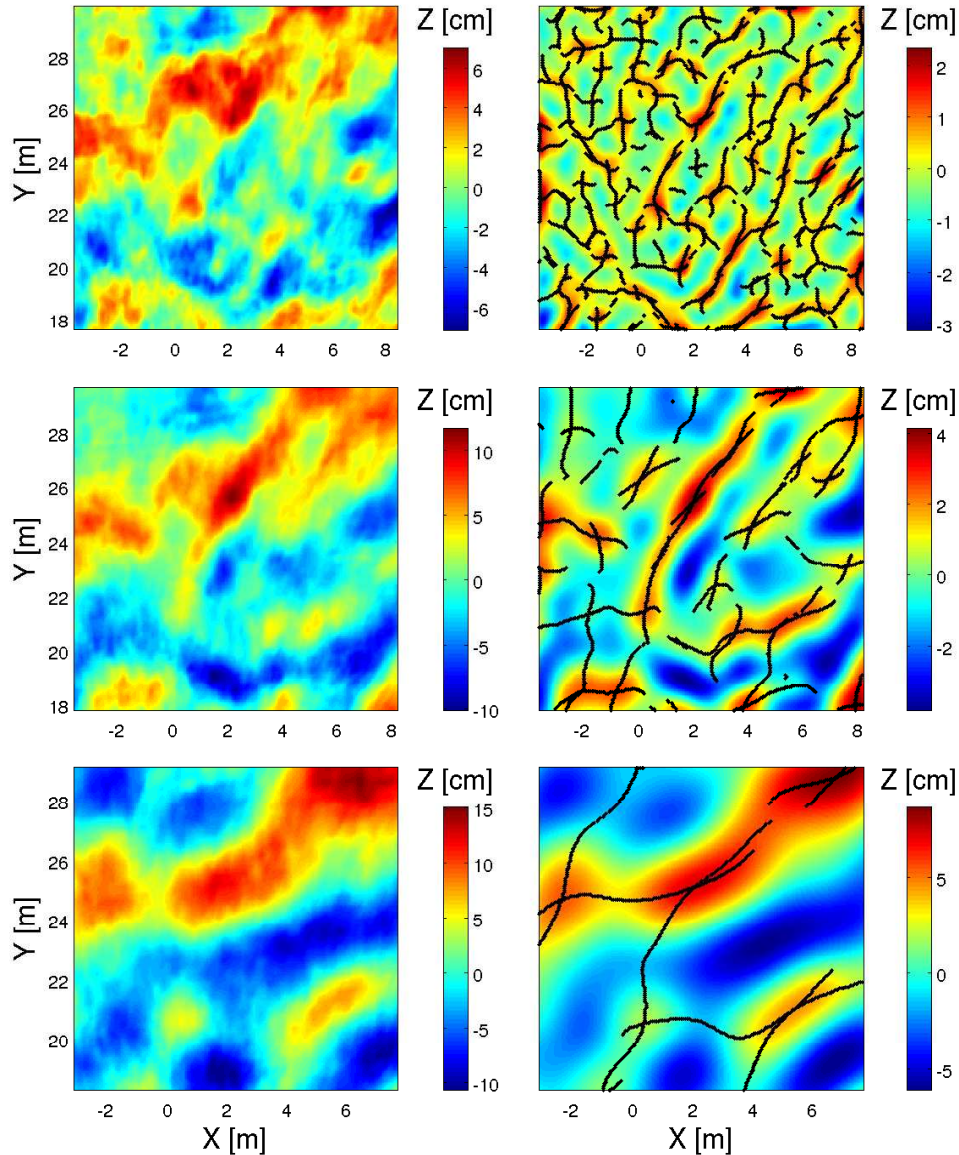


Figure 4.10: Frequency-filtered surfaces (left panels) and the wavenumber-frequency-filtered surfaces (right panels) for $\lambda_c = 1\text{m}$ (top), 3m (middle) and 5m (bottom). The black points are detected to be wave crest points.

are here presented and compared.

The first one is the classical time series analysis. For each point of the filtered surfaces, the elevation time series is analyzed independently. A zero up-crossing is applied to differentiate the individual waves. Then the breaking probability is defined by the ratio between the number of waves affected by an active breaking and the total number of waves.

For the second method, the breaking crest length is defined for each image by the length of crest, as defined previously, which coincides with an active breaking. As for crest length of wave crest, breaking or not, the breaking crest length density is then

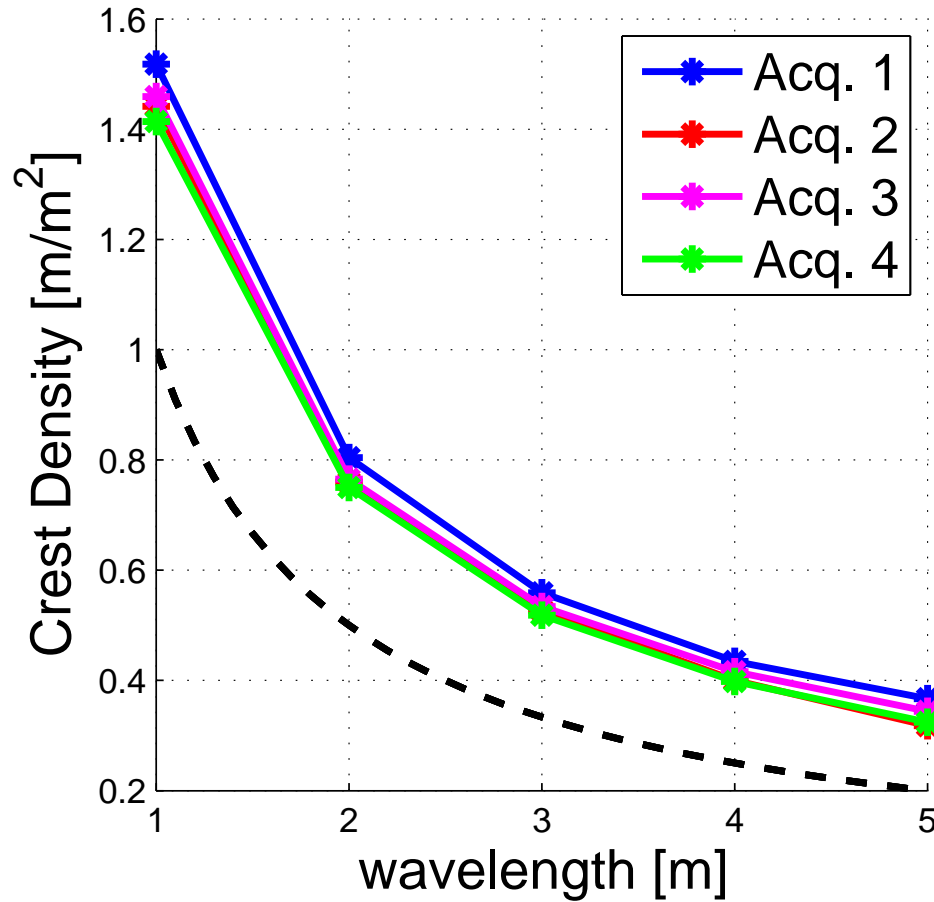


Figure 4.11: Crest length densities for the four acquisitions. Black line represents the crest length densities for monochromatic unidirectional waves.

computed by dividing the length of breaking crest by the surface areas and averaged all the surfaces of each acquisition. We therefore obtain a breaking crest length density for each wave scale. Finally, the breaking probabilities are defined for each wave scale by the ration of breaking crest length density to the crest density of wave breaking or not. As the crest length density is strongly affected by the method of filtering used, only the wave scales both filtered in frequencies and wavenumbers are used for this estimation.

The obtained breaking probabilities are plotted on the figure 4.12 with each method. We note that the highest frequency wave scale covers a large range of frequency in which both breaking can have been filtered by the threshold on minimum breaking speed and breaking occurring without formation of bubbles (so not detectable by visual observations). Also, the active whitecap coverages, computed globally and per wave scales, are reported in table 4.4. The global active whitecap coverage are in line with the empirical crest-foam coverage coverage laws derived by Monahan and Woolf (1989) for a temperature difference about 10°C.

For the breaking probabilities computed in each wave scale with the classical time series analysis, the distribution of the breaking directions are plotted in the figure 4.13.

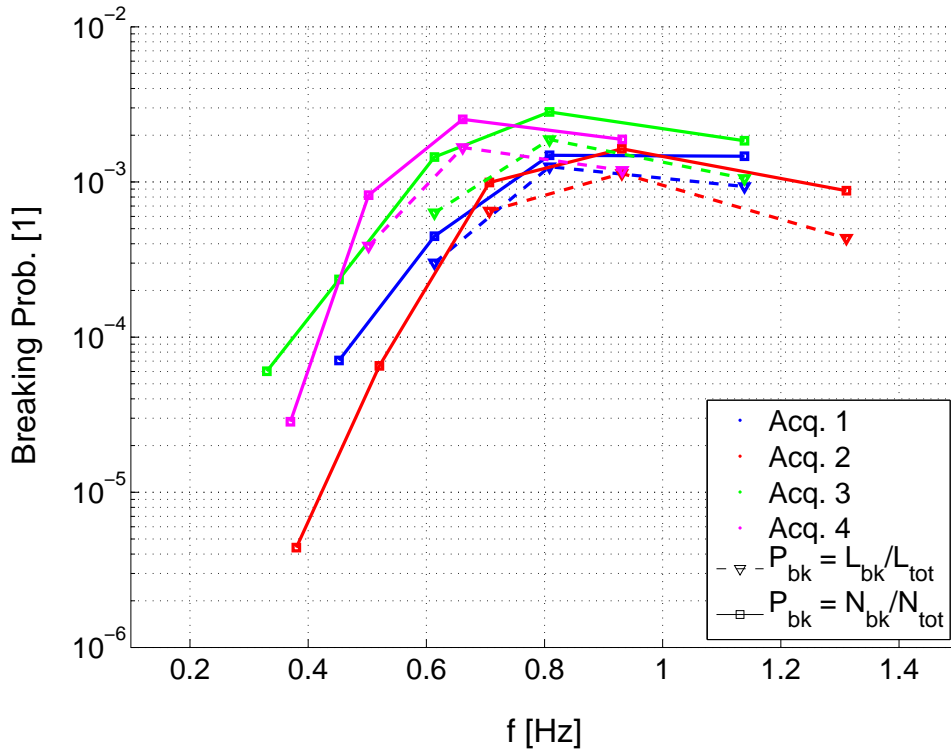


Figure 4.12: Breaking probabilities as ratio of breaking crest length to total crest length, breaking or not (triangles, dashed-line) and as ratio of number of breaking waves to total number of waves, breaking or not (square, full line). Number of waves is defined using a wave-by-wave analysis applied on the time series get from each point of the surface.

Acq. #	W_{glo}	$W_{0.55f_c}$	$W_{0.74f_c}$	W_{f_c}	$W_{1.37f_c}$	$W_{1.86f_c}$	$W_{2.45f_c}$	$W_{3.45f_c}$
1	$3.5 \cdot 10^{-4}$	-	-	-	$6.3 \cdot 10^{-6}$	$5.8 \cdot 10^{-5}$	$2.4 \cdot 10^{-4}$	$3.0 \cdot 10^{-4}$
2	$3.6 \cdot 10^{-4}$	-	-	$7 \cdot 10^{-7}$	$5.9 \cdot 10^{-6}$	$1.5 \cdot 10^{-4}$	$3.3 \cdot 10^{-4}$	$2.0 \cdot 10^{-4}$
3	$5.6 \cdot 10^{-4}$	-	-	-	$5.4 \cdot 10^{-6}$	$1.5 \cdot 10^{-4}$	$4.9 \cdot 10^{-4}$	$4.1 \cdot 10^{-4}$
4	$4.7 \cdot 10^{-4}$	-	-	-	$1.2 \cdot 10^{-6}$	$1.1 \cdot 10^{-4}$	$4.0 \cdot 10^{-4}$	$3.7 \cdot 10^{-4}$

Table 4.1: Global whitecap coverage (first column) and whitecap coverage by wave scale (next columns) obtained for each acquisition.

The directionality of breaking increases with the higher frequency as reported in many studies (Banner et al., 2002; Mironov and Dulov, 2008). This is related to the increasing spread over direction of the energy observed with higher frequencies.

4.5 Wave scale analysis

From the non-directional frequency spectra, the breaking probabilities are computed for each wave scale using the model of Filipot et al. (2010) used in the parameterization of Filipot and Ardhuin (2012). These breaking probabilities are compared to the observed

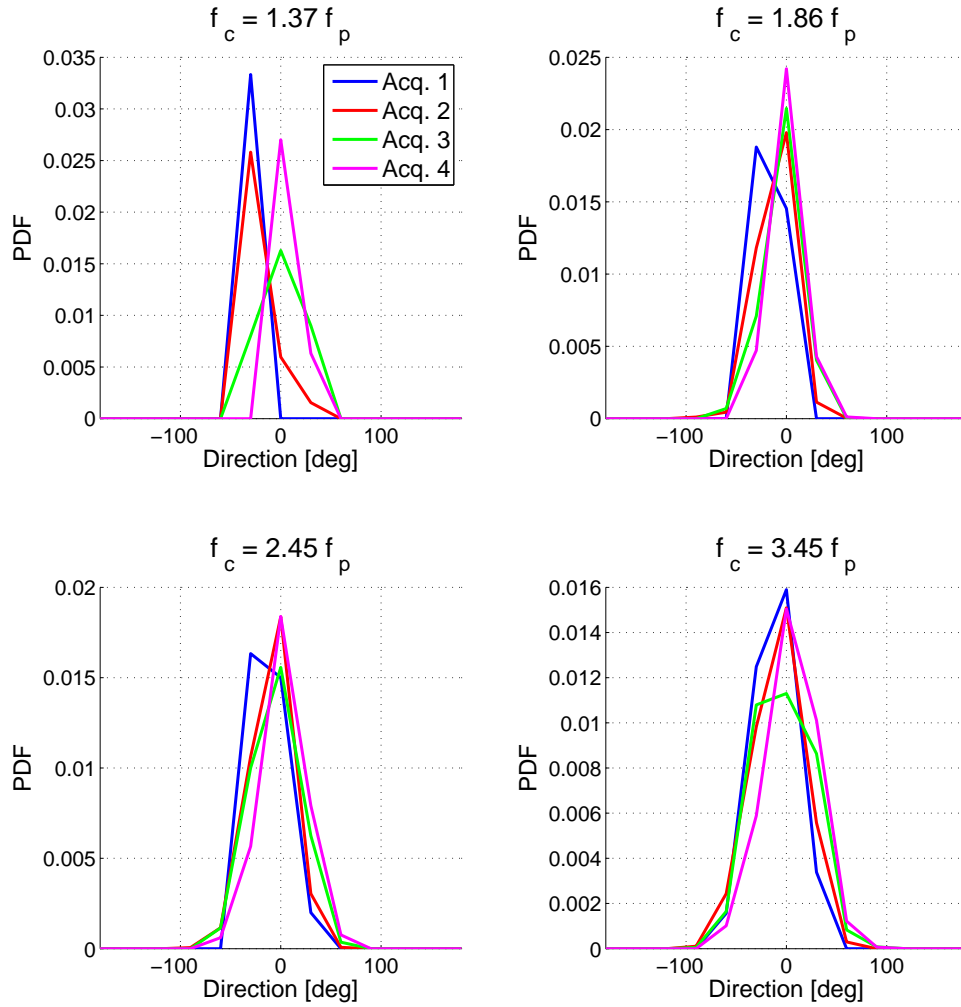


Figure 4.13: Directional distribution of the breaking probabilities in each wave scale for the four acquisitions.

ones. The breaking probabilities obtained from the observations are strongly lower than those computed from the model of Filipot et al. (2010), but with a similar shape over the frequencies. In one hand, we note that Filipot et al. (2010) proposed a model for the frequency spectrum of the linear waves whereas the frequency spectra used here are obtained from wave gauges and also contain energy from the non-linear waves. However, this cannot explain the factor 100. In the other hand, Filipot et al. (2010) used sound records to detect the breaking waves, in which the precise location of the breaking is not known. As a result, all detected breaking events were assigned to the closest wave, even if the breaking did not occur exactly on top of the pressure wave gauge. In our processing, the breaking is assigned to a wave only if the active breaking occurs at the observed point. The large difference can so be explained by the ratio between the areas covered by the sound recorder to the real areas of the active breaking.

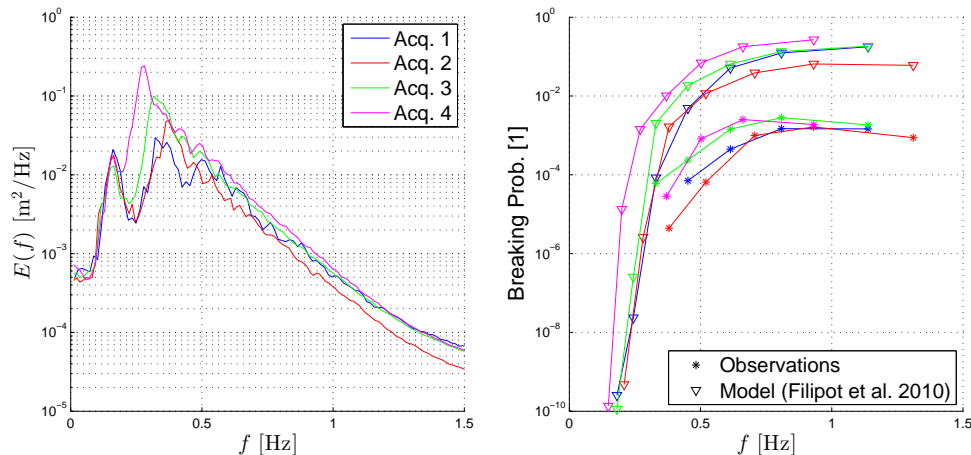


Figure 4.14: Left panel: frequency spectra obtained from wave gauges. Right panel : comparison of the observed unidirectional breaking probabilities with the modeled probabilities of Filipot et al. (2010) computed using the wave gauge frequency spectra.

4.6 Saturation spectrum

Banner et al. (2000) proposed to rely breaking of peak waves to the non directional saturation spectrum B at the peak. Then, Banner et al. (2002) extended this work to the smaller scales, introducing the effect of the directional spreading of the saturation spectrum. The figure 4.15 shows the saturation spectra (left axis) for each acquisition in wavenumber (left panel) and frequencies (right panel) compared to the corresponding breaking PDF (right axis). The breaking speeds V_b are assimilated with the wavenumber (resp. frequency) of the breaking waves, which phase speeds V_p are supposed to be $V_p = V_b/0.8$. We note that the short duration of the acquisition 1, with a small number of breaking events, the statistics obtained for this acquisition could be not significative and must be analyzed carefully. Note that the figures show the breaking occurrence, and not the breaking probability. Our observations do not show a direct link between the non-directional saturation and the breaking occurrence. Indeed, the breaking occurrence decreases for shortest frequencies whereas the non-directional saturation keeps an approximate constant level.

The figure 4.16 shows that the directional saturation decreases with higher frequencies due to the large directional energy spreading, which certainly reliable to the breaking occurrence decreasing. For the parameterization TEST451, Ardhuin et al. (2010) used a directional saturation spectrum $B'(k, \theta)$, partially integrated over directions between $\theta - \Delta_\theta$ and $\theta + \Delta_\theta$, with $\Delta_\theta = 80^\circ$ (see Eq. 2.11). The directional breaking probability $P_b(k, \theta)$ is then defined by the excess of $B'(k, \theta)$ compared to a threshold (see Eq. 2.14). The directional breaking PDF are compared to the saturation spectra $B(k, \theta) = k^4 E(k, \theta)$ and partially integrated saturation spectra $B'(k, \theta)$ as defined by equation 2.11 on the figure 4.16. The value of the threshold is not discussed here but the figures show that the directional spreading of the breaking PDF are in line with the partially integrated saturation spectra $B'(k, \theta)$.

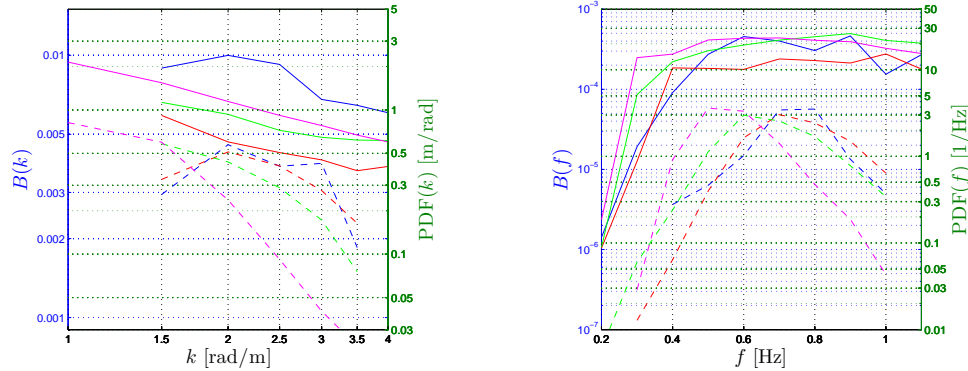


Figure 4.15: Saturation spectra (left axis, full lines) and corresponding breaking PDF (right axis, dashed lines) as function of wavenumbers (left panel) and frequencies (right panel).

4.7 Conclusion

This chapter presents the threshold method for the detection of breaking waves on the video images that maximally eliminates human influence of Mironov and Dulov (2008). The observed active whitecap coverages are consistent with the model of Monahan and Woolf (1989). Then reprojected on the reconstructed sea surfaces, the speed and the direction of the breaking events can be estimated. The obtained distribution over speed and direction are in line with the observations of Mironov and Dulov (2008). In the similar study using a single camera of Mironov and Dulov (2008) in which the breaking detected on the images are projected into the mean sea plane, the elevation of the breaking waves involves errors in the estimation of the speed and the direction of the breaking.

A large number of acquisitions are needed to draw firm results. However, an overview of the various observable parameters shows that the stereo observation of wave breaking can provide an interesting new world of information for the improvement of the breaking parameterization in the spectral model. In particular, we observed that the wave scale analysis of Filipot et al. (2010) provides a smooth breaking probability over wavenumber consistently with the observations. However, the large difference of absolute breaking probability level between the model and the observations must be studied further. Moreover, the use of the partially integrated saturation spectrum over direction for the modeling of the breaking probability is also consistent with our observations. The used of wave scales (or saturation spectrum) partially integrated on both wavenumbers and direction should be interesting direction for the improvement of the dissipation source term in the spectral wave model and the methods presented here should help for such an investigation.

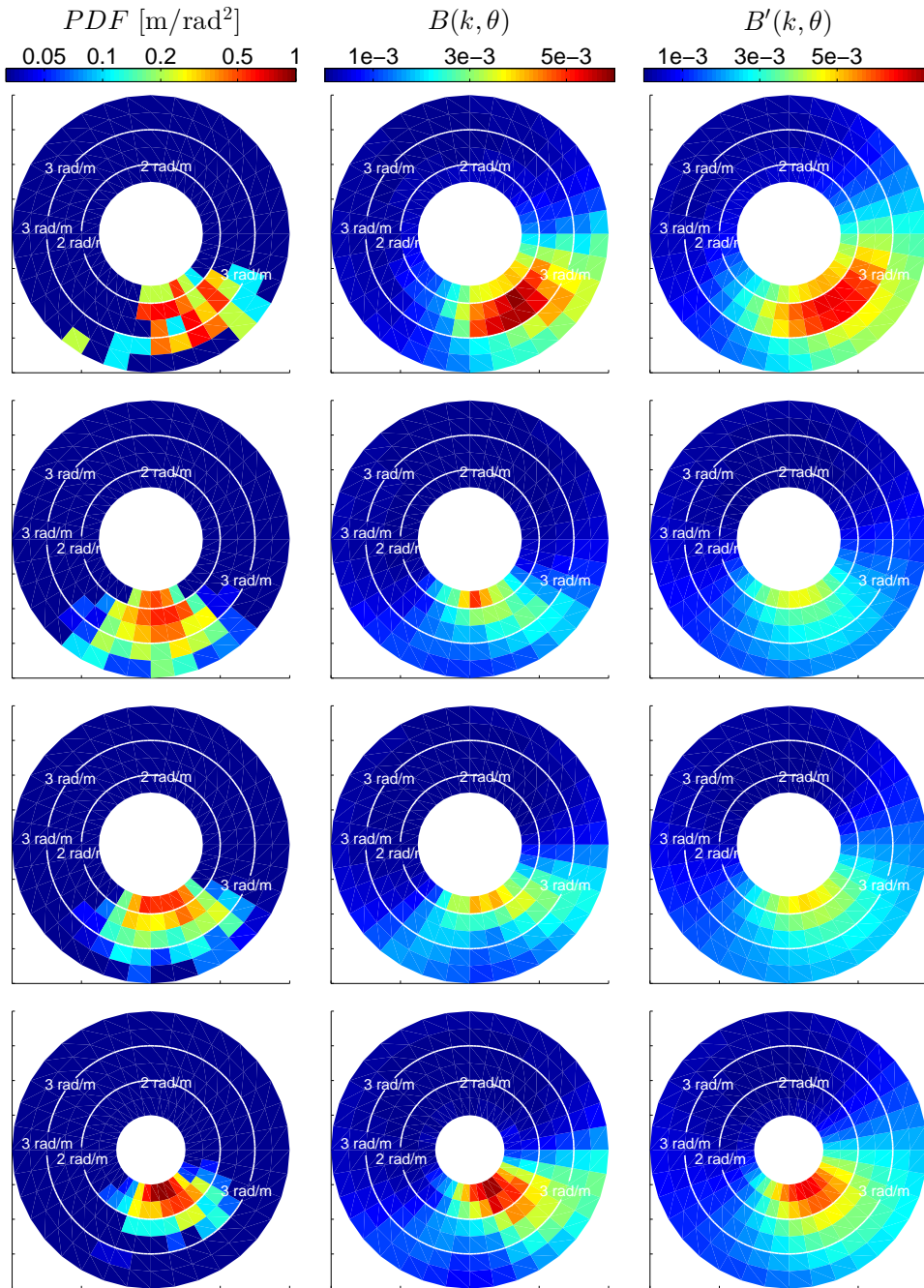


Figure 4.16: Comparison of the direction-wavenumber PDF of the detected breaking (left panels) compared to the wavenumber saturation spectra $B(k, \theta)$ (middle panels) and partially integrated wavenumber saturation spectra $B'(k, \theta)$ as defined by equation 2.11 for each acquisition.

Chapter 5

Conclusion

Starting from an analysis of the capability of spectral wave models to reproduce the evolution of the sea state, this work first focus on the dissipation source term associated to wave breaking in the energy balance equation. This source term have been for long time used as tuning knob balancing the other better understand source terms, but recent efforts have been done to make it closer than the physical processes involved by the wave breaking. Two recent wave breaking parameterizations based on observations were a major focus of the first chapter. The model accuracy is generally evaluated through its ability to reproduce observed wave heights and spectral evolution. Nevertheless, considering only the integration of the whole set of source terms, these validations fails to validate independently each one. Although the explicit modeling of whitecap properties is a constraint on the model dissipation source terms, these recent dissipation parameterizations have seldom been verified in these terms. Therefore, the breaking crest lengths distributions, the whitecap coverage and the foam thickness are extracted from the parameterizations of the wave breaking dissipation and compared to observations.

The two recent parameterizations investigated in this work are the directional saturation based parameterization of Ardhuin et al. (2010) and the parameterization of Filipot and Ardhuin (2012), based on the non directional observations of breaking probabilities per wave scale of Filipot et al. (2010). These parameterizations have been first slight modified in terms of swell dissipation and the physical relationship that intrinsically links spontaneous breaking dissipation and dissipation induced by breaking waves have been made self consistent in the second one. Validated using the classical ways, these slight modifications improve the global accuracy of the models. Nevertheless, these modifications do not influence on the breaking statistics, which are the main purpose of this work. It is found that the breaking parameterization by Filipot and Ardhuin (2012) produces breaking crest length distributions that are in better qualitative agreement with observations, contrary to the parameterization of Ardhuin et al. (2010) which fails to produce smooth Λ -distributions. This difference is clearly associated with the breaking probabilities computed over wave scales compared to those linked the local saturation. The estimation of the breaking parameters after smoothing the local saturations over frequencies could lead to better Λ -distributions (Banner and Morison, 2010). Inversely, the isotropic distribution of the breaking probabilities over frequency afflicting the parameterization of Filipot and Ardhuin (2012) compared to the directional distribution of the breaking done

in the parameterization by Ardhuin et al. (2010), linked to the partial integration over directions of the directional saturation spectra. Indeed, combined with the cumulative effect parameterization, the isotropic distribution of breaking, moreover not observed, tends to reduce the width of the directional spectrum. Inversely, despite producing unrealistic unsmoothed crest lengths distributions, the directional breaking distribution of the parameterization by Ardhuin et al. (2010), linked to the directional saturation spectra, provides spectra directional spreading more in line with the observations. A combination of these two approaches, using directional wave scales or directional saturation partially integrated over both directions and frequencies should lead to better distribution of the breaking.

Comparing the modeled global whitecap coverage to the observations from satellite radiometers interpreted by Anguelova and Webster (2006), it is shown that any parameterization reproduce the large variability of the observations. Nevertheless, it is found that joint estimates of the whitecap coverage and foam thickness could be an interesting way to discriminate between different sea states or parameterizations. Recent results by Reul et al. (2006) with L -band radiometric measurements in Hurricanes using the Soil Moisture and Ocean Salinity space mission, combined with radiometric measurements from different bands should provide information on the distribution of the breaking foam and should be an interesting way to even more constraint the dissipation source terms in the spectral wave models. This deficiency is both attributed to the bad modeling of the breaking in the model, but also to the lack of physical process and external parameters in the model which strongly influence on the quantity of created foam by breaking wave and its lifetime.

The analysis of the existing parameterization shows the need of the synchronized observations of wave spectra and breaking wave distributions. These two parameters can be observed using the stereo observation of the sea. Indeed, recent methods were developed to reconstruct accurate wavy sea surface from the standard stereo triangulation well known in computer vision. Moreover the breaking waves which produce white foam patches over the darker water surface are easily detectable, providing the new world of information combining the observation of the breaking wave and the time-space evolution of the underlying sea surface.

The existing methods of sea surface reconstruction provide good results in terms of sea elevation statistics and spectra. Nevertheless, it is shown in this work that the presence of foam patches on the sea surface strongly disturbs the local shape of the surface. The first effort was to improve the existing reconstruction methods to provide realistic sea surface shape around the foam patches. Four stereo video acquisitions are investigated and a validation of the reconstructed surfaces obtained with the improved method is given by comparison with wave gauge data. The observation of the 3D direction-wavenumber-frequency spectra obtained from the time-space evolution of the surface shows that the reconstructed surfaces show the coherence of the surfaces up to $f = 1.6\text{Hz}$ ($\lambda \approx 60\text{cm}$).

Then, the breaking waves are detected on the images using the threshold method of Mironov and Dulov (2008) that maximally eliminates human influence, then reprojected on the reconstructed sea surfaces. The speed and the direction of the breaking events are computed. The obtained distribution over speed and direction are in line with the observations of Mironov and Dulov (2008). We highlight that the access to the sea surface

elevation in this work allows a better calculation of the breaking speed and direction than in the single camera observations of Mironov and Dulov (2008) in which the breaking detected on the images are projected into the mean sea plane, involving errors related to the elevation of the breaking waves.

In addition to the quantification of the breaking and its precise distributions over wave scales and directions, it was shown that the stereo observation allows the analysis the breaking at the scale of the single breaking waves and thus opens a new world of information about the space-time evolution of the breaking waves for large range of wave scales. Despite these aspects were not addressed in this work, the stereo observation provides the necessary information to study the dissipation of the breaking waves and the quantification of the possibly associated cumulative effect observed by (Banner et al., 1989). A large number of acquisitions is needed to draw firm results, however the provided overview of the various observable parameters shows that the method developed here can provide large information for the validation and the improvement of the breaking parameterization in the spectral model. Moreover, the stereo observations at microwave scale with high resolution camera of Yurovskaya et al. (2013) should also be used to quantify the generation of short waves in all directions from the breaking of long waves. This generation of short waves, also detected on the acoustic measurements of Duennebier et al. (2012), could have a important effect on the transfer of the energy from the wind to the waves.

Finally, a new experiment was done on September 2013 from the scientific platform of Katsively in Ukraine, with a larger range of wind and wave conditions. Two synchronized stereo video systems were deployed with different lenses to observe different wave scales. In addition to the wind and wave measurements also available for the present study, joint measurement have been done with Ka-band radar and stereo-photo. The processing of the data is in progress. Interesting informations over a larger range of wave scales are expected in terms of distribution of wave breaking but also on the relationship of the breaking with the spectrum shape.

Bibliography

- Agrawal, Y., E. Terray, M. Donelan, P. Hwang, A. Williams, W. Drennan, K. Kahma, and S. Krtaigorodskii, 1992: Enhanced dissipation of kinetic energy beneath surface waves.
- Alves, J. H. G. M. and M. L. Banner, 2003: Performance of a saturation-based dissipation-rate source term in modeling the fetch-limited evolution of wind waves. *J. Phys. Oceanogr.*, **33**, 1274–1298.
- Alves, J. H. G. M., M. L. Banner, and I. R. Young, 2003: Revisiting the Pierson-Moskowitz asymptotic limits for fully developed wind waves. *J. Phys. Oceanogr.*, **33**, 1301–1323.
- Anguelova, M. D., J. P. Bobak, W. E. Asher, D. J. Dowgiallo, B. I. Moat, R. W. Pascal, and M. J. Yelland, 2009: Validation of satellite-based estimates of whitecap coverage: Approaches and initial results. *16th Air-Sea Interaction conference, AMS, Phoenix, Arizona*.
- Anguelova, M. D. and F. W. Webster, 2006: Whitecap coverage from satellite measurements: a first step toward modeling the variability of oceanic whitecaps. *J. Geophys. Res.*, **111**, C03017.
- Apel, J., 1994: An improved model of the ocean surface wave vector spectrum and its effects on radar backscatter. *J. Geophys. Res.*, **99**, 16269–16291.
- Ardhuin, F., B. Chapron, and F. Collard, 2009: Observation of swell dissipation across oceans. *Geophys. Res. Lett.*, **36**, L06607.
- Ardhuin, F., J. Hanafin, Y. Quilfen, B. Chapron, P. Queffeuilou, M. Obrebski, J. Sienkiewicz, and D. Vandemark, 2011a: calibration of the IOWAGA global wave hindcast (1991–2011) using ECMWF and CFSR winds. *Proceedings, 12th Int. Workshop of Wave Hindcasting and Forecasting, Hawaii*.
- Ardhuin, F., T. H. C. Herbers, K. P. Watts, G. P. van Vledder, R. Jensen, and H. Graber, 2007: Swell and slanting fetch effects on wind wave growth. *J. Phys. Oceanogr.*, **37**, 908–931.
- Ardhuin, F. and A. D. Jenkins, 2006: On the interaction of surface waves and upper ocean turbulence. *J. Phys. Oceanogr.*, **36**, 551–557.

- Ardhuin, F., E. Rogers, A. Babanin, J.-F. Filipot, R. Magne, A. Roland, A. van der Westhuysen, P. Queffelec, J.-M. Lefevre, L. Aouf, and F. Collard, 2010: Semi-empirical dissipation source functions for wind-wave models: part I, definition, calibration and validation. *J. Phys. Oceanogr.*, **40**, 1917–1941.
- Ardhuin, F. and A. Roland, 2012: Coastal wave reflection, directional spreading, and seismo-acoustic noise sources. *J. Geophys. Res.*, **117**, in press.
- Ardhuin, F., J. Tournadre, P. Queffelec, and F. Girard-Ardhuin, 2011b: Observation and parameterization of small icebergs: drifting breakwaters in the southern ocean. *Ocean Modelling*, **39**, 405–410.
- Aziz, A. Y. I. and H. M. Karara, 1971: Direct linear transformation into object space coordinates in close-range photogrammetry. *Proc. of the Symposium on Close-Range Photogrammetry*, Urbana, Illinois, 1–18.
- Babanin, A., D. Chalikov, I. Young, and I. Savelyev, 2007: Predicting the breaking onset of surface water waves. *Geophys. Res. Lett.*, **34**, L07605.
- Babanin, A., I. Young, and M. Banner, 2001: Breaking probabilities for dominant surface waves on water of finite depth. *J. Geophys. Res.*, **106**, 11659–11676.
- Babanin, A. V., K. N. Tsagareli, I. R. Young, and D. J. Walker, 2010: Numerical investigation of spectral evolution of wind waves. part II: Dissipation term and evolution tests. *J. Phys. Oceanogr.*, **40**, 667–683.
- Banner, M. and W. Melville, 1976: On the separation of air flow over water waves. *Journal of Fluid Mechanics*, **77**, 825–842.
- Banner, M. L., A. V. Babanin, and I. R. Young, 2000: Breaking probability for dominant waves on the sea surface. *J. Phys. Oceanogr.*, **30**, 3145–3160.
- Banner, M. L., J. R. Gemmrich, and D. M. Farmer, 2002: Multiscale measurement of ocean wave breaking probability. *J. Phys. Oceanogr.*, **32**, 3364–3374.
- Banner, M. L., I. S. F. Jones, and J. C. Trinder, 1989: Wavenumber spectra of short gravity waves. *J. Fluid Mech.*, **198**, 321–344.
- Banner, M. L. and R. P. Morison, 2010: Refined source terms in wind wave models with explicit wave breaking prediction. part I: Model framework and validation against field data. *Ocean Modelling*, **33**, 177–189.
- Banner, M. L. and J.-B. Song, 2002: On determining the onset and strength of breaking for deep water waves. part ii: Influence of wind forcing and surface shear. *Journal of physical oceanography*, **32**, 2559–2570.
- Banner, M. L. and X. Tian, 1998: On the determination of the onset of breaking for modulating surface gravity water waves. *J. Fluid Mech.*, **367**, 107–137.

- Barrick, D. E., 1968: Rough surface scattering based on the specular point theory. *IEEE Trans. Antennas Propagat.*, **AP-14**, 449–454.
- Battjes, J., 1974a: *Computations of set-up, longshore currents, run-up and overtopping due to wind-generated waves*. Ph.D. thesis, Delft University of Technology, The Netherlands.
- Battjes, J. A., 1974b: Surf similarity. *Proceedings of the 14th international conference on coastal engineering*, ASCE, 466–480.
- Belcher, S. and J. Hunt, 1993: Turbulent shear flow over slowly moving waves. *Journal of Fluid Mechanics*, **251**, 109–148.
- Benetazzo, A., 2006: Measurements of short water waves using stereo matched image sequences. *Coastal engineering*, **53**, 1013–1032.
- Benetazzo, A., F. Fedele, G. Gallego, P.-C. Shih, and A. Yezzi, 2012: Offshore stereo measurements of gravity waves. *Coastal Engineering*, **64**, 127 – 138.
- Bidlot, J., S. Abdalla, and P. Janssen, 2005: A revised formulation for ocean wave dissipation in CY25R1. Technical Report Memorandum R60.9/JB/0516, Research Department, ECMWF, Reading, U. K.
- Bidlot, J.-R., 2012: Present status of wave forecasting at e.c.m.w.f. *Workshop on Ocean Waves, ECMWF*.
- Bjerkaas, A. and F. Riedel, 1979: Proposed model for the elevation spectrum of a wind-roughened sea surface. Technical report, DTIC Document.
- Bondur, V. and E. Sharkov, 1982: Statistical properties of whitecaps on a rough sea. *Oceanology*, **22**, 274–279.
- Brown, D. C., 1966: Decentering distortion of lenses. *Photometric Engineering*, **32**, 444–462.
- Callaghan, A., G. de Leeuw, L. Cohen, and C. D. O’Dowd, 2008: Relationship of oceanic whitecap coverage to wind speed and wind history. *Geophysical Research Letters*, **35**, n/a–n/a.
- Caprile, B. and V. Torre, 1990: Using vanishing points for camera calibration. *International journal of computer vision*, **4**, 127–139.
- Caulliez, G., 2002: Self-similarity of near-breaking short gravity wind waves. *Physics of Fluids*, **14**, 2917.
- Chanson, H. and P. D. Cummings, 1992: Aeration of the ocean due to plunging breaking waves. Technical report.

- Chase, J., L. J. Cote, W. Marks, E. Mehr, W. J. Pierson, J. F. C. Ronne, G. Stephenson, R. C. Vetter, and R. G. Walden, 1957: *The directional spectrum of a wind generated sea as determined from data obtained by the Stereo Wave Observation Project*. New York University, College of Engineering, Research Division, Dept. of Meteorology and Oceanography and Engineering Statistics Group.
- Chawla, A. and J. T. Kirby, 2002: Monochromatic and random wave breaking at blocking points. *J. Geophys. Res.*, **107**, 3067.
- Clarke, T. A. and J. G. Fryer, 1998: The development of camera calibration methods and models. *The Photogrammetric Record*, **16**, 51–66.
- Claudet, A., 1856: On various phenomena of refraction through semi-lenses or prisms, producing anomalies in the illusion of stereoscopic images.[abstract]. *Proceedings of the Royal Society of London*, **8**, 104–110.
- 1857: On the stereomonoscope, a new instrument by which an apparently single picture produces the stereoscopic illusion. *Proceedings of the Royal Society of London*, **9**, 194–196.
- Conrady, A. E., 1919: Lens-systems, decentered. *Monthly notices of the royal astronomical society*, **79**, 384–390.
- Cote, L. J., J. O. Davis, W. Marks, R. J. McGough, E. Mehr, W. Pierson, J. Ropek, G. Stephenson, and R. C. Vetter, 1960: The directional spectrum of a wind generated sea as determined from data obtained by the {Stereo Wave Observation Project}. **2**, 758–766.
- Cox, C. and W. Munk, 1954: Measurement of the roughness of the sea surface from photographs of the sun’s glitter. *J. Opt. Soc. Am.*, **44**, 838–850.
- Craig, P. D. and M. L. Banner, 1994: Modeling wave-enhanced turbulence in the ocean surface layer. *Journal of Physical Oceanography*, **24**, 2546–2559.
- Cruset, J., 1953: Photogrammetric measurement of the sea swell. *Photogrammetria*, **9**, 122 – 125.
- Dankert, H., J. Horstmann, S. Lehner, and W. Rosenthal, 1939: Stereophotogrammetrische wellenaufnahmen. (stereophotogrammetric wave photos.). *Vernessungsschiff Meteor*, **7**.
- 2003: Detection of wave groups in SAR images and radar-image sequences. *IEEE Trans. on Geosci. and Remote Sensing*, **41**, 1437–1441.
- Donelan, M., M. S. Longuet-Higgins, and J. Turner, 1972: Periodicity in whitecaps.
- Donelan, M. A., F. W. Dobson, S. D. Smith, and R. J. Anderson, 1993: On the dependence of sea surface roughness on wave development. *J. Phys. Oceanogr.*, **23**, 2143–2149.

- Donelan, M. A. and W. J. Pierson, Jr., 1987: Radar scattering and equilibrium ranges in wind-generated waves with application to scatterometry. *J. Geophys. Res.*, **92**, 4971–5029.
- Droppleman, J. D., 1970: Apparent microwave emissivity of sea foam. *J. Geophys. Res.*, **75(3)**, 696–698.
- Duennebier, F. K., R. Lukas, E.-M. Nosal, J. Aucan, and R. A. Weller, 2012: Wind, waves, and acoustic background levels at station aloha. *J. Geophys. Res.*, **117**, in press.
- Dulov, V., V. Kudryavtsev, and A. Bolshakov, 2002: A field study of white caps coverage and its modulations by energy containing wave. *Gas Transfer at the Water Surface, Geophysical Monographs 127*, M. A. D. et al., ed., American Geophysical Union, pages 187–192.
- Duncan, J. H., 1981: An experimental investigation of breaking waves produced by a towed hydrofoil. *Proc. Roy. Soc. Lond. A*, **377**, 331–348.
- Elfouhaily, T., B. Chapron, K. Katsaros, and D. Vandemark, 1997: A unified directional spectrum for long and short wind-driven waves. *Journal of Geophysical Research*, **102**, 15781–15.
- Filipot, J.-F. and F. Ardhuin, 2012: A unified spectral parameterization for wave breaking: from the deep ocean to the surf zone. *J. Geophys. Res.*, **116**.
- Filipot, J.-F., F. Ardhuin, and A. Babanin, 2010: A unified deep-to-shallow-water wave-breaking probability parameterization. *J. Geophys. Res.*, **115**, C04022.
- Gagnaire-Renou, E., M. Benoit, and P. Forget, 2010: Ocean wave spectrum properties as derived from quasi-exact computations of nonlinear wave-wave interactions. *J. Geophys. Res.*, **115**, C12058.
- Gallego, G., A. Benetazzo, A. Yezzi, and F. Fedele, 2008: Wave statistics and spectra via a variational wave acquisition stereo system. *27th Int. Conf. Offshore Mechanics Arctic Engineering (OMAE)*, Lisbon, Portugal.
- Galton, F. and R. C. Galton, 1865: On stereoscopic maps, taken from models of mountainous countries. *Journal of the Royal Geographical Society of London*, **35**, 99–106.
- Gelci, R., H. Cazalé, and J. Vassal, 1957: Prévission de la houle. La méthode des densités spectroangulaires. *Bulletin d'information du Comité d'Océanographie et d'Etude des Côtes*, **9**, 416–435.
- Gemmrich, J. R., M. L. Banner, and C. Garrett, 2008: Spectrally resolved energy dissipation rate and momentum flux of breaking waves. *J. Phys. Oceanogr.*, **38**, 1296–1312.
- Gemmrich, J. R. and D. M. Farmer, 2004: Near-surface turbulence in the presence of breaking waves. *J. Phys. Oceanogr.*, **34**, 1067–1086.

- Golub, G. H. and C. Reinsch, 1970: Singular value decomposition and least squares solutions. *Numerische Mathematik*, **14**, 403–420.
- Hanafin, J., Y. Quilfen, F. Ardhuin, D. Vandemark, B. Chapron, H. Feng, J. Sienkiewicz, P. Queffelec, M. Obrebski, B. Chapron, N. Reul, F. Collard, D. Cormand, E. B. de Azevedo, D. Vandemark, and E. Stutzmann, 2012: Phenomenal sea states and swell radiation: a comprehensive analysis of the 12-16 February 2011 North Atlantic storms. *Bull. Amer. Meteorol. Soc.*, in press.
- Hanson, J. L. and O. M. Phillips, 1999: Wind sea growth and dissipation in the open ocean. *J. Phys. Oceanogr.*, **29**, 1633–1648.
- Hasselmann, K., 1960: Grundgleichungen der seegangsvorhersage. *Schifftechnik*, **7**, 191–195.
- 1962: On the non-linear energy transfer in a gravity wave spectrum, part 1: general theory. *J. Fluid Mech.*, **12**, 481–501.
- 1974: On the spectral dissipation of ocean waves due to white capping. *Boundary-Layer Meteorol.*, **6**, 107–127.
- Hasselmann, S., K. Hasselmann, J. Allender, and T. Barnett, 1985: Computation and parameterizations of the nonlinear energy transfer in a gravity-wave spectrum. Part II: Parameterizations of the nonlinear energy transfer for application in wave models. *J. Phys. Oceanogr.*, **15**, 1378–1391.
- Heikkila, J. and O. Silven, 1997: A four-step camera calibration procedure with implicit image correction. *Computer Vision and Pattern Recognition, 1997. Proceedings., 1997 IEEE Computer Society Conference on*, 1106–1112.
- Holland, K. T. and R. A. Holman, 1997: Video estimation of foreshore topography using trinocular stereo. *Journal of Coastal Research*, **13**, 81–87.
- Holland, K. T., R. A. Holman, T. C. Lippmann, J. Stanley, and N. Plant, 1997: Practical use of video imagery in nearshore oceanographic field studies. *IEEE J. Oceanic Eng.*, **22**, 81–92.
- Holthuijsen, L. and T. Herbers, 1986: Statistics of breaking waves observed as whitecaps in the open sea. *Journal of Physical Oceanography*, **16**, 290–297.
- Holthuijsen, L. H., M. D. Powell, and J. D. Pietrzak, 2012: Wind and waves in extreme hurricanes. *J. Geophys. Res.*, **117**, C09003.
- Hwang, P. A., D. W. Wang, E. J. Walsh, W. B. Krabill, and R. N. Swift, 2000: Airborne measurements of the wavenumber spectra of ocean surface waves. part i: Spectral slope and dimensionless spectral coefficient*. *Journal of Physical Oceanography*, **30**, 2753–2767.
- Jeffreys, H., 1925: On the formation of water waves by wind. *Proceedings of the Royal Society of London. Series A*, **107**, 189–206.

- Jessup, A., C. Zappa, and H. Yeh, 1997: Defining and quantifying microscale wave breaking with infrared imagery. *Journal of Geophysical Research*, **102**, 23145–23.
- Jessup, A. T. and K. R. Phadnis, 2005: Measurement of the geometric and kinematic properties of microscale breaking waves from infrared imagery using a PIV algorithm. *Meas. Sci. Technol.*, **16**, 1961–1969.
- Kanade, T. and D. D. Morris, 1998: Factorization methods for structure from motion. *Philosophical Transactions of the Royal Society of London. Series A: Mathematical, Physical and Engineering Sciences*, **356**, 1153–1173.
- Kantha, L., P. Wittmann, M. Scavo, and S. Carniel, 2009: A preliminary estimate of the stokes dissipation of wave energy in the global ocean. *Geophys. Res. Lett.*, **36**, L02605.
- Kleiss, J. M. and W. K. Melville, 2011: The analysis of sea surface imagery for whitecap kinematics. *J. Atmos. Ocean Technol.*, **28**, 219–243.
- Komen, G., L. Cavaleri, M. Donelan, K. Hasselmann, and S. Hasselmann, 1994: Janssen paem. dynamics and modeling of ocean waves.
- Komen, G. J., K. Hasselmann, and S. Hasselmann, 1984: On the existence of a fully developed windsea spectrum. *J. Phys. Oceanogr.*, **14**, 1271–1285.
- Kosnik, M. V. and V. A. Dulov, 2011: Extraction of short wind wave spectra from stereo images of the sea surface. *Measurement Science and Technology*, **22**, 015504.
- Kudryavtsev, V. and V. Makin, 2001: The impact of air-flow separation on the drag of the sea surface. *Boundary-layer meteorology*, **98**, 155–171.
- Leckler, F., F. Ardhuin, J.-F. Filipot, and A. Mironov, 2013: Dissipation source terms and whitecap statistics. *Ocean Modelling*, **70**, 62 – 74.
- Leykin, I. A. and A. D. Rozenberg, 1984: Sea-tower measurements of wind-wave spectra in the Caspian Sea. *J. Phys. Oceanogr.*, **14**, 168–176.
- Loewen, M. R. and W. K. Melville, 1991: Microwave backscatter and acoustic radiation from breaking waves. *J. Fluid Mech.*, **224**, 601–623.
- Longuet-Higgins, M. and M. Fox, 1978: Theory of the almost-highest wave. part 2. matching and analytic extension. *Journal of Fluid Mechanics*, **85**, 769–786.
- Longuet-Higgins, M. S., 1978: The instabilities of gravity waves of finite amplitude in deep water. i. superharmonics. *Proceedings of the Royal Society of London. A. Mathematical and Physical Sciences*, **360**, 471–488.
- Mach, E., 1896: On the stereoscopic application of roentgen’s rays. *The Monist*, **6**, 321–323.
- Marks, W., 1954: The use of a filter to sort out directions in a short-crested gaussian sea surface. *Transactions, American Geophysical Union*, **35**, 758–766.

- Melen, T., 1994: *Geometrical modelling and calibration of video cameras for underwater navigation*. Institutt for Teknisk Kybernetikk, Universitetet i Trondheim, Norges Tekniske Høgskole.
- Melville, K. W., 1994: Energy dissipation by breaking waves. *Journal of Physical Oceanography*, **24**, 2041–2049.
- Melville, W. K. and P. Matusov, 2002: Distribution of breaking waves at the ocean surface. *Nature*, **417**, 58–63.
- Melville, W. K., F. Verron, and C. J. White, 2002: The velocity field under breaking waves: coherent structures and turbulence. *J. Fluid Mech.*, **454**, 203–233.
- Miche, A., 1944: Mouvements ondulatoires de la mer en profondeur croissante ou décroissante. forme limite de la houle lors de son déferlement. application aux digues maritimes. deuxième partie. mouvements ondulatoires périodiques en profondeur régulièrement décroissante. *Annales des Ponts et Chaussées*, **Tome 114**, 131–164, 270–292.
- Miles, J. W., 1957: On the generation of surface waves by shear flows. *Journal of Fluid Mechanics*, **3**.
- 1962: On the generation of surface waves by shear flows. part 4. *J. Fluid Mech*, **13**, 433–448.
- Mironov, A. S., 2009: *Experimental investigation of statistical and kinematical properties of breaking wind waves*. Ph.D. thesis, Marine Hydrophysics Institute, Sebastopol, in Russian.
- Mironov, A. S. and V. A. Dulov, 2008: Detection of wave breaking using sea surface video records. *Meas. Sci. Technol.*, **19**, 015405.
- Monahan, E. C., C. W. Fairall, K. L. Davidson, and P. J. Boyle, 1983: Observed interrelations between 10m winds, ocean whitecaps and marine aerosols. *Quarterly Journal of the Royal Meteorological Society*, **109**, 379–392.
- Monahan, E. C. and I. Ó. Muircheart, 1981: Optimal power-law description of oceanic whitecap coverage dependence on wind speed. *J. Phys. Oceanogr.*, **10**, 2094–2099.
- Monahan, E. C. and D. K. Woolf, 1989: Comments on "variations of whitecap coverage with wind stress and water temperature". *J. Phys. Oceanogr.*, **19**, 706–709.
- Munk, W., 2008: An inconvenient sea truth: Spread, steepness, and skewness of surface slopes. *Annual review of marine science*, **1**, 377–415.
- Newell, A. C. and V. E. Zakharov, 1992: Rough sea foam. *Physical review letters*, **69**, 1149.
- Phillips, O. M., 1957: On the generation of waves by turbulent wind. *J. Fluid Mech.*, **2**, 415–417.

- 1984: On the response of short ocean wave components at a fixed wavenumber to ocean current variations. *J. Phys. Oceanogr.*, **14**, 1425–1433.
- 1985: Spectral and statistical properties of the equilibrium range in wind-generated gravity waves. *J. Fluid Mech.*, **156**, 505–531.
- Pierson, W. J., 1952: A unified mathematical theory for the analysis, propagation and refraction of storm generated ocean surface waves, parts {I} and {II}.
- Pierson, W. J., Jr and L. Moskowitz, 1964: A proposed spectral form for fully developed wind seas based on the similarity theory of S. A. Kitaigorodskii. *J. Geophys. Res.*, **69**, 5,181–5,190.
- Queffelec, P. and D. Croizé-Fillon, 2010: Global altimeter SWH data set, version 7, may 2010. Technical report, Ifremer.
- Raschle, N., F. Ardhuin, P. Queffelec, and D. Croizé-Fillon, 2008: A global wave parameter database for geophysical applications. part 1: wave-current-turbulence interaction parameters for the open ocean based on traditional parameterizations. *Ocean Modelling*, **25**, 154–171, doi:10.1016/j.ocemod.2008.07.006.
- Raubenheimer, B., R. Guza, and S. Elgar, 1996: Wave transformation across the inner surf zone. *Journal of geophysical research*, **101**, 25589–25.
- Reul, N. and B. Chapron, 2003: A model of sea-foam thickness distribution for passive microwave remote sensing applications. *J. Geophys. Res.*, **108**, 3321, doi:10.1029/2003JC001887.
- Reul, N., J. Tenerelli, B. Chapron, D. Vandemark, Y. Quilfen, and Y. Kerr, 2006: Smos satellite l-band radiometer: A new capability for ocean surface remote sensing in hurricanes. *J. Geophys. Res.*, **117**, C02006.
- Rogers, W. E., A. V. Babanin, and D. W. Wang, 2012: Observation-consistent input and whitecapping dissipation in a model for wind-generated surface waves: Description and simple calculations. *J. Atmos. Ocean Technol.*, **29**, 1329–1346.
- Rozenberg, A. and M. Ritter, 2005: Laboratory study of the fine structure of short surface waves due to breaking: Two-directional wave propagation. *J. Geophys. Res.*, **110**, C02011.
- Ruessink, B. G., D. J. R. Walstra, and H. N. Southgate, 2003: Calibration and verification of a parametric wave model on barred beaches. *Coastal Eng.*, **48**, 139–149.
- Saha, S., S. Moorthi, H.-L. Pan, X. Wu, J. Wang, S. Nadiga, P. Tripp, R. Kistler, J. Woollen, D. Behringer, H. Liu, D. Stokes, R. Grumbine, G. Gayno, J. Wang, Y.-T. Hou, H. ya Chuang, H.-M. H. a. J. S. Juang, M. Iredell, R. Treadon, D. Kleist, P. V. Delst, D. Keyser, J. Derber, M. Ek, J. Meng, H. Wei, R. Yang, S. Lord, H. van den Dool, A. Kumar, W. Wang, C. Long, M. Chelliah, Y. Xue, B. Huang, J.-K. Schemm, W. Ebisuzaki, R. Lin, P. Xie, M. Chen, S. Zhou, W. Higgins, C.-Z. Zou, Q. Liu, Y. Chen,

- Y. Han, L. Cucurull, R. W. Reynolds, G. Rutledge, and M. Goldberg, 2010: The NCEP Climate Forecast System Reanalysis. *Bull. Amer. Meteorol. Soc.*, **91**, 1015–1057.
- Scaramuzza, D., A. Martinelli, and R. Siegwart, 2006: A flexible technique for accurate omnidirectional camera calibration and structure from motion. *Computer Vision Systems, 2006 ICVS '06. IEEE International Conference on*, 45–45.
- Sénéchal, N., H. Dupuis, P. Bonneton, H. Howa, and R. Pedreros, 2001: Observation of irregular wave transformation in the surf zone over a gently sloping sandy beach on the french atlantic coastline. *Oceanol. Acta*, **24**, 545–556.
- Sharma, J. N. and R. G. Dean, 1993: Second order directional wave kinematics in shallow water. *Ocean wave measurement and analysis, Proc. WAVES'93 Conf.*, 165–179.
- Shih, S.-W., Y.-P. Hung, and W.-S. Lin, 1993: Accurate linear technique for camera calibration considering lens distortion by solving an eigenvalue problem. *Optical Engineering*, **32**, 138–149.
- Smith, J., 1986: Short surface waves with growth and dissipation. *J. Geophys. Res.*, **91**, 2616–2632.
- Smith, M., P. Park, and I. Consterdine, 1993: Marine aerosol concentrations and estimated fluxes over the sea. *Quarterly Journal of the Royal Meteorological Society*, **119**, 809–824.
- Song, J.-B. and M. L. Banner, 2002: On determining the onset and strength of breaking for deep water waves. Part I: Unforced irrotational wave groups. *J. Phys. Oceanogr.*, **32**, 2541–2558.
- St Denis, M. and W. J. Pierson Jr, 1953: On the motions of ships in confused seas. Technical report, DTIC Document.
- Stansell, P. and C. MacFarlane, 2002: Experimental investigation of wave breaking criteria based on wave phase speeds. *J. Phys. Oceanogr.*, **32**, 1269–1283.
- Stewart, R., 1960: Changes in the form of short gravity waves on long waves and tidal currents. *J. Fluid Mech.*, **8**, 565–585.
- Stoyanov, D., 2010: Camera calibration toolbox for matlab. *Royal Society/Wolfson Foundation Medical Image Computing Laboratory, Imperial College London, UK*.
- Stramska, M. and T. Petelski, 2003: Observations of oceanic whitecaps in the north polar waters of the atlantic. *Journal of Geophysical Research: Oceans*, **108**.
- Strobl, K., W. Sepp, S. Fuchs, C. Paredes, and K. Arbter, 2006: Camera calibration toolbox for matlab. *Pasadena, CA*.
- Sutherland, P. and W. K. Melville, 2013: Field measurements and scaling of ocean surface wave-breaking statistics. *Geophysical Research Letters*.

- Tanaka, M., 1983: The stability of steep gravity waves. *J. Phys. Soc. Japan*, **52**, 3047–3055.
- 1985: The stability of steep gravity waves. Part 2. *J. Fluid Mech.*, **156**, 281–289.
- Terray, E., M. Donelan, Y. Agrawal, W. Drennan, K. Kahma, A. Williams, P. Hwang, and S. Kitaigorodskii, 1996: Estimates of kinetic energy dissipation under breaking waves. *Journal of Physical Oceanography*, **26**, 792–807.
- Thomson, J., J. R. Gemmrich, and A. T. Jessup, 2009: Energy dissipation and the spectral distribution of whitecaps. *Geophysical Research Letters*, **36**, L11601.
- Thomson, J. and A. T. Jessup, 2008: A fourier-based method for the distribution of breaking crests from video observations. *J. Atmos. Ocean Technol.*, **26**, 1663–1671.
- Thornton, E. B. and R. T. Guza, 1983: Transformation of wave height distribution. *J. Geophys. Res.*, **88**, 5,925–5,938.
- Tsai, R., 1987: A versatile camera calibration technique for high-accuracy 3d machine vision metrology using off-the-shelf tv cameras and lenses. *Robotics and Automation, IEEE Journal of*, **3**, 323–344.
- Tulin, M. P. and T. Waseda, 1999: Laboratory observations of wave group evolution, including breaking effects. *Journal of Fluid Mechanics*, **378**, 197–232.
- Unna, P., 1947: Sea waves. *Nature*, **159**, 239–242.
- van der Westhuysen, A. J., M. Zijlema, and J. A. Battjes, 2005: Implementation of local saturation-based dissipation in SWAN. *Proceedings of the 5th International Symposium Ocean Wave Measurement and Analysis, Madrid, June 2005*, ASCE.
- 2007: Saturation-based whitecapping dissipation in SWAN for deep and shallow water. *Coastal Eng.*, **54**, 151–170.
- van Vledder, G. P., 2006: The WRT method for the computation of non-linear four-wave interactions in discrete spectral wave models. *Coastal Eng.*, **53**, 223–242.
- Vandemark, D., B. Chapron, J. Sun, G. H. Crescenti, and H. C. Graber, 2004: Ocean wave slope observations using radar backscatter and laser altimeters. *J. Phys. Oceanogr.*, **34**, 2825–2842.
- Vezhnevets, V., 2005: Gml matlab camera calibration toolbox.
- Webb, S. and C. Cox, 1986: Observations and modeling of seafloor microseisms. *Journal of Geophysical Research: Solid Earth (1978–2012)*, **91**, 7343–7358.
- Wei, G.-Q. and S. Ma, 1993: A complete two-plane camera calibration method and experimental comparisons. *Computer Vision, 1993. Proceedings., Fourth International Conference on*, IEEE, 439–446.

- Wheatstone, C., 1853: On the binocular microscope, and on stereoscopic pictures of microscopic objects. *Transactions of The Microscopical Society & Journal*, **1**, 99–102.
- Wilson, D. K., G. V. Frisk, T. E. Lindstrom, and C. J. Sellers, 2003: Measurement and prediction of ultralow frequency ocean ambient noise off the eastern u.s. coast. *J. Acoust. Soc. Am.*, **113**, 3117.
- WISE Group, 2007: Wave modelling - the state of the art. *Progress in Oceanography*, **75**, 603–674.
- Young, I. R. and A. V. Babanin, 2006: Spectral distribution of energy dissipation of wind-generated waves due to dominant wave breaking. *J. Phys. Oceanogr.*, **36**, 376–394.
- Yurovskaya, M. V., V. A. Dulov, B. Chapron, and V. N. Kudryavtsev, 2013: Directional short wind wave spectra derived from the sea surface photography. *J. Geophys. Res.*, in press.
- Zakharov, V. E., 1968: Stability of periodic waves of finite amplitude on the surface of a deep fluid. *J. Appl. Mech. Tech. Phys.*, **2**, 190–194.
- Zhang, Z., 1999: Flexible camera calibration by viewing a plane from unknown orientations. *Computer Vision, 1999. The Proceedings of the Seventh IEEE International Conference on*, volume 1, 666–673 vol.1.